Aqueous Synthesis and Computational Modelling of Metal Oxide Nanostructures for Gas Sensing Applications

A thesis submitted in fulfilment of the requirements for the degree of Doctor of Philosophy

Michael Breedon

BAppSci, RMIT University

BAppSci, RMIT University

GCRC, RMIT University

School of Electrical and Computer Engineering

Science, Engineering and Health Portfolio

RMIT University

Melbourne, Australia

August, 2010

Author's Declaration

I certify that except where due acknowledgement has been made, the work is that of the author alone; the work has not been submitted previously, in whole or in part, to qualify for any other academic award; the content of the thesis is the result of work which has been carried out since the official commencement date of the approved research program; any editorial work, paid or unpaid, carried out by a third party is acknowledged; and, ethics procedures and guidelines have been followed.

_____

Michael Breedon

August, 2010

Acknowledgements

First and foremost, I would like to thank my primary supervisor Associate Professor Kourosh Kalantar-zadeh for his tireless encouragement, support, and patience during my PhD candidature. I am also grateful for his enthusiasm, in particular, motivating me to apply for both the RMIT business plan competition and the Australian Endeavour research fellowships. Special thanks also go to my secondary supervisors Dr. Michelle Spencer, Professor Wojtek Wlodarski, and Professor Irene Yarovsky, for their support, enthusiasm, and patience during my PhD studies. I am truly indebted to all of my PhD research supervisors who have bestowed upon me, far more than the technical means to complete this thesis.

I would like to thank the Australian government for supporting me via the Commonwealth research training scheme to pursue a graduate certificate in research commercialisation, as well as a 6 month research fellowship at the University of Tokyo via the Endeavour award program. I am grateful to Associate Professor Masakazu Sugiyama from the Department of Engineering, University of Tokyo and Professor Yoshiaki Nakano for hosting me during my research fellowship. During my stay I was indebted to many Nakano-Sugiyama-Tanemura laboratory members, for not only their friendship and technical expertise, but also for assisting me in the complexities of day to day living in Tokyo: Mr. Ling-Han Li, Dr. Hassanet Sodabanlu, Ms. Ikue Hirata, Mr. Tatsuki Fujiwara, and Dr. Wang Tunpeng.

I am grateful to Professor Norio Miura from Kyushu University for his hospitality during visits to his laboratory, and assistance with securing my JSPS Postdoctoral Fellowship.

I would like to thank past and present Sensors, and Molecular Modelling laboratory members. Special thanks go to the following people for their continuing friendship, advice, and occasionally delicious cooking: Mr. Hanif bin Yaacob, Mrs. Mahnaz Shafiei, Mrs. Ling He (DSP lab), Dr. Abu Zafar Md Sadek, Mr. Kester Wong, Mr. Jerry Yu, Dr. Rashidah Arsat, Dr. Glenn Matthews, Dr. Samuel Ippolito, Mr. Chen Zhang, Mr. Muhammad Zamharir Ahmad, Mr. Jian Zhen Ou, and last but not least Mr. Hai Dong Zheng. I would also like to extend my gratitude to the visiting researchers hosted by RMIT during my PhD candidature: Dr. Xiaofeng Yu from the Chinese Academy of Sciences,

Mohammad Rahmani from Ferdowsi University of Mashhad, and Ms. Audrey Chapelle from the CIRIMAT-Carnot Institute, for their continuing friendship, good humour and cultural exchange.

I would like to thank RMIT University and The University of Tokyo for giving me the opportunity to travel to Taiwan (Taipei), Japan (Takamatsu, Tokyo), and USA (San Francisco) to present my research findings.

I would like to extend my gratitude to the RMIT MMTC staff for their technical assistance and guidance, with a special thanks to Mr. Paul Jones and Mr. Yuxun Cao for teaching me the tricks of the trade. I am also grateful to Dr. Matt Taylor and Dr. Desmond Lau, for their invaluable training and introducing me to the fascinating world of transmission electron microscopy. I am also very grateful to the RMIT RMMF staff: Professor Dougal McCulloch, Mr. Phil Francis, Mr. Peter Rummel for, training and access to their powerful electron microscopes.

I would also very much like to express my sincere gratitude to Dr Kay Latham and Associate Professor Colin Rix, from the department of chemistry for their assistance and advice during my undergraduate years, and later throughout my PhD.

Special thanks to go my parents Chris and Jane; my three younger sisters Amy, Ruth and Alice; and my grandparents: Bill and Muriel Povey, and Denis and Maureen Breedon; for their love and support. I would also like to thank my close friends for understanding that sometimes a PhD candidate must work on weekends.

Last but not least, I would like to thank my predecessors; for without their contribution to the body of knowledge, I would have very little to write about...

Michael Breedon (Age 26)

Abstract

In this thesis, the author pursued a holistic, multi-faceted approach to the development of ZnO, WO_3 and $WO_3 \cdot nH_2O$ nanostructures grown from aqueous chemical techniques, and their application to nitrogen dioxide (NO_2) and hydrogen (H_2) gas sensing; and understanding the adsorption processes of nitrogen oxides (NO_x) on ZnO nanomaterials with Density Functional Theory (DFT).

Several new deposition techniques were developed for the fabrication of corrugated ZnO nanorods from sodium hydroxide driven solutions; and interconnected ZnO nanowires, fabricated via a two-step spray pyrolysis and hydrothermal ZnO growth method. The choice of seed/nucleation layer used during the hydrothermal ZnO deposition was investigated by the author, and was identified to be a major variable in the resultant nanostructured morphology. The use of hemispherically terminated seed/nucleation layers resulted in arrays of nanorods emanating perpendicularly from the plane of the substrate. Interestingly, rougher polygonal seed/nucleation layers were found to facilitate the growth of an interconnected nanostructured morphology. To the best of the author's knowledge, the correlation between seed/nucleation layer texture and the resultant nanostructures was reported for the first time.

A search of current literature revealed that many nanostructured WO_3 deposition techniques required the use of expensive, dangerous or exotic reagents. Hence, deposition from existing methods remained an unfavourable proposition. Considering this, the author pursued the development of an aqueous deposition method capable of forming a nanostructured thin film via inexpensive and relatively innocuous chemical precursors. This led to the development of two new methods: the first being a successive ionic layer adsorption reaction; and the second, a sol-gel method. A thorough analysis was performed on the deposited materials, with the author concluding that the humidity of the atmosphere, in which the samples were dried, had a significant impact on both the nanostructured morphology and the crystallography of the resultant nanostructures.

Using the developed deposition techniques, conductometric gas sensors based on nanostructured ZnO and WO_3 were fabricated, and evaluated towards H_2 and NO_2. ZnO nanorod arrays demonstrated the

highest sensitivity of the developed sensors towards NO_2. Reducing the dimensions of the ZnO nanomaterial further, to an interconnected nanowire array, made it possible to reduce the operational temperature of the sensor by almost 60%, with only a marginal decrease in sensitivity. Optical gasochromic H_2 sensors based on Pt/WO_3 thin films exhibited excellent baseline stability, and the low operational temperature of 100 °C, showing promise for remote and/or harsh environment sensing applications. All developed sensors were assessed towards H_2 concentrations ranging from 0.06 to 1% (600 to 10000 ppm), in a balance of synthetic air. NO_2 sensors were tested towards concentrations ranging from 0.5 to 10 ppm, also in a balance of synthetic air. The concentration ranges investigated were below the lower explosive threshold of H_2, and below NO_2 concentrations that cause negative physiological effects in healthy adults.

The use of DFT to investigate gas sensing mechanisms enabled the author, to examine gas interactions of NO_x molecules and its dissociation products with the ZnO($2\bar{1}\bar{1}0$) surface at the atomic scale. Charge transfer between the surface and adsorbate molecule/atom was found to occur, regardless of the strength of adsorption. The direction of the charge transferwas in good agreement with experimentally observed sensor resistance changes during exposure to NO_2. The calculated binding energies of atomic N and O onto the ZnO($2\bar{1}\bar{1}0$) surface were indicative of chemisorption. Bonding occurred preferentially between the atomic adsorbate, and two or more surface oxygen or zinc atoms. For these atomic species, large changes to the surface geometry were observed, indicating a potential poisoning of the surface. It was found that NO and NO_2 preferentially physisorbed onto ZnO($2\bar{1}\bar{1}0$), over one or more surface zinc atoms, with minimal changes to the surface geometry. On oxygen defect containing ZnO($2\bar{1}\bar{1}0$) surfaces, NO_2 typically chemisorbed onto the defect site zinc atoms, leading to significant surface reconstruction. The NO_2 molecule adsorbed onto the defect surface via two or more zinc atoms, located around the defect site. These theoretical calculations and observations provided a valuable insight into the sensing mechanism of ZnO nanostructure based devices. Comparisons between experimental and theoretical observations were made whenever possible.

List of Tables

List of Figures

Chapter 1- Introduction

In this chapter, the motivation for this PhD work will be presented; covering the justification for sensing hydrogen and oxides of nitrogen, the formation of nanostructured zinc oxide and tungsten trioxide for low concentration gas sensing, and finally, density functional theory studies of N, O, NO and NO_2 adsorption on ZnO.

1.1 Motivation

Recently there has been a resurgence of interest in the environment and environmental responsibility, with many sectors beginning to adopt technologies to reduce the environmental impact of their processes and products. The automotive sector is one such industry that has been forced to adopt emission targets for their products. Carbon dioxide has been long considered an environmental pollutant targeted for emission reduction, whilst nitrogen containing oxides (NO_x) have only been included in the European automotive emission standards since its third implementation in 2000 (Table 1.1), indicating a shift in regulatory awareness of the pollutant. Locally, annual Australian NO_x emissions have been calculated by the Australian Government's Department of the Environment, Water, Heritage and the Arts to be 780,000 ton/year from industry and 620,000 ton/year from non-industrial sources [1]. In addition to NO_x sensing, hydrogen sensing will also be studied.

Hydrogen gas, while not considered a pollutant itself, has been touted as the panacea for the next generation of clean energy technologies. The current generation of hydrogen powered vehicles consume hydrogen chemically in fuel cells or via the combustion of the gas with air in modified internal combustion engines. Hydrogen storage for stationary and automotive applications have a number of unique engineering and safety requirements, which will be further discussed in § 1.1.2. Preference in technology aside, a large volume of hydrogen gas will be required to maintain useful fuel tank ranges. Furthermore, given the potential volatility of hydrogen, low concentration sensing and monitoring will be of paramount importance to ensure a smooth transition to hydrogen's ubiquitous use.

Table 1.1. Current and future Euro NO_x emission standards for passenger vehicles [2-3]; positive ignition refers to standard four cycle engines, compression ignition denotes diesel engines.

Standard and year implemented	Positive ignition NO_x mg/km	Compression ignition NO_x mg/km
Euro 1 (1992)	-	-
Euro 2 (1996)	-	-
Euro 3 (2000)	150	500
Euro 4 (2005)	80	250
Euro 5 (2009)	60	180
Euro 6 (planned)	60	60

In § 1.1.1 and § 1.1.2, the industrial and domestic applications as well as environmental, and health impacts of nitrogen containing oxides and hydrogen gas will be discussed.

1.1.1 Nitrogen Containing Oxides (NO_x)

Nitric oxide (NO) and nitrogen dioxide (NO_2) emissions occur from both natural and anthropogenic sources [4]. Natural sources include but are not limited to: emission from bacteria, volcanic activity, and lightning. Similarly, anthropogenic sources include but are not limited to: power generation, heating, and internal combustion engines in both automobile and naval applications. Direct applications of NO are scarce with the most notable application in the Ostwald process as a feedstock in the industrial synthesis of nitric acid. Under ambient conditions, i.e. in the presence of oxygen, NO spontaneously oxidises forming NO_2, limiting potential applications. Commercial applications of NO_2 are limited, with uses including nitrogen containing precursors, rocket fuel, and the bleaching of flour [5]. Both NO and NO_2 are major contributors to acid rain generation and disruptors to atmospheric processes, such as those governing atmospheric ozone concentrations [4]. NO and NO_2 having been identified as toxic, irritating gases posing significant risks to those suffering respiratory ailments. The WHO's 2005 air quality guidelines have identified that as free radicals, they have the potential to deplete tissue antioxidant defences and as a result, cause injury and inflammation [4]. During acute controlled exposures, concentrations of nitrogen dioxide in excess of 1.0 ppm are known

to induce changes in pulmonary function in healthy adults. On repeated exposure to high concentrations of NO_2 (1–5 ppm) there is some evidence of increased breathing frequency and reduced lung gas exchange capability [4].

Given the ever increasing focus on environmental culpability it is imperative to develop low cost highly sensitive NO_2 sensors which rely on conductometric sensing principles offering excellent compatibility with existing monitoring and sensor packaging systems. When combined with wireless communication systems and appropriate supporting technologies it is possible to create inexpensive NO_x monitoring networks. Such systems could, when coupled with photovoltaic and accumulator battery technology, offer the promise of distributed self supporting sensing networks capable of generating the raw data which can be used to create localised 'pollution' maps. Furthermore, many NO_2 sensors which are suitable for environmental monitoring systems can also be employed for enclosed space monitoring systems. Most recently, there has been interest in applying NO_2 gas sensors for in-car cabin monitoring systems, which when linked with climate control systems can be used to minimise in-car NO_2 accumulation during traffic congestion. Thus, it is important to develop gas sensors which are capable of sensing concentrations below thresholds at which negative physiological effects occur, typically occurring at sub ppm concentrations. The sensor should also operate over a broad range of concentrations so that it does not become over burdened during sensing operations, inevitably failing to respond to large concentration increases.

1.1.2 Hydrogen Gas (H_2)

While the primary motivation and focus of this thesis is concerned with NO_2 sensing, some of the developed sensors were also tested for their hydrogen sensing ability. Hydrogen (H_2) is a colourless odourless gas with an lower and upper explosive limit of 4% - 74% by volume, respectively [5]. The industrial use of H_2 as a feedstock and reagent is widely adopted, with many applications including: the synthesis of ammonia (via the Haber process), methanol production, hydrochloric acid synthesis, the reduction of metal oxides in metallurgical application, the hydrogenation of oils and fats, high temperature welding, and many other specialised applications [5]. Despite the myriad of applications, there are a number of issues regarding the confinement of H_2. Due to its small size, H_2 is capable of

absorbing into most metals, embrittling them, which effectively renders the metal mechanically weakened. This is of serious concern for H_2 gas storage tanks, a necessary component in forthcoming H_2 powered vehicles. Given the impending H_2 fuel revolution there is a strong need to develop stable and sensitive gas sensors capable of accurately sensing leaks in enclosed spaces, such as those that may occur in vehicles. Considering the wide scale adoption of H_2 in an industrial sense, as well as the potential applications in H_2 powered vehicles it is important to develop sensor prototypes which are capable of detecting below the lower explosive limit concentrations of H_2.

1.2 Gas Sensors

The use of sensors greatly influences areas such as environmental monitoring, domestic safety, national security, aerospace and automotive applications. Advances in regulatory policy have forced the widespread adoption of gas sensors in niche applications. Mandates such as the automotive exhaust sensors to combat pollution, natural gas leak detectors fitted to towering apartment complexes in earth quake prone regions, enclosed space oxygen level monitoring for worker safety, and atmospheric pollution monitoring stations are all pitched at improving safety and quality of life for the broader community. Gas sensors exist to sense external stimuli, such as the presence of adsorbed gas molecules into ‘useful’ electrical signals which can then be amplified or directly interpreted by ancillary devices. Traditional gas sensors employ a sensitive material which is typically a polycrystalline metal oxide sensitive layer for sensing of the target gas (target analyte). Ideally, the metal oxide should be exclusively sensitive to the target analyte, mechanically robust, inexpensive, and incapable of interacting with other ambient gases present. The sensitive metal oxide element employed should be affected by the introduction of the target analyte, undergoing complex physiochemical changes on the surface of the sensing element. Such surface bound physiochemical changes include but are not limited to: withdrawal or donation of electron density to and from the sensing surface and the target analyte itself [6-7], changes in carrier density and or carrier mobility [8-9], pre adsorbed species [10], and others. These changes can alter electrical characteristics of the sensing element such as the output voltage, frequency, resistance, capacitance, or current generated.

These subtle electrical signals can be manipulated to drive analogue instrumentation or digitised, effectively integrating with computerised monitoring systems.

1.3 Gas Sensor Technologies

A number of different sensors have been developed for sensing the NO_x family of gases such as NO and NO_2, as well as H_2. Based on the application and sensing environment, a number of different sensors are available when considering electrically based technologies. Conductive polymers for example, are suitable for room temperature detection; impedance and solid state electrochemical gas sensors are well suited to the harsh sensing environments found in engine exhaust systems; surface acoustic wave based sensors and quartz crystal microbalance sensors are suitable for highly sensitive stationary sensing systems. A brief summary and comparison of popular sensing platforms is presented in Table 1.2.

Table1.2. A brief summary of popular electrical sensor technologies utilised in gas sensing applications.

Technology	Measured Output	Advantages	Disadvantages
Metal oxide conductometric	Resistance	Simple, robust, inexpensive, sensitive, fast response and recovery, long operational lifespan	High operating temperature 150 °C - 300 °C, metal oxides or composites may be poisoned by interferrant gases
Conducting polymer conductometric	Resistance	Room temperature operation, simple, inexpensive	Polymers can degrade at > 80 °C, slow response, and in some applications can only be employed for single use detection purposes
Catalytic combustion	Resistance	Simple, robust, compact, sensitive to most combustible gases	Catalyst degrades, high operating temperature, poor selectivity
Surface acoustic wave device	Frequency	High sensitivity, fast response and recovery	May require high temperatures, influenced by stray mechanical vibrations and electromagnetic interference, requires a frequency counter
Quartz crystal microbalance or cantilever technology	Frequency	Simple, capable of sensing ppb concentrations, well suited to sensing high molecular weight molecules	Influenced by stray mechanical vibrations, and electromagnetic interference, requires a frequency counter
Solid state electrochemical	Voltage	Extremely stable, long operational life span	High operating temperatures, can be bulky in nature
Impedance based	Current	Capable of operating in harsh environments, compatible with high resistance materials	Complex measurement and interpretation system required

1.3.1 Synthesis of Metal Oxide Nanostructures for Gas Sensing

There has been a recent well documented trend in the current body of scientific knowledge concerned with the application of nanomaterials in gas sensing applications, with aspirations of improving sensitivity, response and recovery time, dynamic performance, and sensing thresholds [8-9, 11-12]. As dimensions shrink from micro dimensional or larger (i.e. bulk) to the nano dimensional realm, a number of unexpected deviations from the properties observed in their 'bulk' form occurs, namely, electrical, optical and mechanical properties change [13]. Briefly, the reduction from micro to nano dimensional crystallite size affords an increase in surface area to volume ratio, as can be seen in Figure 1.1 the same physical transducer when coated with nanomaterials such as nanowires or nanoplatelets occupy the same physical area as a traditional thin film, but have an intrinsically higher surface area than their thin film counterparts. Hence, a surface area increase of several orders of magnitude can be realistically achieved. The increased surface area also increases the number of available surface reaction sites for the adsorption of gas species, leading to faster sensor response and recovery.

Two different metal oxides were examined in detail by the author during this PhD; zinc oxide and tungsten oxide.

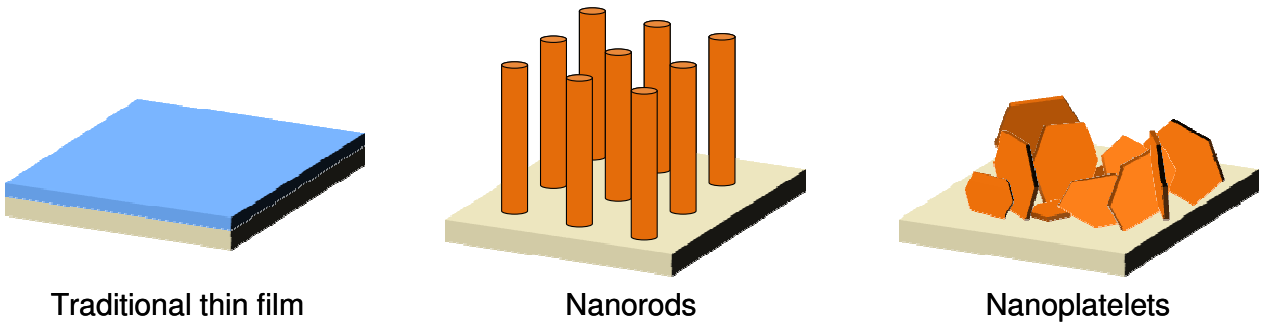

Figure 1.1. The same transducing platform covered in different materials. (not to scale).

Many different morphologies of low dimensional zinc oxide (ZnO) structures have been synthesized [1], and it has been demonstrated that nanostructured ZnO is a suitable candidate for many applications including: piezoelectric power generators [2], resonators and cantilevers [3, 4], one dimensional transistors [5], gas sensors [6], biosensors [5, 7], optical devices [9, 10], solar cells [11],

and many others [12]. However, controlled fabrication of one-dimensional metal oxide nanostructures is still one of the most important technological hurdles for the development of ZnO based nanodimensional devices. There is a distinct absence of low dimensional ZnO nanostructures grown via purely aqueous chemical techniques in the literature which can be scaled to produce coatings of ZnO nanomaterials on large substrate sizes. During the course of this PhD the author has developed a number of different wet chemical deposition techniques. Typically aqueous in nature, these deposition techniques use a soluble metal salt, water and often acid/base to drive deposition. The developed nanostructured metal oxide thin films were characterised using a number of different analytical techniques to elucidate their material properties.

Tungsten trioxide (WO_3) is an intrinsically semiconducting metal oxide, capable of withstanding low pH environments and high temperatures making them excellent choices for robust, nanostructured, inorganic frameworks. WO_3 has been fabricated via a number of different experimental routes which include, but are not limited to: acid precipitation [14-15], chemical etching [16], sol-gel [17], thermal evaporation [18], RF-sputtering [19], chemical vapor deposition (CVD) [20], anodization [21-22], electrodeposition [23], electrospinning [24], pulsed laser deposition [25], and hotwire CVD [26]. However, each of these methods has one or more characteristic drawbacks including: high power consumption, the presence of a vacuum or the need for exotic and often dangerous reagents. Some of these methods are also unable to generate nano-crystalline tungsten oxide morphologies and many methods are capable of only producing loose nano powders, which must be redispersed onto the transducer platform often resulting in incomplete transducer surface coverage. The formation of adherent nanostructured tungsten oxide thin films will be demonstrated using innocuous reagents via an aqueous sol-gel technique.

After successfully developing and adapting a number of new metal oxide deposition techniques, deposited materials were assessed for their ability to sense nitrogen dioxide and hydrogen in realistic operating conditions. Nitrogen dioxide and hydrogen were sensed using zinc oxide and tungsten oxide nanostructured thin films over a wide range of concentrations, with aspirations of developing inexpensive and sensitive sensors. Given the negative impacts that both gases pose either physiologically or environmentally, the author has pursued sensing concentrations below those at

which either gas will pose a significant environmental or health risk. It is important to note that NO readily oxidises in air, forming NO_2 and as such only NO_2 sensing is considered.

1.3.2 Density Functional Theory Studies

Density Functional Theory (DFT) is a powerful theoretical physics/chemistry tool which can be applied to study systems with typically less than one thousand atoms. In DFT simulations each atom is treated quantum mechanically, and are given three dimensional freedom so that individual atoms interact with each other and are reorganised into energetically favourable configurations. It is possible to apply DFT for surface adsorption studies, focusing on a particular molecule adsorbing onto a well defined crystal face, in this thesis N, O, NO, NO_2 and ZnO($2\bar{1}\bar{1}0$), as well as NO_2 onto ZnO($2\bar{1}\bar{1}0$)-V_O have been chosen. Zinc oxide based gas sensors sensing NO and NO_2 can suffer from poor long term stability. Initially sensors demonstrate excellent response and recovery characteristics with large changes in resistance. However, over time sensors deteriorate, with smaller resistance changes to the same concentration of gas and slower sensor response and recovery. The mechanism of this degradation and the actual adsorption mechanism of NO_2 on ZnO is poorly known. The author has delved into the atomistic realm of density functional theory to study the adsorption process in detail, providing valuable insights into the sensing mechanism. While it is computationally not feasible to simulate a complete nanorod due to the number of atoms involved, it is possible to represent the crystal faces present on a ZnO nanorod, by taking the smallest repetitious crystallographic representation of ZnO, i.e. the unit cell. A schematic representation of a ZnO nanorod and its corresponding crystal faces is presented in Figure 1.2. Density functional theory exploits a crystalline material's periodic nature, the unit cell, effectively extending it infinitely in the *-x*, *-y* and *-z* directions, replicating a continuous crystal face. The modelled ZnO nanorods are hexagonal (wurtzite) in crystal structure as depicted in Figure 1.2, with well defined crystal facets being {0001}, {$10\bar{1}0$}, and {$2\bar{1}\bar{1}0$}. Naturally the high aspect ratio of the nanorods, typically 10:1, determines the significance that the crystal face will play during gas sensing, with the higher surface area non-polar ZnO{$10\bar{1}0$} and ZnO{$2\bar{1}\bar{1}0$} facets are of the greatest interest. The ZnO($2\bar{1}\bar{1}0$) crystal face will be studied with aspirations of elucidating the adsorption interactions of NO and NO_2, and where appropriate

theoretical and experimental results shall be compared. Hydrogen gas sensing has not been modelled, as the adsorption of H_2 onto ZnO surfaces has been described in detail by multiple groups elsewhere [27-30].

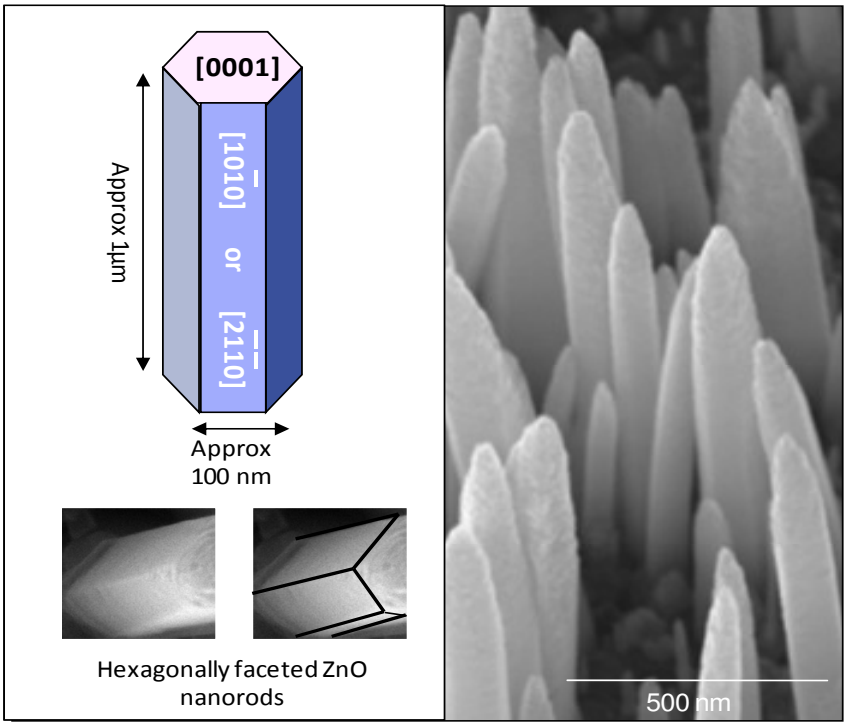

Figure 1.2. ZnO nanorods and their respective crystal faces.

1.4 Objectives

Throughout his candidature the author has utilised aqueous chemical techniques for the growth of nanostructured ZnO and WO_3. Low concentration NO_2 and H_2 gas sensing utilising nanostructured ZnO and WO_3 was explored, typically in the sub ppm regime. The adsorption of NO_x onto the ZnO(2$\bar{1}\bar{1}$0) crystal face was also investigated to understand the complex physiochemical processes which occur on the surface of the sensing element. The primary objectives of this PhD work include:

- The development of safe, inexpensive, environmentally friendly, scalable chemical methods for the deposition of nanostructured metal oxides.
- The development of novel nanostructured ZnO thin films, with aspirations of creating high density, high surface area morphologies.

- Fabrication of nanostructured thin films on conductometric transducing platforms and their assessment for gas sensing of NO_2 and H_2 at low concentrations.

- The application of catalytically coated nanotextured thin films for optical gas sensing applications exploiting the gasochromic effect will be explored as a suitable candidate for low concentration (<1%) H_2 sensing.

- A number of complex scientific instruments will be used to characterise the nanostructured metal oxides synthesised by the author: Scanning Electron Microscopy (SEM), X-Ray Photoelectron Spectroscopy (XPS), X-Ray Diffraction (XRD), Transmission Electron Microscopy (TEM), and Selected Area Electron Diffraction (SAED) will be used to characterise the developed materials. As the stoichiometry of WO_3 is troublesome to accurately elucidate, Raman spectroscopy will be utilised to differentiate between pure WO_3 and $WO_3 \cdot nH_2O$, where n = ⅓, ½, 1, 2.

- The Vienna *Ab-initio* Simulation Package (VASP) a density functional theory code, will be used to gain an insight into the gas adsorption mechanism, movement of electronic charge between the adsorbate molecule and the metal oxide surface, providing information on the type of bonding which exists between the adsorbate and the surface, and to calculate binding energies and vibrational frequencies which may be useful for experimental comparison. Where possible a comparison between theoretical insights and experimental observations will be made, with aspirations of determining experimental parameters which could be altered for enhanced sensing performance.

1.5 Thesis Organisation

This thesis aims to provide the reader with an appreciation for the synthesis of nanostructured metal oxides from environmentally friendly synthetic routes, and to understand the adsorption process of N, O, NO and NO_2 onto the ZnO($2\overline{1}\overline{1}0$) surface and NO_2 on the ZnO($2\overline{1}\overline{1}0$)-$V_O$ surface. This thesis is divided into eight chapters with Chapter 1 providing an introduction; Chapter 2 provides the reader with an appreciation of the historical rise of ZnO and WO_3 in sensing applications, as well as the recent use of nanostructured materials in gas sensing applications. In Chapters 3 and 4, density functional theory and its application to gas sensing surface reactions are presented, providing valuable insights into the gas adsorption process and the associated gas sensing mechanism. Chapters 5 and 6 encompass the synthesis and characterisation of nanostructured metal oxide for gas sensing applications. The gas sensing results of the nanostructured materials developed by the author is presented in Chapter 7 and are linked with the results discussed in Chapter 4, before concluding this work with Chapter 8.

1.6 References

[1] The department of the environment, heritage and the arts - National Pollutant Inventory. (2008, 13/04/2010). *Oxides of Nitrogen Summary - All sources: Australia*.

[2] E. Comission, "Current and future european community emission requirements," 2003.

[3] *Regulation No. 715/2007 on type approval of motor vehicles with respect to emissions from light passenger and commercial vehicles (Euro 5 and Euro 6) and on access to vehicle repair and maintenance information,* European Union, 2007.

[4] A. P. Francesco Forastiere, Frank J. Kelly, Stephen T. Holgate, *Air Quality Guidelines Global Update*: World Health Organisation, 2005.

[5] P. Patnaik, *Handbook of Inorganic Chemicals*, 1st ed.: McGraw-Hill, 2003.

[6] M. Breedon*, et al.*, "Adsorption of NO and NO_2 on the ZnO($2\bar{1}\bar{1}0$) surface: A DFT study," *Surface Science,* vol. 603, pp. 3389-3399, 2009.

[7] M. Breedon*, et al.*, "Adsorption of atomic nitrogen and oxygen on surface: A density functional theory study," *Journal of Physics Condensed Matter,* vol. 21, 2009.

[8] C. Baratto*, et al.*, "Metal oxide nanocrystals for gas sensing," *Sensors and Actuators B: Chemical,* vol. 109, pp. 2-6, 2005/8/24 2005.

[9] I. Simon, *et al.*, "Micromachined metal oxide gas sensors: opportunities to improve sensor performance," *Sensors and Actuators B: Chemical*, vol. 73, pp. 1-26, 2001.

[10] N. Barsan*, et al.*, "Metal oxide-based gas sensor research: How to?," *Sensors and Actuators B: Chemical,* vol. 121, pp. 18-35, 2007.

[11] E. Comini, "Metal oxide nano-crystals for gas sensing," *Analytica Chimica Acta,* vol. 568, pp. 28-40, 2006.

[12] G. Eranna*, et al.*, "Oxide materials for development of integrated gas sensors - A comprehensive review," *Critical Reviews in Solid State and Materials Sciences,* vol. 29, pp. 111-188, 2004.

[13] K. Kalantar-zadeh, F. Benjamin, *Nanotechnology-Enabled Sensors*, Springer, 2008.

[14] A. Chemseddine*, et al.*, "Anisotropic $WO_3 \cdot nH_2O$ layers deposited from gels," *Journal of Non-Crystalline Solids,* vol. 91, pp. 271-278, 1987.

[15] T. Kida*, et al.*, "Highly sensitive NO_2 sensors using lamellar-structured WO_3 particles prepared by an acidification method," *Sensors and Actuators B: Chemical,* vol. 135, pp. 568-574, 2009.

[16] E. Widenkvist*, et al.*, "Synthesis of nanostructured tungsten oxide thin films," *Crystal Growth & Design,* vol. 8, pp. 3750-3753, 2008.

[17] K. Dong Lee, "Preparation and electrochromic properties of WO_3 coating deposited by the sol-gel method," *Solar Energy Materials and Solar Cells,* vol. 57, pp. 21-30, 1999.

[18] K. Hong*, et al.*, "Synthesizing tungsten oxide nanowires by a thermal evaporation method," *Applied Physics Letters,* vol. 90, pp. 173121-173123, 2007.

[19] M. H. Yaacob*, et al.*, "Absorption spectral response of nanotextured WO_3 thin films with Pt catalyst towards H_2," *Sensors and Actuators, B: Chemical,* vol. 137, pp. 115-120, 2009.

[20] O. Bohnke and C. Bohnke, "Comparative study of the electrochromic properties of WO_3 thin films," *Displays,* vol. 9, pp. 199-206, 1988.

[21] A. Sadek*, et al.*, "High-temperature anodized WO_3 nanoplatelet films for photosensitive devices," *Langmuir,* vol. 25, pp. 9545-9551, 2009.

[22] H. Zheng*, et al.*, "Nanoporous WO_3 from anodized RF sputtered tungsten thin films," *Electrochemistry Communications,* vol. 11, pp. 768-771, 2009.

[23] S. Wang*, et al.*, "Controlling Wettability and Photochromism in a Dual-Responsive Tungsten Oxide Film," *Angewandte Chemie International Edition,* vol. 45, pp. 1264-1267, 2006.

[24] H.-S. Shim*, et al.*, "Electrochromic properties of tungsten oxide nanowires fabricated by electrospinning method," *Solar Energy Materials and Solar Cells,* vol. 93, pp. 2062-2068.

[25] G. J. Fang*, et al.*, "Preparation and electrochromic properties of nanocrystalline WO_3 thin films prepared by pulsed excimer laser ablation technique," *Physica Status Solidi a-Applied Research,* vol. 184, pp. 129-137, Mar 2001.

[26] J. Thangala*, et al.*, "A hot-wire chemical vapor deposition (HWCVD) method for metal oxide and their alloy nanowire arrays," *First International Symposium on Transparent Conducting Oxides,* vol. In Press, Corrected Proof.

[27] W. An*, et al.*, "Adsorption of O_2, H_2, CO, NH_3, and NO_2 on ZnO nanotube: A density functional theory study," *Journal of Physical Chemistry C,* vol. 112, pp. 5747-5755, Apr 2008.

[28] M. Casarin*, et al.*, "A theoretical investigation of the relaxation effects induced on the ZnO(10$\bar{1}$0) surface by the chemisorption of H_2 and CO," *Applied Surface Science,* vol. 142, pp. 192-195, 1999.

[29] K. Fink, "*Ab-initio* cluster calculations on the electronic structure of oxygen vacancies at the polar ZnO(0001) surface and on the adsorption of H_2, CO, and CO_2 at these sites," *Physical Chemistry Chemical Physics,* vol. 8, pp. 1482-1489, 2006.

[30] J. B. L. Martins*, et al.*, "*Ab-initio* study of CO and H_2 interaction on ZnO surfaces using a small cluster model," *Journal of Molecular Structure: THEOCHEM World Congress of Theoretically Oriented Chemists,* vol. 398-399, pp. 457-466, 1997.

Chapter 2 – Gas Sensing Fundamentals and Literature Review

Sensing theory, mechanisms and central concepts will be discussed with respect to the materials investigated in this chapter, namely the semiconducting metal oxides, ZnO and WO_3. A brief overview of the progression of metal oxide based sensors from thick films, through to the latest nanodimensional sensors will be presented. Several concepts central to gas sensing, written from the perspective of semiconductor physics and surface science, will be introduced.

2.1 Technological Progression of Metal Oxide Based Gas Sensors

Some of the first generation commercial gas sensors were sold by Naoyoshi Taguchi's private venture in 1968, now the present day Figaro Engineering Inc. [1]. These gas sensors were later known as Taguchi type gas sensors, with the original implementation employing a thick SnO_2 film for combustible gas leak detection, which proved invaluable in a region populated with predominantly wooden buildings built in earthquake prone areas [2]. Following the introduction of thick film technology, it became apparent that thick film sensors fabricated with metal oxide particles suffered from manufacturing irregularities, with initial sensor properties varying slightly from device to device [2].

The next logical step in sensor research was to improve the uniformity and porosity of the gas sensitive element, inspired by the advances in material science and metal oxide deposition techniques originating from the semiconductor industry, many researchers turned to thin films deposited by either physical or chemical vapour deposition techniques. Unfortunately, many of these methods result in the formation of a compact thin film, which have a reduced surface area and porosity. To overcome this reduction in surface area and porosity, many researchers participated in the rapidly emerging field of nanomaterial synthesis, creating high quality materials with an intrinsically large surface area to volume ratio. Noboru Yamazoe [3] was arguably the first to popularise the use of nanodimensional metal oxides for gas sensing, noting that the sensitivity of SnO_2 towards both H_2 and CO was a function of crystallite size. This work introduced the relationship between the Debye length and

crystallite dimensionality, reporting that the greatest sensitivities occurred when the crystallite size approached the Debye length.

2.2 Central Concepts

2.2.1 Surface Area to Volume Ratio

Considering a simple sphere, it is clear from Table 2.1 that as the radius of a sphere decreases, the surface area to volume ratio rapidly begins to increase. Thus, in the volume that a single 5 mm sphere occupies, 10^{18} 5 nm spheres could fit, with a combined surface area some 10^{12} times larger than a single 5 mm sphere. For gas sensing applications, where the surface of the material is directly involved in the physiochemical processes, the effective surface area of the sensing element becomes a critical and sometimes rate limiting variable in the dynamic performance of the sensor.

Table 2.1. Surface area to volume ratio of a sphere.

Radius of sphere	Surface area (m^2)	Volume (m^3)	Surface area/volume (ratio)
5 cm	3.14×10^{-2}	5.24×10^{-4}	60
5 mm	3.14×10^{-4}	5.24×10^{-7}	600
5 μm	3.14×10^{-10}	5.24×10^{-16}	600000
5 nm	3.14×10^{-16}	5.24×10^{-25}	600000000

As will be discussed in the following sections, the depletion of the semiconducting metal oxide sensing surface is an important factor in gas sensing. As the size of a sphere/particle decreases into the nano-dimensional realms a larger volume of the metal oxide structure, regardless of morphology, can be affected by the target gas, often leading to augmented sensor performance.

2.2.2 Debye Length/Space Charge Layer Thickness, and Grain Size

The Debye length (λ_D) or space charge layer thickness is the measure of the depth of the material (metal oxide in this case) that can be affected/depleted by the adsorbing gas. This can be represented by the Schottky approximation [4]:

$$\lambda_D = \frac{\sqrt{\varepsilon \varepsilon_0 k_B T}}{q^2 n_b} \tag{2.1}$$

where ε represents the electrical permittivity of the material, and ε_0 is the electrical permittivity in vacuum; k_B is Boltzmann's constant; T is the temperature in Kelvin; q is the elementary charge on one electron; and finally, n_b is the concentration of free carriers (electrons).

Take the comparison of a thin film comprised of either microstructured or nanostructured grains; as the diameter of the grain (X_g) decreases, λ_D approaches the diameter of the grain.

Here we consider two extremes:

1. λ_D is significantly smaller than X_g, a typical micro structured thick/thin film (Figure 2.1)

In this situation, only a portion of the micro dimensional grain would be depleted and the resistance of the sensing element would be a function of the resistance of the surface of the grain that is capable of interacting with gaseous species, and the bulk of the grain which is unable to interact with any gaseous species. Additionally, the grain-grain interfaces between micro dimensional grains have a significant impact on sensing element conductivity. An excellent discourse on this phenomena can be found in the works of either Barsan and Weimar [4] or Korotcenkov [5].

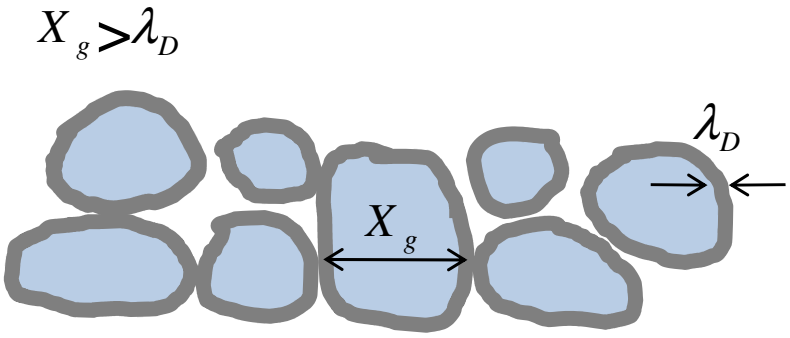

Figure 2.1. The diameter of X_g exceeds λ_D (shaded in grey), adapted from [5].

2. λ_D approaches or is less than X_g, a typical nanostructured thin film (Figure 2.2)

Here, the resistance of the sensing element is a function of the resistance of the surface of the nanostructure, and as a large portion, or indeed the entire nanostructure is fully depleted, this situation represents the highest possible sensitivity. Hence, nanostructured materials were employed where possible to augment sensitivity.

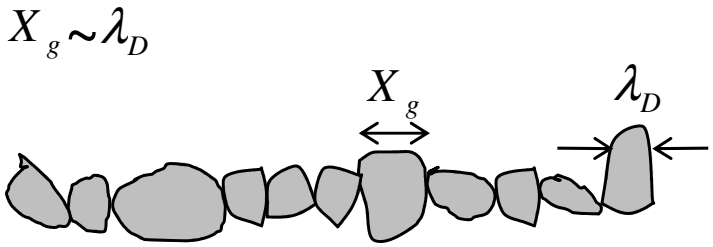

Figure 2.2. The diameter of X_g approaches or is less than λ_D (shaded in grey), adapted from [5].

2.2.3 Defects and Oxygen Vacancies

Defects are deviations from the symmetrical placement of atoms in a crystal lattice in crystalline materials and surfaces. Defects in metal oxide semiconductors are known to occur naturally during both crystallite formation, and as a result of high temperature. These processes play an important role during gas sensing [4-8], and can cause changes in surface states, reactivity, electron transport and electrical properties, depending on the type of defect and their position in the crystal lattice.

Some basic types of defects include:

1. Interstitial – An atom is placed into the crystal lattice between existing atom positions.
2. Vacancy – An atom is removed from the perfect crystal.
3. Frenkel pair – An atom in the crystal lattice displaces into an interstitial site, and as a result creates a vacancy.
4. Substitutional – An atom in the crystal lattice is swapped with a different atom.

Metal oxide gas sensors operating in oxygenated atmospheres have a well known correlation between oxygen partial pressure, defect formation energy, and electrical conductivity [9-10]:

$$\sigma = \sigma_o \exp(-\frac{E_A}{k_B T})\rho_{O_2}{}^{1/m} \tag{2.2}$$

where σ is the conductivity; E_A is the sum of activation energies required to form ionic defects, which is representative of the sensitivity of the electrical conductivity to temperature changes; k_B is Boltzmann's constant; T is the temperature in Kelvin; ρ_{O_2} is the partial pressure of oxygen; and the absolute values of $1/m$ are dependent on the conduction type; for p-type conductivity $1/m$ is positive, conversely for n-type conductivity the value is negative.

While (2.1) or (2.2) can be used explain experimentally observed changes in resistance, the author will use Density Functional Theory (DFT) where possible to examine the adsorption process on the atomic scale.

In the following chapters, the effect of metal oxide exposure to NO_2 and H_2 using well established traditional gas sensing mechanisms will be covered in greater detail in Chapter 7. The author also uses DFT calculations to describe and understand the gas adsorption process. In Chapter 4, the adsorption of NO_2 onto a defect free ZnO($2\bar{1}\bar{1}0$) surface, as well as defect containing ZnO($2\bar{1}\bar{1}0$)$-V_O$ surface will be examined, highlighting the importance of oxygen defects on the reaction chemistry of physisorbed and chemisorbed NO_2.

2.3 Critical Review of Relevant Metal Oxide Based Gas Sensors

2.3.1 An Introduction to ZnO

ZnO is a versatile material with a number of applications in electronics, optics and photonics, enjoying a rapid period of growth during the 1960's [11]. Interest in applying ZnO based devices in the nanotechnological realm has prompted a rapid increase in the number of published papers. New applications for ZnO are constantly emerging, fuelled by a plethora of readily available deposition

methods, its inherent biocompatibility, its low material costs, unique materials properties, and the diverse nanodimensional forms it exhibits [11-14]. The crystal structures shared by ZnO are wurtzite (hexagonal), zinc blende (cubic), and rock salt (cubic). At ambient conditions, the thermodynamically stable phase is wurtzite, the zinc blende phase occurs during growth on cubic substrates, and the rock salt phase is only obtained at relatively high pressures [15].

2.3.2 Conductometric Sensing of NO_x with ZnO Nanostructured Gas Sensors

ZnO thin films have been successfully employed for detecting NO and NO_2 by a number of different experimentalists [16-19]. Some researchers include dopants, with the aspiration of augmenting the NO_x sensitivity, including: indium [16], nickel, tin [17], aluminium [20], erbium, palladium, vanadium [19]. However the inclusion of dopants in ZnO has resulted in varying degrees of success in obtaining better sensitivity and selectivity.

Single crystal ZnO, especially nanodimensional structures such as nanorods and nanowires have been identified as promising candidates for gas sensing [18-19, 21-25]. The reduction from bulk material to the nanodimensional realm has been proven to be a fundamental step in the next generation of highly sensitive, low power consumption ZnO based sensors. Following this step, sensing elements based on nanowires and nanorods have been shown to be sensitive to many different analytes including: H_2 [26], H_2S [27], water vapour (humidity) [28], NO_x [18], hydrazine [29], and ethanol [30].

Recently, there has been an increase in the number of groups investigating ZnO for NO and NO_2 sensing applications. Jun *et al.* [23] successfully demonstrated the use of commercially available ZnO nanopowder in the development of an NO_2 sensor, sensitive to concentrations of 0.4 ppm with a response and recovery time of 13 s and 10 s, respectively. Using hydrothermally grown ZnO nanorods, Liu *et al.* [24] reported NO_2 sensing over a wide range of concentrations (0.2 ppm to 5.0 ppm), noting that the sensor response increased with the aspect ratio of the deposited nanorods. Sadek *et al.* [22] demonstrated the application of ZnO nanobelts for NO_2 sensing over the range of high ppb to low ppm concentrations. Cho *et al.* [31] demonstrated that dispersed ZnO nanorods could be used to detect a 1 ppm concentration of NO_2 at 300 °C. These sensors functioned in a high concentration of CO (50 ppm), showing promise for monitoring automated automotive car ventilation systems. However, the

nanorods used by *Cho et al.* are not contiguous high density arrays, and as such, it may be possible to reduce the operational temperature of the device further. Similarly, Baratto *et al.* [18] have demonstrated that mats made of nanostructured ZnO respond to NO_x at temperatures of ≤ 100 °C, which represents a great improvement over thin film based sensors which operate at approximately 300 °C.

Overall, ZnO nanostructures have demonstrated higher sensitivity at lower temperatures than their thin film counterparts [6, 32]. Furthermore, the sensing process can be strongly influenced by the presence of surface oxygen vacancies (V_O) that alter the electronic properties of ZnO and hence reactivity with the gas. The adsorption of molecules such as NO_2 at vacancy sites results in withdrawal of electrons from the surface, depleting them from the conduction band, and leading to an increase in resistance [33].

2.3.3 Conductometric Sensing of H_2 with ZnO Nanostructured Gas Sensors

ZnO has also been explored for its H_2 gas sensing ability with several well documented reports using both traditional thin films and nanostructure based morphologies [22, 26, 34-35]. Recently, nanodimensional forms such as nanowires and nanorods have been considered to augment device characteristics such as: sensitivity, response and recovery time, as well as a reduction in operational temperature [34]. Another common method to enhance H_2 sensitivity is the addition or inclusion of catalytic metals such as Pt, Pd or Au to enhance H_2 dissociation rates [34]. However, there are reports of severe baseline stability issues associated with the irreversible reduction of the ZnO sensing layer by H_2 concentrations of over 3% [35]. Considering this, and as the author tests with concentrations up to 1% H_2 in air, the ZnO nanostructures employed by the author will not be coated with a catalytic metal. Some more recent examples of ZnO nanomaterials used for H_2 sensing include, the use of ZnO nanobelts by Sadek *et al.*[22] for sensing 1% H_2 at 385 °C in a balance of synthetic air, reporting a response and recovery time of 48 s and 336 s. Qurashi *et al.* [36] utilised ZnO nanowires grown via microwave synthesis to create a conductometric sensor operating at 200 °C capable of sensing 500 ppm H_2 with a response and recovery time of 65 s and 168 s, respectively. Lupan *et al.* [37]

reported on a single ZnO nanorod sensor exposed to 150 ppm H_2 operating at room temperature, with a response and recovery time of 50-80 s and 300 s, respectively.

2.3.4 An Introduction to WO_3

WO_3 has been a topic of great research interest since the discovery of its electrochromic properties of in the 1960's; and more recently, catalytic metal (Pt, Pd, Au) assisted gasochromism (a gas induced colour change) [38-39]. However, long before the discovery of its electrochromic and gasochromic properties, the rich chemistry of tungsten and tungsten oxides has been of great scientific interest, with reports dating back to the 18th century. It should be noted that WO_3 can exist in many different crystal phases (triclinic, monoclinic, hexagonal and orthorhombic) [40]; can form stable sub-stoichiometric WO_{3-x} oxides (where x = 0.33 to 1) [41]; it can exist as tungsten bronzes Na_xWO_3 (where $0 \leq x \leq 1$) [42]; and has several hydration states $WO_3 \cdot nH_2O$ (where n is typically ⅓, ½, 1 or 2) [43]; therefore, there are number of subtle considerations that must be made when characterising these materials.

2.3.5 Optical Sensing of H_2 with WO_3 Nanostructured Gas Sensors

Despite several complications in the analysis of fabricated materials, WO_3 remains at the forefront of gasochromic materials. The use of Pd coated WO_3 thin films for optical H_2 gas sensing was first patented by Ito *et al.* [44] in 1983. Since then, there have been a number of researchers focusing on optical gasochromic H_2 sensing, however, not all test under realistic, and arguably meaningful sensing conditions, i.e. H_2 concentrations below the lower explosive limit of 4% in a balance of air (rather than an inert carrier gas). For example, Ranjbar *et al.* [45] deposited WO_3 thin films via pulsed laser deposition and used a novel electroless plating method to coat samples in Pd, which were then exposed to a mixture of 10% H_2 in a balance of Ar at room temperature. The responses estimated by the author were in the range of 500 s, followed by regeneration in air. Whilst, Chan *et al.* [46] utilised an anhydrous sol-gel method to deposit WO_3 thin films which were then coated in a sputtered Pt thin film (5 – 25 nm). The samples were exposed to pure H_2 or a mixture of H_2 (1% - 50%) in N_2 at room temperature reporting a coloration response time of approximately 5 s, with regeneration occurring in

air. Other notable examples include references [47-52]. In Chapter 7, the author will demonstrate the use of a Pt coated WO_3 thin film for the optical sensing of ≤ 1% H_2 in a balance of synthetic air.

2.3.6 Conductometric Sensing of NO_x with WO_3 Nanostructured Gas Sensors

For over a decade now, WO_3 thin and nanostructured thin films have been successfully employed for sensing of NO and NO_2 [53-54]. Given the high thermal and chemical stability of WO_3, coupled with its relatively low fabrication costs, has positioned WO_3 as a suitable candidate for the next generation of NO_x sensors. One of the largest predicted applications for NO_x sensors is in the implementation of an automotive in-cabin air quality monitoring system [53]. This has driven research interest into nanodimensional WO_3 NO_2 sensors with some recent examples including: Kida *et al.* [53] who fabricated a lamellar nanodimensional WO_3 capable of sensing 1 ppm NO_2 in air at 200 °C with a response and recovery time of 240 s, and 660 s, respectively; Siciliano *et al.* [55] reported on the preparation of nanodimensional WO_3 via the thermal oxidation of tungsten powder, which was sensitive to 200 ppm of NO_2 at 250 °C, with a response time of 108 s, and a recovery time exceeding 1800 s. Additionally, Heidari *et al.* [56] used AC electrophoresis to deposit WO_3 nanoparticles onto a transducing platform, reporting the greatest sensitivity of the device over a range of 50 - 500 ppb, was at 200 °C towards an NO_2 concentration of 500 ppb, with a response and recovery time of 1200 s and 828 s, respectively.

2.4 Computational Materials Modelling

Computational materials modelling is the application of computational code to represent materials on varying length scales. The macro representation (meter length scale) and the atomic representation (angstrom length scale) of materials is separated by some ten orders of magnitude. Naturally, different modelling approaches must be employed to accurately represent the differing length scales. An excellent treatise covering the different methods, and considerations of length scales used in computational materials modelling can be found in Starrost *et al.* [57]. For gas sensing applications, materials modelling on an atomic scale is of the greatest interest. When studying atomic scale systems, the two broad approaches used in computational materials modelling are: molecular mechanics, which

is generally used for studying large systems consisting of tens of thousands of atoms; and quantum mechanical modelling, which is used for studying systems typically involving less than one thousand atoms. A complete discussion of the intricacies of the two different methods will be presented in Chapter 3.

The work in this thesis is focused on computational materials modelling of the adsorption of gaseous NO_x species onto a particular surface of ZnO using the DFT approach.

2.5 Chapter Summary

In this chapter a literature review of central concepts relevant to metal oxide based gas sensors, and a critical review of the current literature with respect to ZnO and WO_3 in the context of conductometric and optical gasochromic gas sensing applications was presented. In Chapter 7, general gas adsorption equations for conductometric gas sensing of NO_2 and H_2, as well as optical gasochromic H_2 sensing will be introduced in detail, from both experimental and theoretical perspectives.

In the next chapter DFT from the perspective of materials modelling will be introduced along with the specific parameters used by the author to perform the simulation results presented in Chapter 4. The new insights gained into the gas sensing mechanism of N, O, NO and NO_2 onto the ZnO($2\bar{1}\bar{1}0$), and NO_2 onto ZnO($2\bar{1}\bar{1}0$)$-V_O$ crystal face with highly specific sensing information to the ($2\bar{1}\bar{1}0$) crystal face are presented.

2.6 References

[1] *Figaro Engineering Inc. Company History*. (Available 26/07/2010). http://www.figaro.co.jp/en/company3.html

[2] E. F. Comini, Guido; Sberveglieri, Giorgio (Eds.), *Solid State Gas Sensing*, Springer, 2009.

[3] N. Yamazoe, "New approaches for improving semiconductor gas sensors," *Sensors and Actuators B: Chemical,* vol. 5, pp. 7-19, 1991.

[4] N. Barsan and U. Weimar, "Conduction Model of Metal Oxide Gas Sensors," *Journal of Electroceramics,* vol. 7, pp. 143-167, 2001.

[5] G. Korotcenkov, "The role of morphology and crystallographic structure of metal oxides in response of conductometric-type gas sensors," *Materials Science and Engineering: R: Reports,* vol. 61, pp. 1-39, 2008.

[6] N. Barsan*, et al.*, "Metal oxide-based gas sensor research: How to?," *Sensors and Actuators B: Chemical,* vol. 121, pp. 18-35, 2007.

[7] G. Korotcenkov, "Metal oxides for solid-state gas sensors: What determines our choice?," *Materials Science and Engineering: B,* vol. 139, pp. 1-23, 2007.

[8] G. Korotcenkov, "Gas response control through structural and chemical modification of metal oxide films: state of the art and approaches," *Sensors and Actuators B: Chemical,* vol. 107, pp. 209-232, 2005.

[9] A. Sadek, "Investigation of Nanostructured Semiconducting Metal Oxide and Conducting Polymer Thin Films for Gas Sensing Applications," School of Electrical and Computer Engineering, RMIT University, Melbourne, 2008.

[10] Y. Xu*, et al.*, "Oxygen sensors based on semiconducting metal oxides: an overview," *Sensors and Actuators B: Chemical,* vol. 65, pp. 2-4, 2000.

[11] Z. L. Wang, "Zinc oxide nanostructures: growth, properties and applications," *Journal of Physics-Condensed Matter,* vol. 16, pp. 829-858, 2004.

[12] L. Vayssieres, "Growth of Arrayed Nanorods and Nanowires of ZnO from Aqueous Solutions," *Advanced Materials,* vol. 15, pp. 464-466, 2003.

[13] Z. L. Wang, "Nanostructures of zinc oxide," *Materials Today,* vol. 7, pp. 26-33, 2004.

[14] C. Wöll, "The chemistry and physics of zinc oxide surfaces," *Progress in Surface Science,* vol. 82, pp. 55-120, 2007.

[15] U. Ozgur*, et al.*, "A comprehensive review of ZnO materials and devices," *Journal of Applied Physics,* vol. 98, Aug 15 2005.

[16] R. Ferro*, et al.*, "Peculiarities of nitrogen dioxide detection with sprayed undoped and indium-doped zinc oxide thin films," *Thin Solid Films,* vol. 516, pp. 2225-2230, 2008.

[17] O. Lupan*, et al.*, "Nanostructured zinc oxide gas sensors by successive ionic layer adsorption and reaction method and rapid photothermal processing," *Thin Solid Films,* vol. 516, pp. 3338-3345, 2008.

[18] C. Baratto*, et al.*, "Low temperature selective NO_2 sensors by nanostructured fibres of ZnO," *Sensors and Actuators B: Chemical,* vol. 100, pp. 261-265, 2004.

[19] N. Koshizaki and T. Oyama, "Sensing characteristics of ZnO-based NO_x sensor," *Sensors and Actuators B: Chemical,* vol. 66, pp. 119-121, 2000.

[20] S. C. Navale*, et al.*, "Low temperature synthesis and NO_x sensing properties of nanostructured Al-doped ZnO," *Sensors and Actuators B: Chemical,* vol. 126, pp. 382-386, 2007.

[21] P. S. Cho*, et al.*, "NO_2 sensing characteristics of ZnO nanorods prepared by hydrothermal method," *Journal of Electroceramics,* vol. 17, pp. 975-978, 2006.

[22] A. Z. Sadek*, et al.*, "Characterization of ZnO Nanobelt-Based Gas Sensor for H_2, NO_2, and Hydrocarbon Sensing," *Sensors Journal, IEEE,* vol. 7, pp. 919-924, 2007.

[23] J. H. Jun*, et al.*, "Necked ZnO nanoparticle-based NO_2 sensors with high and fast response," *Sensors and Actuators B: Chemical,* vol. 140, pp. 412-417, 2009.

[24] F.-T. Liu*, et al.*, "ZnO nanorod gas sensor for NO_2 detection," *Journal of the Taiwan Institute of Chemical Engineers,* vol. 40, pp. 528-532, 2009.

[25] E. Oh*, et al.*, "High-performance NO_2 gas sensor based on ZnO nanorod grown by ultrasonic irradiation," *Sensors and Actuators B: Chemical,* vol. 141, pp. 239-243, 2009.

[26] A. Z. Sadek, *et al.*, "A ZnO nanorod based layered ZnO/64° YX $LiNbO_3$ SAW hydrogen gas sensor," *Thin Solid Films,* vol. 515, pp. 8705-8708, 2007.
[27] C. Wang, *et al.*, "Detection of H_2S down to ppb levels at room temperature using sensors based on ZnO nanorods," *Sensors and Actuators B: Chemical,* vol. 113, pp. 320-323, 2006.
[28] Y. Zhang, *et al.*, "Zinc oxide nanorod and nanowire for humidity sensor," *Applied Surface Science,* vol. 242, pp. 212-217, 2005.
[29] A. Umar, *et al.*, "Ultra-sensitive hydrazine chemical sensor based on high-aspect-ratio ZnO nanowires," *Talanta,* vol. 77, pp. 1376-1380, 2009.
[30] Z. Yang, *et al.*, "High-performance ethanol sensing based on an aligned assembly of ZnO nanorods," *Sensors and Actuators B: Chemical,* vol. 135, pp. 57-60, 2008.
[31] P. S. Cho, *et al.*, "NO_2 sensing characteristics of ZnO nanorods prepared by hydrothermal method,"vol. 17, pp. 975-978, 2006.
[32] K. Kalantar-zadeh, F. Benjamin, *Nanotechnology-Enabled Sensors*, Springer 2008.
[33] L. Schmidt-Mende and J. L. MacManus-Driscoll, "ZnO - nanostructures, defects, and devices," *Materials Today,* vol. 10, pp. 40-48, 2007.
[34] R. Vander Wal, *et al.*, "Synthesis Methods, Microscopy Characterization and Device Integration of Nanoscale Metal Oxide Semiconductors for Gas Sensing," *Sensors,* vol. 9, pp. 7866-7902, 2009.
[35] P. Mitra, *et al.*, "ZnO thin film sensor," *Materials Letters,* vol. 35, pp. 33-38, 1998.
[36] A. Qurashi, *et al.*, "Ultra-fast Microwave Synthesis of ZnO Nanowires and their Dynamic Response Toward Hydrogen Gas," *Nanoscale Research Letters,* vol. 4, pp. 948-954, 2009.
[37] O. Lupan, *et al.*, "Fabrication of ZnO nanorod-based hydrogen gas nanosensor," *Microelectronics Journal,* vol. 38, pp. 1211-1216, 2007.
[38] M. Ando, *et al.*, "Optical hydrogen sensitivity of noble metal-tungsten oxide composite films prepared by sputtering deposition," *Sensors and Actuators B: Chemical,* vol. 76, pp. 13-17, 2001.
[39] S. K. Deb, "Opportunities and challenges in science and technology of WO_3 for electrochromic and related applications," *Solar Energy Materials and Solar Cells,* vol. 92, pp. 245-258, 2008.
[40] C. V. Ramana, *et al.*, "Structural Stability and Phase Transitions in WO_3 Thin Films," *Journal of Physical Chemistry B,* vol. 110, pp. 10430-10435, 2006.
[41] A. P. Shpak, *et al.*, "XPS studies of active elements surface of gas sensors based on WO_{3-x} nanoparticles," *Journal of Electron Spectroscopy and Related Phenomena,* vol. 156-158, pp. 172-175, 2007.
[42] B. Ingham, *et al.*, "Density-functional studies of tungsten trioxide, tungsten bronzes, and related systems," *Physical Review B,* vol. 72, 2005.
[43] M. F. Daniel, *et al.*, "Infrared and Raman study of WO_3 tungsten trioxides and WO_3, xH_2O tungsten trioxide hydrates," *Journal of Solid State Chemistry,* vol. 67, pp. 235-247, 1987.
[44] K. Ito and T. Kubo, "Optical WO_3 Sensor," Patent number 58-147749 , 1983.
[45] M. Ranjbar, *et al.*, "Electroless plating of palladium on WO_3 films for gasochromic applications," *Solar Energy Materials and Solar Cells,* vol. 94, pp. 201-206, 2010.
[46] C.-C. Chan, *et al.*, "Preparation and characterization of gasochromic Pt/WO_3 hydrogen sensor by using the Taguchi design method," *Sensors and Actuators B: Chemical,* vol. 145, pp. 691-697, 2010.
[47] S. Okazaki, *et al.*, "Sensing characteristics of an optical fiber sensor for hydrogen leak," *Sensors and Actuators B: Chemical,* vol. 93, pp. 142-147, 2003.
[48] S. Sumida, *et al.*, "Distributed hydrogen determination with fiber-optic sensor," *Sensors and Actuators B: Chemical,* vol. 108, pp. 508-514, 2005.
[49] T. Watanabe, *et al.*, "A fiber-optic hydrogen gas sensor with low propagation loss," *Sensors and Actuators B: Chemical,* vol. 145, pp. 781-787, 2010.
[50] S. Yamamoto, *et al.*, "Structural and gasochromic properties of epitaxial WO_3 films prepared by pulsed laser deposition," *Nuclear Instruments and Methods in Physics Research Section B: Beam Interactions with Materials and Atoms,* vol. 266, pp. 802-806, 2008.
[51] U. O. Krasovec, *et al.*, "The gasochromic properties of sol-gel WO_3 films with sputtered Pt catalyst," *Solar Energy,* vol. 68, pp. 541-551, 2000.

[52] H. Nakagawa*, et al.*, "A room-temperature operated hydrogen leak sensor," *Sensors and Actuators B: Chemical,* vol. 93, pp. 468-474, 2003.

[53] T. Kida*, et al.*, "Highly sensitive NO_2 sensors using lamellar-structured WO_3 particles prepared by an acidification method," *Sensors and Actuators B: Chemical,* vol. 135, pp. 568-574, 2009.

[54] M. Akiyama*, et al.*, "Tungsten oxide-based semiconductor sensor for detection of nitrogen oxides in combustion exhaust," *Sensors and Actuators B: Chemical,* vol. 14, pp. 619-620, 1993.

[55] T. Siciliano*, et al.*, "WO_3 gas sensors prepared by thermal oxidization of tungsten," *Sensors and Actuators B-Chemical,* vol. 133, pp. 321-326, Jul 2008.

[56] E. K. Heidari*, et al.*, "WO_3-based NO_2 sensors fabricated through low frequency AC electrophoretic deposition," *Sensors and Actuators B: Chemical,* vol. 146, pp. 165-170, 2010.

[57] F. Starrost and E. A. Carter, "Modeling the full monty: baring the nature of surfaces across time and space," *Surface Science,* vol. 500, pp. 323-346, 2002.

Chapter 3 –Materials Modelling with Density Functional Theory

In this chapter, the materials' modelling approach utilised by the author to study gas adsorption process onto ZnO nanostructures will be introduced. The method employed by the author was Density Functional Theory (DFT), and whilst DFT is the focus of this chapter, it is placed in the context of other state-of-the-art material modelling techniques. There are two major formalisms which exist within materials modelling: "molecular mechanics" which relies on the representation of atoms as unique interaction sites to simulate physical processes and properties; and "quantum mechanical modelling" which is based in the realm of quantum physics and considers the electronic structure of atoms.

In the molecular mechanics formalism, non-bonded atoms are treated as individual particles and interactions between neighbouring particles are governed by electrostatic (coloumb) forces, and van der Waals forces [1-2]. Covalently bonded atoms are simulated by applying an appropriate spring constant (Hooke's law) between the connected atoms, i.e. balls connected by a spring, and bond angles and torsions (dihedrals) [1-2]. The mathematical form of all interatomic interactions, which includes terms for non-bonding and covalently bonded atoms, is parameterised from experimental or high level quantum calculation data, and is commonly referred to as forcefield or potential energy function. Examples of the most widely used forcefields can be found in reference [3]. Molecular mechanics approaches are extremely useful for large systems and are capable of modelling tens of thousands of atoms reliably. Despite the flexibility of molecular mechanics for large systems, it is not well suited for studying adsorption processes or chemical reactivity, as electrons and orbitals are not considered in molecular mechanical methods.

Quantum mechanical modelling hinges on several key principles and theoretical frameworks which will be introduced in this chapter. DFT is a quantum mechanical method, which is a powerful tool for the prediction and accurate representation of atomic and electronic structure and properties of molecules, and bulk solids, as well as their surfaces and interfaces. It is computationally efficient to model systems with a relatively small number of atoms, typically less than a one thousand atoms per

unit cell for solids. However, it should be noted that larger systems are becoming ever more attainable given advances in DFT code and raw computational processing power. Due to the high computational requirements of quantum mechanical methods, however, the representation of macro scale materials is computationally intractable due to the sheer number of atoms that would be involved in the calculations. A true atom-by-atom representation of a single ZnO nanorod would require systems containing of the order of 10^8 atoms, and would therefore be computationally intractable. It is, however, possible to model individual surfaces of a ZnO nanorod, as for gas sensing applications the adsorption of gas molecules onto the surface of a crystal face is of primary interest. At the gas-surface interface, interactions occur on the atomic scale and the electronic nature of DFT makes it ideally suited to study these interactions.

Currently, there are a number of different software implementations available for DFT simulations, with most codes implementing DFT differently. Some popular choices, grouped by technology include: VASP [4-5] and CASTEP [6] which are plane-wave codes; DMol^3 [7] and Siesta [8] which are all-electron methods that use numerical basis sets; and Crystal [9] and Gaussian [10] which are all-electron codes with analytical basis sets. The package employed in this study is the plane-wave code called Vienna *Ab-initio* Simulation Package (VASP).

One of the most common crystal faces present on ZnO nanostructures, the ZnO($2\bar{1}\bar{1}0$) crystal face was chosen by the author for study. This is a technologically important crystal face for gas sensing as most hexagonal ZnO nanomaterials expose the $\{2\bar{1}\bar{1}0\}$ family of crystal facets. This family often represents one of the larger surface areas available on ZnO nanostructures. DFT was used by the author to study the adsorption of N, O, NO, and NO_2 on the ZnO($2\bar{1}\bar{1}0$) surface; and NO_2 on the oxygen defect containing ZnO($2\bar{1}\bar{1}0$)-V_O surface. Investigations into the adsorption of atomic nitrogen and oxygen are also important, as they represent potential dissociation products of NO_2 adsorption, which may irreversibly adsorb, or poison, the ZnO surface. The findings from these DFT surface studies are presented in the following chapter.

3.1 Introduction to Density Functional Theory

3.1.1 Schrödinger's Equation

Quantum mechanical modelling is largely concerned with the treatment of the time independent Schrödinger equation. While it is unnecessary to provide a lengthy derivation of this equation from its eigenfunction relation $H\psi = E\psi$, it is useful to introduce the derived time independent Schrödinger equation (3.1) as follows:

$$E\psi(\hat{r}) = -\frac{\hbar^2}{2m}\nabla^2\psi(\hat{r}) + V(\hat{r})\psi(\hat{r}), \qquad (3.1)$$

here $\frac{\hbar^2}{2m}\nabla^2$ represents the kinetic energy of the electron, where m is the mass of the electron, and ∇^2 is the Laplacian operator, $V(\hat{r})$ is the potential energy given at the vector $\hat{r}$, and ψ is the wavefunction.

This equation was modified by Kohn and Sham (§ 3.1.2) through the introduction of several theoretical approximations to variables in the independent Schrödinger equation, such as the use of an exchange-correlation functional and the introduction of Kohn-Sham orbitals.

3.1.2 Kohn-Sham Equations

In 1964 Hohenberg and Kohn [11] proved that the ground-state energy and other properties of a system can be defined by the electron density [3]. For his efforts in establishing DFT, Walter Kohn was awarded the Nobel Prize in chemistry jointly with John Pople. In DFT, this "energy functional" can be written as a sum of two terms [3] as described by (3.2):

$$E[\rho(\hat{r})] = \int V_{ext}(\hat{r})\rho(\hat{r})d\hat{r} + F[\rho(\hat{r})], \qquad (3.2)$$

where, $E[\rho(\hat{r})]$ is the unique functional of the system, i.e. the electron density, and $V_{ext}(\hat{r})$ is the external potential acting upon the system, typically coulombic in nature. $F[p(\hat{r})]$ is the sum of the kinetic energy of the electrons in the system and the contributions from inter-electronic interactions.

However, as $F[\rho(\hat{r})]$ is unknown, Equation (3.2) cannot be solved explicitly. In 1965 Kohn and Sham [3, 12] realised that $F[\rho(\hat{r})]$ could be approximated by the sum of three separate terms as per (3.3):

$$F[\rho(\hat{r})] = E_{KE}[\rho(\hat{r})] + E_H[\rho(\hat{r})] + E_{XC}[\rho(\hat{r})], \qquad (3.3)$$

where $E_{KE}[p(\hat{r})]$ is the kinetic energy, $E_H[p(\hat{r})]$ is the electron-electron coulombic energy, and $E_{XC}[p(\hat{r})]$ is the exchange-correlation functional (discussed in § 3.1.3).

The kinetic energy $E_{KE}[p(\hat{r})]$ is defined as:

$$E_{KE}[\rho(\hat{r})] = \sum_{i=1}^{N} \varphi_i(\hat{r}) \left(-\frac{\nabla^2}{2} \right) \varphi_i(\hat{r}) d\hat{r}, \qquad (3.4)$$

It should be noted that for the kinetic energy of the Kohn-Sham formalism all electrons are non-interacting and have the same electron density $E[\rho(\hat{r})]$ as the real system.

The electron-electron coulombic energy $E_H[p(\hat{r})]$, also known as the Hartree electrostatic energy, is the classical interaction between two charge densities, which, when summed over all possible pairwise interactions, yields (3.5) [3]:

$$E_H[\rho(\hat{r})] = \frac{1}{2} \iint \frac{\rho(\hat{r}_1)\rho(\hat{r}_2)}{|r_1 - r_2|} d\hat{r}_1 d\hat{r}_2 \qquad (3.5)$$

Modern DFT codes use the Kohn-Sham equations to approximate the electron density functional $F[\rho(\hat{r})]$ by solving a fictitious set of Kohn-Sham orbitals defined in (3.6) [13]:

$$\rho(\hat{r}) = 2 \sum_i \left| \psi_i(\hat{r}) \right|^2, \qquad (3.6)$$

where $\rho(\hat{r})$ is the electron density; and $\sum_i \left|\psi_i(\hat{r})\right|^2$ is the sum of all non-interacting electron wavefunctions in the system at any given vector $(\hat{r})$, squared.

A full derivation of the Kohn-Sham equation is outside the scope of this thesis, and for further reading there are excellent reference works in the literature [3, 13-14].

3.1.3 Exchange-correlation Functional

The exchange-correlation functional is a term included in the calculation of the ground state energy and is concerned with the treatment and representation of electron-electron interactions. The exchange-correlation functional E_{XC} is divided into two terms, the exchange term and the correlation term [15-16]. The exchange term is associated with the interactions of electrons with the same spin, whereas the correlation term is used to represent interactions between electrons of opposite spin [15]. There are a few common categories for an exchange-correlation functional, which listed in increasing numerical complexity are: local density approximation (LDA), generalised gradient approximation (GGA), meta-GGA, and hyper-GGA / hybrid methods.

The LDA functional is dependant solely on electron density as per (3.7) and the exchange-correlation functional for the uniform electron gas is known to high precision for all values of the electron density [13].

$$V_{XC(LDA)}(\hat{r}) = V_{XC(e^- gas)}[n(\hat{r})], \qquad (3.7)$$

where $n(\hat{r})$ is the local electron density at $\hat{r}$.

GGA functionals such as that of Perdew and Wang 1991 (PW91), build upon the LDA method by calculating the electron density, and including a term to represent the gradient of the density itself at $\hat{r}$, as presented in (3.8) [13, 17]:

$$V_{XC(GGA)}(\hat{r}) = V_{XC}\ [n(\hat{r}), \nabla n(\hat{r})], \qquad (3.8)$$

where $\nabla n(\hat{r})$ is the gradient of the electron density at $\hat{r}$.

Meta-GGA functionals, such as Tao-Perdew-Staroverov-Scuseria (TPSS), are based upon GGA, however, it also includes a term to calculate the Laplacian of the electron density, to determine the divergence of the gradient in $\pm x$, $\pm y$, and $\pm z$ directions. Increasing further in numerical complexity are hyper GGA / hybrid methods such as Becke-three-parameter-Lee-Yang-Parr (B3LYP). These functionals combine a typical GGA exchange-correlation functional with an exact exchange functional, such as those typically found in all electron methods [13].

Out of the suitable exchange-correlation functionals for plane-wave basis sets, PW91 GGA was used throughout the work presented in this thesis. A thorough treatment of this exchange-correlation functional can be found in Perdew *et al.* [18]. This exchange-correlation functional has been shown to give a good representation of the surface and bulk properties of ZnO [19].

3.1.4 Bloch's Theorem, Periodic Boundary Conditions and Reciprocal/k-Space

Due to the inherent periodicity in crystalline materials, the whole crystal need not be considered during calculations, minimising the computational complexity of the simulation. The crystal can be treated, due to symmetry, as the smallest crystallographic arrangement of atoms in a 3-dimensional lattice, the Bravis lattice; which is defined in reciprocal space as the Brillouin zone. It is the Bravis lattice, which is used in formation of a supercell, and is critical in defining the periodic boundary conditions of the surface model.

The supercell is created when periodic boundary conditions are used to represent a larger surface by replication of a unique unit cell in specified direction(s). An example of a [2×1] supercell (defined by a grey box), named so as the *x*-direction comprises 2 unit cells, while the *y*-direction contains one, is presented in Figure 3.1a. This [2×1] supercell can be multiplied by any whole integer, to extend the surface model. In Figure 3.1b, a 3×3 extension of the [2×1] supercell is presented, which is equivalent to a [6×3] supercell.

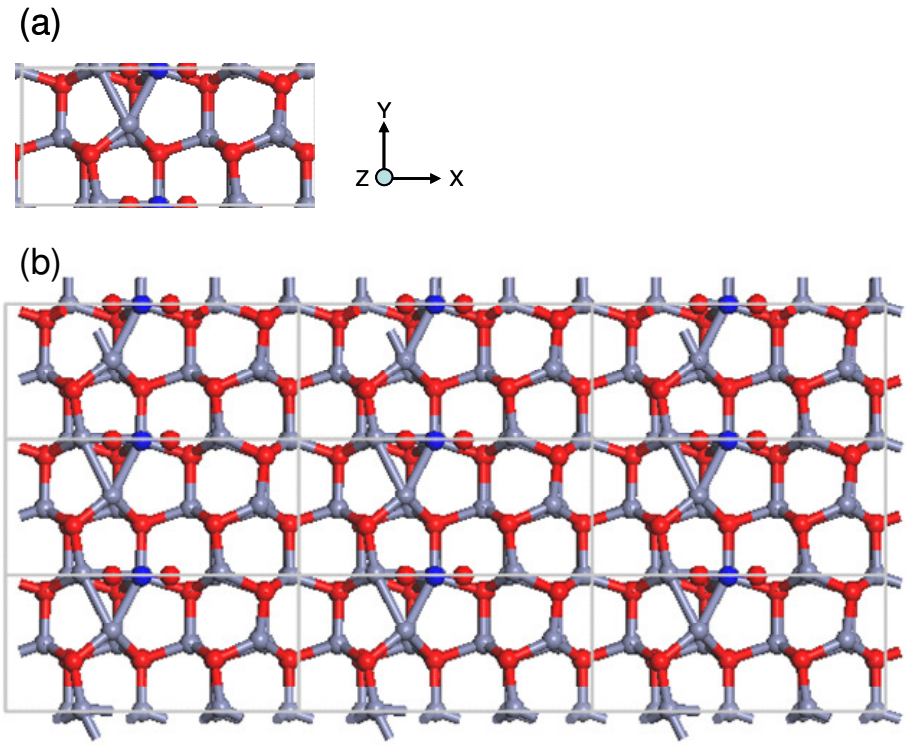

Figure 3.1. The ZnO($2\bar{1}\bar{1}0$)-V_O surface with an NO_2 molecule positioned above its surface: (a) [2×1] supercell; (b) [2×1] supercell extended 3×3 to form a [6×3] equivalent supercell.

Bloch's theorem states that the solution of the Schrödinger equation in a periodic system can be expressed as [13]:

$$\phi_{\hat{k}}(\hat{r}) = \exp(i\hat{k}\cdot\hat{r})u_{\hat{k}}(\hat{r}), \qquad (3.9)$$

where $u_{\hat{k}}(\hat{r})$ is periodic in space with the same periodicity as the supercell, i.e. $u_{\hat{k}}(\hat{r}+n_1\hat{a}_1+n_2\hat{a}_2+n_3\hat{a}_3)=u_k(\hat{r})$ for any integers n_1, n_2 and n_3; and $\hat{a}_1$, $\hat{a}_2$ and $\hat{a}_3$ represent the crystal lattice vectors. The term $\exp(i\hat{k}\cdot\hat{r})$ is used to represent plane-waves, where: vectors $\hat{r}$, are real space vectors; i is the electron variable of the system; and $\hat{k}$ are vectors residing in reciprocal/k-space [13].

Thus, during calculations the Brillouin zone is divided along each of its three reciprocal lattice vectors by its corresponding position in the k-point mesh. Hence, only wavefunctions at the specified

k-points in the unit cell will be calculated, reducing the computational time required. By dividing up the resulting density functional, the ground state energy can be calculated, with the size of the k-point mesh affecting the lowest ground state energy.

In this work, the Monkhorst and Pack k-point Scheme was used to reduce the number of integrals in reciprocal space needed to represent the Brillouin zone as per the implementation in VASP [13]. Further details on this method are described elsewhere [20]. For an 8-slab ZnO surface model used in this study a [1×1] stoichiometrically balanced supercell was $5 \times 5 \times 1$ [19, 21]. Previous testing of k-point mesh size revealed that the minimum number of k-points in the mesh required to reach the true ground state energy of the system, accurate to three decimal places. As a doubling in real space halves the distance in reciprocal space, a $3 \times 5 \times 1$ k-point configuration was used for all [2×1] defect surface calculations. While it is possible to utilise a finer k-point mesh, finer meshes are more computationally expensive and for the purposes of studying gas adsorption on a metal oxide crystal face, the mesh size utilised is more than sufficient to obtain meaningful results, i.e. the total energy was converged to ~4 meV for meshes used in this thesis [22].

3.1.5 Plane-wave Methods

Plane-waves (sinusoidal oscillations with varying phase and amplitude) are one of the most common choices of basis set employed to study periodic systems. They are represented by a Fourier series where a linear combination of plane-waves are used to approximate the wave function of an electron. As the wave function contains all the information about the location and probability density of electrons of the system in question, through implicit knowledge of the wave function, physical properties of the system may be obtained.

In plane-wave methods the core electrons can be replaced by a pseudo potential (frozen core), effectively eliminating the core electrons from the calculation. The core electrons of the atom/ion are replaced with a smoothed region of charge tuned to represent the physical properties of the atom/ion [13, 23]. This is vital to maintain the electrostatic repulsion between core and valence electrons, and to approximate the atom/ion realistically.

Frozen core methods are efficient ways to reduce the number of plane-waves required to accurately represent an atom/ion. The two frozen core methods available in the VASP package are the projector augmented-wave (PAW) method and the Ultrasoft Pseudo Potential (USPP) method. Further details relating to both implementations in the VASP package can be found in the VASP manual [4]. The PAW method was not used by the author, as it was previously found to result in fluctuating surface energies with increasing slab thickness, and as such will not be discussed in detail here. A comprehensive explanation of the method can be found in [24].

Pseudopotentials, in general, are defined as "hard" or "soft", referring to the cut off energy used for the calculation. Large cut-off energies must be used to include plane-waves which oscillate on short length scales in real space, i.e. those associated with tightly bound core electrons [13]. However, it transpires that the tightly bound core electrons play only a minor role in chemical bonding, with valence electrons dictating most of the physical properties of the atom/ion. As can be seen in Table 3.1, the use of USPPs can dramatically reduce the number of electrons that need to be represented by plane waves, decreasing computational requirements.

Table 3.1. Configuration of USPP as implemented in the Vienna *Ab-initio* Simulation Package (VASP).

Element	Number of electrons	Electron configuration	Orbitals represented as an USPP	Valence orbitals not included in the USPP
Nitrogen	7	$1s^2$, $2s^2$, $2p^3$	$1s^2$	$2s^2$, $2p^3$
Oxygen	8	$1s^2$, $2s^2$, $2p^4$	$1s^2$	$2s^2$, $2p^4$
Zinc	30	$1s^2$, $2s^2$, $2p^6$, $3s^2$, $3p^6$, $4s^2$, $3d^{10}$	$1s^2$, $2s^2$, $2p^6$, $3s^2$, $3p^4$, $4s^2$	$3p^2$, $3d^{10}$

In this work, Vanderbilt USPPs were used as implemented in the VASP simulation package [4, 23]. As the core region of charge in an USPP calculation is replaced by a smoothed charge density, as per

the Vanderbilt formalism, the visualisation of electron density and or charge density around the centre of the atom appears as a region of low electron density.

3.1.6 A Summary of Parameters Used in the Vienna *ab-initio* Simulation Package (VASP)

In this thesis, all calculations were performed using VASP [25-27], which performs fully self-consistent DFT calculations to solve the Kohn-Sham equations [12]. The generalized gradient approximation utilising the functional of Perdew and Wang (PW91) [17] was employed for all simulations. The PW91 GGA functional [17] has been shown to accurately calculate the properties of bulk ZnO and ZnO surfaces [19], as well as other materials and their interactions with gases [5, 28-31]. In particular, Miller *et al.* [32] performed a comprehensive study using PW91 GGA calculations with the CASTEP code, which uses the same plane wave approach as VASP. The computational parameters and computational methodology were also similar to that used by the author. In this study over 100 different metals, metal oxides, metal carbides, and other technologically important compounds were studied. It was reported that theoretically determined physical constants, such as lattice parameters and bond lengths, were typically within 2% of the experimentally determined values.

Core electrons were replaced with Vanderbilt USPPs as implemented in the VASP package [23]. The electronic wavefunctions were expanded as a linear combination of plane-waves, and truncated to include only plane-waves with kinetic energies less than 400 eV. K-space sampling was performed using the Monkhorst & Pack scheme [20] with a mesh of $5 \times 5 \times 1$ for the ZnO($2\bar{1}\bar{1}0$) systems, and $3 \times 5 \times 1$ for the ZnO($2\bar{1}\bar{1}0$)-V_O system. The isolated NO and NO_2 molecules were modelled in a 10 Å × 10 Å × 10 Å supercell with a single Γ point calculation.

The conjugate gradient algorithm was used to find the minimum energy states, by making small adjustments to the location of atoms/ions and recalculating to determine if the new position is lower in energy than the previous one. This is repeated until the local (or global) minimum energy state is found, i.e. until the energy increases for all “new” positions of atoms/ions.

3.2 Calculated Properties

3.2.1 Binding Energies

The binding energy (BE) of an adsorbed molecule can be calculated to estimate the strength of the bond between the adsorbate and the surface. Binding energy calculations were performed as per:

$$BE = [E_{ads+surf} - (E_{ads} + E_{surf})], \quad (3.10)$$

where $E_{ads+surf}$ is the total energy of the relaxed adsorbate/ZnO($2\bar{1}\bar{1}0$) or adsorbate/ZnO($2\bar{1}\bar{1}0$)–V_O system; E_{ads} is the total energy of the free adsorbate; and E_{surf} is the total energy of the clean relaxed surface. Therefore, a negative binding energy indicates favourable adsorption, whereas a positive binding energy indicates an unstable system.

3.2.2 Structural Changes

Surface reconstructions and relaxations caused by the adsorption process provide an insight into how much the adsorption process alters the surface. Relaxation is defined as movement in the direction perpendicular to the surface plane, (i.e. *z*-axis). Reconstructions on the other hand, occur when the surface atoms move in the *x*- and *y*- directions of the surface.

3.2.3 Workfunction Changes

Workfunction (ϕ) values can provide an insight into the direction of charge transfer caused by the adsorption of a gaseous species on a surface. The work-function was calculated using the following equation [31]:

$$\phi = E_{VAC} - E_F, \quad (3.11)$$

where E_{VAC} is the electrostatic potential in the vacuum region of the supercell on the adsorbate side and E_F is the Fermi energy. Similarly, work-function changes ($\Delta\phi$) were calculated using the following equation:

$$\Delta\phi = (\phi - \phi_c), \quad (3.12)$$

where ϕ_c is the work-function of the clean ZnO($2\bar{1}\bar{1}0$) or ZnO($2\bar{1}\bar{1}0$)–V_O surface.

3.2.4 Bader Charges

It is often useful to know the charges on individual atoms before and after gas adsorption, to quantify the formation of new bonds, and to track charge migration. Bader charge calculations [33] were used to quantify the charge on atoms in the surface model, providing valuable insight into the migration of charge which can be compared with changes in experimentally observed sensor conductivity.

A Bader charge analysis treats the space inside the supercell by dividing it into regions with surfaces that run through minima in the charge density. These minima exist at a point on a dividing surface where the gradient of the electron density has no component normal to the surface [34]. The Bader analysis was applied to the charge density file calculated by VASP, using the Bader charge analysis tool available from the University of Texas chemistry and biochemistry group [35]. A full treatment of the Bader charge analysis method and a description of the analysis tool is presented in Henkelman *et al.* [33].

3.2.5 Density of States

Density of states (DOS) plots of selected systems were calculated to provide valuable information about the formation of new electronic states, i.e. the affect that the adsorbate has on the surface electronic properties. It should be noted that GGA based exchange-correlation functionals have been shown to underestimate the band gap of metal oxides, however, changes to states in the valence and conduction band are faithfully represented. Such calculations have previously been used to examine a wide variety of systems [22, 36-37].

3.2.6 Charge Density and Electron Localisation Functions

Planar averaged charge density difference plots in the *z*-direction of selected structures were generated to visualise the redistribution of charge after adsorption. Such plots provide valuable insights into the type of adsorbate-surface bonding and charge rearrangement after adsorption. Plots were calculated using the following equation:

$$\Delta\rho(z) = [\rho(z)_{ads+surf} - \rho(z)_{ads} - \rho(z)_{surf}], \qquad (3.13)$$

where $\rho(z)_{ads+surf}$ is the planar averaged charge density of the relaxed adsorbate/ZnO($2\bar{1}\bar{1}0$) or adsorbate/ZnO($2\bar{1}\bar{1}0$)–V_O system; $\rho(z)_{ads}$, is the planar averaged charge density of the free adsorbate; and $\rho(z)_{surf}$, is the planar averaged charge density of the clean relaxed ZnO($2\bar{1}\bar{1}0$) or ZnO($2\bar{1}\bar{1}0$)–V_O surface, taken in their respective positions in the adsorbed minimum energy structure.

Electron localisation functions (ELF) plots were created to visualise the probability of finding bonding and non-bonding electron pairs. The ELF data was calculated by VASP and visualised in Vaspdataviewer [38] provides information on the type of bonding occurring between the surface and the adsorbate as well as redistribution of charge on the adsorbate.

3.2.7 Vibrational Frequencies

Vibrational frequency calculations yield information about the type of stationary point on the potential energy surface, i.e. a minimum (all real frequencies), transition state (one imaginary frequency) or a higher order saddle point (more than one imaginary frequency). These calculations were performed by permitting directional freedom to the adsorbate in the *x-, y-, z-* directions, while fixing all of the surface atoms, and diagonalizing a finite difference construction of the Hessian matrix with displacements of 0.015Å. The vibrational data of the adsorbed molecules is also presented in this thesis. They are useful for comparison with experimentally obtained vibrational frequencies such as those obtained via infra-red (IR), and high resolution electron energy loss (HREEL) spectroscopy.

3.2.8 Magnetic Moments

Magnetic moment calculations provide insights into whether the adsorption of a gaseous species has induced a characteristic magnetic moment on the surface. In this thesis, magnetic moment analysis was performed on selected systems. Magnetic moments of individual atoms and the associated orbitals contributing to the magnetic moment were calculated using the VASP package.

3.3 Surface Adsorption Studies and Gas Sensing Technologies

In this thesis, DFT has been used to study the adsorption of N, O, NO, and NO_2 on the ZnO($2\bar{1}\bar{1}0$) surface. The adsorption of NO_2 on the ZnO($2\bar{1}\bar{1}0$)–V_O surface has also been examined. ZnO($2\bar{1}\bar{1}0$) is a technologically important crystal face for gas sensing as many hexagonal ZnO nanomaterials preferentially expose the this crystal face, representing one of the larger surface areas available on ZnO nanostructures. ZnO nanostructures that are dominated by large area {$2\bar{1}\bar{1}0$} planes include but are not limited to: nanorods [39], nanobelts [40], nanosprings, nanohelices, and nanobows [41].

It is possible to extract information from the DFT calculations, which can be used to provide insights into the type of bonding that occurs between the adsorbate and the ZnO($2\bar{1}\bar{1}0$) surface, the strength of the bond between the adsorbate and the surface, the stable adsorption sites on ZnO($2\bar{1}\bar{1}0$) and their adsorbed orientations, the changes to the surface after adsorption, offering insights into long term stability of the surface. The potential for surface poisoning by the dissociation products of NO and NO_2, the ability of the surfaces to self-repair, and potential reaction barriers to dissociative adsorption. Such calculations offer the experimentalist a wealth of data which was previously inaccessible, providing valuable insights which may lead to an augmentation in ZnO based sensor performance facilitated by a holistic understanding of the sensing mechanism.

Geometry optimisations are performed at absolute zero (0 K). Whilst many sensors operate at several hundreds of degrees, at absolute zero there are no thermally induced vibrations by atoms. The representation of the system is via the interaction from core electrons, and orbital interactions from valance electrons. The addition of temperature to the system adds a kinetic energy component to the representation of an atom, which is implemented in molecular dynamics simulations. Such simulations, however, are outside the scope of this thesis.

3.4 Surface Models

The non-polar ($2\bar{1}\bar{1}0$) surface was cleaved from the bulk wurtzite structure of ZnO to form a stoichiometrically balanced [1×1] surface model. To model the defect surface, ZnO($2\bar{1}\bar{1}0$)–V_O, a single

oxygen atom was removed from a stoichiometrically balanced [2×1] surface model. Both surfaces were generated with optimised lattice constants of $a = b = 3.268$ *Å*, $c = 5.233$ *Å* [42-43]. For both [1×1] and [2×1] supercells, a vacuum spacer of 14 Å was introduced in the *z*- direction to prevent interactions with neighbouring images. The relaxed [1×1] ZnO($2\bar{1}\bar{1}0$) and [2×1] ZnO($2\bar{1}\bar{1}0$)–V_O supercells are presented in Figures 3.2 and 3.3, respectively.

The adsorption process was modelled by initially placing O, N, NO or NO_2 ~3Å above a relaxed 8 layer (32 atom) ZnO($2\bar{1}\bar{1}0$) surface, or NO_2 above a relaxed 8 layer (63 atom) ZnO($2\bar{1}\bar{1}0$)–V_O surface. Several initial adsorption sites were investigated, denoted with "×" in Figure 3.4. Different initial orientations of the molecules were also investigated, which will be described in detail in Chapter 4. The surface energy for these 8-layer/slab models was previously determined to be converged to 0.01 Jm^{-2} [19].

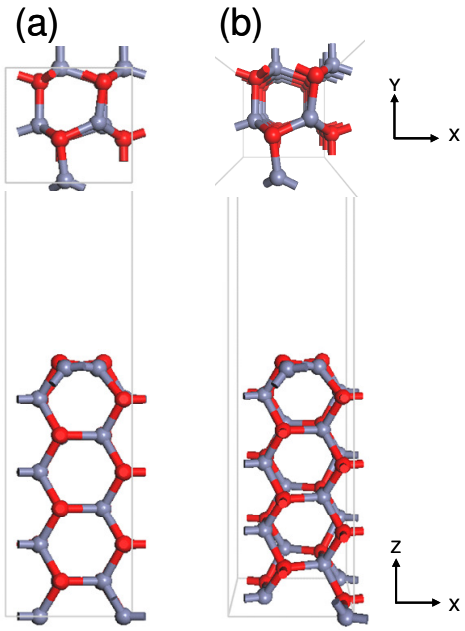

Figure 3.2. ZnO($2\bar{1}\bar{1}0$) [1×1] surface model: (a) orthographic representation; (b) perspective representation.

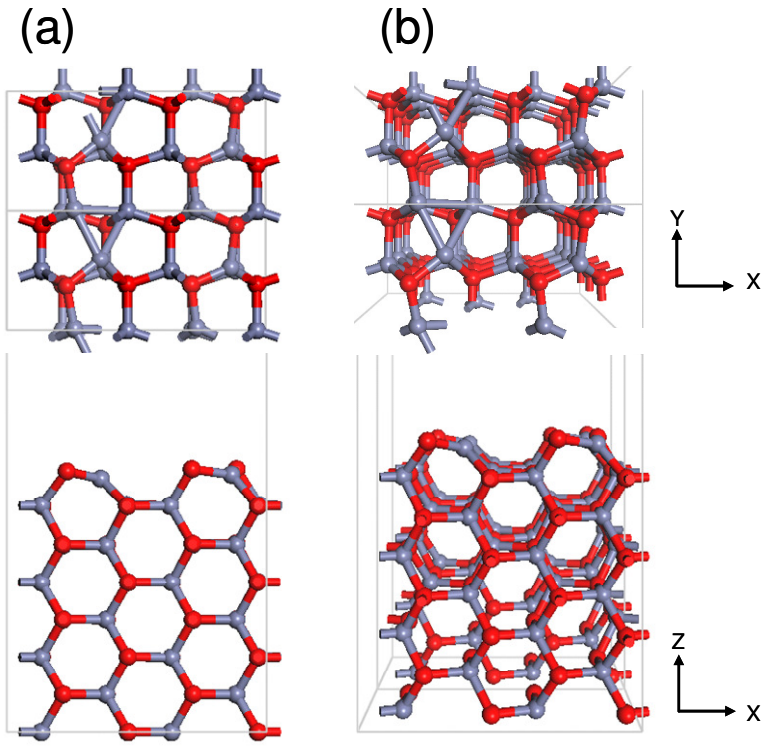

Figure 3.3. ZnO(2$\bar{1}\bar{1}$0)–V_O [2×1] surface model: (a) orthographic representation; (b) perspective representation.

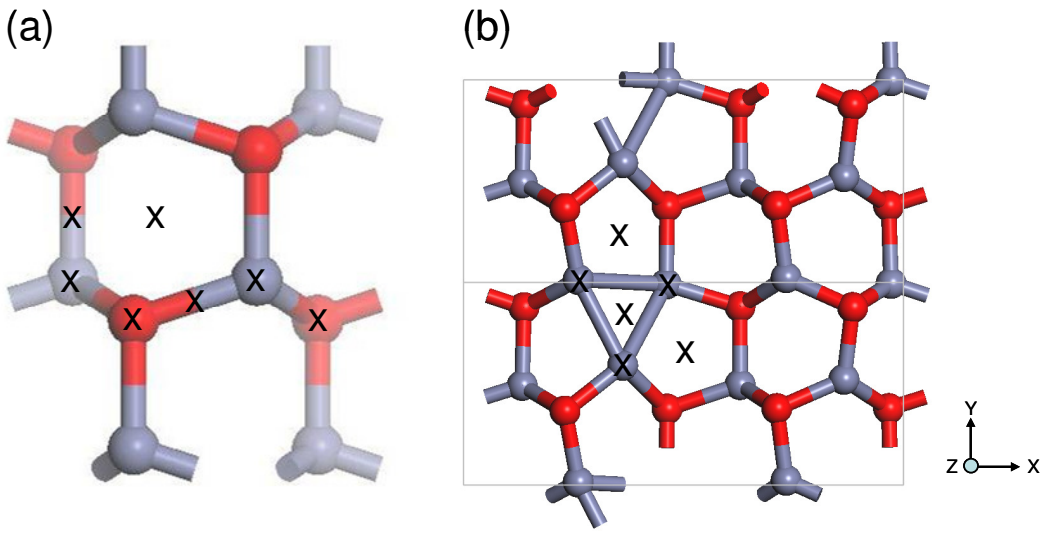

Figure 3.4. Top view of surface models showing different adsorption sites (indicated by an ×) on: (a) the [1×1] ZnO(2$\bar{1}\bar{1}$0) surface (b) the [2×1] ZnO(2$\bar{1}\bar{1}$0)–V_O surface. Oxygen atoms denoted in red, zinc atoms in grey.

3.5 Chapter Summary

In this chapter the materials modelling approach utilised by the author to study gas adsorption process onto ZnO nanostructures was introduced, together with the specific parameters used by the author in his work. DFT calculations of N, O, NO and NO_2 adsorption onto the ZnO($2\overline{1}\overline{1}0$) and NO_2 adsorption onto the ZnO($2\overline{1}\overline{1}0$)$-V_O$, will be presented in the next chapter, and where possible will be compared with experimental sensing observations.

3.6 References

[1] A. K. Rappe*, et al.*, "UFF, a full periodic table force field for molecular mechanics and molecular dynamics simulations," *Journal of the American Chemical Society,* vol. 114, pp. 10024-10035, 1992.

[2] A. Richon, "An Introduction to Molecular Modelling," *Mathematech,* vol. 1, p. 83, 1994.

[3] A. Leach, *Molecular Modelling: Principles and Applications*, Prentice Hall, 2001.

[4] M. M. Georg Kresse, and Jurgen Furthmuller, "VASP the Guide", University of Wien, 2009.

[5] J. Hafner, "Materials simulations using VASP - a quantum perspective to materials science," *Computer Physics Communications,* vol. 177, pp. 6-13, 2007.

[6] M. D. Segall, *et al.*, "First-principles simulation: ideas, illustrations and the CASTEP code," *Journal of Physics: Condensed Matter,* vol. 14, pp. 2717-2743, 2002.

[7] B. Delley, "DMol methodology and applications," in *Density functional methods in chemistry*, Springer-Verlag, pp. 101-107, 1991.

[8] M. S. José and et al., "The SIESTA method for *ab-initio* order- N materials simulation," *Journal of Physics: Condensed Matter,* vol. 14, p. 2745, 2002.

[9] R. Dovesi, *et al.*, "CRYSTAL06 User's Manual," Crystal Inc., 2006.

[10] M. J. Frisch, *et al.*, "Gaussian 09 User's Manual," Gaussian Inc., 2009.

[11] P. Hohenberg and W. Kohn, "Inhomogeneous Electron Gas," *Physical Review,* vol. 136, p. B864, 1964.

[12] W. Kohn and L. J. Sham, "Self-Consistent Equations Including Exchange and Correlation Effects," *Physical Review,* vol. 140, p. A1133, 1965.

[13] D. Sholl and J. Steckel, *Density Functional Theory. A Practical Introduction*, John Wiley and Sons, 2009.

[14] C. Fiolhais*, et al.*, *A primer in Density Functional Theory*, Springer, 2003.

[15] S. F. Sousa*, et al.*, "General performance of density functionals," *Journal of Physical Chemistry A,* vol. 111, pp. 10439-10452, 2007.

[16] K. Capelle, "A bird's-eye view of density-functional theory," *Brazilian Journal of Physics*, vol.36, pp. 1381-1343, 2006.

[17] J. P. Perdew and Y. Wang, "Accurate and simple analytic representation of the electron-gas correlation energy," *Physical Review B,* vol. 45, p. 13244, 1992.

[18] J. P. Perdew*, et al.*, "Generalized Gradient Approximation Made Simple," *Physical Review Letters,* vol. 77, p. 3865, 1996.

[19] M. J. S. Spencer*, et al.*, "Density functional theory modelling of ZnO $(10\bar{1}0)$ and ZnO ZnO$(2\bar{1}\bar{1}0)$ surfaces: Structure, properties and adsorption of N_2O," *Materials Chemistry and Physics,* vol. 119, pp. 505-514, 2010.

[20] H. J. Monkhorst and J. D. Pack, "Special points for Brillouin-zone integrations," *Physical Review B,* vol. 13, p. 5188, 1976.

[21] M. J. S. Spencer*, et al.*, "Density Functional Theory Study of ZnO Nanostructures for NO and NO_2 Sensing," *Solid-State Sensors, Actuators and Microsystems Conference, 2007. TRANSDUCERS 2007. International,* vol. 1, pp. 987-990, 2007.

[22] M. J. S. Spencer and I. Yarovsky, "ZnO Nanostructures for Gas Sensing: Interaction of NO_2, NO, O, and N with the ZnO$(10\bar{1}0)$ Surface," *The Journal of Physical Chemistry C,* 2010.

[23] D. Vanderbilt, "Soft self-consistent pseudopotentials in a generalized eigenvalue formalism," *Physical Review B,* vol. 41, p. 7892, 1990.

[24] P. E. Blöchl, "Projector augmented-wave method," *Physical Review B,* vol. 50, p. 17953, 1994.

[25] G. Kresse and J. Furthmuller, "Efficiency of *ab-initio* total energy calculations for metals and semiconductors using a plane-wave basis set," *Computational Materials Science,* vol. 6, pp. 15-50, 1996.

[26] G. Kresse and J. Furthmüller, "Efficient iterative schemes for *ab-initio* total-energy calculations using a plane-wave basis set," *Physical Review B,* vol. 54, p. 11169, 1996.

[27] G. Kresse and J. Hafner, "*Ab-initio* molecular dynamics for open-shell transition metals," *Physical Review B,* vol. 48, p. 13115, 1993.

[28] M. J. S. Spencer, *et al.*, "Effect of sulfur impurity on Fe(110) adhesion: A DFT study," *Journal of Physical Chemistry B,* vol. 108, pp. 10965-10972, 2004.
[29] M. J. S. Spencer, *et al.*, "Effect of sulfur coverage on Fe(110) adhesion: A DFT study," *Journal of Physical Chemistry B,* vol. 109, pp. 10204-10212, 2005.
[30] M. J. S. Spencer, *et al.*, "Coverage-dependent adsorption of atomic sulfur on Fe(110): A DFT study," *Journal of Physical Chemistry B,* vol. 109, pp. 9604-9612, 2005.
[31] M. J. S. Spencer, *et al.*, "Effect of S Arrangement on Fe(110) Properties at 1/3 Monolayer Coverage: A DFT Study," *J. Phys. Chem. B,* vol. 110, pp. 956-962, 2006.
[32] V. Milman, *et al.*, "Electronic structure, properties, and phase stability of inorganic crystals: A pseudopotential plane-wave study," *International Journal of Quantum Chemistry,* vol. 77, pp. 895-910, 2000.
[33] G. Henkelman, *et al.*, "A fast and robust algorithm for Bader decomposition of charge density," *Computational Materials Science,* vol. 36, pp. 354-360, 2006.
[34] R. Bader, *Atoms in Molecules: A Quantum Theory,* Oxford University Press, 1990.
[35] A. Arnaldsson, *et al.*, "Bader Charge Analysis Tool", Version 0.26b, 2009.
[36] J. D. Baniecki, *et al.*, "Chemisorption of water and carbon dioxide on nanostructured $BaTiO_3$-$SrTiO_3$(001) surfaces," *Journal of Applied Physics,* vol. 106, pp. 054109-12, 2009.
[37] B. Ingham, *et al.*, "Density-functional studies of tungsten trioxide, tungsten bronzes, and related systems," *Physical Review B,* vol. 72, 2005.
[38] T. B. Terriberry, *et al.*, "A tool for the interactive 3D visualization of electronic structure in molecules and solids," *Computers & Chemistry,* vol. 26, pp. 313-319, 2002.
[39] M. Breedon, *et al.*, "ZnO nanostructures grown on epitaxial GaN," *First International Symposium on Transparent Conducting Oxides,* vol. 518, pp. 1053-1056, 2009.
[40] Z. L. Wang, "Nanostructures of zinc oxide," *Materials Today,* vol. 7, pp. 26-33, 2004.
[41] Z. L. Wang, "Novel Zinc Oxide Nanostructures Discovery by Electron Microscopy," *Journal of Physics: Conference Series,* vol. 26, pp. 1-6, 2006.
[42] M. Breedon, *et al.*, "Adsorption of NO and NO_2 on the ZnO($2\bar{1}\bar{1}0$) surface: A DFT study," *Surface Science,* vol. 603, pp. 3389-3399, 2009.
[43] M. Breedon, *et al.*, "Adsorption of atomic nitrogen and oxygen on ZnO($2\bar{1}\bar{1}0$) surface: A density functional theory study," *Journal of Physics Condensed Matter,* vol. 21, 2009.

Chapter 4 - Density Functional Theory Adsorption Studies

4.1 Introduction

Computationally, there have been few studies focusing specifically on gas reactions with the ZnO($2\bar{1}\bar{1}0$) surface, with the reactive polar faces, as well as the non-polar ($10\bar{1}0$) surface, generally receiving the bulk of attention [1-13]. The effects of stoichiometric disruptions to ZnO surface chemistry, such as those caused by lattice defects, have also proven popular research topics (see for example Refs. [5, 14-20]).

As was discussed in previous chapters, the ZnO($2\bar{1}\bar{1}0$) surface is one of the most technologically important surfaces for gas sensors, as well as the {$10\bar{1}0$} family of crystal facets often represent the largest surface area on ZnO nanostructures [21]. To the best of the author's knowledge, theoretical studies employing Density Functional Theory (DFT) on the ZnO{$2\bar{1}\bar{1}0$} set of surfaces include investigations of the adsorption of H_2 [22], H_2O [23], SO_2 and NO_2 [24].

Cooke *et al.* [15] investigated atomic hydrogen, hydroxyl and water adsorption onto the ZnO($11\bar{2}0$) surface, generating a phase diagram describing the surface species present at different partial pressures of oxygen and hydrogen. Nyberg *et al.* [22] investigated the adsorption of molecular hydrogen on both the ($10\bar{1}0$) and ($11\bar{2}0$) ZnO surfaces and found that molecular hydrogen did not dissociatively adsorb. Recently, Wang *et al.* [25] presented a study of the effects of atomic hydrogen adsorption on a ZnO nanowire including a ($2\bar{1}\bar{1}0$) surface, concluding that the electronic character of the ($2\bar{1}\bar{1}0$) surface became more metallic after adsorption.

Most recently, Spencer *et al.* [11] comprehensively studied the adsorption of N, O, NO and NO_2 onto ZnO($10\bar{1}0$) with DFT and *ab-initio* molecular dynamics, showing multiple minimum energy structures were found for all adsorbed species. Adsorption of atomic N and O resulted in large surface reconstructions, with atomic O withdrawing charge from the surface and atomic N generally donating charge to the surface. NO and NO_2 adsorbed weakly on ZnO($10\bar{1}0$), resulting in a charge transfer from the substrate to the adsorbate. The binding energy of adsorbed NO_2 on the ZnO($10\bar{1}0$)$-V_O$ surface was greater than that on the stoichiometric ZnO($10\bar{1}0$) surface. Additionally, it was found that the

adsorption of NO_2 over the vacancy site of ZnO(10$\bar{1}$0)–V_O was dissociative, yielding O and NO. The dissociated O atom filled the defect site, reforming the stoichiometric surface, while the NO desorbed from the surface [11]. Studies of N_2O adsorption [26] on the ZnO (10$\bar{1}$0) and (2$\bar{1}\bar{1}$0) surfaces calculated that N_2O physisorbs on the surface, with a small charge transfer from the surface to the adsorbate.

Prades *et al.* [24] used DFT to examine NO_2 and SO_2 adsorption on the (10$\bar{1}$0) and (11$\bar{2}$0) surface of ZnO, with and without an O vacancy (using a [2×2] supercell, corresponding to an O vacancy concentration of 12.5%). The focus of this paper was to examine the relative stabilities of the two gases and the poisoning effect of SO_2 for gas sensing purposes. They found multiple adsorption configurations, with NO_2 preferring to adsorb on Zn surface atoms, and with stronger binding energies on the defect surface. For all structures they calculated that NO_2 withdraws charge from the surface. While they examined the effect of one concentration of O vacancies (25%) and one coverage of NO_2, it would be interesting to investigate how other concentrations of O vacancies or NO_2 affect the adsorption properties. Calculations of the electronic properties, including density of states and charge density differences may also shed further light on this interesting system. To the best of the PhD candidate's knowledge there have been no other studies investigating NO_2 adsorption on the ZnO(2$\bar{1}\bar{1}$0)–V_O surface. Additionally, the adsorption of atomic N and O has not been previously considered on the ZnO(2$\bar{1}\bar{1}$0) surface. These investigations are important as they represent the dissociation products of larger molecules such as NO and NO_2.

This chapter will be split into three different sections, each describing the following systems:

1. *The adsorption of* NO_x *dissociation products on* ZnO(2$\bar{1}\bar{1}$0): N/ZnO(2$\bar{1}\bar{1}$0) and O/ZnO(2$\bar{1}\bar{1}$0)
2. *The adsorption of* NO_x *on* ZnO(2$\bar{1}\bar{1}$0): NO/ZnO(2$\bar{1}\bar{1}$0) and NO_2/ZnO(2$\bar{1}\bar{1}$0)
3. *The adsorption of* NO_2 *on* ZnO(2$\bar{1}\bar{1}$0)*, containing oxygen defects:* NO_2/ZnO(2$\bar{1}\bar{1}$0)–V_O

The computational details and surface models employed were described in Chapter 3. The findings for the adsorption of N, O, NO, N_2O and NO_2 onto stoichiometrically balanced ZnO(2$\bar{1}\bar{1}$0) surfaces using DFT have been published in references [26-29].

4.2 Adsorption of Atomic O and N on ZnO($2\bar{1}\bar{1}0$)

4.2.1 Binding Energies and Adsorbate Geometries

The calculated binding energy values for O/ZnO($2\bar{1}\bar{1}0$) and N/ZnO($2\bar{1}\bar{1}0$) are presented in Table 4.1 and Table 4.2, respectively. There were three local minimum energy structures found for each adsorbate. The most stable O adsorbate (structure 1_O) had a binding energy of –2.47eV, while the most stable N adsorbate (structure 1_N) had a binding energy of –1.42eV, indicating that O binds more strongly on the ZnO($2\bar{1}\bar{1}0$) surface. The other two O local minima (structures 2_O and 3_O) have the same binding energy value of –1.55eV. The second most stable N system (structure 2_N) has a binding energy of –1.16eV, while the least stable structure (structure 3_N) has a much weaker binding energy of –0.12eV. The magnitude of the binding energy of the most stable systems indicates that O and N are chemisorbed on the surface. Conversely, the small binding energy of the least stable N structure indicates that the interaction is very weak, suggestive of physisorption.

Table 4.1. Calculated parameters for minimum energy structures of atomic O on ZnO($2\bar{1}\bar{1}0$).

Structure	BE (eV)	$\Delta\phi$ (eV)	Bonded to	d(ads-surf) (Å)	$d_\perp$ (Å)	ν_{sym} (cm^{-1})
1_O	–2.47	–0.04	Zn, Zn, O	2.39, 1.95, 1.50	0.25	595
2_O	–1.55	0.03	Zn	1.96	0.54	362
3_O	–1.55	0.50	Zn, Zn	2.08, 1.95	1.18	397

Binding energy, BE; work-function change, $\Delta\phi$; perpendicular distance between the top surface layer and adsorbate, $d_\perp$; distance between adsorbate and surface, d(ads-surf); symmetric vibrational frequency of the adsorbed species, ν_{sym}.

Table 4.2. Calculated parameters for minimum energy structures of atomic N on ZnO($2\bar{1}\bar{1}0$).

Structure	BE (eV)	$\Delta\phi$ (eV)	Bonded to	d(ads-surf) (Å)	d⊥ (Å)	ν_{sym} (cm^{-1})
1_N	–1.42	–1.13	Zn, Zn, O	2.15, 2.01, 1.39	0.19	759
2_N	–1.16	–1.27	Zn, O	2.12, 1.39	0.43	681
3_N	–0.12	0.07	Zn	2.07	1.68	297

The geometries of these six structures are presented in Figures 4.1 and 4.2. The distances between the top surface layer and the adsorbate (measured as the height of the adsorbate on the top surface plane) as well as the shortest adsorbate to surface atom distance for the O/ZnO($2\bar{1}\bar{1}0$) and N/ZnO($2\bar{1}\bar{1}0$) systems are presented in Table 4.1 and Table 4.2, respectively.

It was calculated that both atomic species will adsorb preferentially on the surface in more highly coordinated sites, as seen in Figures 4.1 and 4.2. The geometries of the most stable atomic O and N systems are very similar, with both adsorbates interacting with two neighbouring Zn atoms as well as one neighbouring oxygen surface atom. The geometry of the other minima are also very similar to each other, with one structure showing the adsorbate bonding to two surface atoms (structures 3_O and 2_N). It is noteworthy that atomic O bonds to two surface zinc atoms, whilst N bonds to a surface zinc atom and one atomic O atom. For the other minima, both O and N only bond to one surface Zn atom (structures 2_O and 3_N).

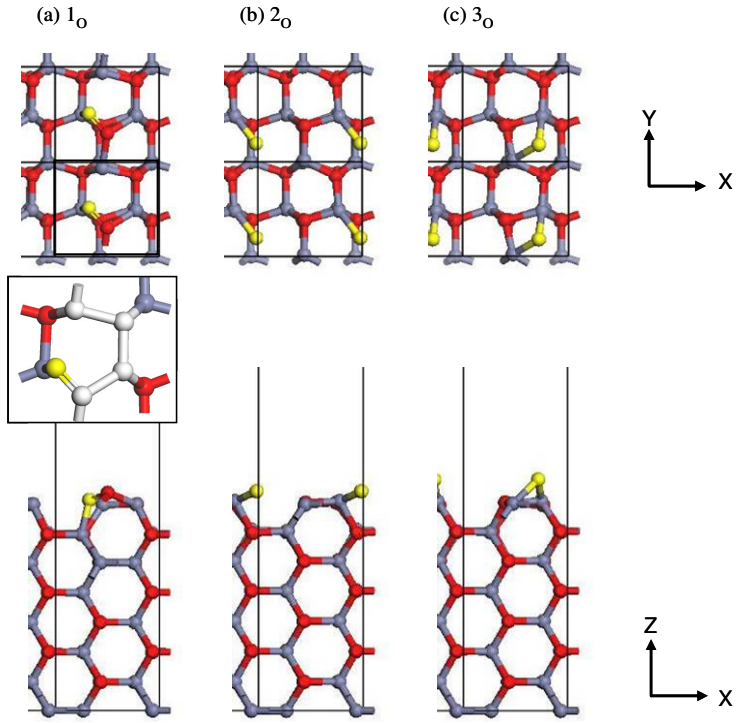

Figure 4.1. Optimised geometries of the three local minimum structures for O/ZnO(2$\bar{1}\bar{1}$0), showing structures (a) 1_O, (b) 2_O and (c) 3_O. Inset of (a) shows enlarged view of adsorbate and top layer atoms. Surface oxygen atoms denoted in red, zinc atoms in grey, oxygen adsorbate atom in yellow (for clarity), other top layer atoms of structure 1_O inset in white.

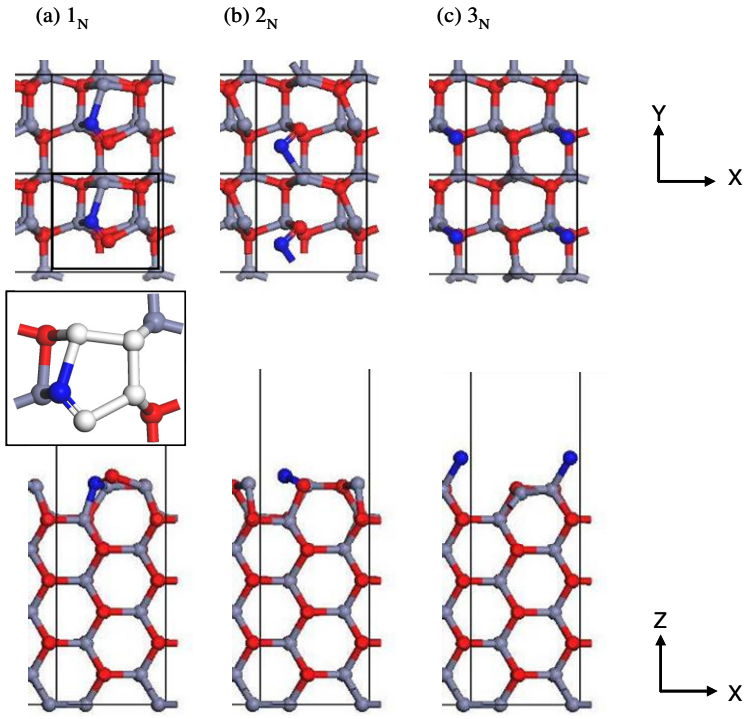

Figure 4.2. Optimised geometries of the three local minimum structures for N/ZnO(2$\bar{1}\bar{1}$0), showing structures (a) 1_N, (b) 2_N and (c) 3_N. Inset of (a) shows enlarged view of adsorbate and top layer atoms. Surface oxygen atoms denoted in red, zinc atoms in grey, nitrogen adsorbate atom in blue, other top layer atoms of structure 1_N inset in white.

The upper layer of the clean ZnO surface comprises two zinc atoms and two oxygen atoms arranged into a hexagonal pattern which can be seen in Figure 4.3. For the most stable O and N structures, the adsorbate atom was found to integrate itself into the upper layer of the $(2\bar{1}\bar{1}0)$ surface. Interestingly, when the N adsorbate incorporates itself into the top surface layer, it forms a distorted 5-membered ring with the top layer ZnO surface atoms (inset Figure 4.2a). Atomic O was also found to integrate itself in a similar manner (inset Figure 4.1a). In these integrated systems, the shortest distances are between the adsorbate atom and a surface oxygen atom, resulting in the formation of an O-O bond or an N-O bond, that are shorter than the clean Zn-O bond length of 1.96 Å in the relaxed surface. The O-O bond is 1.52 Å, which is 0.29 Å longer than the molecular bond length for O_2 of 1.23 Å. Similarly, the N-O bond was measured to be 1.39 Å, which is 0.22 Å longer than the molecular NO bond length of 1.17 Å. The increase in these distances compared to the free molecule is due to the fact that atomic O and N are also bonded to other surface atoms, reducing their interaction with the closest surface atom and lengthening the bond.

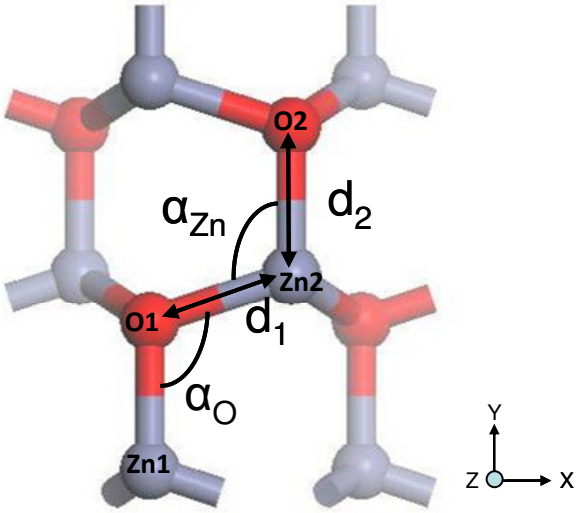

Figure 4.3. Surface parameters measured for ZnO$(2\bar{1}\bar{1}0)$ (oxygen atoms denoted in red, zinc atoms in grey). α_{Zn} is the O-Zn-O angle; α_O is the Zn-O-Zn angle; d_1 and d_2 are the surface Zn-O bond distances.

As can be seen in the top view of structure 3_O (Figure 4.1c), the chemisorbed O forms a bridging bond between two surface zinc atoms, positioning itself over the hollow site that is formed by the hexagonal structure of wurtzite ZnO. Importantly, the O-Zn adsorbate-substrate bond length is identical to those found in the relaxed ZnO surface (1.96Å). Additionally, the height of the adsorbate above the upper layer is 1.52 Å which is only slightly larger than the first interlayer distance of 1.42Å, indicating that O adsorbs in an attempt to retain the surface geometry.

The shortest distance between the adsorbate and substrate atoms was observed in the integrated surface models, being as low as 1.39 Å for atomic N bonded to a surface O atom (Figure 4.2a). The perpendicular distance between the top surface layer and the adsorbate was found to be less than 2 Å for all six minima. The shortest perpendicular distance was 0.19 Å for the three-fold adsorption of atomic N (structure 1_N) reflecting the integration of the adsorbate into the top surface layer, whilst the largest distance was measured for the adsorption of atomic N onto the atop zinc site was structure 3_N (1.68 Å), indicating a physisorbed species.

4.2.2 Relaxation and Reconstruction of the ZnO($2\bar{1}\bar{1}0$) Surface

The displacements of atoms in the top two layers of the surface after the adsorption of atomic O and N species are reported in Table 4.3 and Table 4.4, respectively. Relaxation of the two zinc and two oxygen surface atoms (movement in the direction perpendicular to the surface plane, i.e. *z*- axis) is referenced against their original positions in the relaxed clean surface. Here, negative values represent a movement towards the bulk (contraction) and positive values indicate a displacement away from the surface (expansion). Reconstructions on the other hand, occur when the surface atoms move in the *x*- and *y*- directions of the surface.

Table 4.3. Atomic displacements (Å) upon adsorption of atomic O on ZnO($2\bar{1}\bar{1}0$).

	Reconstruction				Relaxation							
Structure	α_{Zn} (°)	α_O (°)	d_1 (Å)	d_2 (Å)	Layer 1				Layer 2			
Clean ZnO	119.6	105.4	1.90	1.88	Zn1	Zn2	O1	O2	Zn1	Zn2	O1	O2
1_O	120	117	1.95	1.89	0.08	0.10	0.74	0.12	0.03	–0.06	–0.06	–0.03
2_O	100	107	1.93	1.93	–0.07	0.14	0.05	0.05	0.09	0.01	–0.11	–0.03
3_O	107	92	2.03	1.90	0.14	–0.07	0.04	0.05	0.01	0.09	–0.04	–0.11

α_{Zn} is the O-Zn-O angle; α_O is the Zn-O-Zn angle; d_1 and d_2 are the surface Zn-O bond distances, as shown in Figure 4.3.

Table 4.4. Atomic displacements (Å) upon adsorption of atomic N on ZnO($2\bar{1}\bar{1}0$).

	Reconstruction				Relaxation							
Structure	α_{Zn} (°)	α_O (°)	d_1 (Å)	d_2 (Å)	Layer 1				Layer 2			
Clean ZnO	119.6	105.4	1.90	1.88	Zn1	Zn2	O1	O2	Zn1	Zn2	O1	O2
1_N	116	118	2.02	1.89	0.17	0.13	0.70	0.19	0.03	–0.06	–0.06	–0.02
2_N	72	92	2.83	1.96	0.21	0.30	0.21	0.16	0.11	–0.18	–0.06	–0.02
3_N	115	105	1.93	1.90	–0.14	0.05	0.10	0.07	0.01	0.02	0.00	–0.04

The first interlayer spacing of the relaxed clean ZnO($2\bar{1}\bar{1}0$) surface was 1.52 Å, while the second to third layer separation was relatively larger measuring 1.68 Å. Buckling (an uneven movement of the atoms in the z-axis) was seen for all minimum energy structures, where the surface oxygen atom relaxed by a different amount to the surface zinc atom. This was most predominant in the first layer, with the largest displacement being 0.74 Å. The average displacement of either oxygen or zinc in this layer (regardless of whether the movement was a contraction or expansion of the layer) for any of the structures was 0.12 Å. Buckling also occurred in the second layer but to a lesser extent with

displacements up to 0.24 Å in magnitude, and an average displacement for this layer of 0.09 Å. Hence, relaxation of layers 1 and 2 in the surface model, caused by O and N indicates that the adsorbates interact with both surface layers, however, the larger displacements observed in layer 1 indicate a stronger interaction with these atoms. The relaxations of the third layer of surface atoms were <0.001Å, indicating weaker or no interaction with the adsorbate.

In addition to the surface relaxations seen after adsorption of both atomic species, considerable surface reconstructions were also observed. Surface reconstructions were largest when the adsorbate atoms integrated themselves into the upper layer of the ZnO surface model distorting the structure of the clean surface (as seen in Figure 4.1a and Figure 4.2a). In these models the second layer atoms can be seen when inspecting the top view of the surface, whereas in the clean surface model they are aligned directly under the top layer of atoms. Smaller surface reconstructions are apparent in the two fold adsorption configurations where the second layer is almost completely obfuscated by the first layer, as seen in Figures 4.1 and 4.2.

The geometric features characterising surface reconstruction are listed in Tables 4.3 and 4.4, and shown in Figure 4.3, where α_{Zn} is the O-Zn-O angle; α_O is the Zn-O-Zn angle; and d_1 and d_2 are the surface Zn-O distances. The corresponding values for the clean relaxed surface are also presented. After adsorption, the d_1 length was found to increase for both O and N systems, with the increase being in the range of 0.03Å to 0.93Å. Similarly, the d_2 length was found to increase in all systems, however, the bond length change was much smaller in magnitude, ranging from 0.01Å – 0.08 Å. Adsorption also caused a distortion of the α_{Zn} and α_O angles, with the O systems having a maximum α_{Zn} distortion of 19.6° and a maximum α_O distortion of 13.0°. The N systems had similar changes as reflected by their similar bonding arrangements, however, large changes of α_{Zn} of 47° and α_O of 13° were observed in structure 2_N. The changes in these distances as well as the measured angles after adsorption were found to specifically depend on which adsorbate-substrate bonds were formed. In structure 1_O the adsorbate does not bond to the surface Zn2 or O2 atom, hence, it is not surprising that the d_2 bond length barely changes. For structure 2_O, atomic O bonds to the surface Zn2 atom, resulting in an equal lengthening of d_1 and d_2 bonds. In structure 3_O, atomic O bonds to the surface Zn1 and Zn2 atoms, hence d_1 and d_2 both increase. As structure 1_N shows similar bonding to structure 1_O, it is not

surprising that the lengthening of the d_1 bond is similar. In structure 2_N, the large movements of the surface Zn2, O2 and O1 atoms result in large changes of d_1, α_O and α_{Zn}. For structure 3_N, where N bonds to only the surface Zn2 atom, both lengths change by similar amounts. Overall, the interaction of the adsorbates with the surface tends to weaken the strength of the Zn-O surface bonds directly involved in the bonding, resulting in a lengthening of the surface bond.

4.2.3 Workfunction Changes

The work-function changes of the adsorbate atoms (O and N), as presented in Table 4.1 and 4.2, show that structures 2_O, 3_O and 3_N induce a positive work-function change, whereas structures 2_O, 1_N and 2_O have a negative work-function change. If an adsorbate induces a positive work-function change, this indicates that they withdraw electrons from the surface upon adsorption. Conversely, a negative work-function change indicates a donation of charge from the adsorbate to the surface. Comparison of the six minimum energy structures reveals that a positive work-function change occurs when atomic O or N interacts with surface zinc atoms only, whereas a negative work-function change arises when the atomic O or N atom interact with both surface zinc and oxygen atoms.

Osbourne *et al.* [30] reported a drop in conductivity when sensors were exposed to a flux of atomic O; this observation can be related to our calculated positive work-function changes for structures 2_O and 3_O which indicated that atomic O withdraws charge from the ZnO surface. This removal of electrons from the surface leads to an increased resistance, i.e. a decrease in conductivity, supporting Osbourne's observations. Interestingly, the most stable structure 1_O has a small negative function change, however, as we find more than one stable structure, it is possible that the experimentally measured work function change reflects a combination of more than one minima. As the magnitude of the work function change for structure 1_O is smaller than for structures 2_O and 3_O, the net change may still be positive, in agreement with experiment.

4.2.4 Vibrational Frequencies

The symmetric stretch vibrational frequency of the adsorbed atomic species is presented in Table 4.1 and 4.2. For adsorbed O, the stretching mode occurs over a smaller range of frequencies (362 cm^{-1} – 595 cm^{-1}) than for adsorbed N (297 cm^{-1} – 759 cm^{-1}). Furthermore, the magnitude of the symmetric vibrational frequency of the different structures is dependent upon the adsorption geometry, with the more highly co-ordinated adsorbates having larger symmetric stretches than the adsorbates that interact with a single surface atom. Hence for structures 1_O and 1_N, the calculated frequencies are the largest. In structures 3_O and 2_N, where O and N interact with two surface atoms, they have the second largest frequencies. The lowest vibrational frequencies were calculated for the systems that involve adsorption onto a single zinc surface atom (structures 3_O and 2_N). In summary, it was found that as the degree of coordination increases, the peaks are further bathochromically (red) shifted. To the best of our knowledge there has been no Infrared (IR), Vibrational Electron Energy Loss, (VEELS) or Reflection Adsorption Infrared (RAIRS) spectroscopy studies of the atomic species of O and N adsorbing onto the ZnO($2\bar{1}\bar{1}0$) surface for comparison.

4.2.5 Charge Density and Electron Localisation Functions

Charge density difference plots and Electron Localisation Function (ELF) plots of the minimum energy structures of O/ZnO($2\bar{1}\bar{1}0$) and N/ZnO($2\bar{1}\bar{1}0$) structures are presented in Figure 4.4 and Figure 4.5, respectively. The charge density difference slices were generated by subtracting the charge density of the clean surface and the isolated adsorbate atom from that of the adsorbed surface structure in all their positions after atomic O or N adsorption and relaxation. For each adsorbate, separate charge density and electron localisation function plots were generated; these plots were aligned to cut through the adsorbate atom and its closest neighbouring surface atoms. For the ELF plots, high regions (indicated in red) can be interpreted as bonding and non-bonding electron pairs [31].

For structure 1_O, where the O adsorbate (O_{ads}) interacts with both surface zinc (Zn_{surf}) and surface oxygen (O_{surf}) atoms, the electron density maps are taken along slice 1 (O_{ads}-O_{surf}) and slice 2 (O_{ads}-Zn_{surf}). Along the direction of the O_{ads}-O_{surf} bond in slice 1, there is a region of charge depletion followed by accumulation, then depletion. The symmetric distribution of charge

accumulation/depletion between O_{ads} and O_{surf} suggests a covalent type of bonding. For the ELF plot, high regions of electron localisation are found on the adsorbate and substrate oxygen atoms aligned perpendicular to the bond, representative of p-orbitals. In contrast, the charge density difference plot along slice 2 (O_{ads}-Zn_{surf}) mainly shows regions of charge accumulation and depletion located on the O atom, with little change on the zinc atom. Such an uneven distribution suggests a degree of ionic character in this bond. This slice also cuts through the second layer zinc atom, showing a similar interaction with the O_{ads} as the top layer zinc atom, indicating most of the charge redistribution occurs between the adsorbate atom and the surface oxygen atom. Overall, the regions of charge accumulation, as well as depletion, located on the adsorbate atom may result in the small work function change observed for this structure.

The charge density difference plots and ELF of structure 2_O shows a smaller redistribution of charge, consistent with the smaller binding energy value of this structure. Along the O_{ads}-Zn_{sub} bond (slice 1) there is a region of charge accumulation close to the O atom, while there is a region of depletion around the Zn atom, indicating a bond of ionic nature. Furthermore, there is a large region of charge depletion around the O atom in the direction away from the bond. In the ELF plot, the region of high localisation occurs on the adsorbate O atom, similar to the bulk, indicating that the bonding is similar and mainly ionic in nature.

The charge density difference and ELF slices of structure 3_O, shown along slice 1 (Zn_{sub}-O_{ads}-Zn_{sub}), indicate that the O adsorbate atom has formed an ionic-type bond to both surface zinc atoms, given that along the two bonds there is a region of charge depletion close to either zinc atom and a region of accumulation close to the adsorbate O atom. As one zinc atom is 0.13 Å closer to the adsorbate than the other, the charge depletion is larger, indicating a stronger interaction between the closer atoms. The ELF plot confirms the mainly ionic character of the bond, with localised electron pairs residing on the O adsorbate atom. The charge density difference plots of structures 2_O and 3_O indicate an overall withdrawal of charge from the surface, in line with the calculated positive work-function changes. It is noteworthy that the sign of the work-function change is affected by the surface atoms that the adsorbate interacts with. Positive work-function changes were calculated for both adsorbed O and N when the adsorbate bonded with zinc atoms. In contrast, negative work-function changes were

calculated when the adsorbate interacted with both surface oxygen and zinc atoms. Interactions between the adsorbate and the surface zinc atoms resulted in ionic-type bonding, whereas interactions with O atoms were more likely to results in the formation of covalent-type bonding as expected from the electronegativity of the atoms. The small negative work-function change of structure 1_O is most likely due to donation of charge to the surface in an attempt to stabilise the covalent-type bond observed in slice 1.

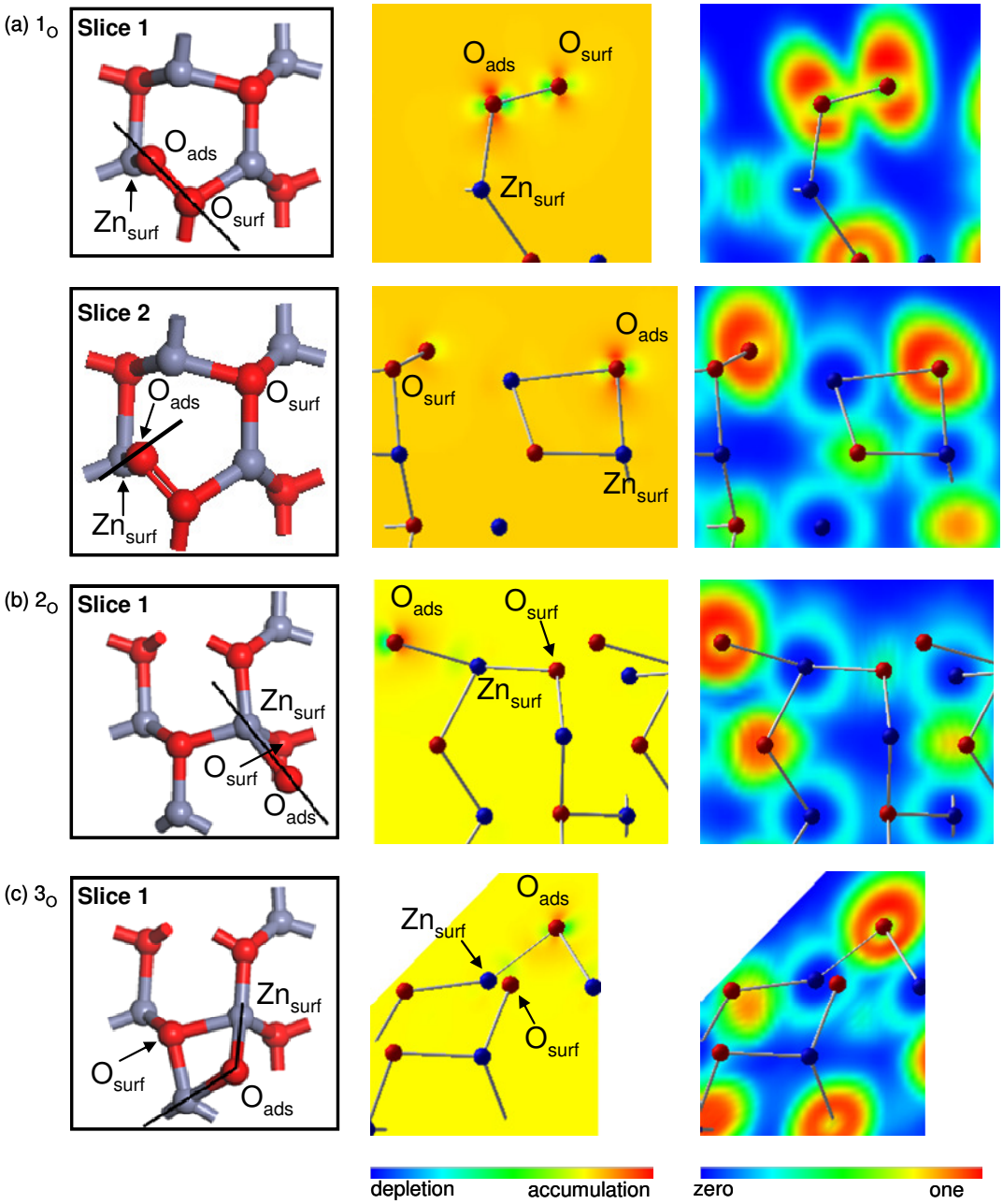

Figure 4.4. Charge density difference plots (middle) and ELF plots (right) of the O/ZnO($2\bar{1}\bar{1}0$) structures, (oxygen atoms denoted in red and zinc atoms in blue). The slices are taken along the shortest adsorbate-substrate distances, as indicated in the top view of the structures (left).

For structure 1_N, the charge density difference plots again show large regions of charge accumulation and depletion. Going along slice 1 (N_{ads}-O_{sub}), there is a region of depletion followed by accumulation and then depletion, similar to what was observed in slice 1 of structure 1_O. Again, there are regions of charge accumulation perpendicular to the bond direction, located on the O and N atoms, resembling p orbital lobes. Such changes again indicate a high degree of covalency in the bonding. In the ELF plot, there is again a large region of localisation on both the oxygen atom and adsorbate N atom, just as in structure 1_O. Slice 2 (N_{ads}-Zn_{sub}) highlights a distinct accumulation of charge on the N adsorbate atom suggesting an ionic interaction with the surface zinc atom. This is accompanied by a small depletion of charge located around the surface zinc atom. This charge rearrangement is not observed in slice 2 of the 1_O system, as the geometry of the 1_N system is more highly strained than that of the 1_O system. Comparing structures 1_O and 1_N in Figure 4.1 and Figure 4.2, respectively, it can be clearly seen that the bonds formed in the top layer of structure 1_O are longer than those in structure 1_N. The ELF plot of structure 1_N (N_{ads}-Zn_{surf}) exemplifies this withdrawal of charge from surrounding atoms, visible as distortions in the lobes of the orbitals on the N adsorbate atom. The close proximity of the N adsorbate atom to the surface has an interesting effect on the calculated work-function change. For both structures 1_N and 2_N, the charge density difference and ELF plots show that the N atom is close enough to neighbouring surface atoms to affect the electron density of atoms in the second layer. This proximity is anticipated to cause the N atom to donate electronic charge to its immediate surroundings, which results in the negative work-function change.

The charge density difference plot of structure 2_N, along slice 1 (N_{ads}-O_{sub}) indicates covalent bonding between these atoms. The ELF plot shows a significant flaring of the N atom p-orbitals in the z-direction away from the surface. Slice 2 (N_{ads}-Zn_{surf}) shows a somewhat unusual pattern of electron density between the N and zinc atom, with a region of charge depletion near the zinc atom and a region of accumulation near the N atom. This region of accumulation lies along the bond as well as perpendicular to the surface. This unusual density profile creates an ELF plot that has a region of paired electrons on the N adsorbate atom which lies along the bond as well as located away from the surface.

The charge density difference and ELF plots of the least stable structure 3_N still contain considerable charge differences despite the small binding energy value of –0.12 eV. Moving along the bond from the zinc atom to the N adsorbate atom, there is a large depletion of charge, followed by an accumulation near the N atom. There is also a small region of charge depletion near the N atom which indicates an ionic bond with some covalent character. It is noteworthy that the accumulation of charge on the N atom has also affected the oxygen atom directly underneath it. The small accumulation of charge on the second layer atoms was not observed in the other structures. The accumulation of electron density on the N adsorbate atom may also be responsible for the positive work-function change of 0.07 eV.

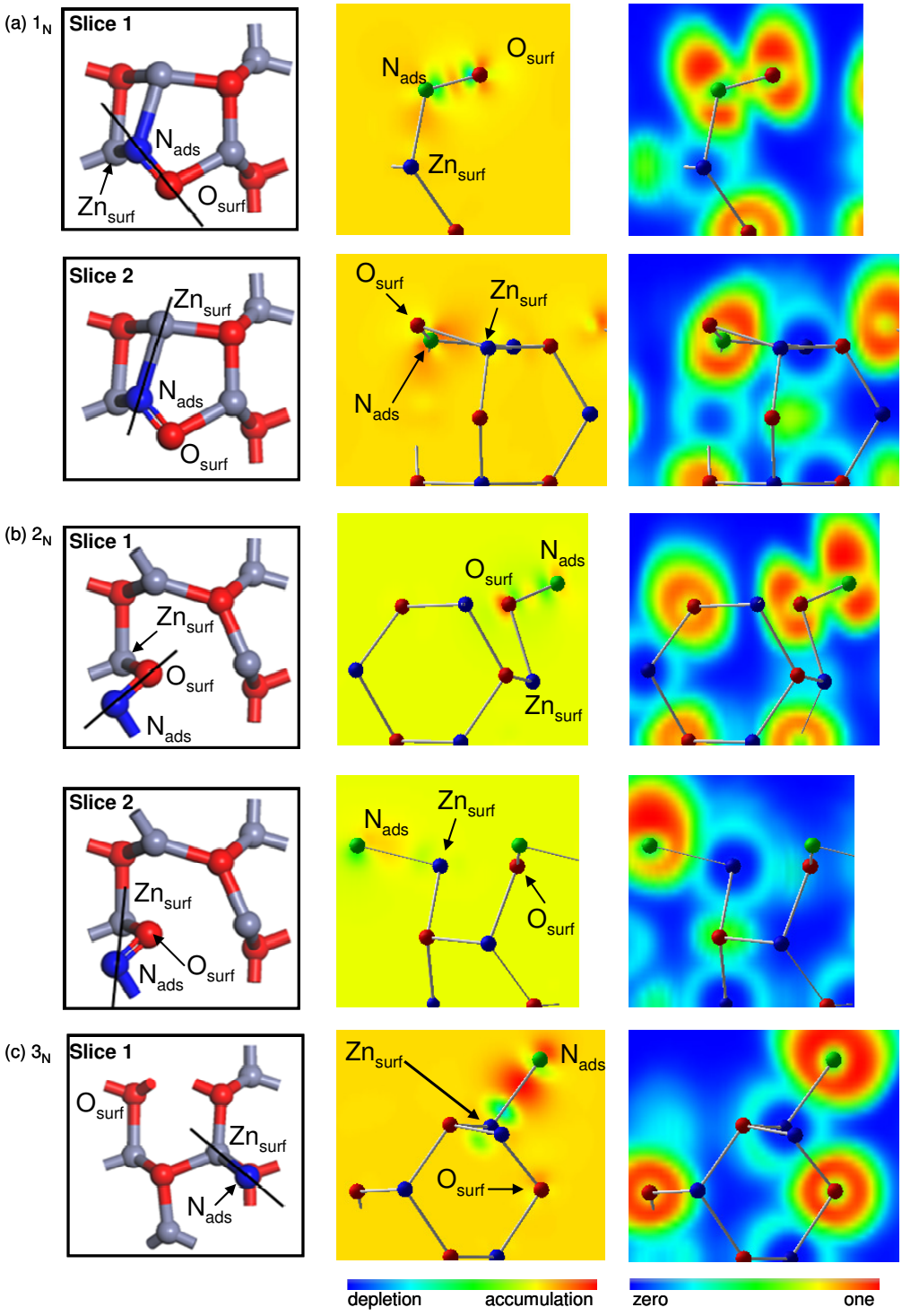

Figure 4.5. Charge density difference plots (middle) and ELF plots (right) of the N/ZnO($2\bar{1}\bar{1}0$) structures, (oxygen atoms denoted in red, nitrogen atoms in green, and zinc atoms in blue). The slices are taken along the shortest adsorbate-substrate distances, as indicated on the top view of the structures (left).

4.2.6 Summary and Implications for Gas Sensing

The interactions between the ZnO($2\overline{1}\overline{1}0$) surface and the atomic O and N adsorbates are for the most part strong, indicating chemisorption. The most stable adsorbed O structure had a binding energy of –2.47eV, while the most stable N adsorbate had a binding energy of –1.42eV, indicating that O binds more strongly on the ZnO($2\overline{1}\overline{1}0$) surface. For these two structures the adsorbate bonded to two or three surface atoms. Two additional local minimum structures were found for O as well as for N, where the adsorbate atom bonded to only one or two surface atoms, resulting in less stable structures. Surface relaxation after adsorption was found to be largest in the top two surface layers, and negligible in subsequent layers, indicating the interaction between the adsorbate and surface was primarily confined to the surface region. Surface reconstructions were also observed, being prominent for the most stable minima of both adsorbates, but minor in the less stable structures. Both ionic and covalent type bonds were observed between the adsorbate and the surface. When the O or N atoms bonded to a surface oxygen atom, a bond of mainly covalent nature was formed. In contrast, when the adsorbates bonded to a surface Zn atom the bond was mainly ionic in nature with some covalent character. Workfunction calculations showed positive changes after adsorption in less highly coordinated sites and negative changes for more highly coordinated sites. The positive work-function changes of adsorbed atomic O may be correlated with the experimentally observed decreases in conductivity of ZnO conductometric sensor technologies after exposure to atomic O. Conversely, it is hypothesised that the large negative work-function change calculated for Stuctures 1_N and 2_N would cause the ZnO sensor to decrease in resistance, resulting in an increase in conductivity upon exposure to atomic N, effectively functioning in the opposite mode of operation than compared with exposure to O. The ZnO($2\overline{1}\overline{1}0$) surface may prove to be useful in the development of an atomic N sensor.

4.3 Adsorption of NO and NO_2 on ZnO($2\bar{1}\bar{1}0$)

4.3.1 Binding Energies and Adsorbate Geometries

The calculated properties of unique minimum energy structures obtained after adsorption of NO and NO_2 are presented in Table 4.5 and Table 4.6, respectively. Eleven minimum energy structures were identified for the NO/ZnO($2\bar{1}\bar{1}0$) system (Figure 4.6), and a further nineteen for the NO_2/ZnO($2\bar{1}\bar{1}0$) system (Figure 4.7).

The most stable NO system (1a) had a binding energy of –0.40 eV, and the most stable NO_2 system (2a) had a binding energy of –0.31 eV. The binding energies of all NO systems ranged from –0.09 eV to –0.40 eV, while the binding energies of the NO_2 systems ranged from –0.02 eV to –0.31 eV. The binding energies of all 30 minimum energy structures suggest that both NO and NO_2 adsorbed weakly onto ZnO($2\bar{1}\bar{1}0$).

The calculated height of NO adsorbed onto the surface (see Table 4.5) ranged from 1.35 Å – 3.35 Å. NO prefers to adsorb with its nitrogen atom positioned towards the surface, with the most stable NO systems adsorbing in an offset bridge type configuration as seen in structures 1a and 1b. The hollow site was found to be the least stable NO adsorption site. NO_2 typically adsorbed onto the ZnO($2\bar{1}\bar{1}0$) surface (Table 4.6) at a height of 1.60 Å – 3.34 Å above the surface, via the interaction of an adsorbate oxygen atom with a surface zinc atom. As can be seen in Figure 4.7, the majority of adsorbed systems have the NO_2 orientated such that the nitrogen atom is further away from the surface than either of the oxygen atoms. The exceptions to this orientation scheme are structures 2b, 2d, 2m, 2n, 2o and 2p. The orientation of the NO_2 molecule with respect to the surface model and the formation of multiple Zn_{surf} - O_{ads} bonds (structure 2g) was found to have an impact on the electronic properties of the system as will be discussed in § 4.3.3 and § 4.3.5.

Table 4.5. Calculated parameters for minimum energy structures of NO/ZnO($2\bar{1}\bar{1}0$).

Structure	BE (eV)	$\Delta\phi$ (eV)	d(ads-surf) (Å)	$d_{\perp}$(Å)	d(O=N) (Å)	Symmetric stretch (cm^{-1})
NO	-	-	-	-	1.17 (1.15)*	1890 (1904)*
1a	–0.40	–0.99	2.34	1.35	1.18	1803
1b	–0.35	–1.08	2.33	1.68	1.18	1814
1c	–0.30	–0.99	2.26	1.81	1.17	1850
1d	–0.30	–1.10	2.15	1.46	1.20	1672
1e	–0.26	–0.98	2.30	2.14	1.17	1847
1f	–0.24	–1.04	2.36	2.18	1.18	1803
1g	–0.18	–1.35	2.52	2.41	1.18	1835
1h	–0.11	–1.21	3.01	2.33	1.17	1848
1i	–0.11	–1.18	3.12	2.90	1.17	1891
1j	–0.09	–1.23	3.50	3.21	1.17	1854
1k	–0.09	–1.28	3.40	3.35	1.17	1851

Binding energy (BE); work-function change ($\Delta\phi$); perpendicular distance between the top surface layer and adsorbate ($d_{\perp}$); distance between adsorbate and surface (d(ads-surf)); bond length of NO (d(O=N)); *Experimental values [39].

Unlike the NO species, the bent NO_2 molecule has a higher degree of flexibility with respect to both its bond length and its internal bond angle upon adsorption, with the internal bond angle of the free NO_2 molecule calculated to be 133.8°. Post adsorption, this angle was found to decrease or remain the same. Contractions ranged from –1° to –12°, with the largest contraction corresponding to the greatest elongation of both N=O bonds. These geometric changes were largest for structure 2g, where the NO_2 molecule has adsorbed over the hollow site (parallel to the surface) with both oxygen atoms of the NO_2 molecule interacting with atop zinc atoms, effectively stretching the NO_2 molecule. Overall, the largest changes are seen for the most stable structures, while the weakest structures show little if any changes to these geometric parameters.

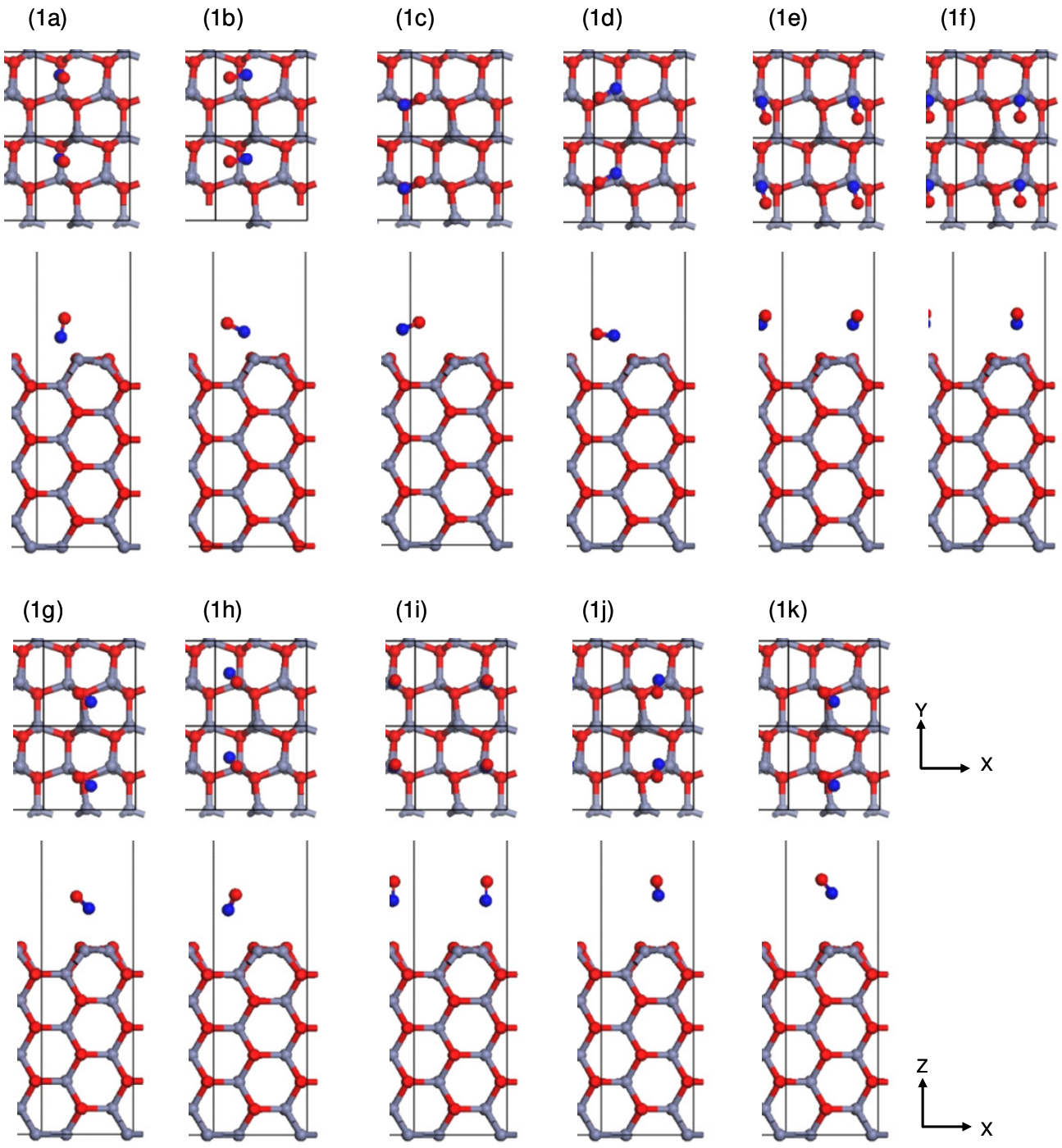

Figure 4.6. (a-k) NO/ZnO(2$\bar{1}\bar{1}$0) surface models.

Table 4.6. Calculated parameters for minimum energy structures of NO_2/ZnO($2\bar{1}\bar{1}0$).

Structure	BE (eV)	$\Delta\phi$ (eV)	d(ads-surf) (Å)	d⊥ (Å)	Δ bond angle (°)	d(O-N, N-O) (Å)	Symmetric stretch (cm^{-1})	Asymmetric stretch (cm^{-1})	Bending (cm^{-1})
NO_2	-	-	-	-	-	1.22 (1.19)*	1332 (1318)*	1672 (1610)*	725 (750)*
2a	–0.31	–0.13	2.19	1.66	–6	1.22, 1.24	1221	1529	699
2b	–0.28	0.26	2.17	1.80	–6	1.25, 1.21	1216	1529	727
2c	–0.28	–0.24	2.22	1.92	–4	1.23, 1.23	1228	1562	685
2d	–0.26	0.25	2.17	2.96	–7	1.25, 1.21	1218	1605	727
2e	–0.26	–0.19	2.22	2.14	–5	1.24, 1.22	1234	1581	695
2f	–0.24	–0.18	2.60	2.45	–5	1.24, 1.22	1237	1573	690
2g	–0.23	0.03	2.12-2.16	1.60	–12	1.25, 1.25	1367	1205	742
2h	–0.23	–0.28	2.18	1.89	–5	1.24, 1.22	1228	1581	715
2i	–0.23	–0.07	2.18	2.00	–5	1.22, 1.24	1235	1577	706
2j	–0.13	–0.06	1.80	1.79	0	1.22, 1.22	1221	1614	681
2k	–0.10	–0.20	2.50	2.21	–3	1.23, 1.21	1239	1634	718
2l	–0.09	–0.20	3.32	2.87	–1	1.22, 1.22	1310	1654	697
2m	–0.08	0.09	3.80	2.06	–1	1.21, 1.22	1289	1611	719
2n	–0.07	0.07	2.06-1.72	2.21	0	1.22, 1.22	1306	1657	706
2o	–0.05	0.34	2.80	2.86	–1	1.22, 1.22	1292	1608	719
2p	–0.05	0.27	2.81	3.03	–1	1.22, 1.22	1324	1660	718
2q	–0.04	–0.22	3.50	3.08	–1	1.22, 1.22	1315	1651	722
2r	–0.03	–0.10	3.13	3.05	0	1.22, 1.22	1317	1675	716
2s	–0.02	–0.15	3.40	3.34	0	1.22, 1.22	1327	1683	725

Adsorption site refers to the position of the adsorbate once it has been relaxed onto the surface; Binding energy (BE); work-function change ($\Delta\phi$); perpendicular distance between the top surface layer and adsorbate (d⊥); distance between adsorbate and surface (d(ads-surf)); bond length of O-N and NO-O (d(O-N, N-O)); change in internal bond angle of the NO_2 molecule (Δbond angle); *Corresponding experimental value [39]; calculated bond angle of free NO_2 is 133.8° (134.1°)*.

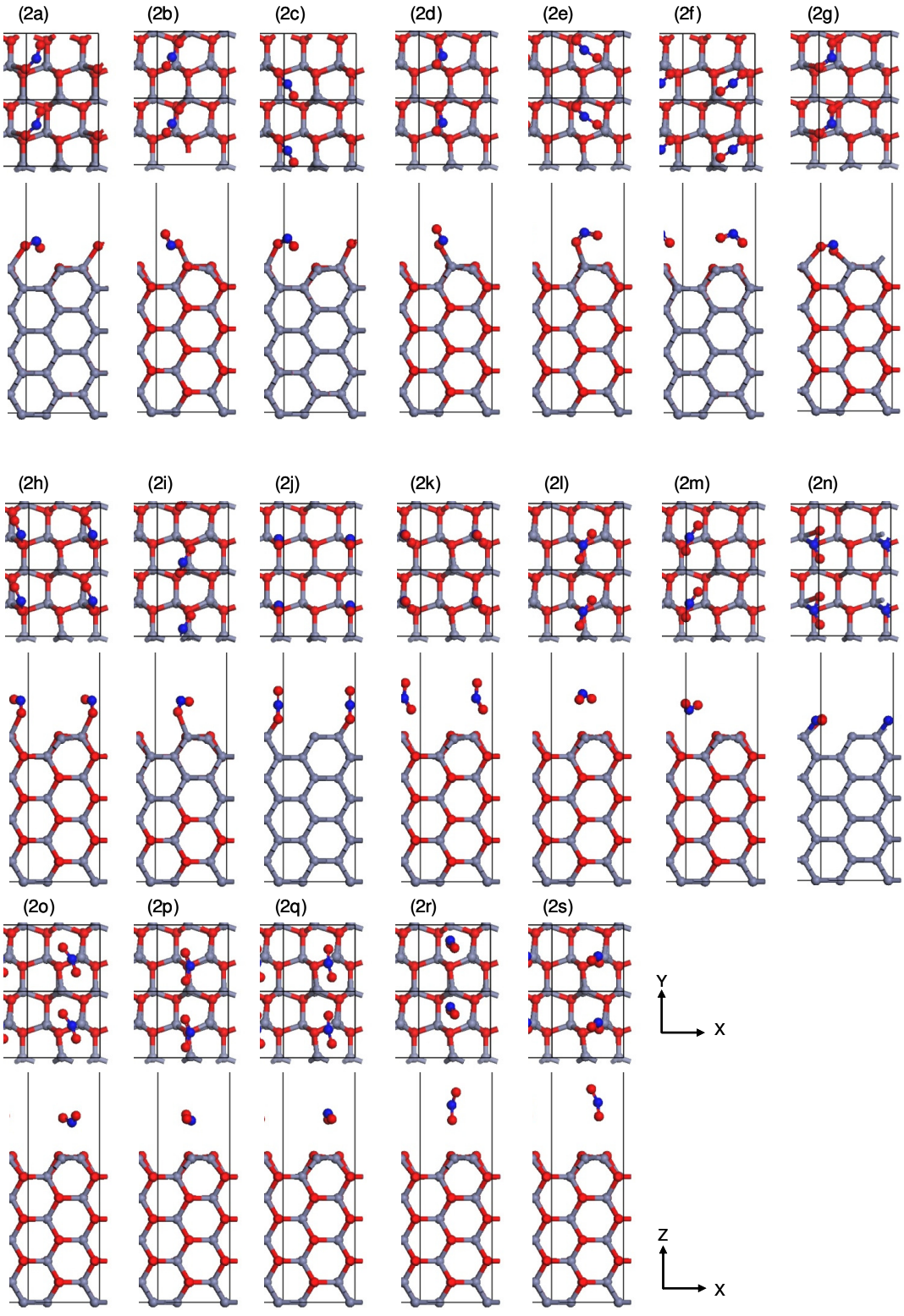

Figure 4.7. (a-s) NO_2/ZnO(2$\bar{1}$ $\bar{1}$0) surface models.

4.3.2 Relaxation and Reconstruction of the ZnO(2$\bar{1}\bar{1}$0) Surface

Due to the weak interaction that NO and NO_2 have with the ZnO(2$\bar{1}\bar{1}$0) surface, both reconstructions and relaxations are minor. First we discuss the relaxation of the two zinc and two oxygen surface atoms (movement in the direction perpendicular to the surface plane, i.e. *z*-axis) referenced against their original positions in the relaxed clean surface. Negative values represent a movement towards the bulk (contraction) and positive values indicate a displacement away from the surface (expansion). The first interlayer spacing of the relaxed clean ZnO(2$\bar{1}\bar{1}$0) surface is 1.52 Å, while the second to third layer separation is larger, measuring 1.68 Å. Buckling was observed in the most stable NO and NO_2 systems, with displacements (averaged from all atoms in the first layer) of 0.03 Å and –0.11 Å, respectively. The second layer displacements of the NO system were found to be smaller in magnitude than the first layer, being –0.01 Å. A more significant buckling of –0.14 Å was calculated for the second layer of the NO_2 system, which was larger than displacements of the first layer. The relaxations of the 3rd layer of surface atoms for both systems were <0.002 Å indicating little or no interaction of the surface atoms with the adsorbate. In summary, the most stable NO_2 system caused larger relaxations of the ZnO surface than the most stable NO system. The other minimum energy structures were found to relax in a similar manner, and hence are not discussed in further detail.

The geometric features describing the surface reconstructions (Figure 4.3) and listed in Table 4.7 and Table 4.8, where α_{Zn} is the O-Zn-O angle; α_O is the Zn-O-Zn angle; and d_1 and d_2 are the surface Zn-O bond lengths. Reconstructions occur when the surface atoms move in the *x*- and *y*- directions after adsorption. The corresponding reference values for the relaxed clean surface are also presented for reference.

Table 4.7. Surface reconstructions, post adsorption of NO on ZnO(2$\bar{1}\bar{1}$0).

NO Structures	α_{Zn} (°)	α_O (°)	d_1 (Å)	d_2 (Å)
Clean ZnO	*119.6*	*105.4*	*1.90*	*1.88*
1a	117.7	110.3	1.91	1.89
1b	119.4	108.8	1.93	1.88
1c	117.3	103.8	1.94	1.91
1d	115.1	109.1	1.94	1.90
1e	116.9	104.3	1.94	1.90
1f	117.5	104.1	1.90	1.90
1g	119.2	105.2	1.91	1.88
1h	119.8	105.3	1.91	1.88
1i	118.2	105.0	1.90	1.89
1j	119.0	106.8	1.90	1.89
1k	119.7	105.6	1.90	1.88

α_{Zn} is the O-Zn-O angle; α_O is the Zn-O-Zn angle; d_1 and d_2 are the surface Zn-O bond distances, as shown in Figure 4.3.

Table 4.8. Surface reconstructions, post adsorption of NO_2 on ZnO($2\bar{1}\bar{1}0$).

NO_2 Structures	α_{Zn} (°)	α_O (°)	d_1 (Å)	d_2 (Å)
2a	113.7	108.2	1.92	1.91
2b	119.1	110.7	1.90	1.88
2c	112.9	106.4	1.92	1.91
2d	118.6	110.2	1.91	1.88
2e	119.4	109.2	1.90	1.89
2f	117.0	104.5	1.92	1.90
2g	110.4	113.5	1.92	1.92
2h	114.6	104.6	1.92	1.90
2i	119.4	110.6	1.89	1.88
2j	108.3	108.3	1.99	1.99
2k	117.2	104.6	1.92	1.90
2l	120.0	105.7	1.90	1.88
2m	118.5	105.7	1.91	1.89
2n	108.3	108.3	1.99	1.99
2o	119.9	105.6	1.90	1.88
2p	119.4	106.0	1.90	1.88
2q	120.4	105.2	1.90	1.88
2r	120.4	105.5	1.90	1.88
2s	120.0	104.9	1.90	1.88

α_{Zn} is the O-Zn-O angle; α_O is the Zn-O-Zn angle; d_1 and d_2 are the surface Zn-O bond distances, as shown in Figure 4.3.

Typically, adsorption causes distortion in the α_{Zn} and α_O angles, with the largest distortions found in the NO_2 systems. The NO systems were found to have maximum α_{Zn} and α_O distortions of 2.5° and 6.5°, respectively, whereas the NO_2 systems were calculated to have a maximum α_{Zn} distortion of 12.1° and α_O distortion of 8.9°. Thus, adsorption causes the d_1 and d_2 lengths to change in response to the distortion caused by surface rearrangement when the α_{Zn} and α_O angles change. After adsorption

the d_1 and d_2 bond lengths were found to increase by up to 0.04 Å and 0.03 Å, respectively, for all the NO systems. For the NO_2 systems, the d_1 and d_2 bond lengths also increased by small amounts. However, in structure 2i, d_1 was found to decrease by only 0.01 Å. Changes in the d_2 bond length for the NO_2 structures 2j and 2n were largest, increasing by 0.11 Å. It should be noted that overall, the changes in the α_{Zn}, α_O, d_1 and d_2 values for the NO and NO_2 systems are small because of the weak binding to the ZnO($2\bar{1}\bar{1}0$) surface. In the previous section (§ 4.2), larger changes in these values were seen for the more strongly bound atomic oxygen and nitrogen species.

4.3.3 Workfunction Changes

The work-function changes of NO and NO_2 upon adsorption onto the ($2\bar{1}\bar{1}0$) surface are reported in Table 4.5 and Table 4.6, respectively. When adsorbates induce a positive work-function change upon adsorption, they are expected to withdraw electrons from the surface. Conversely, a negative work-function change indicates a donation of charge from the adsorbate to the surface. Here, work-function changes were found to be negative, ranging from –0.98 eV to –1.35 eV for all NO systems. Similarly, most of the work-function changes for the NO_2 systems were also negative, but smaller in absolute values, in the range of –0.07 eV to –0.24 eV. Several structures, however, were found to induce a positive work-function change (structures 2b, 2d, 2g, 2m, 2n, 2o, 2p) corresponding to increases of 0.03 eV to 0.34 eV. The adsorbed orientation of NO_2 with respect to the surface was found to be related to the direction of the work-function change. When the nitrogen atom of NO_2 is positioned closer to the surface than the oxygen atoms, a positive work-function change is observed. Conversely, the opposite orientation results in a negative work-function change.

As discussed earlier, ZnO($2\bar{1}\bar{1}0$) is an important sensing surface which is observed in a large number of ZnO nanostructures. Negative work-function changes which are caused by a donation of electronic charge to the surface correlate with a decrease in sensor resistance upon exposure to the target adsorbate, here either NO or NO_2. The opposite applies to adsorbate orientations that affect a positive work-function change, which will cause a resistance increase in the conductometric sensor upon exposure to the target gas. Cho *et al.* [12] experimentally determined that the adsorption of NO_2 on a loose ZnO nanorod conductometric gas sensor resulted in an increase in resistance upon exposure

to 1% NO_2. This increase in resistance correlates with a withdrawal of electronic charge from the surface, consistent with a positive work-function change.

While we have previously been able to relate the calculated work-function changes directly to the experimental observations of resistance changes in conductometric sensing platforms [35], it should be noted that the presence of multiple surfaces in experiments can complicate such a comparison. In addition, it has been discussed in the literature that the work function changes do not necessarily correlate with the direction of the charge transfer due to the surface overspill of electron density into the adsorbate region [37]. Therefore in this work, we do not intend to directly correlate the work function changes with the experimentally measured changes in conductivity.

Interestingly, less than half of the calculated minimum energy structures reported in this study have a positive work-function change. Furthermore, the structures with positive work-function changes correspond with geometries where the nitrogen atom of the NO_2 molecule is closer to the surface than the adsorbate oxygen atoms. Such a switch in the sign of the work-function change with changing adsorbate geometry is not unheard of, having been shown previously to occur for NO/Pt(111) [36] and N/W(100) [37].

As all our reported structures are stable minima with relatively small energy differences, the experimental work function change is likely to be produced by more than one minimum energy structure. If one assumes a Boltzmann distribution of the multiple unique minimum energy structures, the overall work-function change would be negative (i.e. decrease in resistance). Given that the experimentally measured work-function change is positive (i.e. increase in resistance), we can attribute the difference to the contributing effects of other ZnO crystal facets that are also present in the real sensing element. While the ZnO($2\bar{1}\bar{1}0$) surface represents one of the most common facets on ZnO nanostructures, it is by no means the only crystal face present, nor will it be the sole contributor to the electrical changes observed when the sensor is exposed to NO_2. The experimentally observed changes in resistance can be affected by the presence of other major crystal facets, namely the $\{10\bar{1}0\}$ and {0001} surfaces of ZnO. Furthermore, the presence of surface defects and impurities may also affect the observed work-function change. Hence, further work investigating other crystal facets as well as

defect surfaces may shed light on the inconsistency between experiment and theory. Such an investigation will be presented, later on in § 4.4.

4.3.4 Vibrational Frequencies

The calculated vibrational frequencies of NO and NO_2 adsorbed on ZnO($2\bar{1}\bar{1}0$) are presented in Table 4.5 and Table 4.6, respectively. The experimental and theoretically derived frequency values for the free NO and NO_2 molecules are also presented. It can be seen that the calculated vibrational characteristics of the adsorbate molecules are in good agreement with experimental values. Vibrational shifts shall be defined as bathochromically (red) shifted, or hypsochromically (blue) shifted.

For NO/ZnO($2\bar{1}\bar{1}0$), the vibrational frequencies are in the range of 1672 cm^{-1} – 1891 cm^{-1}, compared to the symmetric stretch of the free NO molecule which was calculated to be 1890 cm^{-1}. Hence, adsorption tends to cause a shift in the N-O stretching band to a lower frequency (bathochromically shifted). Structure 2d seems to show an inconsistently large shift in this frequency, which may be explained by fact that NO is adsorbed parallel to the surface, whereas it is adsorbed perpendicular or at an angle to the surface for the other structures. Generally, however, the shift in the frequency after adsorption was greater for the more stable structures which also had shorter adsorbate-substrate distances.

The calculated symmetric stretch values of NO_2/ZnO($2\bar{1}\bar{1}0$), presented in Table 4.6, show frequencies of 1216 cm^{-1} – 1367 cm^{-1}. The symmetric stretch was generally found to shift to lower frequencies with increasing stability. The asymmetric stretches of adsorbed NO_2 (1529 cm^{-1} – 1660 cm^{-1}) were mostly bathochromically shifted upon adsorption, showing larger displacements with increasing stability of the adsorbate on the surface. The bending modes of NO_2/ZnO($2\bar{1}\bar{1}0$), for the majority of systems, were found to be bathochromically shifted, with frequencies between 681 cm^{-1} – 742 cm^{-1}. The notable exceptions are structures 2b, 2d and 2g with particularly large bond angle contractions, which result in small hypsochromic shifts, in particular structures 2b and 2d being only 2 cm^{-1} higher than the free molecule.

As seen from Table 4.6, the vibrational frequencies of structure 2g do not follow the general trends discussed above which can be ascribed to the adsorption geometry which involves both oxygen atoms

interacting with the underlying surface. The strained 2g system has the smallest calculated asymmetric stretch of 1205 cm^{-1}, which is believed to be a result of the electrostatic repulsion between the two oxygen atoms which are 0.05 Å closer than in the free molecule, reducing the asymmetric stretch by 472 cm^{-1}. Additionally, it is the only structure which has a symmetric stretch higher than its asymmetric stretch, which may be caused by the uniform elongation of both nitrogen-oxygen bonds by 0.03 Å and a bond angle contraction of 12 °.

To the best of our knowledge, no experimentally determined vibrational frequency values for adsorption of either NO or NO_2 on the ZnO($2\bar{1}\bar{1}0$) surface have been published. It is expected, however, that due to the large number of stable minima we have determined from our calculations, that any experimentally observed vibrational frequencies (determined by techniques such as Infrared (IR), Vibrational Electron Energy Loss, (VEELS) or Reflection Adsorption Infrared (RAIRS) spectroscopy) will be the result of one or more structures, and hence a combination of the vibrational frequencies reported in this work.

4.3.5 Charge Density and Electron Localisation Functions

Charge density difference plots and ELF of the most stable minimum energy structures of NO/ZnO($2\bar{1}\bar{1}0$) and NO_2/ZnO($2\bar{1}\bar{1}0$) are presented in Figure 4.8. The charge density difference slices were generated by subtracting the charge density of the clean surface and the isolated adsorbate molecules in their positions in the optimised adsorbed structure. For each adsorbate, the plots were aligned to slice directly through the atoms forming the shortest adsorbate-substrate distance, together with other adsorbate atoms where possible. In the ELF plots, high regions (indicated in red) can be interpreted as bonding and non-bonding electron pairs [38].

For NO, the slices of system 1a (Figure 4.8a) are taken through the nitrogen atom of the NO molecule and the closest surface zinc and oxygen atoms. Large regions of depletion and accumulation can be seen on the nitrogen atom, with regions of depletion orthogonal to the accumulation. The ELF plot shows a region of high electron density and orbital overlap between the N_{ads} atom and the closest Zn_{surf} atom; on the other side of the nitrogen atom there is slight orbital overlap with the surface oxygen atom.

The charge density difference plot of the most stable NO_2 system (structure 2a, Figure 4.8b), where the oxygen atoms on the adsorbate molecule are positioned closer to the surface than the nitrogen atom, show a substantial redistribution of charge between the adsorbate and the surface. On the adsorbate molecule there is an accumulation of charge centred about the nitrogen atom, with small regions of relative charge depletion directed along each bond towards the peripheral oxygen atoms. O_{ads1} has a small region of depletion, which propagates away from the oxygen atom, and a more significant accumulation of charge projected towards the nitrogen atom. There is a region of charge accumulation around O_{ads2}, and a region of depletion around Zn_{surf}, with additional regions of charge accumulation on O_{ads2} and Zn_{surf} individually. The ELF plot reveals a region of electron density about the nitrogen atom, projected away from the surface, while both oxygen atoms exhibit charge localisation patterns which resemble two separate p-orbitals on each oxygen atom. Between each adsorbate oxygen atom and the nitrogen atom there is a small region of high electron localisation which may be interpreted as s-orbital overlap. The sp^2 hybridisation of N in the NO_2 molecule, with uniform s and p-orbital contributions typical of covalent bonding, can also be seen.

The second set of slices of the most stable NO_2 system (3a) focuses on the interaction between O_{ads1} and the closest surface oxygen atom. It is quite clear from the slices that while there is some accumulation and depletion individually on both O_{ads1} and O_{surf}, there is no interaction between them; it is also clear from the ELF plot that the orbitals do not overlap.

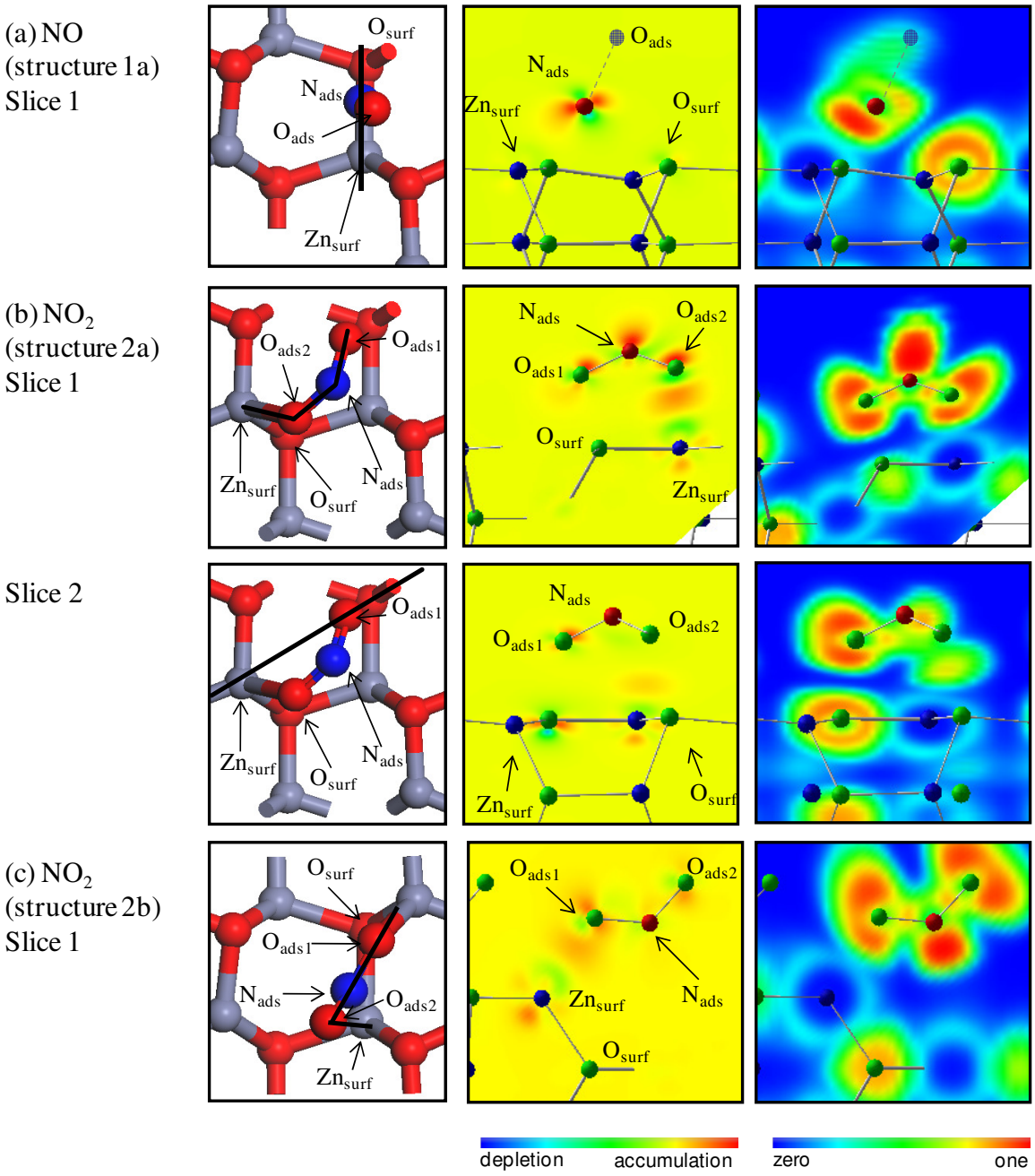

Figure 4.8. Charge density difference (middle) and ELF (right) plots of (a) the most stable NO/ZnO($2\bar{1}\bar{1}0$) structure; (b) and (c) the two most stable NO_2/ZnO($2\bar{1}\ \bar{1}0$) structures, (oxygen atoms denoted in green, nitrogen atoms in red, and zinc atoms in blue). The slices are taken along the axis of the adsorbate bond, and or the shortest adsorbate-substrate distances, as indicated by the thick black lines of the top down view of the surface (left).

Charge density difference plots of the second most stable NO_2 system (2b), where the nitrogen atom is closer to the surface than the oxygen atoms, are shown in Figure 4.8c. The surface zinc atom has a region of charge depletion directed towards O_{ads1}, with a smaller region of charge accumulation in the opposite direction. Moving towards O_{ads1} there is a region of charge accumulation, followed by a small region of depletion. Minor regions of electron accumulation and depletion are visible about the nitrogen atom, with the O_{ads2} atom showing a region of accumulation perpendicular to the surface, and small regions of depletion, orthogonal to the accumulative regions. The ELF plot reveals that both oxygen atoms have a larger area of high electron localisation than in system 2a, having gained electron density from the surface.

NO_2 may be interpreted as two oxygen atoms each bonding to a positively charged nitrogen atom with a 1.5 bond order. If nitrogen is sufficiently close to the surface it may try and obtain electronic charge in an attempt to stabilise its lone electron pair. Such a stabilisation would involve withdrawal of charge from the surface, which may cause an overall positive work-function change, which was observed for all geometric configurations where the adsorbate nitrogen atom is closer to the surface than the peripheral oxygen atoms.

More detailed analysis of the charge density of the systems may also shed light on the work-function results. The calculated Bader charge for the atoms in the most stable structures are presented in Table 4.9. It is clear that the most significant charge transfer is confined to the top surface layer of atoms, with the atom(s) that are closest to the adsorbate undergoing the largest charge transfer. Moving into the centre of the slab, any charge transfer is minor, in agreement with the geometric changes of the adsorbed systems which indicate little if any relaxation or reconstruction due to the presence of the adsorbed NO or NO_2 molecules.

For adsorbed NO, both adsorbate atoms have gained charge, while the closest surface atoms have lost charge, resulting in an overall transfer of charge from the surface to the adsorbate. Such a change would be expected to result in a positive work function change, however, we will discuss later how the presence of an electronegative surface species can still result in a negative work-function change.

Table 4.9. Calculated Bader charges of the most stable NO and NO_2 structures adsorbed on ZnO($2\bar{1}\bar{1}0$). The calculated values for the clean surface and free molecules are also shown.

	Charge					
Atom	**NO_2**	**NO**	**Clean ZnO($2\bar{1}\bar{1}0$)**	**NO structure 1a**	**NO_2 structure 2a**	**NO_2 structure 2b**
O1 (ads)	–0.31	–0.44	-	–0.46	–0.41	–0.36
O2 (ads)	–0.37	-	-	-	–0.47	–0.48
N (ads)	0.68	0.44	-	0.38	0.67	0.68
O_{1a}, O_{1b}	-	-	**–1.14, –1.14**	**–1.09, –1.14**	**–1.12, –1.08**	**–1.06, –1.14**
O_{2a}, O_{2b}	-	-	–1.18, –1.18	–1.20, –1.19	–1.20, –1.19	–1.19, –1.20
O_{3a}, O_{3b}	-	-	–1.19, –1.19	–1.20, –1.20	–1.21, –1.20	–1.20, –1.20
O_{4a}, O_{4b}	-	-	–1.20, –1.20	–1.20, –1.20	–1.20, –1.20	–1.20, –1.20
O_{5a}, O_{5b}	-	-	–1.19, –1.19	–1.20, –1.20	–1.21, –1.20	–1.20, –1.20
O_{6a}, O_{6b}	-	-	–1.18, –1.18	–1.20, –1.20	–1.21, –1.21	–1.21, –1.21
O_{7a}, O_{7b}	-	-	–1.18, –1.18	–1.18, –1.18	–1.20, –1.20	–1.19, –1.19
O_{8a}, O_{8b}	-	-	–1.15, –1.15	–1.15, –1.15	–1.16, –1.16	–1.15, –1.15
Zn_{1a}, Zn_{1b}	-	-	**1.14, 1.14**	**1.13, 1.17**	**1.20, 1.18**	**1.14, 1.21**
Zn_{2a}, Zn_{2b}	-	-	1.18, 1.18	1.20, 1.20	1.20, 1.21	1.20, 1.20
Zn_{3a}, Zn_{3b}	-	-	1.18, 1.18	1.19, 1.20	1.21, 1.21	1.20, 1.20
Zn_{4a}, Zn_{4b}	-	-	1.20, 1.20	1.20, 1.20	1.20, 1.20	1.20, 1.19
Zn_{5a}, Zn_{5b}	-	-	1.19, 1.19	1.20, 1.20	1.20, 1.21	1.20, 1.20
Zn_{6a}, Zn_{6b}	-	-	1.19, 1.19	1.20, 1.20	1.21, 1.21	1.21, 1.21
Zn_{7a}, Zn_{7b}	-	-	1.19, 1.19	1.19, 1.19	1.21, 1.21	1.20, 1.20
Zn_{8a}, Zn_{8b}	-	-	1.13, 1.13	1.13, 1.13	1.15, 1.15	1.14, 1.14

1a represents the first atom in the first layer and 1b represents the second atom in the first layer.

The planar averaged charge density difference plots (in the *z*-direction), for NO structure 1a and NO_2 structures 2a and 2b are presented in Figure 4.9. The plots are aligned so that the position of the top surface layer atom lies at zero.

For NO_2, the two most stable structures also show an overall transfer of charge from the surface to the adsorbate, with the transferred charge residing on the adsorbate O atoms. Hence, NO_2 is behaving as an electronegative adsorbate, as expected. For structure 2a, the charge on both surface Zn and O atoms is affected by the adsorbate, indicating that the adsorbate O atom that points towards the surface also interacts with the surface. In contrast, for structure 2b, only the charge of one of the topmost surface O and Zn atoms is altered by the adsorbed NO_2.

As can be seen in Figure 4.9a for NO adsorption, there is a region of charge depletion at the surface, followed a region of charge accumulation close to the adsorbed N atom. In between the adsorbate N and O atom there is a region of charge depletion followed by accumulation. These changes are consistent with the Bader charges that indicate NO withdraws charge from the surface, however, the changes are inconsistent with the calculated negative work function change. It has been shown previously that an electronegative adsorbate can still withdraw charge from the surface while displaying a positive work function change [37] due to other changes in the planar averaged charge density difference plots away from the adsorbate-surface interface. In particular, for our system, the presence of the small depletion in charge located at ~3.5 Å beyond the surface may contribute to the negative work function change, while still being consistent with a transfer of charge from the adsorbate to the surface.

For the two most stable NO_2 systems (Figure 4.9b and Figure 4.9c), there is a region of charge depletion followed by accumulation in between the adsorbed NO_2 and the topmost surface layer, again indicating NO_2 is behaving as an electronegative adsorbate withdrawing charge from the surface. Despite the similarities for both structures, there is a region of charge accumulation at the surface for structure 2a, which is absent for structure 2b. Such a difference may explain the difference in the sign of the negative work-function change for these structures. The different adsorbate geometries are also found to give rise to minor changes in the charge redistribution in between the adsorbate atoms themselves, showing in particular a region of charge depletion that is present for structure 2b but absent for structure 2a. This difference, together with the charge differences in the surface region, may also impact on the charge redistribution at the surface and hence the change in work-function.

(a) NO
(structure 1a)

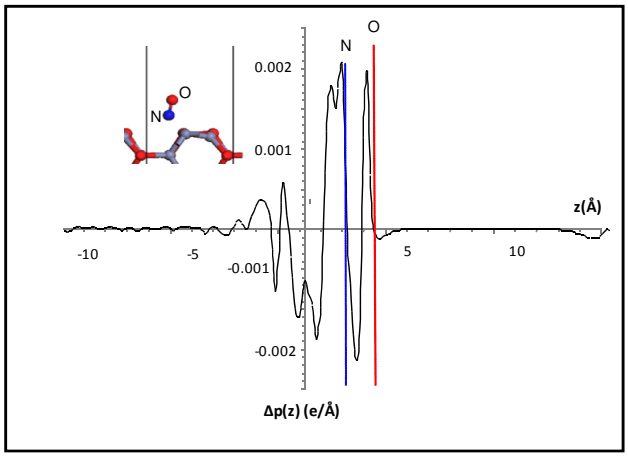

(b) NO_2
(structure 2a)

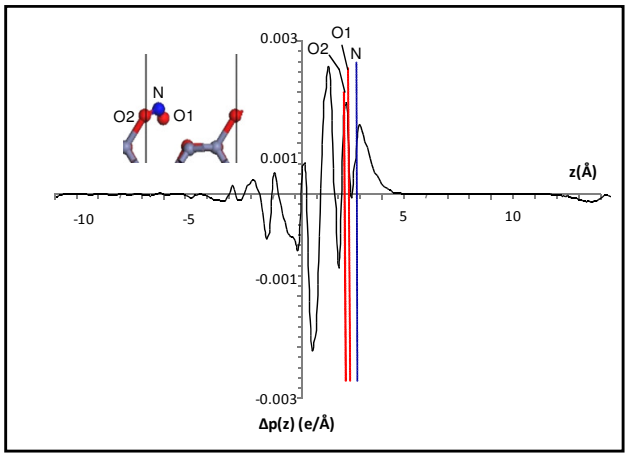

(c) NO_2
(structure 2b)

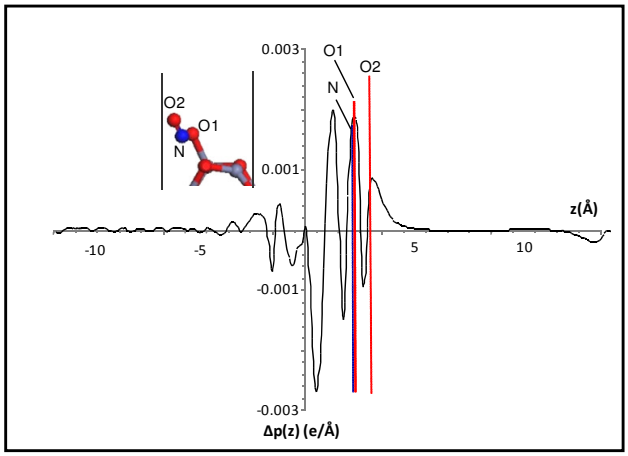

Figure 4.9. Planar averaged charge density difference plots of (a) the most stable NO/ZnO($2\bar{1}\bar{1}0$) structure; (b) and (c) the two most stable NO_2/ZnO($2\bar{1}\bar{1}0$) structures.

4.3.6 Summary and Implications for Gas Sensing

The calculated binding energies of NO and NO_2 indicate weak adsorption occurs on the stoichiometrically balanced ZnO($2\bar{1}\bar{1}0$) surface with a large number of minimum energy structures calculated for both adsorbates. NO was more stable than NO_2 on the ZnO($2\bar{1}\bar{1}0$) surface, interacting with either Zn or O surface atoms via the nitrogen atom. The NO_2 systems with the highest stability were those which interacted with an atop zinc atom via an adsorbate oxygen atom. The more stable structures show larger vibrational frequency shifts, and shorter adsorbate-substrate distances. Surface relaxation after adsorption was found to be largest in the top two surface layers, and negligible in subsequent layers indicating that the adsorbate interaction is localised to the uppermost surface layers. Similarly, surface reconstructions were also observed, however, these were minor. Despite showing weak binding energies, the charge density plots indicate that there is a transfer of charge from the surface to the adsorbate molecule. Fine differences in the charge density difference plots within the surface region and adsorbate region may give rise to the unexpected negative work function value for some structures.

The large number of minimum energy structures; the barrier-less physisorption process; and comparatively negligible surface reconstruction and relaxation suggests that at appropriate operating conditions, ZnO($2\bar{1}\bar{1}0$) crystal surfaces may be suitable for NO and NO_2 sensing applications where long term stability is desired.

4.4 Adsorption of NO_2 on $ZnO(2\bar{1}\bar{1}0)$–V_O

4.4.1 Binding Energies and Adsorbate Geometries

The relaxed $ZnO(2\bar{1}\bar{1}0)$–V_O and $NO_2/ZnO(2\bar{1}\bar{1}0)$–$V_O$ surface models, and the calculated properties of these structures are presented in Figure 4.10 and Figure 4.11. The five unique $NO_2/ZnO(2\bar{1}\bar{1}0)$–$V_O$ minimum energy structures are depicted in Figure 4.10, presented in descending order of stability, with binding energies from –1.58 eV to –0.81 eV (Table 4.10). The magnitude of these values suggests that the adsorbate chemisorbs on the surface, in contrast to adsorption on the non-defect surface, where markedly weaker adsorption was calculated (§ 4.3).

The calculated binding energies for the two structures of $NO_2/ZnO(11\bar{2}0)$–V_O reported by Prades *et al*. [24] were –0.94 and –0.79 eV, which are similar to the reported values in this thesis, despite the different concentration of O vacancies present. It is interesting to note that our binding energy values are almost three times greater than the binding energy of the most stable adsorbed NO_2 configuration on the stoichiometric $ZnO(2\bar{1}\bar{1}0)$ surface [27].

For all minimum energy structures presented in Figure 4.10, the interaction between the adsorbate and the surface occurs through the adsorbate oxygen, and or, nitrogen atoms and one or more surface Zn atoms. For structure 1, each atom in NO_2 is adsorbed to a surface Zn atom surrounding the vacancy site. For structures 2-5, either both O atoms or one O atom and the N atom of NO_2 are adsorbed to two surface Zn atoms. Specifically, for structures 2 and 4, NO_2 only interacts with surface Zn atoms directly surrounding the defect site, while structures 1, 3 and 5, NO_2 also interacts with a surface Zn atom not directly surrounding the O vacancy. For structures 1 and 5, some of the adsorbate atoms are located in positions where the next surface ZnO atoms would be located, resulting in an attempt to continue the periodicity of the crystal lattice.

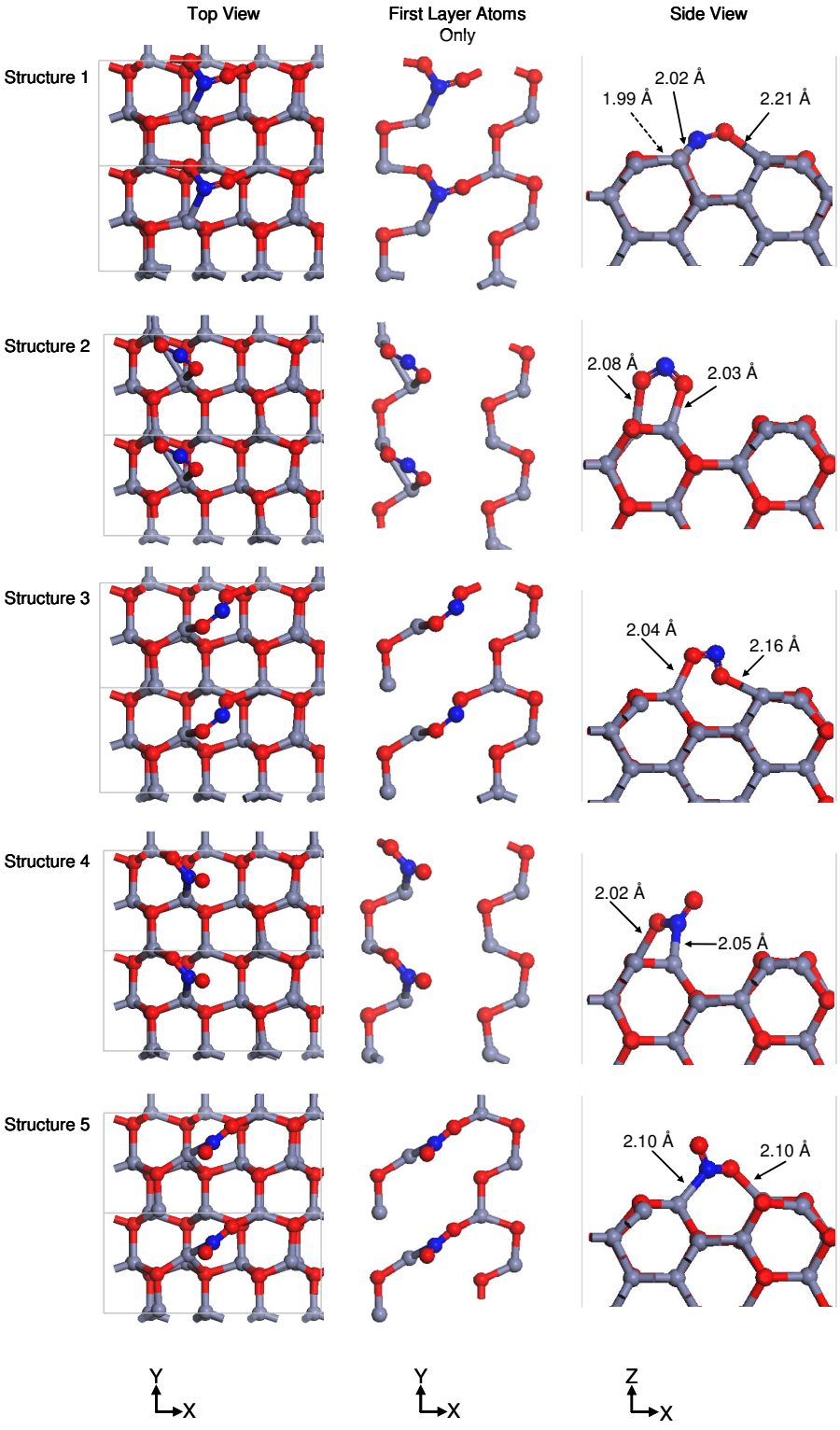

Figure 4.10. $NO_2/ZnO(2\bar{1}\bar{1}0)-V_O$ surface models.

Table 4.10. Calculated parameters for the minimum energy structures of NO_2/ZnO($2\bar{1}\bar{1}0$)–V_O.

Structure	BE (eV)	d⊥ (Å)	d(O-N) (Å)	d(N-O) (Å)	Δd(O-N) (Å)	Δd(N-O) (Å)	Δ<ONO (°)	L_1 (Å)	L_2 (Å)	L_3 (Å)	Symmetric stretch (cm^{-1})	Asymmetric stretch (cm^{-1})	Bend (cm^{-1})
ZnO($2\bar{1}\bar{1}0$)–V_O	-	-	-	-	-	-	-	2.50	2.56	2.64	-	-	-
NO_2	-	-	1.22 (1.19)*	1.22 (1.19)*	-	-	-	-	-	-	1332 (1318)*	1672 (1610)*	725 (750)*
1	–1.58	0.30	1.53	1.26	0.32	0.04	–22	3.55	3.21	3.54	1351	682	479
2	–1.07	1.63	2.03	2.08	0.81	0.86	–16	2.76	2.93	2.96	1292	1210	794
3	–1.02	0.88	2.04	2.16	0.83	0.94	–20	2.83	2.87	3.12	1265	1246	829
4	–0.95	1.53	1.31	1.22	0.09	0.00	–16	3.09	3.23	3.20	1563	1122	789
5	–0.81	1.45	2.10	2.11	0.89	0.89	–15	2.83	2.80	2.94	1475	1213	786

Binding energy (BE); perpendicular distance between the top surface layer and closest adsorbate atom (d⊥); Δd(N-O) (Å) and Δd(N=O) (Å) are the change in O-N bond lengths after adsorption; Δ<ONO is the change in bond angle of the NO_2 molecule after adsorption; L_1, L_2 and L_3 are the distance between the Zn atoms that make up the triangular oxygen vacancy site as labelled in Figure 4.11; the bond angle of free NO_2 is 133.8° (134.1°)*.

*Corresponding experimental value [32].

Overall, the more highly coordinated bonding leads to a stronger binding energy. Compared to the study by Prades *et al.*[24], it appears that our structures 2 and 4 are most similar to the two structures that they found. The difference in binding energies of the structures reported in this study and those reported in Prades *et al*. is –0.13 eV and –0.16 eV for structures 2 and 4, respectively. While we employ a different computational procedure and software package, it appears that the structures are very similar between our study and theirs. The binding energy values can also be attributed to the different O vacancy concentration and coverage of NO_2.

The closest bond distances between the adsorbate atoms and the surface atoms are labelled in Figure 4.10. These distances were calculated to range from 1.99 Å to 2.21 Å, which are the same or close to the Zn-O distances in bulk ZnO (1.98 Å - 2.00 Å). For structure 1, two of the adsorbate atoms are bonded to surface Zn atoms (Zn_{d1} and Zn_{d3}) at distances of 1.99 and 2.02 Å, while the third atom is located 2.21 Å from the Zn_1 surface atom. Hence, while the coordination is three-fold, one of the bond lengths is slightly larger than the other two. For structures 2-5, the bond distances were in the range 2.02 Å – 2.10 Å, and were found to be similar regardless of whether N or O bonds to the surface. Furthermore, the adsorption geometry appears to be such that the position of some of the adsorbate atoms extend the surface, with N capable of assuming positions typically occupied by O atoms in the crystal lattice.

The perpendicular height of NO_2 adsorbed above the surface for all structures (measured as the difference between the *z*-coordinate of the highest surface atom and the lowest adsorbate atom) was calculated to be less than 1.7 Å (Table 4.10). The values were found to vary significantly, with structure 1 showing NO_2 almost integrating itself into the upper surface layer, resulting in a perpendicular height of only 0.3 Å, whereas the two-fold adsorption configuration of structure 2, where NO_2 adsorbed further from the surface, had a calculated perpendicular height of 1.63 Å.

After adsorption the geometry of the NO_2 molecule was distorted for all structures. Elongation of either of the N-O bonds ranged from 0.04 Å to 0.94 Å, with the smallest change in either bond being calculated for structure 4, and the largest change being calculated for structure 5. After adsorption the bond angle of NO_2 was calculated to contract by 15 - 22 °, with contractions occurring in an attempt to compensate for the elongation of N-O bonds.

4.4.2 Relaxation and Reconstruction of the ZnO(2$\bar{1}\bar{1}$0)–V_O Surface

After relaxation of the clean defect surface a large reconstruction was found, where the three Zn atoms surrounding the vacancy formed strong Zn-Zn interactions to compensate for the loss of the oxygen atom in the crystal lattice. The Zn-Zn bond separations, labelled as L_1, L_2 and L_3 in Figure 4.11, after NO_2 adsorption are presented in Table 4.10.

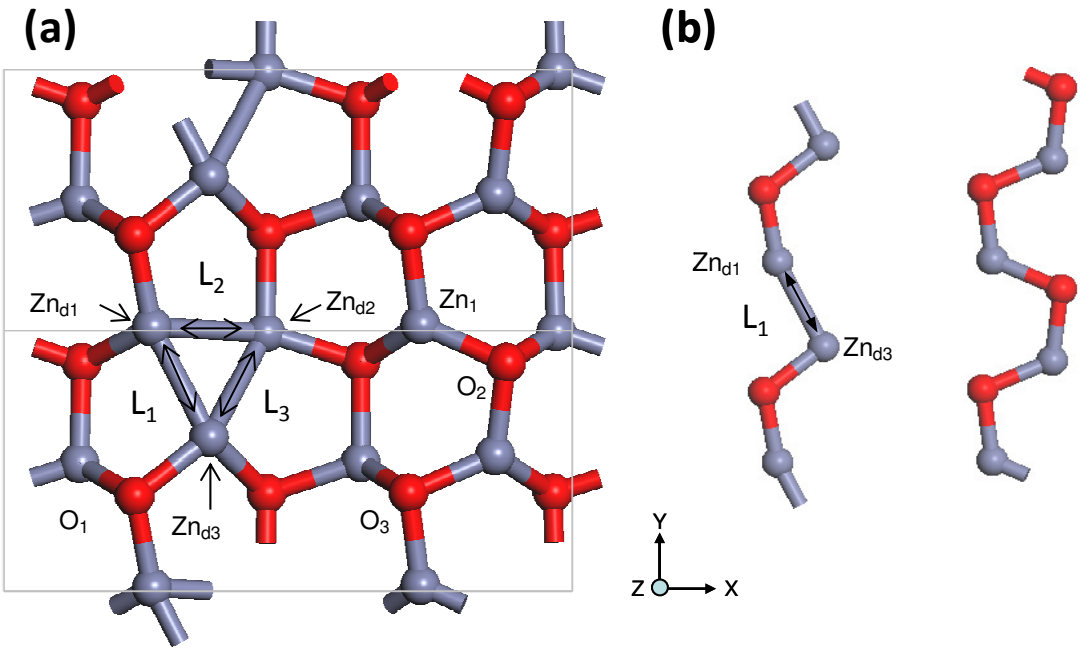

Figure 4.11. (a) Surface parameters measured for ZnO(2$\bar{1}\bar{1}$0)–V_O, the three defect site Zn atoms (denoted Zn_{d1}, Zn_{d2}, Zn_{d3}); (b) first layer atoms only. (oxygen atoms denoted in red, zinc atoms in grey).

On the clean ZnO(2$\bar{1}\bar{1}$0)–V_O surface, distances (L_1, L_2 and L_3) were calculated to be 2.50 Å, 2.56 Å and 2.64 Å, respectively, indicating the formation of an almost equilateral triangular defect site. The Zn-Zn bond length in metallic zinc is 2.66 Å, which is slightly longer than the Zn-Zn separations around the oxygen vacancy site, suggesting the formation of metallic Zn-Zn bonds resulting in the defect site having metallic character.

After adsorption, the surface was found to reconstruct significantly. Due to the complexity of the reconstructions, the first layer of atoms is presented separately in Figure 4.10b, providing a clearer visualisation of only the uppermost surface atoms. For all structures, the bond lengths L_1, L_2 and L_3 were calculated to increase after adsorption of the NO_2 molecule, due to the preferential interaction of

NO_2 with the Zn atoms surrounding the vacancy (as seen in Figure 4.10), reducing the Zn-Zn interactions.

Lengths L_1, L_2 and L_3 after NO_2 adsorption in structure 1 were calculated to increase more than any other structure, believed to be due to the strong three-fold coordination of the adsorbate with the Znd_1, Znd_3 and Zn_1 atoms. The O adsorbate atoms in structure 2 interacted with Zn_{d1} and Zn_{d3}, causing only a minor change in L_1, with lengths L_2 and L_3 increasing due to the reconstruction of the surface vacancy. The adsorption configuration of structure 3 was similar to structure 2, however, the O adsorbate atoms bonded with Znd_3 and Zn_1, increasing L_3, with Zn_{d1} relaxing away from lattice registry, and Zn_{d2} moving back to the lattice position it would assume in the stoichiometrically balanced surface. This caused L_1 and L_2 to slightly increase due the opening up of the defect site. Structure 4 where NO_2 adsorbs with one O atom and the N atom interacting with Zn_{d1} and Zn_{d3} atoms, respectively, resulted in an elongation of L_1, L_2 and L_3, as the defect site Zn atoms relaxing back to their positions on the stoichiometric surface. The similarity of structure 5 with structure 4, (where adsorbate atoms prefer to bind with Zn_{d3} and Zn_1) also resulted in an elongation of L_1, L_2, and L_3.

Overall, adsorption resulted in opening of the vacancy site, where the Zn atoms relaxed almost back to their positions in the stoichiometric surface. This reconstruction pattern is similar to that calculated for NO_2 on the ZnO(10$\bar{1}$0)–V_O surface [11]. In most systems, the adsorption of NO_2 resulted in the complete reconfiguration of the vacancy site, where the oxygen or nitrogen atom of NO_2 assumed the position which oxygen would normally occupy in the next layer of a stoichiometrically balanced ZnO(2$\bar{1}\bar{1}$0) crystal lattice.

The relaxations of the four zinc and three oxygen surface atoms, which constitute the uppermost ZnO(2$\bar{1}\bar{1}$0)–V_O layer are presented in Table 4.11. Here, movement in the direction perpendicular to the surface plane, i.e. *z*-axis, is referenced against their original positions in the relaxed clean surface. Negative values represent a movement towards the bulk (contraction) and positive values indicate a displacement away from the surface (expansion). Only the relaxations of the uppermost surface layer atoms are reported, as displacements of the second surface layer atoms were calculated to be less than 0.03 Å, indicating that the NO_2 interaction is localised to the topmost surface layer. Relaxations of the

uppermost Zn atoms and most of the O atoms were all positive, indicating an expansion of the surface layer. The largest relaxations were calculated for structure 1, which can be ascribed to the close proximity of the adsorbate molecule to the surface and its three-fold coordination.

Table 4.11. Relaxation (Å) in the *z*-direction of the upper surface layer atoms of ZnO($2\bar{1}\bar{1}0$)–V_O after adsorption of NO_2.

Structure	Zn_1	Zn_{d1}	Zn_{d2}	Zn_{d3}	O_1	O_2	O_3
1	0.40	0.05	0.25	0.21	0.13	0.04	–0.04
2	0.17	0.04	0.04	0.26	–0.03	0.02	0.01
3	0.34	0.03	0.22	0.05	0.04	0.01	–0.02
4	0.24	0.05	0.04	0.34	0.04	0.03	0.03
5	0.23	0.05	0.26	0.02	0.02	0.01	–0.05

4.4.3 Magnetic Moments

Prior to adsorption, the spin on the NO_2 molecule is distributed with 38% located on the N atom and 31% on each of the O atoms. After adsorption, only the most stable structure was calculated to still have a magnetic moment, with 50% of the spin on the nitrogen atom, 32 and 5 % on the adsorbate oxygen atoms, respectively, and the remaining 13% of the spin located on the ZnO surface. The spin on the surface is located primarily on the surface Zn atoms Zn_{d3} and Zn_1, coming from the d-orbitals. These are the two Zn atoms that NO_2 bonds directly to. The spin on the NO_2 molecule arises primarily from the N s-orbitals (which contribute 24% of the total spin) and N d-orbitals (contributing 26 % of the total spin), suggesting d-orbital back-donation from the Zn atoms. For the O atoms in NO_2, the spin is primarily located on the O atom that bonds closest to the surface Zn atom (Zn_{d1}), having 16% of the total spin arising from the s- and p-orbitals each. The other O atom, which bonds to surface Zn_1, only has 2% of the total spin arising from the s-orbitals and 3% from the d-orbitals. The presence of an induced magnetic moment on only one of the calculated structures may be helpful in distinguishing the adsorption arrangement of NO_2 on the surface experimentally.

4.4.4 Vibrational Frequencies

The calculated vibrational frequencies of NO_2 adsorbed on ZnO($2\bar{1}\bar{1}0$)–V_O are presented in Table 4.10. The experimental and theoretically determined frequency values for the free NO_2 molecule are also presented, and are in good agreement with each other. Vibrational shifts are defined as bathochromically (red) shifted, or hypsochromically (blue) shifted.

The shift in symmetric stretch of the different NO_2/ZnO($2\bar{1}\bar{1}0$)–V_O structures was found to be highly sensitive to the adsorption geometry, especially the number of adsorbate atoms interacting with the surface, as well as the type of adsorbate atom forming the interaction. The symmetric stretch of the two-fold O-Zn interaction in structures 2 and 3 resulted in bathochromic (red) shifts of the symmetric stretch of 40 cm^{-1} and 67 cm^{-1}, respectively. Contrasting this, the N-Zn and O-Zn interactions in structures 4 and 5 resulted in hypsochromic (blue) shifts of the symmetric stretch of 143 cm^{-1} and 231 cm^{-1}. The symmetric stretch of structure 1 was calculated to have a smaller hypsochromic shift of 19 cm^{-1}, probably due to the highly coordinated nature of the adsorbed NO_2 molecule.

The asymmetric stretch was found to be bathochromically shifted (with respect to the free NO_2 molecule) for all structures. The highly coordinated three-fold adsorption geometry of structure 1 is believed to be responsible for the extremely large bathochromic shift (990 cm^{-1}). Structures 2-5 were calculated to have smaller bathochromic shifts of 426 cm^{-1} – 550 cm^{-1} due to their two-fold surface coordination.

The bending modes of NO_2/ZnO($2\bar{1}\bar{1}0$)–V_O were found to be hypsochromically shifted by 61 cm^{-1} – 104 cm^{-1} for structures 2-5, whereas, the bending mode of structure 1 was calculated to be bathochromically shifted by 246 cm^{-1}. As has been previously discussed, the deviation of structure 1 from the rest of the dataset can be ascribed to the higher (three-fold) surface coordination geometry.

To the best of our knowledge there are no publications presenting the vibrational frequency values of NO_2/ZnO($2\bar{1}\bar{1}0$)–V_O. It is anticipated that experimentally observed vibrational frequencies via Infrared (IR), Vibrational Electron Energy Loss, (VEELS) or Reflection Adsorption Infrared (RAIRS) spectroscopy will be able to resolve/confirm one or multiple frequencies/structures reported in this

work. The results presented in this paper may prove useful for refining experimentally observed adsorption configurations.

4.4.5 Charge Density and Electron Localisation Functions

ELF plots of the most stable minimum energy structures of $NO_2/ZnO(2\bar{1}\bar{1}0)-V_O$ and clean $ZnO(2\bar{1}\bar{1}0)-V_O$ are presented in Figure 4.12. ELF plots of $ZnO(2\bar{1}\bar{1}0)-V_O$ and $NO_2/ZnO(2\bar{1}\bar{1}0)-V_O$ were taken parallel to the surface, along the *x*-*y* plane at the position of the highest Zn atom surrounding the vacancy. In addition to the uppermost layer of atoms, the ELF plots were also obtained by slicing through the atoms forming the shortest adsorbate-substrate distance of the most stable structure 1 (Figure 4.13). High regions of electron localisation (indicated in red) can be interpreted as bonding and non-bonding electron pairs [31].

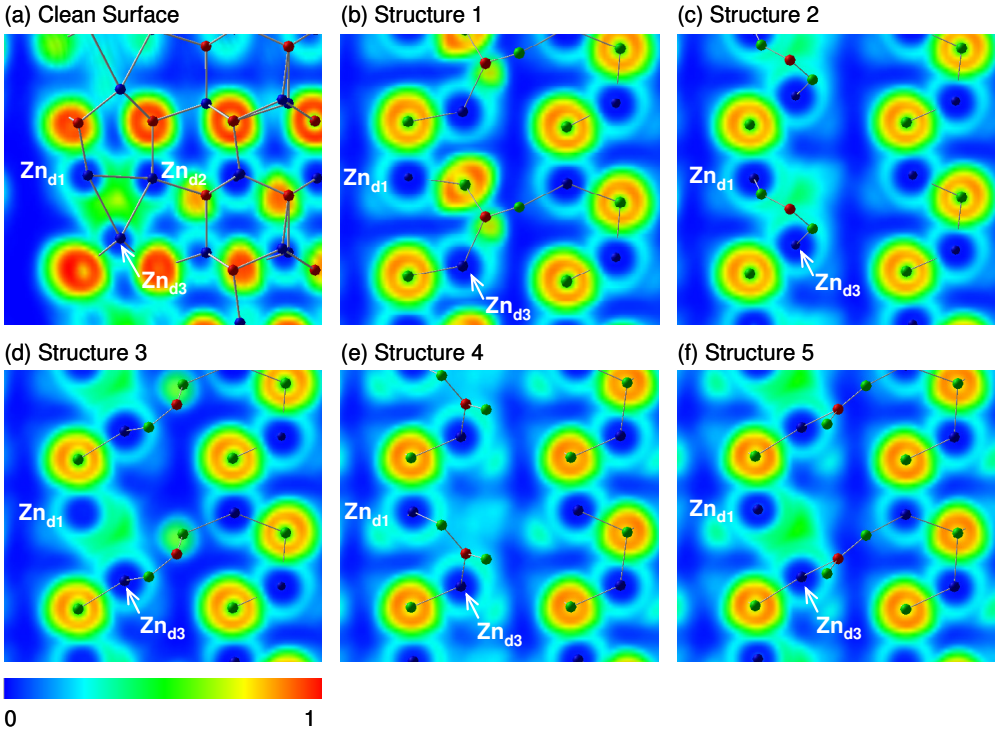

Figure 4.12. ELF contour plots taken along the plane of the uppermost Zn atoms in (a) the clean surface and (b)-(f) $NO_2/ZnO(2\bar{1}\bar{1}0)-V_O$ structures 1-5. (blue spheres represent Zn, green O, and red N).

In the ELF plots of the clean $ZnO(2\bar{1}\bar{1}0)-V_O$ surface (Figure 4.12a) there is a region of delocalised electron density along lengths L_1, L_2 and L_3, indicating that the defect site has metallic character. For

structure 1, after adsorption of NO_2 (Figure 4.12b), the electron localisation along L_1 (between atoms Zn_{d1} and Zn_{d3}) is absent due to the elongation caused by adsorption. Slices taken along the adsorbate O and N atoms (Figure 4.13a) highlight the covalent nature of the bond as seen by the red (high electron localisation) region in between these atoms. Slices taken along the closest adsorbate-substrate atoms (Figure 4.13b and Figure 4.13c) indicate that the bonding of the adsorbate to the surface is ionic in nature and consistent with chemisorption, as suggested by the calculated binding energy.

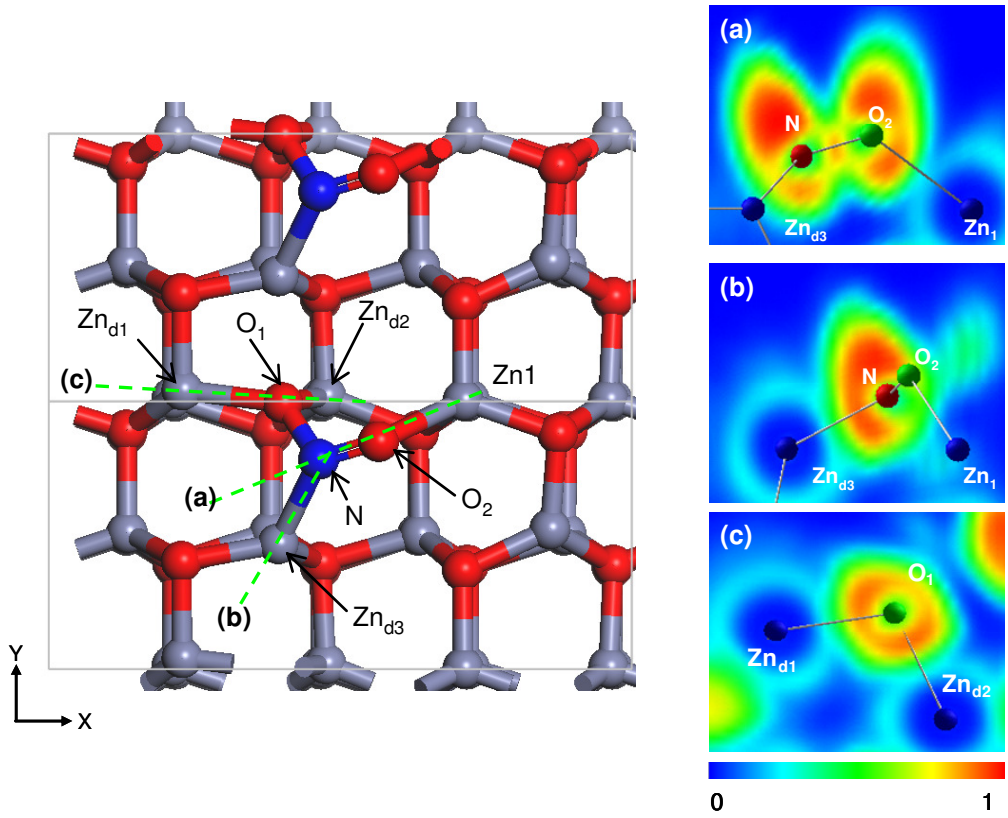

Figure 4.13. (a)-(c) ELF contour plots taken along the three most stable adsorbate-surface bonds of structure 1 (left). The green dashed lines indicate the plane of the three ELF slices. (blue spheres represent Zn, green O, and red N).

The ELF plot of structure 2, particularly along L_1 shows a lack of electron localisation, again caused by the adsorption of NO_2 increasing the separation between the Zn atoms along L_1. As the separation between Zn_{d1} and Zn_{d3} was not as large as for structure 1, there was still some electron localisation along L_1. Similar trends were seen for structures 3 and 5 which were also two-fold

coordinated to the surface. For structure 4 where L_1 >3 Å, the electron localisation between Zn_{d1} and Zn_{d3} is similar in nature to that observed for structure 1.

The Bader charges for each atom in the two uppermost ZnO layers, and the NO_2 molecule, as well as the calculated charge transfer for the whole system are presented in Table 4.12. As mentioned previously, the calculated direction of charge transfer (Δq) between the surface and the adsorbate is a useful parameter for comparison with conductivity changes measured in gas sensing experiments. All structures were calculated to have a negative Δq, indicating transfer of charge from the surface to the adsorbate. The magnitude of Δq was calculated to be approximately six times greater than NO_2 adsorbed on the non-defect ZnO($2\bar{1}\bar{1}0$) surface. The calculations presented in this work are in good agreement with experimental observations of ZnO nanostructure based conductometric gas sensors [33-36] that all show a decrease in conducitivity after exposure to NO_2. Experimentally, Sadek *et al.* [36] hypothesised that during the adsorption process of NO_2 onto ZnO nanostructures, NO_2 consumes conduction electrons and subsequently increases the depletion region at the surface, thus, reducing conductivity. Specifically, structure 1 was calculated to have a Δq of 1.25 e, while structures 2 through to 5 had smaller calculated charge transfer values of 0.59 e - 0.64 e. The larger Δq value calculated for structure 1 may be attributed to the higher binding energy and higher coordination of this structure. structures 2-5 which all adsorbed in two-fold coordinated sites, were calculated to have a similar magnitude of charge transfer, regardless of the adsorbate atom directly involved in bonding and their respective electronegativities. This suggests that redistribution of the electron density occurs within the adsorbed NO_2 molecule, as well as between the adsorbate and the surface.

The calculated Bader charges indicated that the transfer of charge between the adsorbate and the surface was confined to the upper two layers of the ZnO surface, consistent with the small or negligible relaxations of lower surface layers. Zinc atoms within the top layer of the surface model (Zn_1, and Zn_{d1}), were calculated to have the greatest charge transfer, with only minor changes calculated for the second layer Zn atoms. Not surprisingly, the oxygen atoms in the top two surface layers exhibited negligible charge transfer as they were generally not bonded to the adsorbate.

Table 4.12. Calculated change in the Bader charges of the top two surface layer of atoms and the NO_2 molecule of the $NO_2/(2\bar{1}\bar{1}0)$**–**V_O minimum energy structures. The Bader charges for the free NO_2 molecule and the clean surface are also shown. The calculated charge transfer Δq is also presented.

		Change in Bader charge of $NO_2/(2\bar{1}\bar{1}0)$–V_O minimum energy structures					**Bader charges**
Location	Atom	Structure 1	Structure 2	Structure 3	Structure 4	Structure 5	Clean
NO_2	O1	0.48	0.23	0.22	0.24	0.08	–0.37
	O2	0.26	0.28	0.33	0.10	0.28	–0.31
	N	0.51	0.07	0.09	0.28	0.24	0.68
Layer 1	**Zn_{d1}**	–0.44	–0.45	–0.45	–0.44	–0.44	0.75
Layer 1	**Zn_{d2}**	–0.08	–0.01	–0.08	0.00	–0.09	0.93
Layer 1	**Zn_{d3}**	–0.01	0.16	0.35	0.07	0.33	0.69
Layer 1	Zn_1	–0.44	–0.25	–0.26	–0.29	–0.22	1.14
Layer 2	Zn_1	–0.26	–0.24	–0.27	–0.24	–0.25	1.13
Layer 2	Zn_2	–0.01	–0.01	–0.01	–0.01	–0.03	1.18
Layer 2	Zn_3	0.00	–0.01	0.00	0.01	–0.02	1.19
Layer 2	Zn_4	0.01	0.24	0.13	0.21	0.18	1.19
Layer 1	O_1	0.00	0.00	–0.02	–0.01	–0.03	–1.13
Layer 1	O_2	0.01	–0.01	0.01	0.00	0.00	–1.14
Layer 1	O_3	–0.01	–0.01	–0.01	0.00	–0.01	–1.14
Layer 2	O_1	–0.02	0.00	–0.01	0.00	0.01	–1.18
Layer 2	O_2	0.00	–0.02	0.00	0.00	–0.01	–1.19
Layer 2	O_3	0.00	0.01	0.01	0.00	0.01	–1.19
Layer 2	O_4	0.01	0.00	0.01	0.00	0.00	–1.18
Δq		–1.25	–0.59	–0.64	–0.62	–0.61	0.00

Planar averaged charge density difference plots (in the *z*-direction) of all structures are presented in Figure 4.14. For structure 1, there is a small region of charge depletion below the topmost surface layer. Moving away from the surface, there is a large accumulation of electron density followed by a small depletion and then accumulation close to the second oxygen atom position. For structures 2, 4 and 5, where the adsorbate atoms occupied similar locations to those normally occupied by surface Zn and O atoms in the crystal lattice, all have similar planar averaged charge density difference plots.

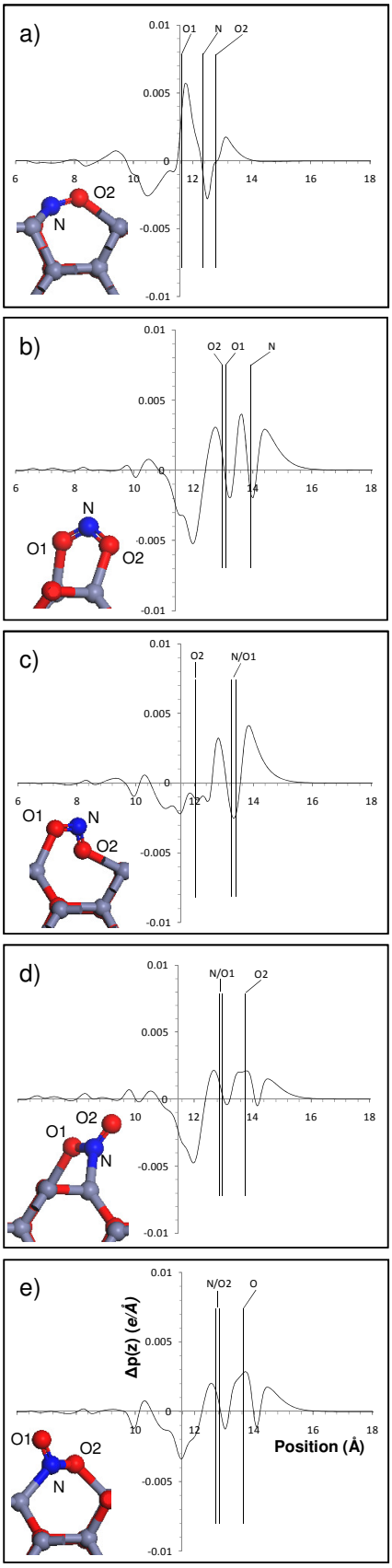

Figure 4.14. (a)-(e) Planar averaged charge density difference plots of $NO_2/ZnO(2\bar{1}\bar{1}0)$–$V_O$ structures 1 - 5.

Specifically, there is a region of electron depletion near the upper surface layer which rapidly diminishes moving away from the surface. After this depletion, there is a small region of accumulation located below the two adsorbate atoms closest to the surface. Following this, there is a minor region of charge depletion. The same pattern of accumulation and depletion can be seen near the third adsorbate atom, which does not bond directly with the surface. For structure 3, the planar averaged charge density difference plot is slightly different to the other structures as one adsorbate atom sits closer to the surface than the other two atoms, unlike structures 2, 4, and 5. The plots for structure 2-5 are different to structure 1, due to its three-fold adsorption geometry. It is clear, however, that the position of the adsorbate atoms relative to the surface is far more influential in the redistribution of charge than the electronegativity of the adsorbate atom involved.

4.4.6 Density of States

While it is well known that the PW91 GGA exchange-correlation functional underestimates the band gap of metal oxides, it does provide useful data about the electronic properties and changes to the electronic configuration of the surface after adsorption. Total density of states (DOS) and orbital resolved partial DOS (PDOS) of the most stable structure of $NO_2/ZnO(2\bar{1}\bar{1}0)-V_O$ are presented in Figure 4.15a and Figure 4.15b. The Fermi level is aligned at zero. The total DOS (Figure 4.15a) for the adsorbed structure show little changes to that of the clean surface, with some new states at –8.6 eV and –8.1 eV, arising from the adsorbate s-orbitals. Deep within the valence band (–5 eV to –8 eV) the majority of states can be attributed to surface d-orbitals. States from 0 eV to –5 eV are mainly due to p-orbital contributions, with minor contributions from d and s-orbitals (inset Figure 4.15b). In the conduction band, the largest contributors to the calculated states in decreasing order were; s-orbitals, followed by p-orbitals, and only minor contributions from d-orbitals. The most significant difference between the adsorbed and clean surface was the presence of an additional state within the band gap of the clean surface. This peak is primarily ascribed to the NO_2 molecule (see Figure 4.15b), with contributions from the N 2p and O 2p orbitals, with very minor contributions from the surface s, p and d-orbitals.

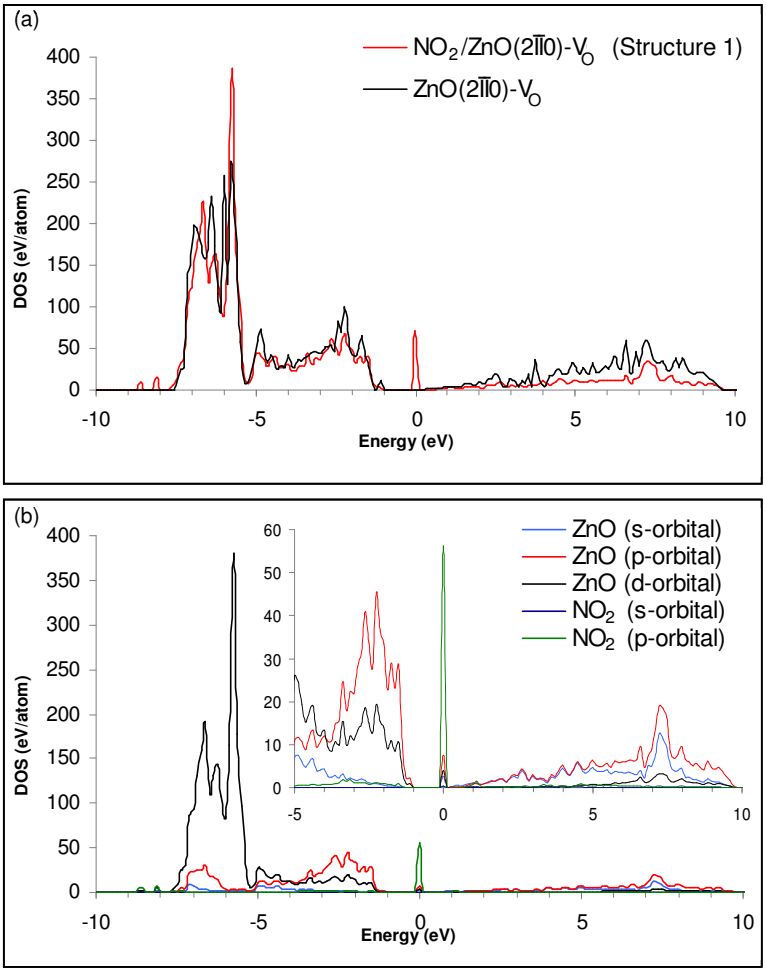

Figure 4.15. (a) Total DOS of ZnO(2$\bar{1}\bar{1}$0)–V_O and NO_2/ZnO(2$\bar{1}\bar{1}$0)–V_O (structure 1); (b) orbital resolved PDOS of the most stable NO_2/ZnO(2$\bar{1}\bar{1}$0)–V_O system (structure 1), inset is a magnified PDOS plot of the same structure.

4.4.7 Summary and Implications for Gas Sensing

Multiple adsorption configurations of adsorbed NO_2 were identified on ZnO(2$\bar{1}\bar{1}$0)–V_O. NO_2 binds more strongly to the oxygen vacancy site (V_O) with binding energies of the order of ~1eV, indicating chemisorption on the surface. These values are almost three times greater than for adsorption of NO_2 on the clean stoichiometric ZnO(2$\bar{1}\bar{1}$0) surface. Large surface reconstructions around the oxygen vacancy site were observed after NO_2 adsorption, while surface relaxations were minor. Adsorption in the most stable site gave rise to an impurity state within the band gap of the clean defect surface, and was found to induce a magnetic moment on the most stable structure only. Together with the significantly different vibrational frequency values compared to the other structures, these properties may allow distinction of surface structures/geometry in experiment. The charge transfer of all the

minimum energy structures was calculated to occur in the direction from the surface to the adsorbate, indicating that NO_2 behaves as a charge acceptor, which correlates with the experimentally observed increase in resistance of ZnO after exposure to NO_2 gas. The magnitude of the transfer of charge was calculated to be approximately six times that for NO_2 adsorbed on the non-defect surface. While it is unlikely that the charge transfer is the sole cause of experimentally observed resistance increases, it does indicate that electron density, depleted from the ZnO nanostructures, may be used in the creation of chemical bonds between the adsorbate and surface, contributing to the experimentally measured increase in resistance. Given the larger magnitude of charge transfer for the defect surface compared with the stoichiometric surface, it can be expected that gas detectors and sensors utilising defect rich nanostructures may yield significantly higher NO_2 sensitivities than those based on stoichiometric ZnO($2\bar{1}\bar{1}0$) nanostructures.

4.5 Chapter Summary

There was no reaction barrier for the adsorption of N, O, NO and NO_2 onto either ZnO($2\bar{1}\bar{1}0$); or NO_2 onto ZnO($2\bar{1}\bar{1}0$)–V_O, with all molecules and molecular dissociation products spontaneously adsorbing at 0 K. While it is unlikely that the charge transfer is the sole cause of experimentally observed resistance increases, it does indicate that electron density, depleted from the ZnO nanostructures, may be used in the creation of chemical bonds between the adsorbate and surface, contributing to the experimentally measured increase in resistance.

The main conclusions from these systems are as follows:

Adsorption of O and N onto ZnO($2\bar{1}\bar{1}0$)

- The adsorption of O and N onto ZnO($2\bar{1}\bar{1}0$) was for the most part strong, with binding energies indicative of chemisorption.
- Six minimum energy structures were found with adsorbate interactions limited to the first two layers of the surface model.
- Adsorbate atoms bonded to two or more surface oxygen and or zinc atoms.

- Ionic and covalent type bonds were calculated between the adsorbate and the surface. Bonding between surface oxygen atoms and either adsorbate O or N atoms resulted in the formation of a covalent type bond, whereas interactions with surface zinc atoms were ionic in nature.

- Surface relaxation after adsorption was found to be the largest in the top two surface layers. Surface reconstructions were also observed, being prominent for the most stable minima of both adsorbates, but minor in the less stable structures.

- The positive work-function changes of adsorbed oxygen may be correlated with the experimentally observed decreases in conductivity of ZnO conductometric sensor technologies.

- The use of ZnO($2\bar{1}\bar{1}0$) based sensing elements may prove useful for dosimeter based sensing applications in low earth orbit where the presence of naturally occurring atomic O and N fluxes can cause damage to space borne satellites.

Adsorption of NO and NO_2 onto ZnO($2\bar{1}\bar{1}0$)

- The adsorption of NO and NO_2 onto ZnO($2\bar{1}\bar{1}0$) was weak, with binding energies indicative of physisorption.

- Thirty minimum energy structures were found in total for adsorbed NO and NO_2 onto the ZnO($2\bar{1}\bar{1}0$) surface, with eleven unique NO adsorption configurations and nineteen unique NO_2 configurations.

- Adsorbate molecules preferentially interacted with one or more surface zinc atoms.

- Despite showing weak binding energies, the charge density plots and Bader charge calculations indicate that there is a transfer of charge from the surface to the adsorbate molecule in good agreement with experimental observations.

- The surface was largely unchanged after adsorption, with little or no surface reconstruction or relaxation.

- The large number of minimum energy structures, barrier-less physisorption process, and comparatively negligible surface reconstruction and relaxation, suggests that at appropriate operating conditions, perfect ZnO($2\bar{1}\bar{1}0$) crystal surfaces may be suitable for NO and NO_2 sensing applications where long term stability is desired.

Adsorption of NO_2 onto ZnO($2\bar{1}\bar{1}0$)$-V_O$

- The adsorption of NO_2 onto ZnO($2\bar{1}\bar{1}0$)$-V_O$ was for the most part strong, with binding energies indicative of chemisorption.

- Five minimum energy structures were found for the adsorption of NO_2 on the ZnO($2\bar{1}\bar{1}0$)$-V_O$ surface.

- NO_2 preferentially interacted with defect site zinc atoms via O-Zn or N-Zn bonds.

- Large surface reconstructions around the oxygen vacancy site were observed after NO_2 adsorption, while surface relaxations were minor.

- The adsorption of NO_2 onto ZnO($2\bar{1}\bar{1}0$)$-V_O$ attempts to repair the oxygen vacancy by adsorption of NO_2 in a bridging configuration over the oxygen vacancy site. However, this does not cleanly restore the stoichiometry of the surface to ZnO($2\bar{1}\bar{1}0$).

- Given the larger magnitude of charge transfer (more than six times greater) for the defect surface compared with the stoichiometric surface, it can be expected that gas detectors and sensors utilising defect rich nanostructures may yield significantly higher NO_2 sensitivities than those based on stoichiometric ZnO($2\bar{1}\bar{1}0$) nanostructures.

4.6 References

[1] M. Casarin, *et al.*, "An LCAO-LDF study of the chemisorption of H_2O and H_2S on ZnO(0001) and ZnO(10$\bar{1}$0)," *Surface Science,* vol. 377-379, pp. 587-591, 1997.

[2] W.D. Tang, *et al.*, "Adsorption of urea onto a ZnO(10$\bar{1}$0) surface," *Wuli Huaxue Xuebao / Acta Physico - Chimica Sinica*, vol. 26, pp. 1373-1377, 2010.

[3] M. Casarin, *et al.*, "A comparative study of the NH_3 chemisorption on ZnO(10$\bar{1}$0) and Cu_2O(111) non-polar surfaces," *Chemical Physics Letters,* vol. 300, pp. 403-408, 1999.

[4] K. Fink, "*Ab-initio* cluster calculations on the electronic structure of oxygen vacancies at the polar ZnO(0001) surface and on the adsorption of H_2, CO, and CO_2 at these sites," *Physical Chemistry Chemical Physics,* vol. 8, pp. 1482-1489, 2006.

[5] M. Kunat, *et al.*, "Structure and dynamics of CO overlayers on a hydroxylated metal oxide: The polar ZnO(0001) surface," *Physical Chemistry Chemical Physics,* vol. 8, pp. 1499-1504, 2006.

[6] J. B. L. Martins, *et al.*, "A theoretical study of (10$\bar{1}$0) and (0001) ZnO surfaces: molecular cluster model, basis set and effective core potential dependence," *Journal of Molecular Structure: THEOCHEM,* vol. 330, pp. 301-306, 1995.

[7] J. B. L. Martins, *et al.*, "A theoretical study of water adsorption on (10$\bar{1}$0) and (0001) ZnO surfaces: molecular cluster, basis set and effective core potential dependence," *Journal of Molecular Structure: THEOCHEM,* vol. 330, pp. 347-351, 1995.

[8] J. B. L. Martins, *et al.*, "*Ab-initio* study of CO and H_2 interaction on ZnO surfaces using a small cluster model," *Journal of Molecular Structure: THEOCHEM World Congress of Theoretically Oriented Chemists,* vol. 398-399, pp. 457-466, 1997.

[9] J. A. Rodriguez, *et al.*, "Chemistry of SO_2 and NO_2 on ZnO(0001)-Zn and ZnO powders: changes in reactivity with surface structure and composition," *Journal of Molecular Catalysis A: Chemical,* vol. 167, pp. 47-57, 2001.

[10] J. A. Rodriguez, *et al.*, "Reaction of NO_2 with Zn and ZnO: Photoemission, XANES, and Density Functional Studies on the Formation of NO_3," *J. Phys. Chem. B,* vol. 104, pp. 319-328, 2000.

[11] M. J. S. Spencer and I. Yarovsky, "ZnO Nanostructures for Gas Sensing: Interaction of NO_2, NO, O, and N with the ZnO(10$\bar{1}$0) Surface," *The Journal of Physical Chemistry C,* 2010.

[12] Y. Yan, *et al.*, "Oxygen-vacancy mediated adsorption and reactions of molecular oxygen on the ZnO(10$\bar{1}$0) surface," *Physical Review B (Condensed Matter and Materials Physics),* vol. 72, pp. 161307-4, 2005.

[13] P. Zapol, *et al.*, "*Ab-initio* study of hydrogen adsorption on the ZnO(10$\bar{1}$0) surface," *Surface Science,* vol. 422, pp. 1-7, 1999.

[14] M. Casarin, *et al.*, "A theoretical investigation of the relaxation effects induced on the ZnO(10$\bar{1}$0) surface by the chemisorption of H2 and CO," *Applied Surface Science,* vol. 142, pp. 192-195, 1999.

[15] D. J. Cooke, *et al.*, "Surface Structure of (10$\bar{1}$0) and (11$\bar{2}$0) Surfaces of ZnO with Density Functional Theory and Atomistic Simulation," *J. Phys. Chem. B,* vol. 110, pp. 7985-7991, 2006.

[16] F. Wang, *et al.*, "Theoretical study of the magnetic interaction of Cr-doped ZnO with and without vacancies," *Journal of Magnetism and Magnetic Materials*, vol. 321, pp. 3067-3070, 2009.

[17] B. Meyer, "First-principles study of the polar O-terminated ZnO surface in thermodynamic equilibrium with oxygen and hydrogen," *Physical Review B,* vol. 69, Jan 2004.

[18] A. Wander and N. M. Harrison, "An *ab-initio* study of ZnO(10$\bar{1}$0)," *Surface Science,* vol. 457, pp. 342-346, 2000.

[19] A. Wander and N. M. Harrison, "An *ab-initio* study of ZnO(11$\bar{2}$0)," *Surface Science,* vol. 468, pp. 851-855, 2000.

[20] P. Zapol, *et al.*, "*Ab-initio* study of hydrogen adsorption on the ZnO surface," *Surface Science,* vol. 422, pp. 1-7, 1999.

[21] Z. L. Wang, "Nanobelts, nanowires, and nanodiskettes of semiconducting oxides - From materials to nanodevices," *Advanced Materials,* vol. 15, pp. 432-436, 2003.

[22] M. Nyberg*, et al.*, "Hydrogen Dissociation on Reconstructed ZnO Surfaces," *J. Phys. Chem.,* vol. 100, pp. 9054-9063, 1996.

[23] D. J. Cooke*, et al.*, "Surface Structure of $(10\bar{1}0)$ and $(11\bar{2}0)$ Surfaces of ZnO with Density Functional Theory and Atomistic Simulation," *J. Phys. Chem. B,* vol. 110, pp. 7985-7991, April 20, 2006 2006.

[24] J. D. Prades*, et al.*, "*Ab-initio* calculations of NO_2 and SO_2 chemisorption onto non-polar ZnO surfaces," *Sensors and Actuators B: Chemical,* vol. 142, pp. 179-184, 2009.

[25] C. C. Wang*, et al.*, "Hydrogen-induced metallization of zinc oxide $(2\bar{1}\bar{1}0)$ surface and nanowires: The effect of curvature - art. no. 245303," *Physical Review B,* vol. 77, pp. 5303-5303, 2008.

[26] M. J. S. Spencer*, et al.*, "Density functional theory modelling of ZnO $(10\bar{1}0)$ and ZnO ZnO$(2\bar{1}\bar{1}0)$ surfaces: Structure, properties and adsorption of N_2O," *Materials Chemistry and Physics,* vol. 119, pp. 505-514, 2010.

[27] M. Breedon*, et al.*, "Adsorption of NO and NO_2 on the ZnO$(2\bar{1}\bar{1}0)$ surface: A DFT study," *Surface Science,* vol. 603, pp. 3389-3399, 2009.

[28] M. Breedon*, et al.*, "Adsorption of atomic nitrogen and oxygen on ZnO$(2\bar{1}\bar{1}0)$ surface: A density functional theory study," *Journal of Physics Condensed Matter,* vol. 21, 2009.

[29] M. J. S. Spencer*, et al.*, "Density Functional Theory Study of ZnO Nanostructures for NO and NO_2 Sensing," *Solid-State Sensors, Actuators and Microsystems Conference, 2007. TRANSDUCERS 2007. International,* vol. 1, pp. 987-990, 2007.

[30] J. J. Osborne*, et al.*, "Thin-film semiconductor sensors for hyperthermal oxygen atoms," *Sensors and Actuators B: Chemical,* vol. 63, pp. 55-62, 2000.

[31] T. B. Terriberry*, et al.*, "A tool for the interactive 3D visualization of electronic structure in molecules and solids," *Computers & Chemistry,* vol. 26, pp. 313-319, 2002.

[32] D. R. Lide. *Physical Constants of Organic Compounds (CRC Handbook of Chemistry and Physics),* CRC Press, 2007.

[33] E. Oh*, et al.*, "High-performance NO_2 gas sensor based on ZnO nanorod grown by ultrasonic irradiation," *Sensors and Actuators B: Chemical,* vol. 141, pp. 239-243, 2009.

[34] F.-T. Liu*, et al.*, "ZnO nanorod gas sensor for NO_2 detection," *Journal of the Taiwan Institute of Chemical Engineers,* vol. 40, pp. 528-532, 2009.

[35] J. H. Jun*, et al.*, "Necked ZnO nanoparticle-based NO_2 sensors with high and fast response," *Sensors and Actuators B: Chemical,* vol. 140, pp. 412-417, 2009.

[36] A. Z. Sadek*, et al.*, "Characterization of ZnO Nanobelt-Based Gas Sensor for H_2, NO_2, and Hydrocarbon Sensing," *Sensors Journal, IEEE,* vol. 7, pp. 919-924, 2007.

Chapter 5 - Metal Oxide Nanostructure Synthesis

In this chapter different growth methods of ZnO and WO_3 nanostructures used by the author during the course of his PhD will be explained in detail. The formation of nanostructured metal oxides for gas sensing applications dictated the following material requirements:

- High surface area to volume ratio, highly crystalline, contiguous nanostructured thin films which are sensitive to ppm or lower concentrations of NO_2 and H_2.
- Low cost repeatable nanomaterial synthesis, with processes that are compatible with existing semiconductor device manufacturing processes and infrastructures
- Elegant, repeatable nanomaterial synthesis methods that, where appropriate, should utilise environmentally friendly reagents and fabrication processes

ZnO nanostructure synthesis has enjoyed continuing popularity in the sensing community with an ever increasing list of applications. Within this research field, aqueous chemical methods have arguably attracted the most attention due to the relative ease with which high quality nanomaterials are capable of being produced. While the formulation and application of aqueous chemical deposition methods is a major focus in this chapter, at times conventional thin film deposition techniques have been employed as a processing step for the fabrication of ZnO nanorods and interconnected nanowires. Conventional deposition techniques were also used in the fabrication of Pt/WO_3 gasochromic sensing applications, as discussed in Chapter 7. For gas sensing applications the formation of an underlying contiguous nucleation layer was necessitated by the need for crystallite nucleation, and a stable and continuous electrical contact. Hydrothermally grown ZnO nanorods often emerge perpendicularly to the substrate [1], however, without an underlying seed/nucleation layer there is no guarantee that the synthesised nanomaterials will bridge electrode pairs and provide a stable means for electrical characterisation. In this thesis seed/nucleation layers were deposited via radiofrequency (RF) sputtering and spray pyrolysis methods, their application is discussed in § 5.1.3 and § 5.1.5.

While there are many synthetic methods for the synthesis of WO_3 nanostructures, there are few methods which are capable of directly depositing a contiguous nanostructured thin film. As will be discussed in § 5.2 and § 5.2.4, most methods utilise reactive reagents which may be corrosive, unstable, irritating, and or toxic. This prompted the author to develop a successive ionic layer adsorption reaction, as well as an aqueous sol-gel method, capable of forming high density nanostructured thin films, several micrometers thick. The formation of gas sensitive WO_3 nanomaterials did not require the use of an underlying nucleation layer for crystallite nucleation or electrical continuity. In these films, individual platelets made contact with at least one neighbouring nanocrystallite.

5.1 ZnO Nanostructured Thin Film Synthesis

ZnO nanomaterial synthesis represents one of the most furtive and popular research topics of the past decade. ZnO thin films, nanostructured or otherwise, can be deposited via a number of different techniques and processes including but not limited to: molecular beam epitaxy [2], thermal evaporation (vapor-liquid-solid) [3], chemical vapor deposition [4], hydrothermal decomposition of chemical solutions [5], successive ion layer adsorption reaction (SILAR) deposition [6], RF sputtering [7], and others. In this thesis, predominantly aqueous chemical methods were used to deposit a variety of nanostructures with different morphologies onto conductometric transducers and substrates. The study of ZnO nanostructured thin films with different morphologies resulted in the publication of four co-authored papers [1, 8-10].

The methods developed by the author were in part, modified from established synthetic routes for ZnO deposition [5, 11], with aspirations of improving uniformity of the nanostructured arrays, and to ensure electrical continuity across the interdigitated electrodes via underlying seed/nucleation layer crystallite grain-grain interfaces. These methods have the potential to eventually replace gas based deposition systems, and have excellent compatibility with temperature sensitive substrates (excluding spray pyrolysis), as most aqueous ZnO deposition methods described in the thesis occur at less than 100 °C.

The first modification was the use of a ZnO seed/nucleation layer, either deposited via RF sputtering (§ 5.1.1) or spray pyrolysis (§ 5.1.4), which provides an abundance of nucleation sites and acts as a source of zinc ions. These ions may be later used to fortify the ZnO nanostructures, via an extension of the Ostwald ripening process [12]. The second modification is the development of a sample holder as seen in Figure 5.1. Each sample holder consists of a stainless steel support rod (later changed to glass, as the vanadium and chromium leached from the stainless steel), and a Teflon disc with a machined recess. This recess exposed the sample to the growth solution as depicted in Figure 5.2.

Sealed reaction vessels (autoclavable chemical storage bottles), provided an inexpensive and effective means of preventing the evaporation of solution, which would greatly affect solution concentration. This consideration also served to eliminate experimental variables such as changes to: pH, solution volume, growth solution concentration, which could affect experimental repeatability. To further enhance repeatability, all reaction vessels and apparatus components were cleaned between experiments with weak nitric acid to remove any residual zinc oxide precipitates.

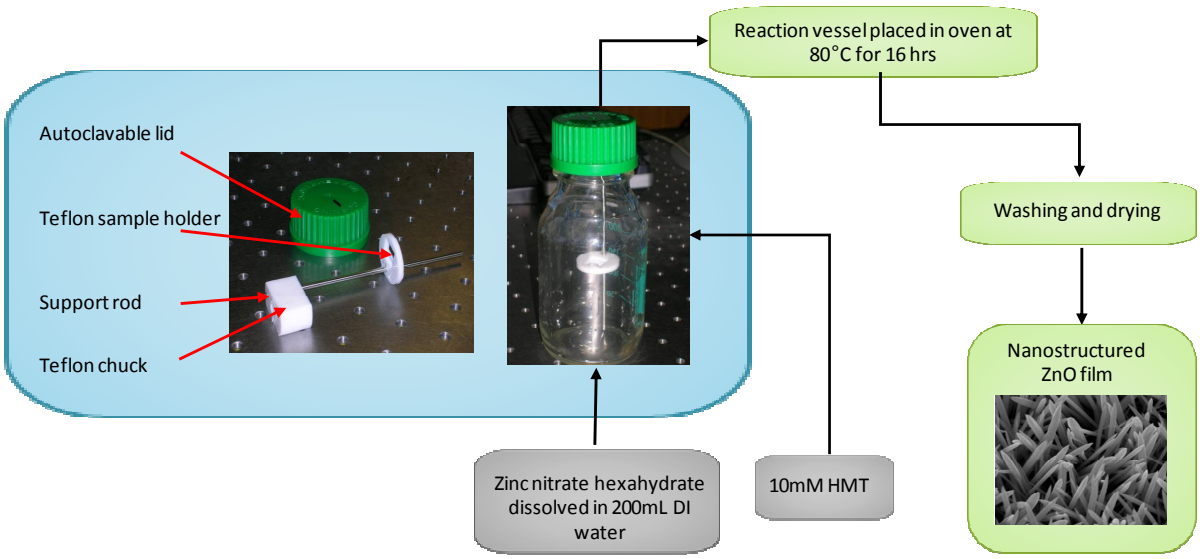

Figure 5.1. Hydrothermal growth apparatus including sample holder.

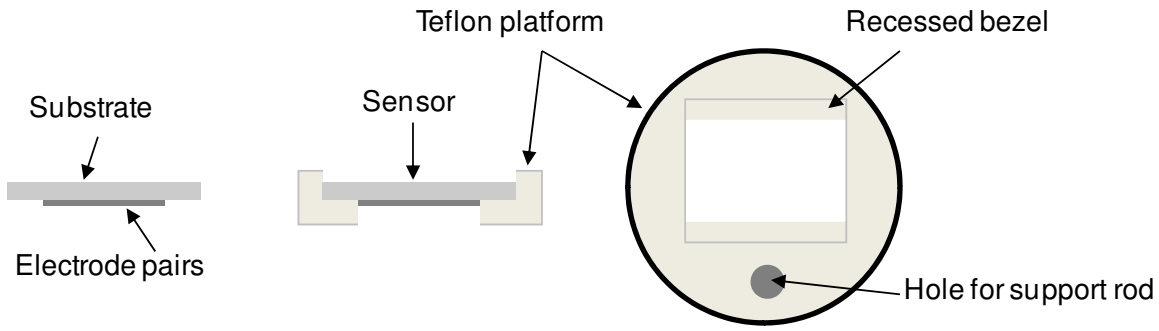

Figure 5.2. Schematic of the sample retention system.

All of the methods investigated rely on the controlled precipitation (deposition) of zinc oxide from solution. This is achieved by the addition of hydroxyl (OH^-) ions to a solution of Zn^{2+} ions, forming a zinc hydroxide complex which in the presence of heat forces the precipitation of ZnO as per (5.1):

$$[Zn(OH)_4]^{2-} \underset{}{\overset{\text{Heat}}{\rightleftharpoons}} [Zn(OH)_2]^0 + 2OH^- \underset{}{\overset{\text{Heat}}{\rightleftharpoons}} ZnO + 2H_2O \quad \text{(precipitation of ZnO)} \qquad (5.1)$$

The first method employed a solution of sodium hydroxide and zinc nitrate, which upon heating deposited ZnO. While this method was effective for the deposition of corrugated ZnO nanorods, the high initial pH of the solution often etched the ZnO seed/nucleation layer rapidly at low temperatures as per (5.2):

$$ZnO \underset{}{\overset{H_2O/OH^-}{\rightleftharpoons}} [Zn(OH)_2]^0 \underset{}{\overset{H_2O/OH^-}{\rightleftharpoons}} [Zn(OH)_4]^{2-} \quad \text{(dissolution of ZnO)} \qquad (5.2)$$

The second method employed in this study was the hydrothermal decomposition of hexamethylenetetramine (HMT) in the presence of zinc nitrate. Unlike the sodium hydroxide method, the hydrothermal method is believed to be rate limited by the thermal decomposition of HMT to ammonia (5.3), which in solution will form ammonium hydroxide (5.4).

$$C_6H_{12}N_4 + 6H_2O \xrightarrow{\text{heat}} 6HCHO + 4NH_3 \quad \text{(hydrothermal decomposition)} \qquad (5.3)$$

$$4NH_3 + 4H_2O \longrightarrow 4NH_4^+ + 4OH^- \quad \text{(generation of hydroxyl ions)} \qquad (5.4)$$

This decomposition process gradually raises the pH of the solution, forcing the precipitation of ZnO as per (5.5), (5.6) and (5.7). Deposition of ZnO proceeds through the formation of zinc hydroxide from Zn^{2+} ions and OH^- ions in solution (5.5) which in the presence of heat undergoes the following dehydration reaction (5.6) to precipitate ZnO.

$$2OH^- + Zn^{2+} \longrightarrow Zn(OH)_2 \quad \text{(formation of zinc hydroxide)} \qquad (5.5)$$

$$Zn(OH)_2 \xrightarrow{\text{heat}} ZnO + H_2O \quad \text{(dehydration)} \qquad (5.6)$$

$$Zn(NO_3)_2 + C_6H_{12}N_4 + 9H_2O \xrightarrow{\text{heat}} ZnO + 6HCHO + 2NO_3^- + 2OH^- + 4NH_4^+ \quad \text{(total equation)} \qquad (5.7)$$

As the reaction vessels were placed cold into laboratory oven, the hydrothermal growth method proved to be more repeatable than the high pH sodium hydroxide method, and is the primary means of depositing ZnO nanostructures throughout this thesis.

Considering the suitability of ZnO nanostructures for gas sensing as discussed in Chapter 4, the author endeavoured to fabricate fine ZnO nanowire arrays. It was believed that this nanowire array may offer an intrinsically higher surface area than its nanorod counterpart. It was found that by modifying the seed/nucleation layer used during hydrothermal growth from well ordered hemispherical nucleation sites to a rougher polygonal nucleation sites, such an array was achieved.

In the following sections the five different deposition techniques and synthetic approaches used by the author will be introduced. The characterisation of the synthesised nanostructures will be presented in detail in Chapter 6.

5.1.1 Nanotextured ZnO RF Sputtered Thin Films

Nanotextured ZnO thin films were deposited onto a variety of different substrates via RF sputtering and used as seed/nucleation layers during hydrothermal growth. The experimental parameters used for the deposition of ZnO nanotextured thin films are presented in Table 5.1. As RF sputtering is a conventional deposition technique, a detailed description of the sputtering process will not be covered in this thesis.

Table 5.1. ZnO sputtering parameters.

Target composition	ZnO 99.99%
Target to substrate distance	7.5 cm
Sputtering power	100W
Process gas	60% N_2 / 40% O_2
Working pressure	1 x 10^{-2} Torr
Deposition time	60 mins
Substrate temperature	260 °C
Film thickness	1.2 µm

5.1.2 Sodium Hydroxide Driven ZnO Deposition Method

Inspired by the work of Peterson *et al.* [11] the author adopted a 1:40 ratio mix of zinc salt to sodium hydroxide to form ZnO nanostructures. By using a 3 – 5 µm sputtered ZnO seed/nucleation layer, it was possible to form corrugated ZnO nanorod arrays using this method. In this process, substrates were held submerged in the growth medium containing an aqueous solution comprising a 1:40 mol ratio mix of zinc nitrate hexahydrate to sodium hydroxide solution, into which a custom-made sample holder was placed into the reaction vessel (Figure 5.1). A fixed reaction volume of 200 mL was chosen with a solution composition of 0.002 moles of zinc nitrate hexahydrate ($Zn(NO_3)_2 \cdot 6H_2O$) and 0.08 moles of sodium hydroxide (NaOH). Zinc nitrate hexahydrate acts as a source of Zn^{2+} ions as described in (5.8), and NaOH dissociates in water as per (5.9). This resulted in the formation of corrugated ZnO nanorod arrays, in a process which is schematically proposed in Figure 5.3.

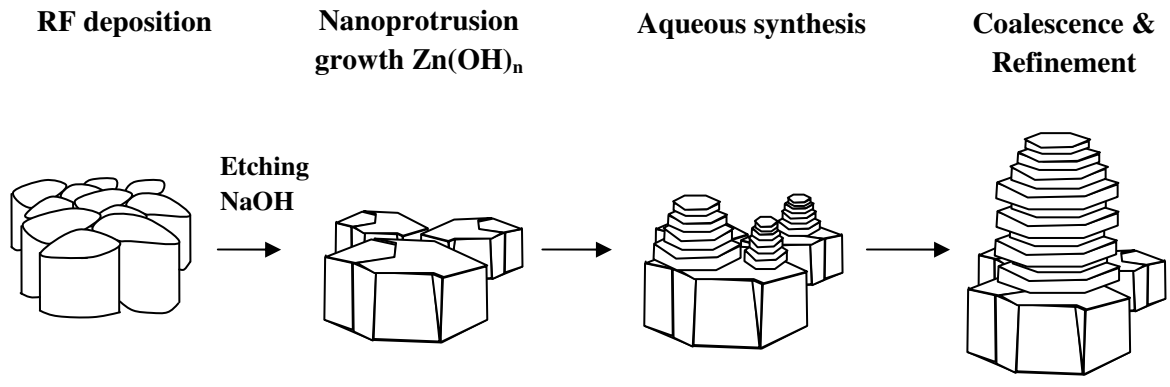

Figure 5.3. Proposed growth mechanism of corrugated ZnO nanorods grown from sodium hydroxide driven solutions.

$$Zn(NO_3)_2{\cdot}6H_2O \xrightarrow{H_2O} Zn^{2+} + 2NO_3^- + 6H_2O \quad \text{(dissolution of zinc salt)} \tag{5.8}$$

$$NaOH \xrightarrow{H_2O} Na^+ + OH^- \quad \text{(dissolution of sodium hydroxide)} \tag{5.9}$$

At room temperature the rate of dissolution of ZnO as described in (5.2), is greater than the rate of ZnO deposition. At high temperatures the rate of dissolution of ZnO is less than the rate of ZnO deposition (5.1), which facilitates the deposition of ZnO nanostructures.

As previously discussed the sodium hydroxide driven growth method was modified to suit gas sensing applications as listed below:

1. ZnO sputtered samples were placed into the growth solution. Considering that ZnO is an amphoteric material, and that the addition of NaOH to water at room temperature drives up the pH of the growth solution, a significant volume of the sputtered seed/nucleation layer will be etched away. Hence, samples were placed into the reaction vessel and then immediately placed into the laboratory oven to prevent the complete dissolution of the sputtered seed/nucleation layer. ZnO seed/nucleation layers were typically 3 - 5 µm thick. Thinner layers were easily etched away by the high pH (typically >10) growth solution.

2. After the samples were removed from the reaction vessel, they were immediately immersed in cold water to prevent etching of the ZnO nanorods, via the cold (high pH) growth solution.

3. A fixed growth time (typically 16 hrs) was used to promote Ostwald ripening of the nanorods.

4. Samples were held inverted (with the interdigitated electrode pairs facing downwards) to prevent any unwanted precipitates from covering the sensor/substrate surface.

While this method was effective at producing an unusual nanostructured morphology, its use for the formation of nanostructures was discontinued due to the long time (>3hrs) required for the deposition of thick RF sputtered ZnO seed/nucleation layers.

5.1.3 Hydrothermal ZnO Growth Method

In light of the high pH growth solution used in the sodium hydroxide driven growth method, which at times completely etched the sputtered ZnO seed/nucleation layer, the author sought a method with a near neutral initial pH. The most suitable of the available methods was the hydrothermal growth of ZnO, popularised by Lionel Vayssieres [5]. This allows a thinner 1.2 µm seed/nucleation layer to be used. In this process, cleaned sputtered samples were placed into a sample holder inside a reaction vessel filled with 200 mL of a 10 mM equimolar solution of hexamethylenetetramine (HMT) $C_6H_{12}N_4$ and zinc nitrate hexahydrate $Zn(NO_3)_2{\cdot}6H_2O$. Vessels sitting at room temperature were sealed, and then placed inside a standard laboratory grade oven for 16 hrs at 80 °C. Subsequently, samples were extracted and washed with DI water to remove any residual zinc salts and dried in a stream of N_2.

The hydrothermal growth method was modified to suit gas sensing applications as listed below:

1. ZnO sputtered samples (1.2 µm) were placed into an equimolar growth solution, the etching rate was less than the sodium hydroxide driven method due to the near neutral solution pH. In this process, samples were placed into the reaction vessel and then immediately placed into a preheated laboratory oven.

2. After the reaction (typically 16 hrs), samples were removed and immediately immersed in cold water to prevent etching of the ZnO nanorods that would otherwise occur, albeit very slowly, in a cold ~pH 8 growth solution.

3. Fixed growth time of ~16 hrs as compared with the ambiguous growth time specified by Lionel Vayssieres of ‘several hours’ [5] was used to promote Ostwald ripening of the nanorods, so that only highly crystalline material remained on the transducer/substrate surface.

4. Samples were held inverted to prevent any unwanted precipitates from covering the sensor/substrate surface.

The hydrothermal deposition of ZnO occurs via (5.7) and is outlined in Figure 5.4.

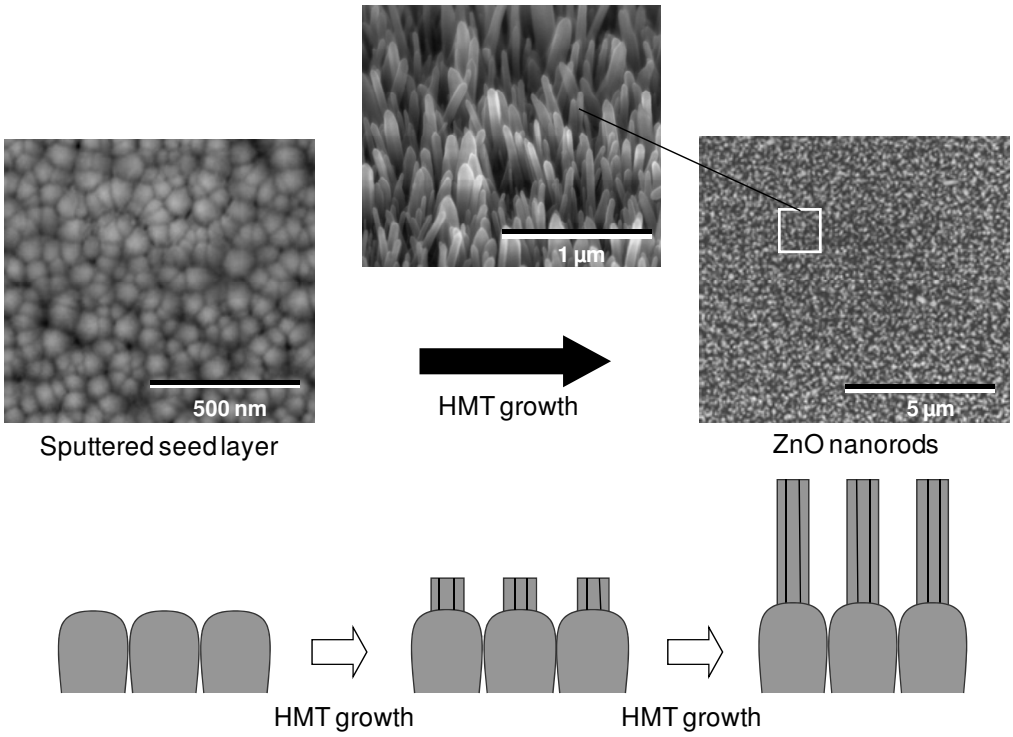

Figure 5.4. Typical ZnO nanorod growth from RF sputtered seed/nucleation layers (seed/nucleation layer is partially etched, not shown here).

HMT undergoes hydrothermal decomposition at the temperature utilised for this reaction [13] as previously described by (5.3), resulting in the formation of ammonium hydroxide from the liberated ammonia (5.4). This step is critical, as not all of HMT is utilised as a hydroxide source immediately. Instead, the hydrothermal decomposition is gradual, which governs the rate at which ZnO precipitation can occur.

The dissolution the of zinc salt, zinc nitrate hexahydrate as outlined in (5.8), releases the majority of the Zn^{2+} ions which are consumed by (5.5). The dissolution of the sputtered ZnO nucleation layer can also occur as per (5.10), the liberated Zn^{2+}can be re-precipitated as ZnO nanorods.

$$ZnO + OH^{-} \longrightarrow Zn^{2+} + H_2O \quad \text{(dissolution)} \tag{5.10}$$

A detailed analysis of the dissolution of sputtered seed/nucleation lays will be presented in Chapter 6 when the electron microscopy studies of ZnO grown on epitaxial GaN layers are presented.

5.1.4 Nanotextured ZnO Thin Films Deposited Via Spray Pyrolysis

As part of two collaborative publications [1, 14] spray pyrolysis deposited ZnO nanotextured thin films were utilised as seed/nucleation layers. The author was not directly involved in the fabrication of spray pyrolysis deposited thin films, only in their application for forming interconnected ZnO nanowires. Despite this fact, it is, however, pertinent to describe their fabrication.

ZnO nanotextured thin films were deposited on glass substrates at a fixed substrate temperature of 450 °C using a typical spray pyrolysis deposition system [15]. The precursor solution (100 mL) was prepared by dissolving 0.15 M of zinc acetate dihydrate [$Zn(CH_3COO)_2 \cdot 2H_2O$] in a solvent mixture of double de-ionised water and isopropyl alcohol with a volume ratio of 1:3. To enhance the solubility of zinc acetate, 0.4 mL of acetic acid was also added to the solution. Prior to deposition, glass substrates were cleaned and placed on the hot plate maintained at 450 °C. ZnO thin films were deposited on rotating hot substrates at 25 rpm. The solutions were sprayed onto substrates through a 0.2 mm nozzle, using a N_2 carrier gas. The solution flow rate, carrier gas pressure and nozzle to substrate distance were held constant at 10 mL per minute, 2 atm and 40 cm, respectively [1].

5.1.5 Synthesis of Interconnected ZnO Nanowires

The influence that the underlying seed/nucleation layer had on the resultant nanostructures was explored by substituting RF deposited seed/nucleation layers with rougher seed layers deposited via spray pyrolysis. It was observed that by utilising rougher seed/nuelcation layers it was possible to engineer interconnected ZnO nanowire arrays. As previously shown in Figure 5.4, the growth of ZnO nanorods from a highly orientated seed/nucleation layer consisting of regular sputtered crystallites (with hemispherical terminations) resulted in an array of high density ZnO nanorods, which rarely deviate from their perpendicular growth habits.

Unlike the ZnO sputtered seed/nucleation layers with almost periodic crystallites, ZnO seed/nucleation layers deposited via spray pyrolysis are comparatively rougher, typically consisting of sharp polygonal crystallites. As the ZnO nanorods emerge from their underlying seed/nucleation crystallite they do so perpendicularly, and as the underlying layer is non-uniform, many of the

nanorods grow very close to one another or at different angles, as is schematically presented in Figure 5.5 The scanning electron micrograph presented in Figure 5.5 indicates that the nanowires stem directly from the tip of a ZnO nanorod, with nanowires typically connecting with neighbouring structures, resulting in freestanding nanowire clusters.

It is possible that the close proximity between the emerging nanorods generates a localized electric field, attracting charged precursors in solution, promoting rapid growth at the sharp hexagonal tips and, resulting in the fine ZnO nanowires. This may sustain the rapid growth of ZnO, effectively decreasing the width of the nanostructures, resulting in nanowires: ~15 nm from spray pyrolysis samples vs ~100 nm from sputtered seed/nucleation layers grown under the same conditions. It is also possible that during the growth process, these tips generete strong dipoles which have the potential to bend the highly flexible piezoelectric nanowire tips towards each other, which later coalesce along the terminations of their non-polar crystal facets.

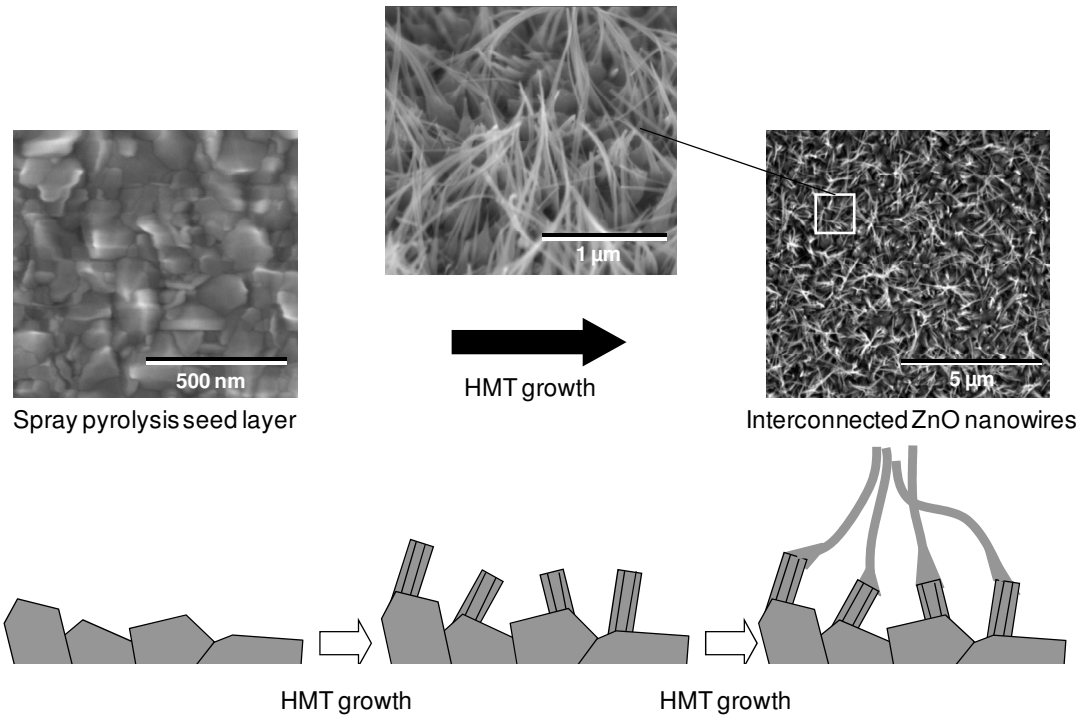

Figure 5.5. The growth of interconnected ZnO nanowire arrays from spray pyrolysis deposited seed/nucleation layers.

5.2 WO_3 Nanostructured Thin Film Synthesis

During the course of his PhD candidature, the author has endeavoured to develop a number of new aqueous chemical methods for the controllable synthesis of tungsten oxides from aqueous solutions. Many synthetic methods for the formulation of micro/nano dimensional WO_3 rely on using highly reactive reagents which may be corrosive, irritating and toxic, as is the case with high concentration hydrogen peroxide used to oxidise tungsten metal [16], tungsten ethoxide [17] or the inorganic tungsten hexachloride salt [18], which are often used as tungsten precursors. In this thesis, two different aqueous techniques were developed for the controlled deposition of nanodimensional WO_3 from a solution of disodium tungstate dihydrate and nitric acid. Nitric acid is a common laboratory reagent and while corrosive itself, it is more stable than hydrogen peroxide. Disodium tungstate dihydrate is a comparatively innocuous salt of tungsten; and being the dihydrate one does not have to be concerned with mass increase due to hygroscopic action, unlike tungsten hexachloride. As these methods do not require the use of vacuum equipment, limiting autoclave reaction vessel volumes, and organic solvents, they may be easily applied to larger industrial processes. The residual tungstate effluent may be recycled by acid/base precipitation and re-dissolution, offering the promise of a "green" closed loop fabrication cycle. This work resulted in the publication of a co-authored paper [19]. In this section four different fabrication methods will be introduced, the characterisation of the synthesised materials will be presented in detail in Chapter 6.

5.2.1 Nanotextured WO_3 RF Sputtered Thin Films

Nanotextured WO_3 thin films for gasochomic hydrogen sensing studies were deposited onto quartz substrates via RF sputtering. The experimental parameters used for the deposition of WO_3 nanotextured thin films are presented in Table 5.2.

Table 5.2. WO_3 sputtering parameters.

Target composition	W 99.99%
Target to substrate distance	7.0 cm
Sputtering power	80 W
Process gas	90% O_2 / 10% Ar
Working pressure	1 x 10^{-2} Torr
Deposition time	180 min
Substrate temperature	260 °C
Film thickness	1.2 µm

5.2.2 Precipitation Method

Tungsten oxide can be readily precipitated by introducing concentrated nitric acid into a tungstate ion solution [20]; this reaction occurs rapidly resulting in a bright yellow precipitate forming almost instantaneously. Unfortunately, this method formed unsuitably large precipitates, which were several millimetres across and non-porous.

5.2.3 Successive Ion Layer Adsorption Reaction (SILAR)

The successive ion layer adsorption reaction (SILAR) method, such as that described for the deposition of ZnO by Mitra *et al.* [6] are capable of producing micro/nano dimensional thin films on any substrate, providing that the substrate is resistant to both high and low pH environments for short periods of time. This method is capable of nanomaterial deposition onto plastics, ceramics, metals, and semiconductors. Due to the lack of literature surrounding WO_3 SILAR methods, the SILAR method presented in this thesis was developed by the author. The process involves the controlled dipping of a substrate between two different beakers containing the reagents required for the reaction. The first beaker was a 0.5 M sodium tungstate ion solution, which had been adjusted to have a pH of 11 – 14; and the second a small beaker filled with water and nitric acid, with a pH of –0.1 to –0.4. Outside their respective pH regions, nanostructured thin film growth was found to be unfavourable.

A thin film began to form when the substrate was immersed in the tungstate ion solution for two seconds, followed by an immersion in the acid bath for two seconds. This step was repeated to form an increasingly thick film of tungsten oxide hydrate, with the thickness of the thin film being affected by solution pH and the number of immersions performed. When substrates are immersed into the

tungstate ion solution, a thin liquid film of tungstate ions is adhered to the substrate. These ions are then precipitated out of the liquid film when they come into contact with the acidic contents of the beaker as per (5.11):

$$WO_4^{2-} + 2H^+ \xrightarrow{H_2O} WO_3{\cdot}nH_2O + H_2O \quad (H_2WO_4 \text{ intermediate not shown}) \qquad (5.11)$$

Di Natale *et al.* [21] reported that the tungstate ion in distilled water exists in a variety of different forms over a large pH range. At near neutral pH the following species exist in solution: WO_4^{2-}, HWO_4^-, H_2WO_4, $HW_5O_{22}^{5-}$, and $W_6O_{21}^{6-}$, with the predominant species at a pH of >11 being WO_4^{2-}. To drive (5.11), an abundance of the WO_4^{2-} ions will be required, thus the pH of the tungstate solution was adjusted to fall between 11 and 14 pH units.

Tungsten oxide(s) are acidic oxides, which are readily dissolved by basic solutions, and slowly by acidic solutions. Thus, the basic environment in the tungstate solution not only serves to provide an abundance of WO_4^{2-} ions, but it is also capable of redissolving any poorly adhered tungsten oxide precipitates on the immersed substrate, aiding in the removal of crystallites loosely bound to the surface. This dissolution process refines the crystal structure of the adherent tungstate percipitates in a similar but different manner to Ostwald ripening, ensuring that the most thermodynamically stable crystallites are fortified. It should be noted that as the immersion steps are repeated, a degree of cross-contamination between beakers will occur. During the repetitive processing steps, excess un-adhered precipitated tungsten oxides are capable of forming a semi-stable colloidal suspension in the acidic beaker. Due care should be exercised as this suspension is capable of redepositing back onto the substrate, during subsequent re-immersions.

It was observed via pH measurements, that when the substrate is removed from the acidic beaker and immersed into the tungstate ion solution, a small volume of acid is carried on the surface of the substrate as a thin liquid film. Gradually this small volume of acid consumes the hydroxide ions (in addition to the consumption caused by the tungsten oxide precipitation) in solution, disturbing the pH of the solution, and hence, the speciation of the tungstate ions. During experimentation, this manifests as a sudden drop from pH ≈ 12 to ≈ 8. It is critical to restore the pH of the tungstate ion solution to

12 – 14. If the pH falls below 11, tungstate oxides do not precipitate on the substrate as a nanostructured thin film, preferring to form a colloidal suspension in the acid beaker. The opacity of the dried tungsten oxide thin films was observed to increase with the number of immersion steps performed.

Drying conditions of the gel-like films greatly affects their uniformity and coverage of the dried film. Placing coated substrates onto a warm surface at 40 °C causes the gel to rapidly dehydrate, which distorts and cracks the tungstate oxide thin film, disrupting film uniformity. It was observed throughout experimentation that as the gel-like film ages, it darkens from beige to pale yellow, with the degree of coloration intensity increasing with the sample thickness.

SEM analysis presented in Chapter 6, revealed that the number of dips has a subtle impact in morphology once the gel-like sample had dried. It was observed that a small number of immersions created a more uniform film with less macroscopic cracks, presumably caused by the interfacial tension of the gel during drying. The adhesion of the thinner tungsten oxide films was better than thicker films, which were easily scratched with plastic forceps.

5.2.4 Sol-gel Method

In order to improve the uniformity and reduce the size of the nano precipitates a more controllable method than the previously investigated SILAR method was developed by the author. Whilst there are examples of WO_3 nanomaterials deposited via sol-gel techniques [18, 22-23] and references within, most techniques require the use of precursors such as tungsten butoxide or tungsten hexachloride which are well known for their expense, and instability. These chemicals should be handled under inert atmospheres to prevent interaction with oxygen and water vapour. The developed method is novel in the fact that the sol-gel utilises water as a “leaving group” rather than an organic molecule such as an alcohol during the condensation polymerisation reaction outlined in Figure 5.6 This approach has several advantages as the reagents are relatively innocuous, at least two orders of magnitude cheaper, and can be easily handled under atmospheric conditions.

The synthesis procedure developed by the author is as follows: in this process two 20 mL syringes were placed into a programmable syringe pump (Oxford Instruments PhD 2000) with one syringe filled with a nitric acid solution (pH –0.1), and the other a 0.25M Na_2WO_4 solution which had been adjusted to pH 11. Previous experimentation outlined in § 5.2.3 identified the necessity to adjust the pH of the tungstate ion solution to 11 to maximise the number of WO_4^{2-} ions. The syringe pump was programmed to deliver 5 mL of each solution onto a spinning quartz substrate, rotating between 1000 and 8000 rpm, with a constant flow rate of either: 0.25 mL/min, 0.5 mL/min, 1.0 mL/min, 2.5 mL/min or 5.0 mL/min. The outlets of each syringe were connected to Tygon laboratory tubing and fed separately into a standard Y-connector, which was then suspended over the spinning substrate in manner that ensured the mixed liquid was dropped directly onto the centre of the rotating substrate. Samples were subsequently spun for 5 minutes to assist in removing excess liquid, and dried overnight in a fume-cupboard at room temperature in either high humidity or low humidity environments.

As previously discussed, tungstate ions which exist in a number of different species in an aqueous environment (HWO^{4-}, H_2WO_4, $HW_6O_{22}^{5-}$, $W_6O_{21}^{6-}$) are forced to exist as WO_4^{2-} at pH 11. When combined with nitric acid (pH of –0.1) forces tungstate ions to precipitate out of solution, yielding WO_3 and water as per (5.11). Unlike the traditional addition of concentrated acid to a tungstate ion solution, the high concentration acid solution and basic tungstate solution are designed to be in a close to a 1:1 stoichiometric ratio, with a slight excess of acid to controllably drive the condensation polymerisation reaction as per (5.11) and Figure 5.6 Outside of these ratios and pH values, nanostructured thin film deposition was unfavorable.

It should be noted that once the two solutions are mixed the viscosity rapidly increases as the resultant solution forms a sol-gel. By feeding separate reagents into a Y-connector it is possible to tune the viscosity of the droplet exiting the connector. Slow flow rates (0.25 mL/min) result in a comparatively high viscosity sol-gel, leading to thick film formation at 3000 rpm. Similarly, faster flow rates (5 mL/min) causes a similar viscosity to water, being rapidly spun off the substrate, leading to very thin films. Optical properties such as opacity which is a function of thickness can also be controlled with flow rate.

The condensation polymerization reaction that forms the basis of the sol-gel method is schematically represented in Figure 5.6.

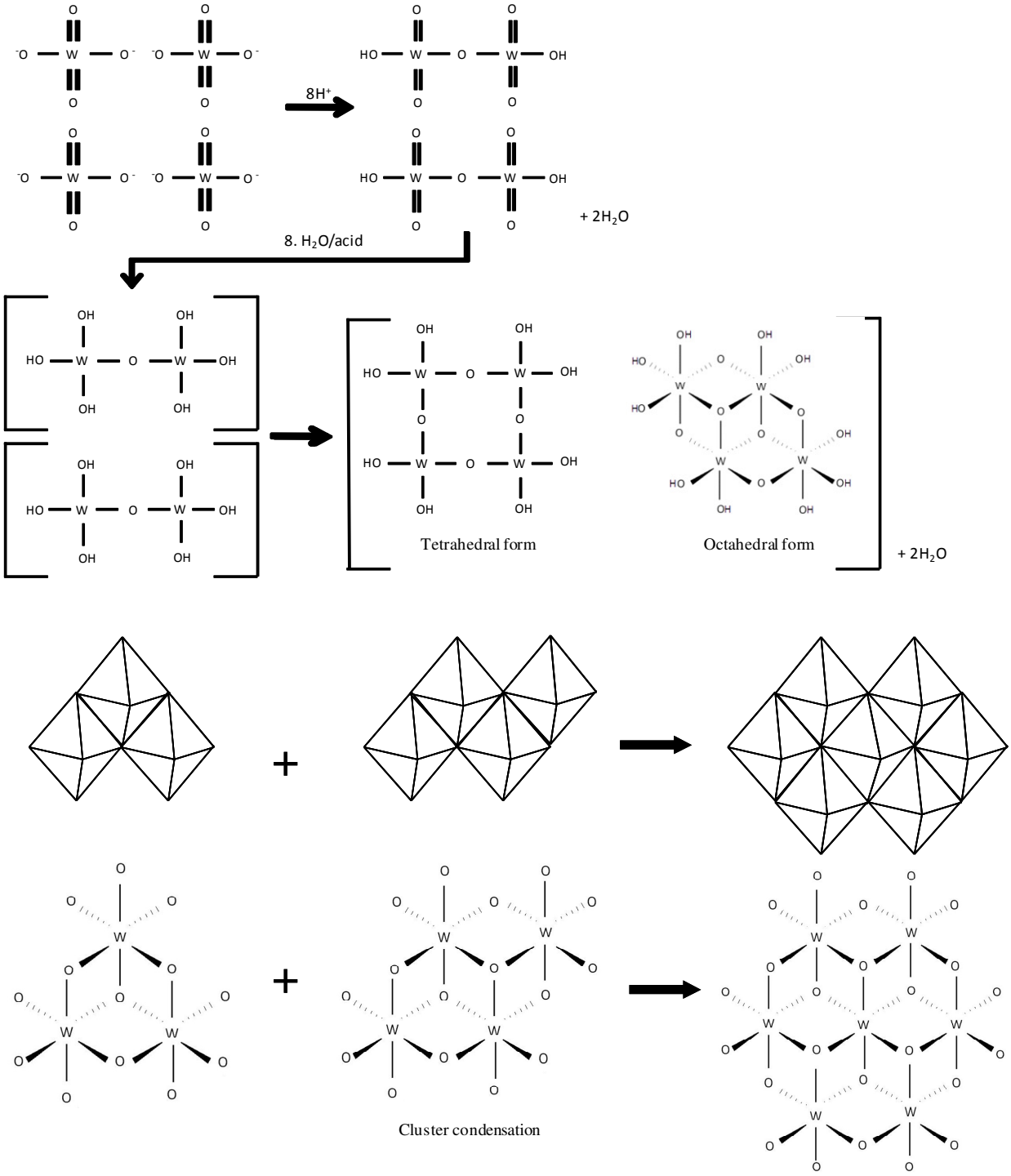

Figure 5.6. Tungstic acid condensation polymerisation pathway [19].

During the deposition process, H_2WO_4 is formed when the two reagents are mixed in the Y-connector. As H_2WO_4 comes into contact with other H_2WO_4 molecules, they undergo partial

condensation polymerization, where two hydroxyl ligands combine to eliminate water and form a shared oxygen bond between the two tungsten centres. Further addition of acid to the partially polymerized system causes tungsten oxo ligands (W=O) to become progressively hydrated resulting in the formation of di-hydroxy ligands W-$(OH)_2$. These ligands then further condense to increase the degree of cross-linking, eventually leading to a 3-dimensional structure in which tungsten centres are completely crosslinked to adjacent tungsten centres via four or six shared oxygen bonds, resulting in structures similar to those found in polyoxo-tungstates [20]. These polyoxo-tungstates (tungstic clusters) later coalesce and form into extended oxide sheets [24], resulting in the formation of nanoplatelets as schematically represented in Figure 5.6.

Samples were observed to intensify in colour during the drying stage as the gel aged. During the drying stage thin films often developed cracks, presumably due to the interfacial tension caused by the superhydrophobic quartz substrate and the gel. To investigate possible methods to reduce the appearance of cracks a number of different post processing / ageing treatments were explored. Such methods involved directly adding water or acetone to the sol-gel film. Acetone was directly added to displace the water in the sol-gel, as acetone is miscible in water, and has a lower viscosity than water. This was observed to reduce cracks formation during the drying process, while this improved film uniformity, some cracks remained. Adding two droplets of water directly to the sol-gel film, made no appreciable difference to the uniformity or extent of the observed cracking.

Exposing the sol-gel to an atmosphere of either acetone or water vapour during drying had an interesting effect on the dried sol-gel. These atmospheres were generated by placing a small Teflon spacer into the bottom of a 3 inch glass Petri dish, puddling the chosen solvent into the bottom of the Petri dish and placing the sol-gel coated substrate on top of a 4 mm thick Teflon spacer. The lid of the Petri dish was then used to partially cover the substrate, reducing the evaporation rate of solvent. For water vapour atmospheres this resulted in a relative humidity of 55% or greater. An atmosphere of acetone had little effect on the morphology of the dried film as it evaporated in a matter of hours. The water filled Petri dish, remained partially filled with water for many days (placed into a fume cupboard at 25 °C), after the water evaporated a uniform almost crack free tungstate coating was achieved. This had an interesting effect on the dimensions of the nanostructured film, by extending the time taken for

the sol-gel to completely dry the nanostructures enlarged by a factor of 5 or greater, when compared with their untreated counterparts. The post processed sol-gel films were comprised of significantly larger nanocrystallites, and were more adherent to the surface with adhesion approaching that of traditional thin films.

5.3 Chapter Summary

In this chapter the different techniques, justifications, as well as a detailed description of the processes involved in the deposition of ZnO and WO_3 nanostructured thin films have been presented. To the best of the author's knowledge, many of the techniques employed were applied by the author for the first time, resulting in several publications [1, 8-10, 14, 19, 25-27].

ZnO Nanostructures and Nanostructured Thin Films

ZnO nanostructures and nanostructured thin films were fabricated using seed/nucleation layers deposited via RF sputtering or spray pyrolysis. Three different ZnO morphologies were created, nanorods, corrugated nanorods, and interconnected nanowires, with the later two morphologies synthesised for the first time using aqueous chemical methods.

To the best of the author's knowledge the following have been demonstrated for the first time:

1. Fabrication of corrugated ZnO nanorod arrays from aqueous solutions.
2. The utilisation of spray pyrolysis deposited seed/nucleation layers in the fabrication of ZnO interconnected nanowire arrays from aqueous solutions.

WO_3 Nanostructures and Nanostructured Thin Films

WO_3 nanostructures and nanostructured thin films were fabricated via SILAR and sol-gel methods. WO_3 nanotextured thin films for gasochromic sensing applications were deposited via RF sputtering.

To the best of the author's knowledge the following have been demonstrated for the first time:

1. A SILAR method capable of depositing nanostructured WO_3 thin films.

2. The development and implementation of an aqueous sol-gel technique capable of depositing a nanostructured WO_3 thin film.

The characterisation of ZnO and WO_3 nanostructured and nanotextured thin films introduced in this chapter will be covered in detail in Chapter 6. Furthermore, the gas sensitivity of sensors based on these materials will be presented in Chapter 7.

5.4 References

[1] M. Breedon, *et al.*, "Aqueous synthesis of interconnected ZnO nanowires using spray pyrolysis deposited seed layers," *Materials Letters,* vol. 64, pp. 291-294, 2010.

[2] J. S. Hua Li , Chang Liu, Hongbing Lu and Juncheng Cao, "Microstructural study of MBE-grown ZnO film on GaN/sapphire (0001) substrate," *Central European Journal of Physics,* vol. 6, pp. 638-642, 2008.

[3] W. Mai, *et al.*, "Vertically aligned ZnO nanowire arrays on GaN and SiC substrates," *Chemical Physics Letters,* vol. 460, pp. 253-256, 2008.

[4] F. Mao, *et al.*, "High quality p-type ZnO film growth by a simple method and its properties," *Chinese Science Bulletin,* vol. 53, pp. 2582-2585, 2008.

[5] L. Vayssieres, "Growth of Arrayed Nanorods and Nanowires of ZnO from Aqueous Solutions," *Advanced Materials,* vol. 15, pp. 464-466, 2003.

[6] P. Mitra and J. Khan, "Chemical deposition of ZnO films from ammonium zincate bath," *Materials Chemistry and Physics,* vol. 98, pp. 279-284, 2006.

[7] Y. T. Zhang, *et al.*, "Crystal growth of undoped ZnO films on Si substrates under different sputtering conditions," *Journal of Crystal Growth,* vol. 243, pp. 439-443, 2002.

[8] M. Breedon, *et al.*, "ZnO nanostructures grown on epitaxial GaN," *First International Symposium on Transparent Conducting Oxides,* vol. 518, pp. 1053-1056, 2009.

[9] M. Breedon, *et al.*, "Seeded growth of ZnO nanorods from NaOH solutions," *Materials Letters,* vol. 63, pp. 249-251, 2009.

[10] M. Breedon, *et al.*, "ZnO nanostructured arrays grown from aqueous solutions on different substrates," in *Nanoscience and Nanotechnology, 2008. ICONN 2008. International Conference on*, pp. 9-12, 2008.

[11] R. B. Peterson, *et al.*, "Epitaxial Chemical Deposition of ZnO Nanocolumns from NaOH Solutions," *Langmuir,* vol. 20, pp. 5114-5118, 2004.

[12] G. Madras and B. J. McCoy, "Temperature effects during Ostwald ripening," *The Journal of Chemical Physics,* vol. 119, pp. 1683-1693, 2003.

[13] L. Vayssieres, *et al.*, "Purpose-Built Anisotropic Metal Oxide Material: 3D Highly Oriented Microrod Array of ZnO," *The Journal of Physical Chemistry B,* vol. 105, pp. 3350-3352, 2001.

[14] M. Rahmani, Breedon, M., Keshmiri, S., Moafie, A., McCoulloch, D., Wlodarski, W., Kalantar-zadeh, K., "Gas Sensing Properties of Interconnected ZnO Nanowires," *Sensors and Actuators B: Chemical,* Under Review, 2010.

[15] A. Ashour, *et al.*, "Physical properties of ZnO thin films deposited by spray pyrolysis technique," *Applied Surface Science,* vol. 252, pp. 7844-7848, 2006.

[16] A. Patra, *et al.*, "Sol-gel electrochromic WO_3 coatings on glass," *Materials Letters,* vol. 58, pp. 1059-1063, 2004.

[17] K. Galatsis, *et al.*, "Sol-gel prepared MoO_3-WO_3 thin-films for O_2 gas sensing," *Sensors and Actuators B: Chemical,* vol. 77, pp. 478-483, 2001.

[18] Y. Djaoued, *et al.*, "Low temperature synthesis of nanocrystalline WO_3 films by sol-gel process," pp. 673-679, 2008.

[19] M. Breedon, *et al.*, "Synthesis of nanostructured tungsten oxide thin films: A simple, controllable, inexpensive, aqueous sol-gel method," *Crystal Growth and Design,* vol. 10, pp. 430-439, 2010.

[20] G. W. Albert Cotton, Carlos A. Murillo, Manfred Bochmann, *Advanced Inorganic Chemistry* 6th ed., Wiley Interscience, 1999.

[21] F. Di Natale and A. Lancia, "Recovery of Tungstate from Aqueous Solutions by Ion Exchange," *Industrial & Engineering Chemistry Research,* vol. 46, pp. 6777-6782, 2007.

[22] O. Bohnke and C. Bohnke, "Comparative study of the electrochromic properties of WO_3 thin films," *Displays,* vol. 9, pp. 199-206, 1988.

[23] K. Dong Lee, "Preparation and electrochromic properties of WO_3 coating deposited by the sol-gel method," *Solar Energy Materials and Solar Cells,* vol. 57, pp. 21-30, 1999.

[24] A. Chemseddine and U. Bloeck, "How isopolyanions self-assemble and condense into a 2D tungsten oxide crystal: HRTEM imaging of atomic arrangement in an intermediate new hexagonal phase," *Journal of Solid State Chemistry,* vol. 181, pp. 2731-2736, 2008.

[25] J. L. Campbell*, et al.*, "Electrowetting of Superhydrophobic ZnO Nanorods," *Langmuir,* vol. 24, pp. 5091-5098, 2008.

[26] M. H. Yaacob*, et al.*, "Absorption spectral response of nanotextured WO_3 thin films with Pt catalyst towards H_2," *Sensors and Actuators, B: Chemical,* vol. 137, pp. 115-120, 2009.

[27] J. Yu*, et al.*, "A comparison of forward and reverse bias operation in a Pt/nanostructured ZnO Schottky diode based hydrogen sensor," *Procedia Chemistry,* vol. 1, pp. 979-982, 2009.

Chapter 6 - Characterisation of Metal Oxide Nanostructures

Directly continuing from Chapter 5, which introduced the different processing and synthesis techniques used for the deposition of ZnO and WO_3 nanostructures, this chapter will present a thorough analysis of the nanostructures and nanostructured thin films developed by the author. Scanning Electron Microscope (SEM) images were obtained for all investigated synthetic procedures and their processing steps, providing valuable morphological and dimensional information. Transmission Electron Micropscopy (TEM) investigations proved insightful for selected samples, where unexpected morphologies were created. ZnO nanomaterial characterisation was simplified by the availability of previously published data; confirmed the formation of single crystalline ZnO from the adapted deposition methods. The body of knowledge considering WO_3 and $WO_3 \cdot nH_2O$ synthesis via aqueous chemical methods indicated a number of subtle considerations which must be observed. Tungsten oxide itself rarely exists as WO_3 often the presence of lattice bound water molecules complicates the analysis, as does the considerable number of different crystallographies possible. Compounding the complexities of tungsten oxide and tungsten oxide hydrate characterisation is the capacity of WO_3 to exist with a sub-stoichiometric oxygen balance, i.e. $WO_{2.9}$, $W_{24}O_{68}$, etc. To confirm the nature of the deposited nanostructured thin film a number of complementary analytical techniques were employed such as; X-ray diffraction, Raman spectroscopy, and X-Ray photoelectron spectroscopy; for comprehensive and conclusive material analysis.

6.1 Characterisation Equipment and Methods

Many different analytical and scientific techniques were utilised to study and elucidate the properties of the developed materials in this thesis. Outlined below are the characterisation techniques employed, the relevant procedures for sample preparation, and the conditions under which analysis was performed.

6.1.1 Scanning Electron Microscopy

A FEI Nova NanoSEM 200 was used in both low vacuum and high vacuum imaging modes to analyse the morphology of ZnO and WO_3 nanostructured thin films. A Gatan Precision Etching and Coating System (PECS) model 682, designed for coating electron microscopy samples, was used to sputter Pt onto metal oxide nanostructures, if serious 'charging' prevented stable imaging. The sputtering was carried out by two penning ion guns trained on a 99.99% Pt target. The PECS coating system is designed to slowly deposit electron transparent amorphous coatings of Pt with a built in thickness monitor, 25Å Pt was typically deposited.

6.1.2 Transmission Electron Microscopy / Selected Area Electron Diffraction

A Jeol 1010 Transmission Electron Microscope (TEM) and 2010 High Resolution Transmission Electron Microscopy (HRTEM) were used to investigate the morphology and crystallography of most metal oxide nanostrutures, all images were captured on electron sensitive film which were processed and scanned into electronic format for integration into this thesis. Selected Area Electron Diffraction (SAED) patterns were obtained for $WO_3 \cdot nH_2O$ and WO_3 nanostructures only, as the formation of ZnO nanostructures from HMT solutions is well known to result only in the formation of a hexagonal in crystal structure. TEM samples were prepared by mechanically agitating nanostructured thin films over a watch glass dish, followed by the addition of a few droplets of water, into which a copper TEM grid (either holy carbon or amorphous carbon grids) were placed with the dispersed nanomaterials and left to dry before being imaged.

A JEM-40001X TEM at Nanjing University was used for imaging $WO_3 \cdot nH_2O$, which was prepared by mechanically agitating samples as previously discussed. This work resulted in the generation of single figure which appeared in a co-authored publication [1]. XTEM (Cross-sectional TEM) analysis of ZnO nanostructures on GaN was conducted by Thomas Kehagias of the Physics Department, Aristotle University of Thessaloniki, Greece. XTEM samples were prepared by mechanical, then dimple grinding followed by argon ion-milling to electron transparency. HRTEM

observations were carried out in a 200 kV Jeol 2011 electron microscope with a 0.19 nm point resolution and C_s=0.5 mm. This work also resulted in the publication of a co-authored paper [2].

6.1.3 Optical Microscopy

An Olympus SZ-CTV optical microscope with Pixel link CCD camera was used to capture the appearance of the sol-gel deposited samples presented in § 6.3.4.

6.1.4 X-Ray Diffraction

XRD patterns were collected at room temperature on a Bruker D8 ADVANCE X-ray diffractometer, fitted with a graphite-monochromated copper tube source (Cu-Kα radiation, λ = 1.5406 Å), and a scintillation counter detector. Samples were matched to reference diffraction data supplied by the International Centre for Diffraction Data (ICDD) database.

6.1.5 Raman Spectroscopy

Micro-Raman measurements were performed on a Renishaw RM1000 spectrometer in a backscattering geometry. The 514.5 nm line from an argon ion laser was used as the excitation source at low excitation powers to prevent localised heating during the measurement that may otherwise have altered the crystal structure or hydration level of the fabricated materials. The notch filter spectral response profile of the instrument prevented measurement below ~100 cm^{-1}.

6.1.6 X-Ray Photoelectron Spectroscopy

XPS measurements were performed on a VG-310F instrument using Al non-monochromated X-rays (20 kV, 15 mA) with the hemispherical energy analyser set at a pass energy of 100 eV for the survey spectrum and 20 eV for peak scans. Photoelectrons were taken off normally to the surface. All spectra presented were charge shift corrected taking the C1s peak at 285.0 eV.

6.2 ZnO Nanostructured Thin Film Characterisation

6.2.1 SEM Analysis of Nanotextured RF Sputtered ZnO Thin Films

RF sputtered nanotextured ZnO thin films were used as seed/nucleation layers deposited onto different substrates for both the sodium hydroxide driven and HMT deposition methods. The choice of substrate was observed to have an effect on the morphology of the RF sputtered thin film, and the subsequent orientation and surface coverage of the nanostructured arrays. ZnO thin films were deposited under identical deposition conditions outlined in Chapter 5. Figure 6.1 provides a comparison of the different nanotextured morphologies that were deposited over a range of substrates investigated.

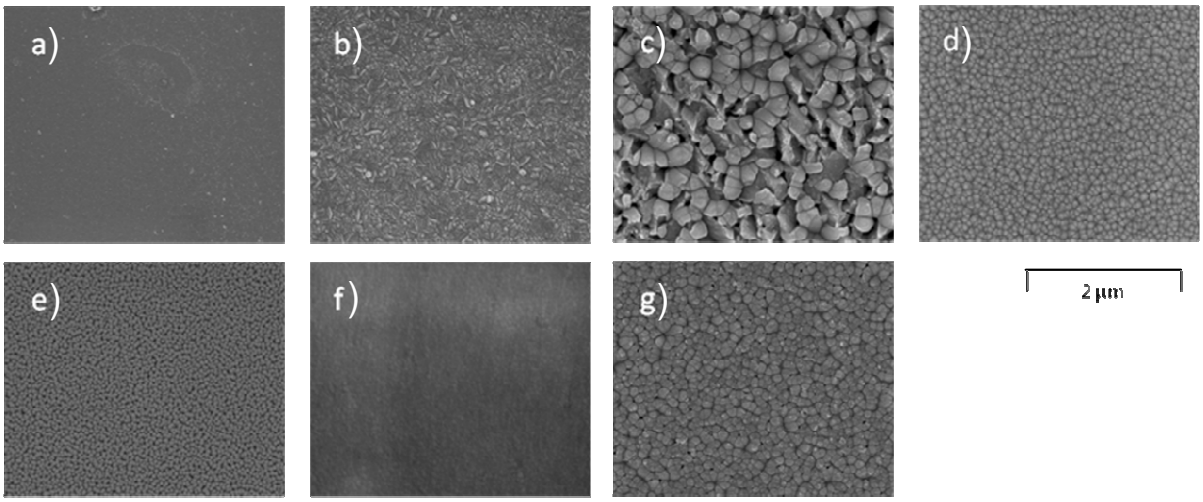

Figure 6.1. ZnO RF sputtered onto different substrates (a) glass; (b) ITO glass; (c) $LiTaO_3$; (d) quartz; (e) $LiNbO_3$; (f) 6H-SiC; (g) gold on $LiTaO_3$.

As can be seen in Figure 6.1 there is a large difference between the resulting ZnO nanotextured seed/nucleation layer, which can in turn, affect the density and distribution of hydrothermally grown ZnO nanostructured thin films as will be discussed in § 6.2.4.

6.2.2 SEM Analysis of Nanotextured Spray Pyrolysis Deposited ZnO Thin Films

Spray pyrolysis deposited ZnO seed/nucleation layers (Figure 6.2 and Figure 6.3) were used in the fabrication of interconnected ZnO nanowire arrays. Unlike RF sputtered ZnO seed/nucleation layers, which consist of hemispherically terminated crystallites, spray pyrolysis deposited layers are

comprised of sharp polygonal crystallites, with individual crystallite facet dimensions typically in excess of 100 nm in length. The sharp polygonal crystallites have no uniform alignment or preferential orientation as can be seen in Figure 6.2.

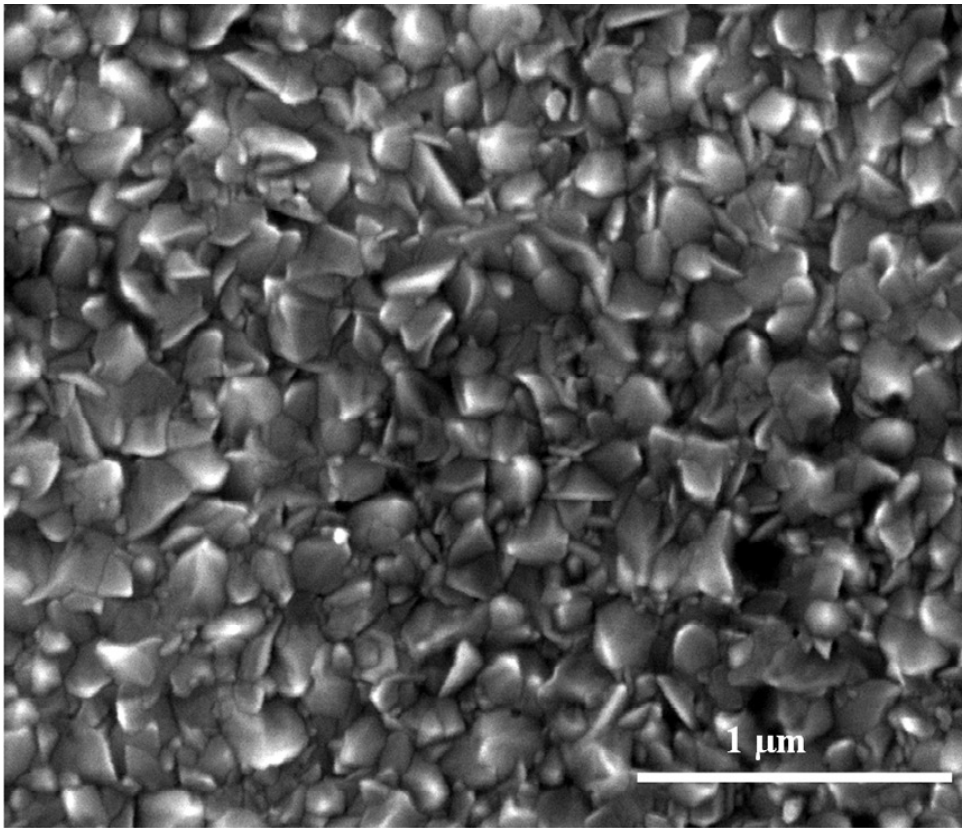

Figure 6.2. A typical spray pyrolysis deposited ZnO seed/nucleation layer [3]**.**

6.2.3 SEM Analysis of Sodium Hydroxide Deposited ZnO Nanostructured Thin Films

RF sputtered ZnO was used as a seed/nucleation layer for corrugated ZnO nanostructured thin films. Scanning electron micrographs taken at different deposition times suggest that the growth mechanism of corrugated ZnO nanorods from RF sputtered seed/nucleation layers in a NaOH solution begins with preferential etching, which occurs between adjacent sputtered ZnO crystallites. Preferential etching is responsible for the regular faceted nature of the hexagonal bases observed in Figure 6.3a and Figure 6.3b. From these hexagonal bases, multiple protrusions (40 nm – 100 nm in width) grow atop the etched hexagonal bases (>500 nm in width).

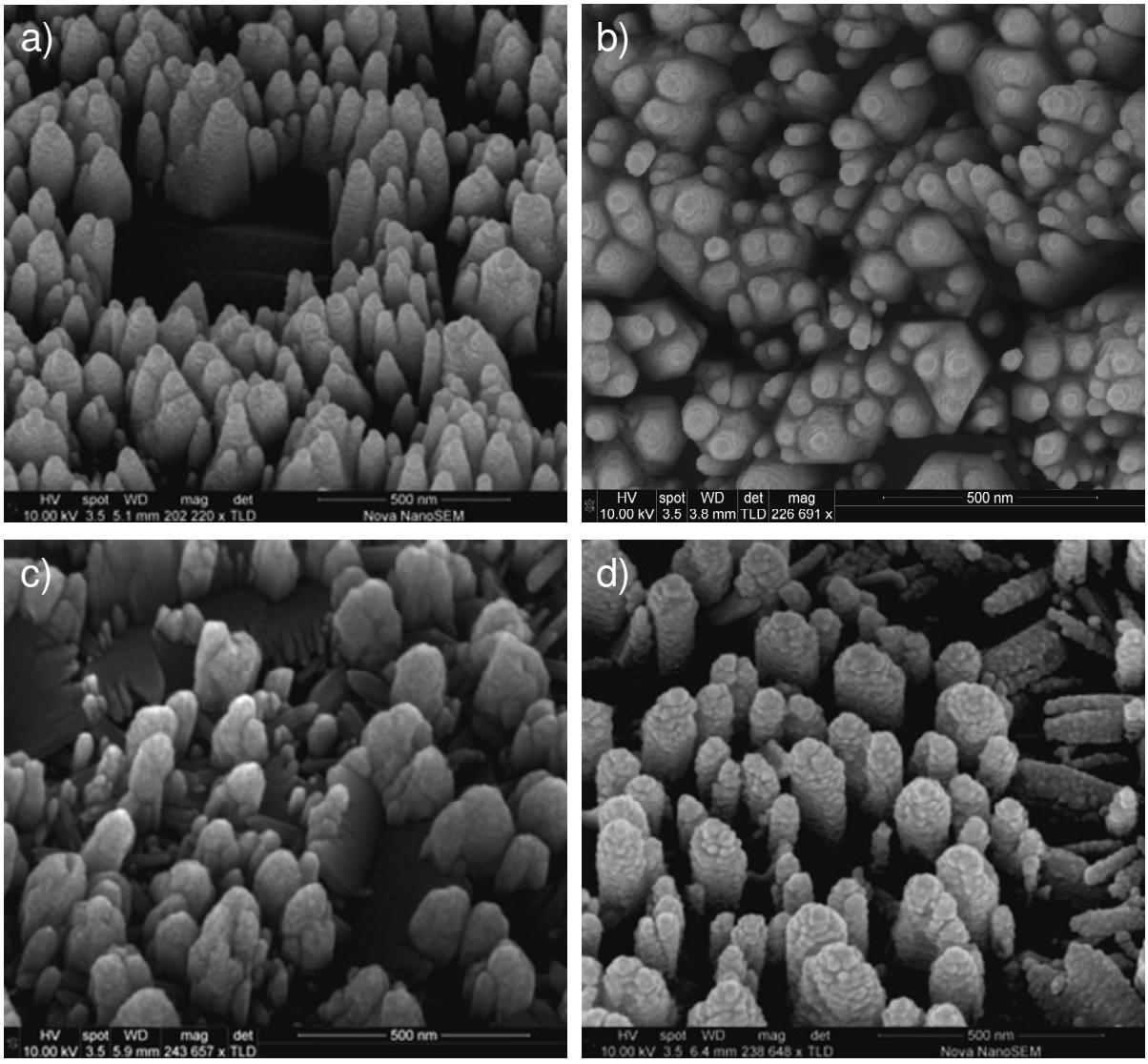

Figure 6.3. ZnO corrugated nanorods (a-b) growth after 1½ hrs; (c); growth after 3 hrs (d) growth after 16 hrs.

These nano-protrusions later coalesce into larger nanorods as seen in Figure 6.3c to Figure 6.3d. Comparing these figures it is apparent that after coalescence, further refinement of the crystallite occurs in a process that is analogist to Ostwald ripening, which is defined as "the last stage of a condensation transition from liquid to solid" [4]. This refinement, results in nanorods that appear to be constituted of multiple rough edged discs stacked upon each other forming a corrugated surface. However, it can be clearly seen in Figures 6.3d that the ZnO nanorods form into rods in hexagonal or polygonal motifs. It is hypothesised that surface defects in the crystal lattice of the faceted ZnO nanorods act as preferential sites for removal of lattice bound zinc atoms, facilitated by the hostile high pH 13 environment. Furthermore, this refinement is enhanced as a function of the high localised

concentrations that result from a lack of solution agitation, and the large timescale of the reaction. This treatment at an elevated temperature leads to extensive etching of the nanostructures, such that they are reduced to "nodular pillars", unlike those grown by Peterson *et al.* [5] whose work inspired the author to use sodium hydroxide solutions for ZnO growth. The nanostructures generated by the author grow as regular arrays of corrugated nanorods, aligned perpendicularly to the substrate surface. The unique morphology of the corrugated ZnO nanorods presented in Figure 6.3d is believed to be linked to the harsh chemical environment that exists at pH 13, the static reaction volume offered by the sealed reaction vessel and the long reaction time.

6.2.4 SEM Analysis of Hydrothermally Grown ZnO Nanostructured Thin Films

The morphologies of ZnO nanostructures from RF sputtered ZnO seed/nucleation layers via the hydrothermal growth method are presented in Figures 6.4 and 6.5.

ZnO growth on 6H-SiC substrates forms as clusters of nanorods and dispersed thin sheets of ZnO measuring approx 30 nm. These nanosheets grow from the substrate and fold under their own weight, draping over the nanorods. Using a 10 kV accelerating voltage during SEM imaging, there is sufficient penetration depth associated with the accelerated electrons to pass through the ~30 nm nanosheets, interacting with the underlying nanorods. However, this decelerates the electrons as they pass through the nanosheets, and the interaction with the underlying nanorods is weaker, thus reducing the number of detected secondary electrons, observed as obfuscated regions. Obfuscated regions are those that appear to be out of focus in Figure 6.4a. ZnO nanorods grown on $LiNbO_3$ substrates exhibit uniform growth that occurs at relatively low densities as seen in Figure 6.4b. $LiNbO_3$ substrate bound nanorods have one of the largest variations in width, measuring between approx 125 nm – 200 nm.

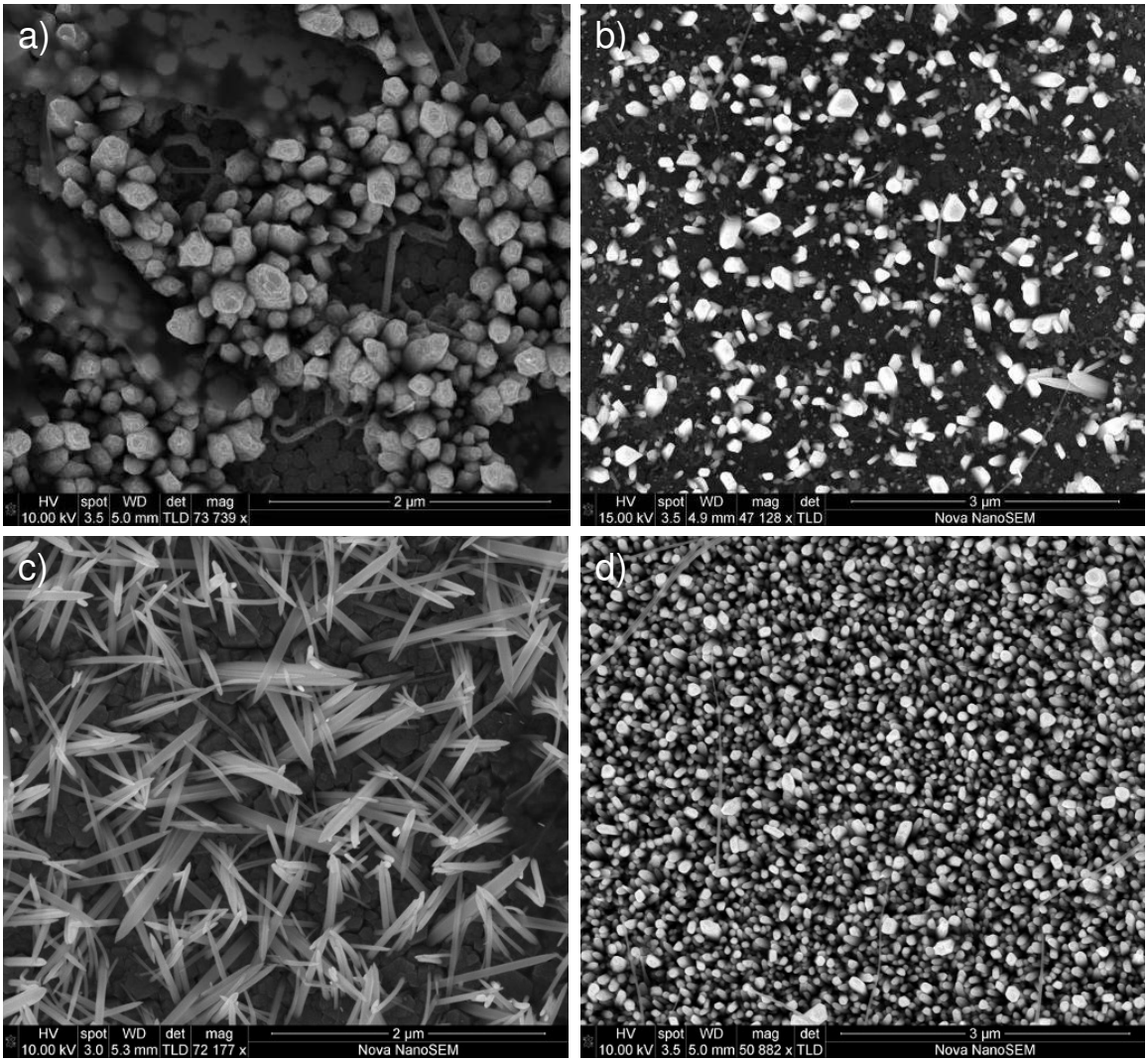

Figure 6.4. ZnO nanostructured thin films grown on: (a) 6H-SiC; (b) $LiNbO_3$; (c) ITO glass; (d) glass.

ZnO nanostructured thin films developed by the author were observed to grow as perpendicular arrays on all substrates, with the exception of ITO coated glass (as shown in Figure 6.4c) displaying no preferential growth angle. Nanorods grown on ITO coated glass have widths of approx 120 nm with minimal variation between nanorods. Interestingly ITO substrates had a comparatively rougher surface than the other substrates. It is hypothesized that this roughness may be a contributing factor in the disordered orientation of the nanorod arrays observed in Figure 6.4c. ZnO nanorod growth on glass substrates exhibit the smallest nanorod interspacing among samples, with excellent substrate coverage (Figure 6.4d). These nanorods are by far the thinnest, with dimensions of approx 100 nm or less.

Nanorod growth on quartz, as seen in Figure 6.5a, was found to have excellent coverage, but suffered from minor deviations in perpendicular growth. This has been ascribed to substrate roughness, as quartz substrates were polished for optical clarity, and were not chemically-mechanically polished like other substrates. ZnO nanorods grown on $LiTaO_3$ and gold on $LiTaO_3$ (Figure 6.5b) were measured to have identical densities, despite the fact that different initial sputtered crystallite densities were recorded. On an epi-GaN surface ZnO nanostructures grew in a unique hierarchical morphology comprising of ZnO nanorods (widths of 150 nm – 450 nm, with heights exceeding 1μm), which may be bridged with adjacent neighbouring structures, as seen in Figure 6.5c and Figure 6.5d. Interestingly, smaller secondary ZnO nanostructures (typically 30 nm in width and 150 nm tall) grew atop these bridges, protruding like vertical antennae, visible as white dots in Figure 6.5c. It is believed that the high density of the ZnO sputtered seed/nucleation layer provides an abundance of nucleation sites (>1500 crystallites per square μm), which may result in the formation of the bridged morphology. The growth of the secondary ZnO nanowires, protruding from the bridged structures, will be discussed in detail in § 6.2.6.

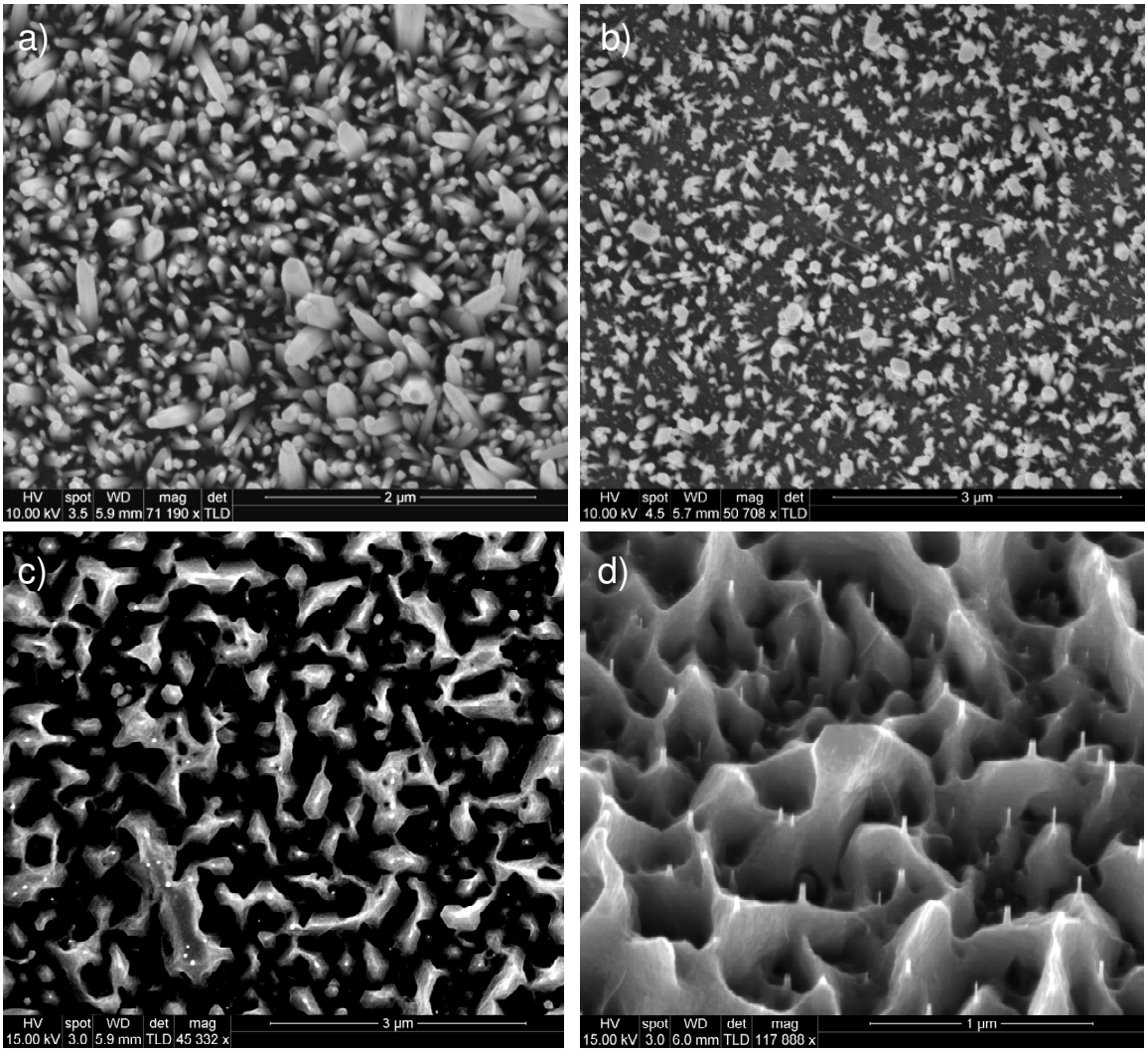

Figure 6.5. ZnO nanostructured thin films grown on: (a) Quartz; (b) Au/$LiTaO_3$; (c) GaN epitaxial layer; (d) GaN epitaxial layer (rotated).

Interconnected ZnO nanowire arrays were fabricated using spray pyrolysis seed/nucleation layers as previously discussed in Chapter 5. Electron microscopy observations (Figure 6.6) indicate that the ZnO nanowires emanate from the tips of larger ZnO nanorods, and these nanowires frequently connect at the terminations of the ZnO nanowires. Many nanowires bundle together along the ends of their non-polar crystal facets, with individual nanowires having an average width of approximately 15 – 30 nm.

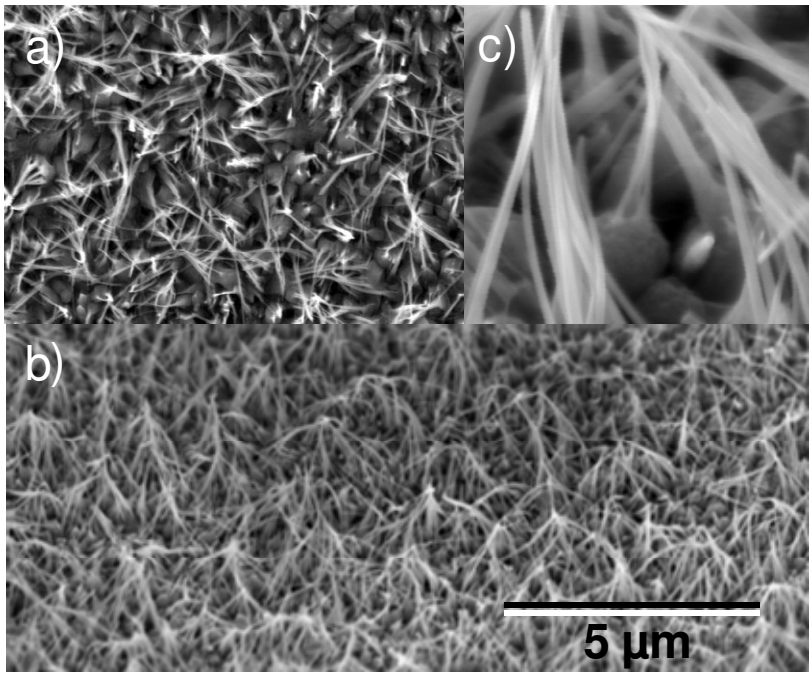

Figure 6.6. Interconnected ZnO nanowire arrays grown from spray pyrolysis deposited seed/nucleation layers (a) top down view; (b) 45° rotation; (c) higher magnification image highlighting nanowire interconnects.

6.2.5 XRD Analysis of Selected ZnO Nanostructured Thin Films and Seed/Nucleation Layers

XRD patterns of nanostructured ZnO arrays on epitaxial GaN layers are presented in Figure 6.7. Diffraction patterns were taken at each step in the fabrication process, considering: the epitaxial GaN layer/substrate, RF sputtered ZnO seed/nucleation on top of the epitaxial GaN layer, and finally the resultant nanostructured array after hydrothermal growth. All samples were in good agreement with ICDD #36-1451 corresponding to wurtzite ZnO, with some minor contributions from ICDD #38-0385 $Zn(OH)_2$ denoted in Figure 6.7 as "*". Here "e" is used to denote a substrate induced reflections.

Epitaxial GaN layers were grown on buffer layers supported by sapphire substrates, "e" reflections do not match with ZnO or GaN, it is therefore reasonable to assign these peaks to the GaN buffer layer and or the sapphire substrate. After removal from reaction vessels, samples were washed in DI water and dried in a stream of N_2. It is clear from minor contributions of $Zn(OH)_2$ (ICDD #38-0385) denoted in Figure 6.8 as "*", that for the fabrication of devices from hydrothermally grown ZnO a further

annealing step may be required to transform residual $Zn(OH)_2$ to ZnO. The pre-sensing stabilisation of samples tested towards NO_2 and H_2 in Chapter 7 was considered sufficient to render the $Zn(OH)_2$ detected via XRD to ZnO; by virtue of the sensing temperature employed >150°C.

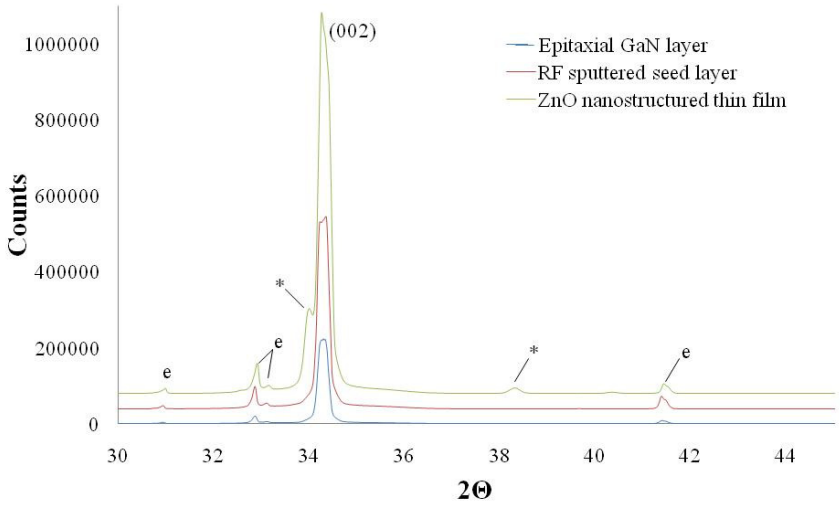

Figure 6.7. XRD of an epitaxial GaN layer, ZnO seed/nucleation layer and ZnO nanostructured thin film.

X-ray diffraction studies of the two different seed/nucleation layers used in the hydrothermal growth of ZnO nanostructured thin films; and their effect on the ensuing hydrothermally grown nanostructured thin film is presented in Figure 6.8. Here it is clear that the sputtered seed/nucleation layer had a preferential (002) reflection centred upon 34.4° which intensifies and splits into two well defined peaks at 34.4° and 34.8° after hydrothermal treatment. Sprayed seed/nucleation layers demonstrated comparatively weaker reflections corresponding with (002) and {100} crystal planes. It was observed in the sputtered films, that the (002) plane was also intensified after hydrothermal treatment, notably, the minor reflections of {100} were also augmented. Confirming that the interconnected nanowires adopted the crystallographic orientation of the underlying sprayed seed/nucleation layer. All samples were in good agreement with ICDD #36-1451 corresponding to wurtzite ZnO with some minor contributions from ICDD #38-0385 $Zn(OH)_2$ denoted in Figure 6.8 as "*".

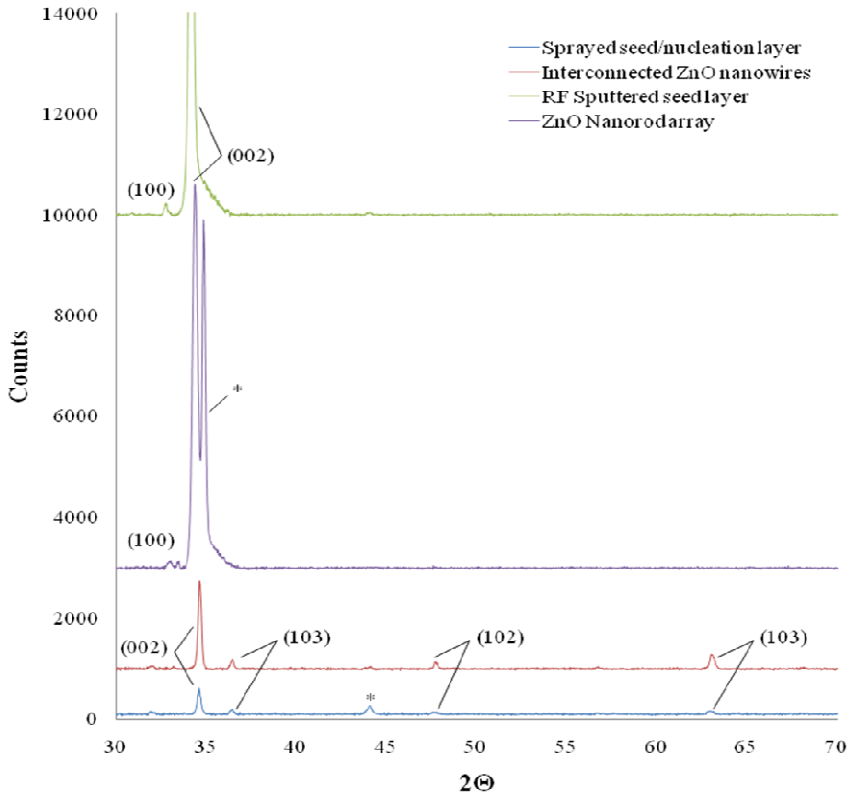

Figure 6.8. XRD comparison of different ZnO seed/nucleation layers and the ensuing nanostructures after hydrothermal growth.

6.2.6 TEM Analysis of Hydrothermally Deposited ZnO Nanostructures

Given the time required to prepare, image and analyse a full dataset of transmission electron micrographs and selected area electron diffraction patterns, hierarchical ZnO nanostructures grown on GaN epitaxial layers were chosen for analysis, due to the importance of ZnO/GaN combinations in device manufacturing and the unusual two tier hierarchical morphology.

ZnO nanostructures were grown onto an epitaxial GaN layer, supported by a sapphire substrate. GaN epitaxial layers were deposited via MOCVD, which were supplied by M. Kocan, G. Parish, J. Antoszewski, and L. Faraone, from the University of Western Australia. Cross-sectional studies were performed to investigate the unusual hierarchical morphology and to ascertain if hydrothermally grown ZnO nanostructures utilising a seed/nucleation layer could be suitable for the fabrication of ZnO/GaN based devices. ZnO/GaN devices have been predicted to be useful in a myriad of

applications and devices such as: light emitting diodes [6], heterojunction transistors [7], metal oxide semiconductor (MOS) devices [4-6], and Schottky diode based gas sensing [8-11].

A functional heterostructured device based on ZnO nanostructures and GaN has a typical layered composition of: metal/nanostructured ZnO/GaN/metal, where the two metal layers are formed for the purpose of electrical connections. Metal films deposited on devices can either result in an ohmic or Schottky contact, which are dependent on the type of metal used; however, care should be exercised in the deposition of metals. If metal is deposited directly onto nanostructured thin films, the metal may penetrate through gaps of the array, depositing onto GaN instead of ZnO, rendering the device useless. As such, a thin protective ZnO layer on GaN is of vital importance to ensure functional devices.

As discussed in Chapter 5, at room temperature the major contributor of the growth solution's pH is the zinc nitrate which causes a slight acidification of the reaction solution. Being an amphoteric material ZnO will readily dissolve in either acid or base. During the time it takes for the reaction solution to reach 80 °C the slightly acidic solution will attack the sputtered ZnO seed/nucleation layer, reducing its thickness. Once deposition temperature has been reached, the rate of deposition exceeds the rate of dissolution yielding a net growth of ZnO. Bearing this in mind, thoughtful consideration should be taken when deciding the thickness of the sputtered seed/nucleation layer, as the seed/nucleation layer is partially consumed. It was found that there was a reduction in the thickness of the ZnO sputtered seed/nucleation layer from 1.2 μm to 0.3 μm as can be seen in Figure 6.9, confirming that the nucleation layer was partially consumed during the growth of the nanostructures. The density of the nanorods suggests that the majority of the nucleation layer is dissolved into the growth solution as previously discussed in Chapter 5, and could be used as a source of zinc ions for the fortification larger (more thermodynamically favourable) nanostructures, as per Ostwald ripening [4].

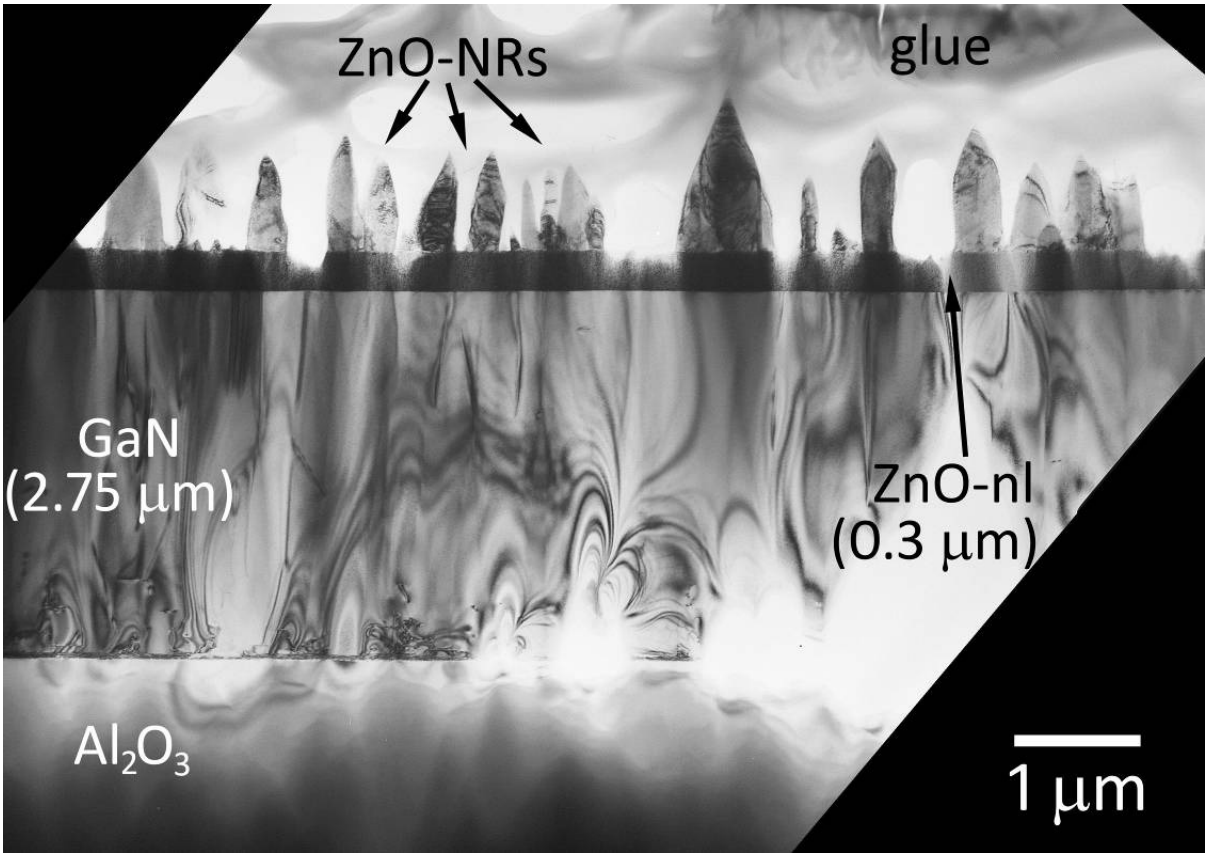

Figure 6.9. Cross-sectional TEM image illustrating the overall architecture of the sample along the [11 $\bar{2}$ 0] GaN/ZnO direction. The ZnO seed/nucleation layer (ZnO-nl) has reduced from 1.2 μm to 0.3 μm.

The nanostructured morphology was hierarchal with larger nanorods in close proximity with each other bridging. Finer secondary nanostructures emerged from less crystalline bridge regions, growing as hexagonal nanowires. An example of these nanostructures is presented in Figure 6.10, where a wurtzite ZnO nanowire emerged from a bridged area between two larger nanorods.

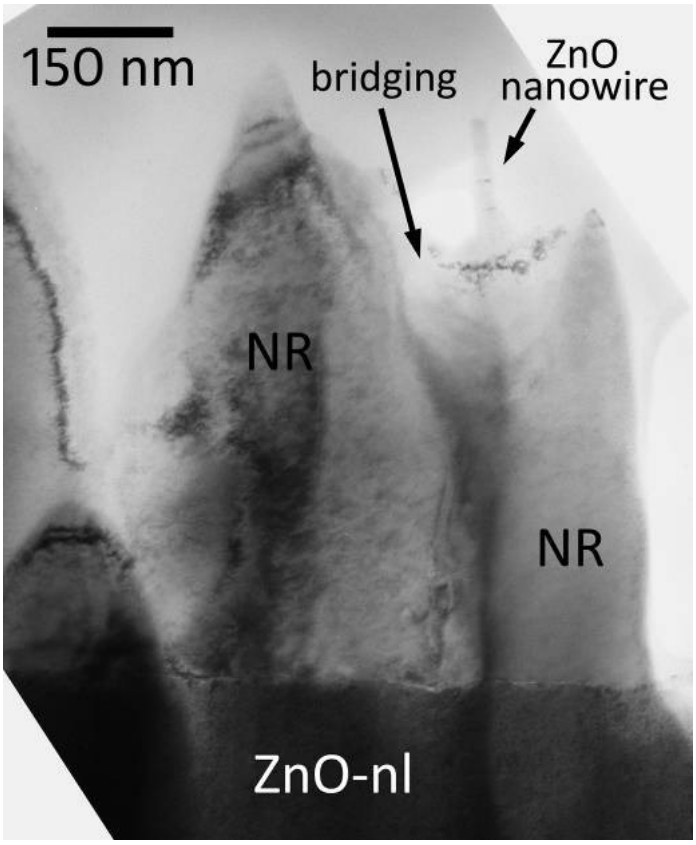

Figure 6.10. XTEM micrograph depicting a ZnO nanowire emerging from the bridged crystalline area between two large ZnO nanorods.

HRTEM observations and detailed electron diffraction analysis revealed that the ZnO seed/nucleation layer had clearly adopted the wurtzite structure of the underlying GaN film (Figure 6.11 – middle). Moreover, the ZnO nucleation layer appears to grow in good epitaxy with GaN, having an exact [0001]GaN / [0001]ZnO, (1$\bar{1}$00)GaN / (1$\bar{1}$00)ZnO orientation relationship. The lattice mismatch of the two crystal structures is minimal (GaN: a=0.3189 nm, c=0.5185 nm and ZnO: a=0.3250 nm, c=0.5207 nm); hence, the two crystal structures are in register [12]. HRTEM revealed the presence of basal stacking faults (SFs) confined at the GaN/ZnO interface (Figure 6.11-middle). These seem to compensate any residual strain caused by the in-plane lattice misfit. In addition, partial dislocations bounding SFs are potential nucleation sites of threading dislocations (TDs), which were observed to propagate throughout the ZnO seed/nucleation layer, labelled 'nl' in Figure 6.9, Figure 6.10, and Figure 6.11. ZnO nanorods also adopted the wurtzite structure but their homoepitaxy with the ZnO nucleation layer, was observed to deviate several times from the exact orientation

relationship. Hence, nanorods did not always grow with their axial [0001] direction parallel to the growth direction, causing nanorods to tilt from their typical perpendicular growth habits. Furthermore, their interface with the ZnO nucleation layer is not free of defects as shown in Figure 6.11-top, here a V-defect originating from the screw component of a TD is situated at the ZnO/ZnO nanorod interface. V-defects are characteristic crystal defects that appear in III-V layered structures. The heteroepitaxy between Al_2O_3 and the GaN buffer layer was ideal (Figure 6.11-bottom), despite the presence of a considerable amount of interfacial amorphous regions and basal SFs. In the first 50 nm of the buffer layer SFs were often so dense that locally GaN exhibited the zinc-blende (cubic) structure. Above these first layers basal SFs became uncommon and GaN presented an almost undisturbed wurtzite structure. This was supported by the fact that a large number of TDs emanating from the Al_2O_3/GaN interface bended and annihilated in the first 300 nm of the GaN buffer layer.

There has been a recent interest in hydrothermal growth of ZnO nanostructures on GaN, most notably the recent work reported by Jang *et al.* [13-14]. Nanostructured arrays of ZnO have been grown on GaN epitaxial layers via the hydrothermal decomposition a 25mM equimolar of Zn^{2+} / diethylenetriamine solution without the use of a nucleation layer. In this method substrates were immersed directly into a 95 °C growth solution, yielding well spaced ZnO nanoarrays. However, such samples are unsuitable for use in fabricating electronic devices comprising of metal junctions in contact with ZnO nanostructures. The deposited metal electrical contacts may fill the voids that exist in conventional ZnO nanostructured arrays. Because electronic devices; such as light emitting diodes, photodetecetors, laser and Schottky diode based gas sensors, rely on a metal/ZnO/GaN, any metal/GaN formation would render the device inoperative.

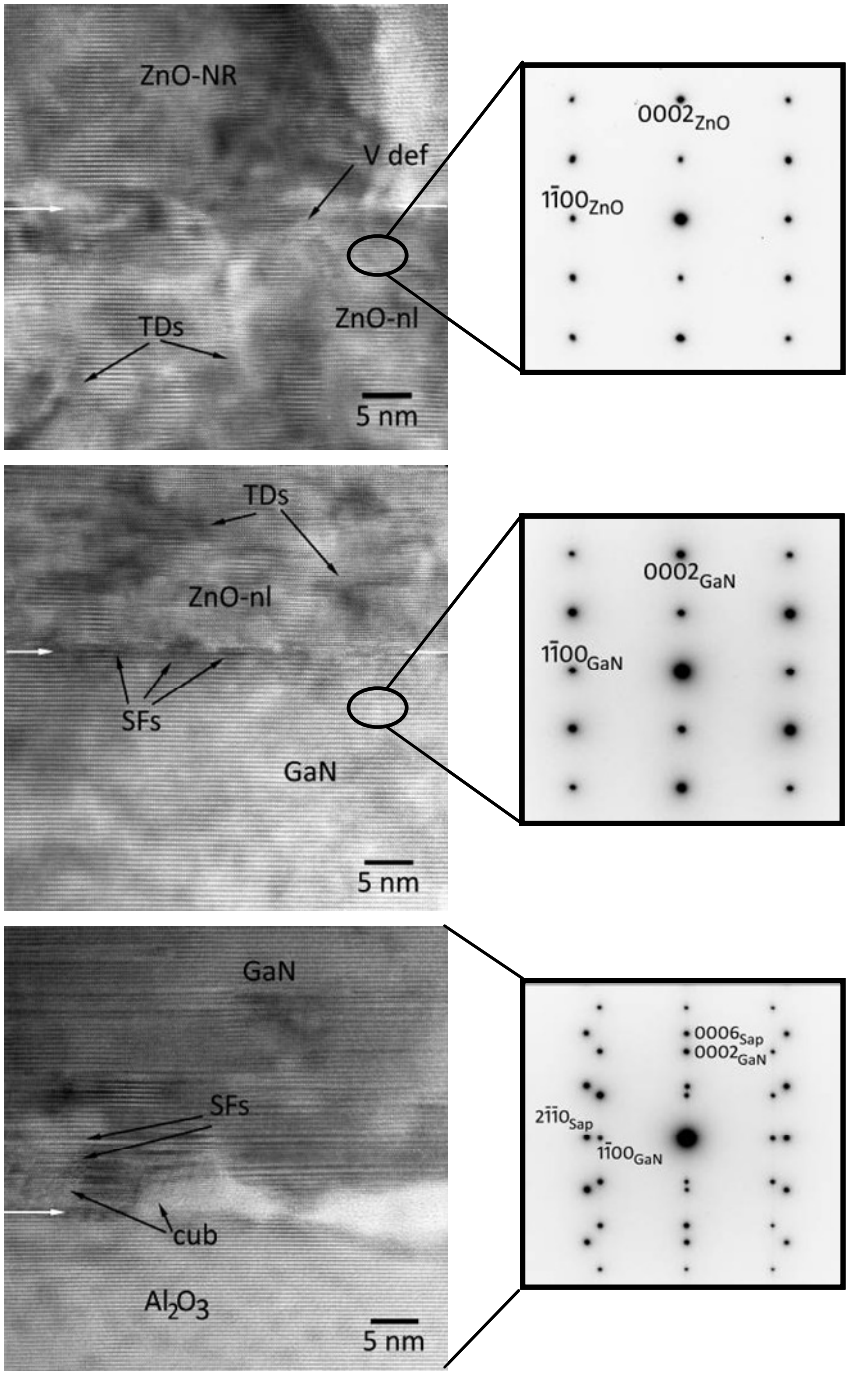

Figure 6.11. HRTEM micrographs showing the atomic structure of the different interfaces (denoted by white arrows) in the sample along the $[11\bar{2}0]$ GaN/ZnO direction, together with the corresponding electron diffraction patterns. The ZnO-nl/ZnO nanorod (ZnO-NR) interface is shown on the top micrograph, whereas the GaN/ZnO and the Al_2O_3/GaN buffer layer interfaces are depicted in the middle and the bottom micrographs, respectively.

6.3 $WO_3 \cdot nH_2O$ and WO_3 Nanostructured Thin Film Characterisation

Two unique deposition techniques were developed by the author during the investigations into the formation of WO_3 nanostructured metal oxides from aqueous solutions. Considering that the SILAR and sol-gel methods were investigated for the first time, comprehensive characterisation of the material was undertaken. The deposited nanostructured thin films could be used directly as hydrated tungsten oxides or annealed to induce the desired pure or mixed nanostructured WO_3 polymorphs (i.e. monoclinic, triclinic, hexagonal or orthorhombic). This permits some degree of freedom in tailoring the physical and chemical characteristics of the processed material. Due to the complexity of tungsten oxide and tungsten oxide hydrate chemistry many complimentary characterisation techniques including Raman spectroscopy were required for analysis.

6.3.1 SEM Analysis of Nanotextured RF Sputtered WO_3 Thin Films

RF sputtered nanotextured WO_3 thin films were deposited onto quartz substrates for studying H_2 induced gasochromism of Pt coated WO_3 nanotextured thin films. These films were ideally suited for gasochromic sensing applications given their high optical transparency, controllable thickness, and excellent uniformity of the nanotextured morphology across the whole sample.

A high magnification SEM micrograph of the Pt coated nanotextured WO_3 thin film is presented in Figure 6.12. Additionally, a cross sectional SEM image of the Pt coated nanotextured thin film is presented in Figure 6.13. It should be noted that the 25 Å Pt coating was deposited using the PECS coating system outlined in § 6.1.1. This system is designed for the deposition of electron transparent amorphous coatings, several Angstroms thick, and as such cannot be directly observed during imaging.

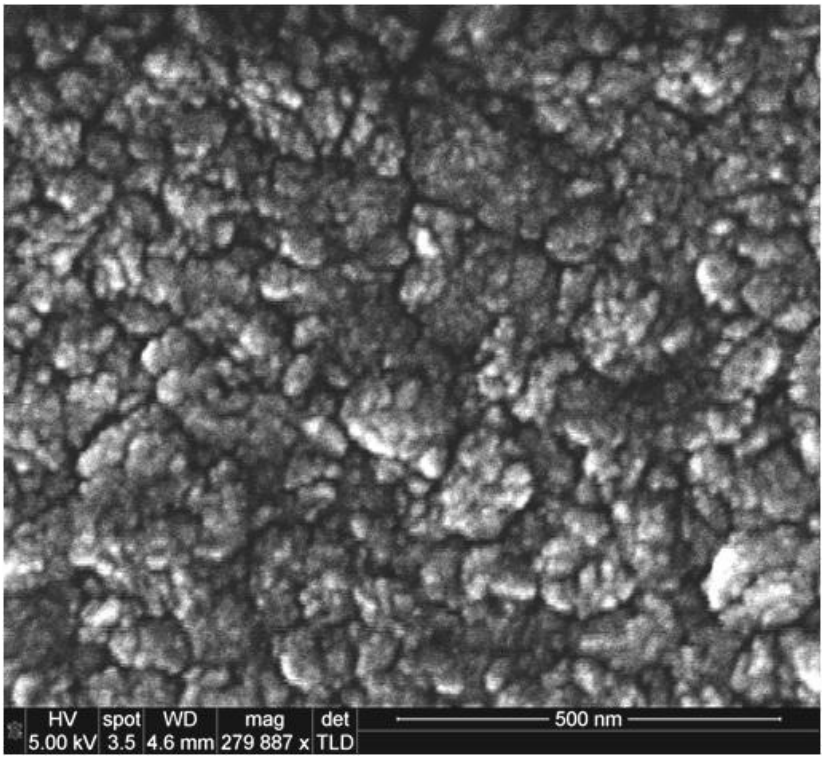

Figure 6.12. High magnification image of the Pt coated nanotextured RF sputtered WO_3 thin film.

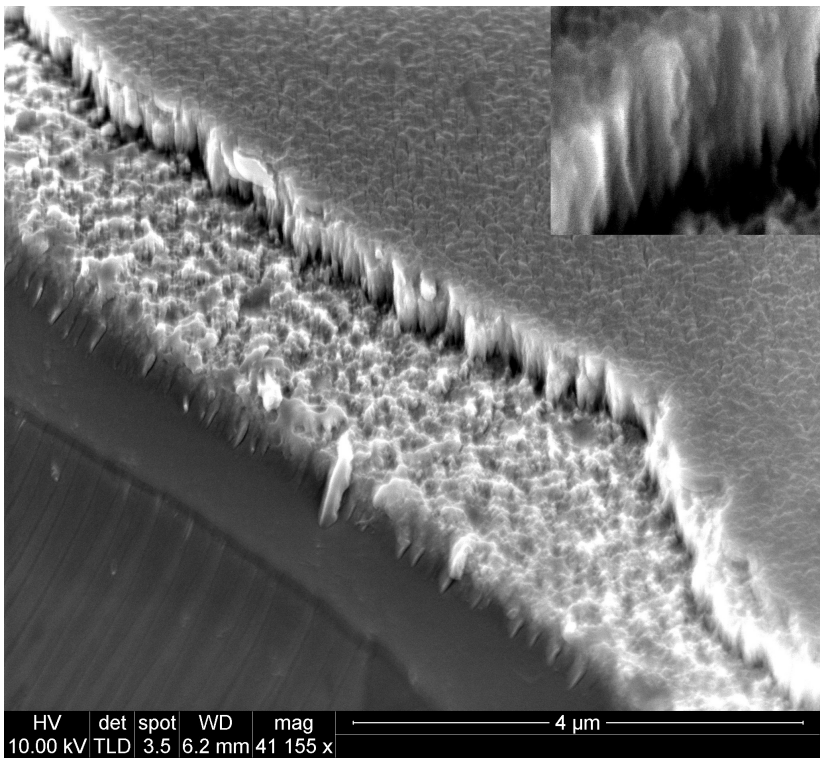

Figure 6.13. Cross sectional SEM image of RF sputtered nanotextured WO_3 deposited onto quartz substrates, inset highlighting the nanocolumnar cross sectional of the thin film.

6.3.2 SEM Analysis of Acid Precipitated $WO_3 \cdot nH_2O$

The rapid addition of concentrated acid to a tungstate ion solution forces an almost instantaneous precipitation, resulting in $WO_3 \cdot nH_2O$ shown in Figure 16.4. As discussed previously in Chapter 5, this reaction chemistry was heavily modified to produce nanostructured morphologies by adjusting reagent concentrations and limiting reaction rates.

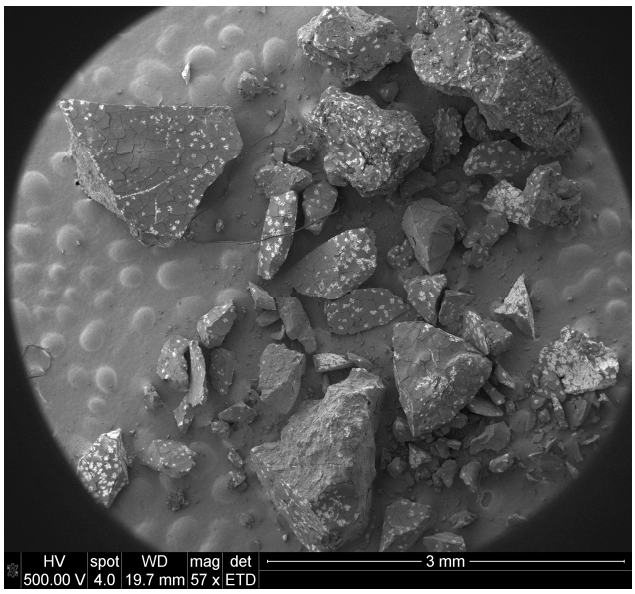

Figure 6.14. Partially crushed tungsten oxide precipitates formed by dropping concentrated nitric acid into a sodium tungstate solution.

6.3.3 SEM Analysis of SILAR Deposited Nanostructured Thin Films

The SILAR deposited $WO_3 \cdot nH_2O$ nanostructured thin films were formed by alternating dipping quartz substrates into a tungstate ion solution, then followed by an immersion in a solution of nitric acid. Initial results of SILAR deposited thin films indicated that this method was capable of depositing nanostructured morphologies, comprised of individual nanoparticles with dimensions in the order of ~15 nm as seen in Figure 6.15a and Figure 6.15b.

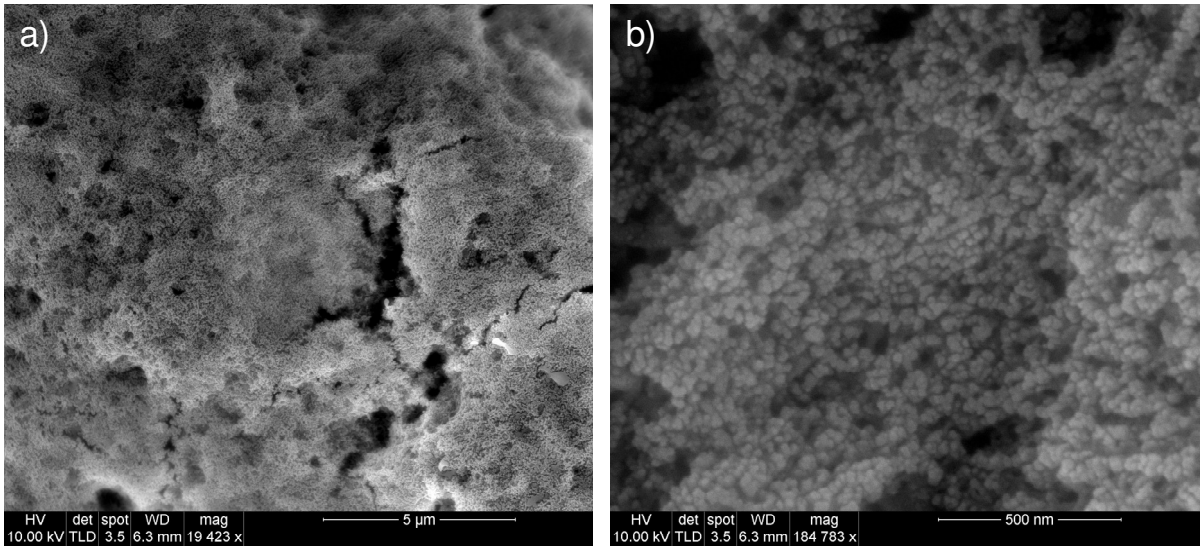

Figure 6.15. SEM image of SILAR deposited film, 5 dips at 2 seconds per dip (a) low magnification; (b) high magnification.

The results presented in Figure 6.15 represent excellent progress in the formation of nanostructured $WO_3 \cdot nH_2O$ thin films from low cost, innocuous chemicals. However, further investigations revealed inadequacies in surface adhesion, and to a lesser extent, nanostructure uniformity was observed to waiver between samples. The developed method had many experimental variables which must be considered by the researcher, such as: maintaining solution pH, manual sample manipulation, dip timing, nanostructure size and shape distribution, and unwanted precipitation formation. As such, the author reapplied the optimised reagent solutions and repurposed the SILAR method into a sol-gel method, with superior control of experimental variables, improving sample repeatability, and uniformity of the nanostructured morphology.

6.3.4 Optical Analysis of Sol-gel Deposited Nanostructured Thin Films

Having established the ability of the SILAR process to form nanostructured tungsten oxides using innocuous reagents, the author adapted this method to address several shortcomings of the SILAR method, such as distribution of nanostructure size, less than ideal surface coverage, and adhesion issues.

The first modification to this method was to use a spin coater to improve the macro uniformity of the deposited film. The second modification was to merge the two reagents in a microfluidic

Y-connector, ensuring adequate mixing and removing cross contamination by eliminating alternate dipping of substrates. The third modification was to remove the human error in the deposition process; dipping cycles were replaced with a programmable liquid delivery system. For all experiments, 5 mL of tungstate ion solution and a further 5 mL of nitric acid was considered to be sufficient to achieve a nanostructured thin film, several micrometers thick, suitable for characterization and device applications.

The deposition parameters of the spin coating procedure such as substrate rotation, the total volume of liquid delivered onto the spinning substrate, and the rate at which the reagents are mixed in the Y-connector were examined. The first variable to be examined was the flow rate, which was examined by depositing 5 mL of each liquid onto a quartz substrate spinning at 3000 rpm. The rate at which the reactants were mixed had a large impact on the viscosity of the deposited gel. Slow mixing rates resulting in low viscosity gels, which dried in air to form larger particle agglomerates than higher mixing rates of 5 mL/min shown in Figure 6.16. Flow rates were also observed to have a significant impact on the resulting nanostructured morphology, which will be discussed in 6.3.5.

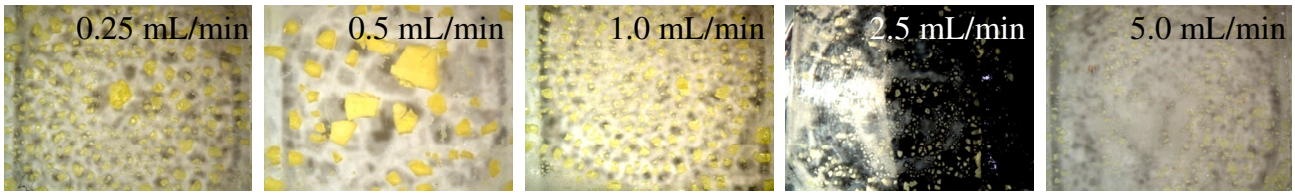

Figure 6.16. Optical microscopy comparison of flow rate at 3000 rpm.

A moderate deposition flow rate of 2.5 mL/min was chosen to examine affects on the resultant nanostructured thin film. The viscosity of the emerging gel was found to be the most compatible at 2.5 mL/min over a wide range of rotational speeds. As can be seen in Figure 6.17, low deposition speeds resulted in extremely poor uniformity films, with intense yellow coloration which has been ascribed to the relatively large amount of tungsten oxide, which was not removed via the centripetal force of the rotating substrate. At 8000 rpm the tightest distribution of surface bound particle sizes was observed.

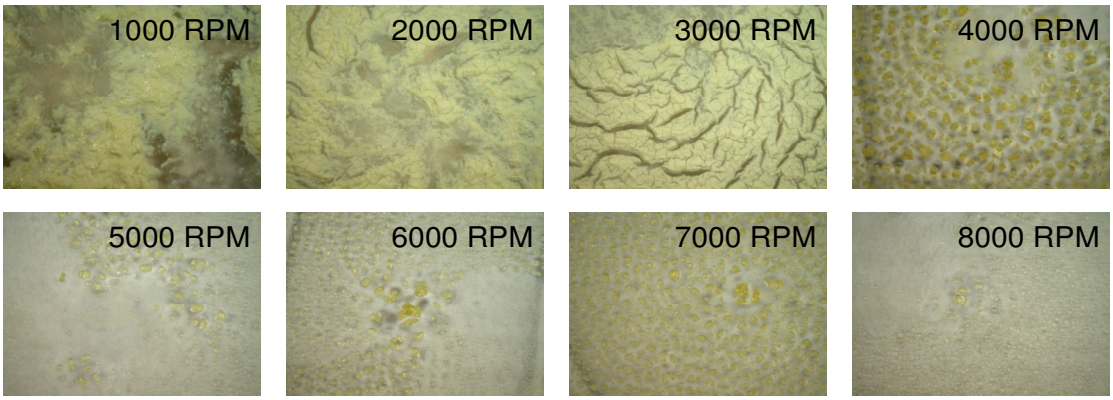

Figure 6.17. Optical microscopy comparison of sol-gel coverage at 2.5 mL/min deposition rate.

Further optimisation of deposition parameters yielded an optimal deposition rate of 1 mL/min at 8000 rpm. As a result, these deposition parameters were exclusively used for sample fabrication from herein. As previously discussed in Chapter 5, the atmosphere in which samples were post-processed / aged had a marked affect on the resulting thin film both to the naked eye and imaged via electron microscopy. The treatment of wet sol-gel films directly with water and acetone, and indirectly in water vapour or acetone vapour atmospheres was investigated (Figure 6.18). Treatment of freshly deposited sol-gel samples in water vapour atmospheres was found to facilitate contiguous coatings. This also had an interesting affect on the crystallography, nanostructure size and hydration of the nanostructured WO_3 thin film, which will be discussed in detail in the following sections.

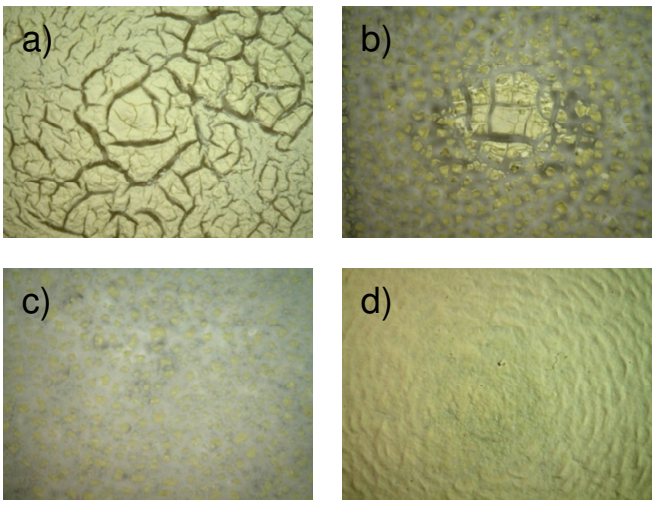

Figure 6.18. Post treatment of samples (1 mL/min, 8000 rpm): (a) two drops of acetone placed onto the sol-gel; (b) two drops of acetone placed onto the sol-gel; (c) surrounded by an atmosphere of acetone; (d) surrounded by an atmosphere of water.

6.3.5 SEM Analysis of Sol-gel Deposited Nanostructured Thin Films

As discussed in § 6.3.4, the deposition parameters not only had an influence on the macroscopic uniformity of the dried sol-gel films, but also had a significant impact on the resultant nanostructured morphologies. Samples were analysed as deposited or annealed for 2 hrs at either 300 °C or 550 °C in an oxygen rich atmosphere (90 % O_2 – 10 % Ar) to drive water from the crystal lattice, and to prevent the formation of sub-stoichiometric tungsten oxides. From herein, freshly deposited samples dried in ambient humidity air (typically 35% RH) will be labelled as "dried in air"; those dried in high humidity atmosphere as "as prepared". Later, "as prepared" samples were annealed, dehydrating the as prepared $WO_3 \cdot nH_2O$ to WO_3. In this thesis, as prepared samples were annealed at 300 °C or 550 °C to promote a single crystal phase. Furthermore, annealing temperatures fall below the operational temperature of the developed sensor, assisting in the reduction of baseline instabilities during gas testing.

WO_3 is known to undergo several crystallographic transition temperatures with the monoclinic phase existing between room temperature and 350 °C, and orthorhombic existing above 500 °C [15]. A hexagonal phase of WO_3 was identified less than three decades ago [15], and references reported therein. Many reports of hexagonal phase WO_3 originated from acid precipitated and or tungsten oxide hydrate samples after annealing [15-16].

As discussed in previous chapters, the environment in which the sol-gel samples were dried had a significant effect on the resultant nanostructured thin film. A comparison matrix of optical and scanning electron microscope images is presented in Figure 6.19. The most obvious difference between dried in air and as prepared samples is the surface coverage of the sol-gel synthesised material as seen in the insets of Figure 6.19a and Figure 6.19b. The nanoplatelets shown have thicknesses of the order of 10 - 30 nm, and had a high affinity for each other, readily agglomerating during the deposition process to form nanostructured films, some several microns thick. Figure 6.19 shows that many of the nanoplatelets attempt to align orthogonally to their nearest neighbours generating a small degree of long range order in the thin films.

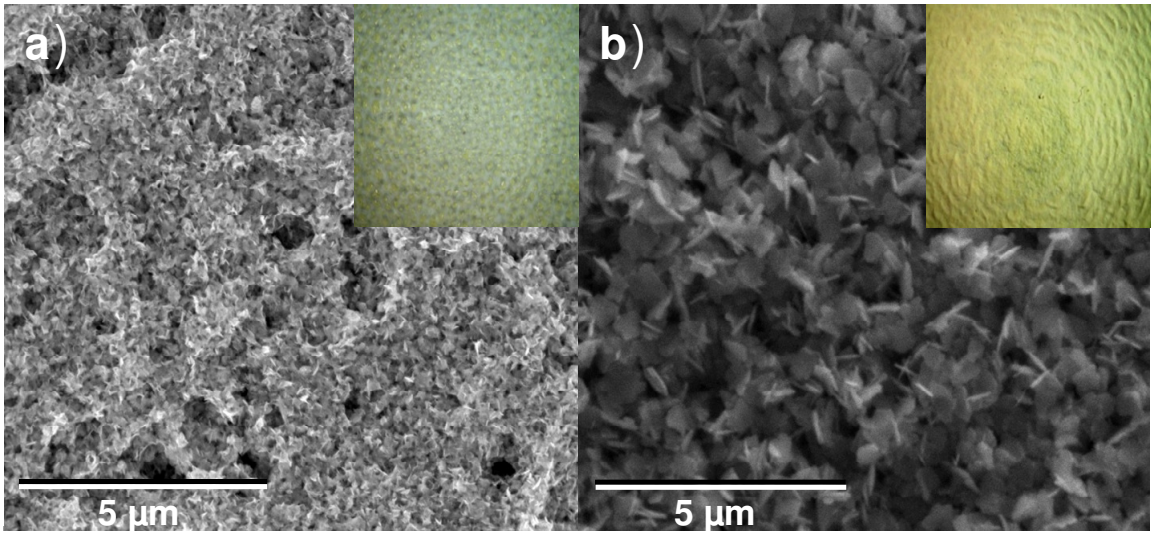

Figure 6.19. Microscopy comparison matrix of $WO_3 \cdot nH_2O$ (a) dried at low humidity, "dried in air" (inset is a low magnification optical image); (b) dried in a humid environment, "as prepared" (inset is a low magnification optical image). All samples were processed at 8000 rpm with a flow rate of 1 mL/min.

Flow rate had a significant impact on the resultant morphology of the as prepared samples. Fast flow rates (5 mL/min) resulted in low porosity nanoparticulate agglomerations as seen in Figure 6.20a, whereas lower flow rates of 1 mL/min resulted in high density, high porosity nanoplatelets with long range morphological order as per Figure 6.20b.

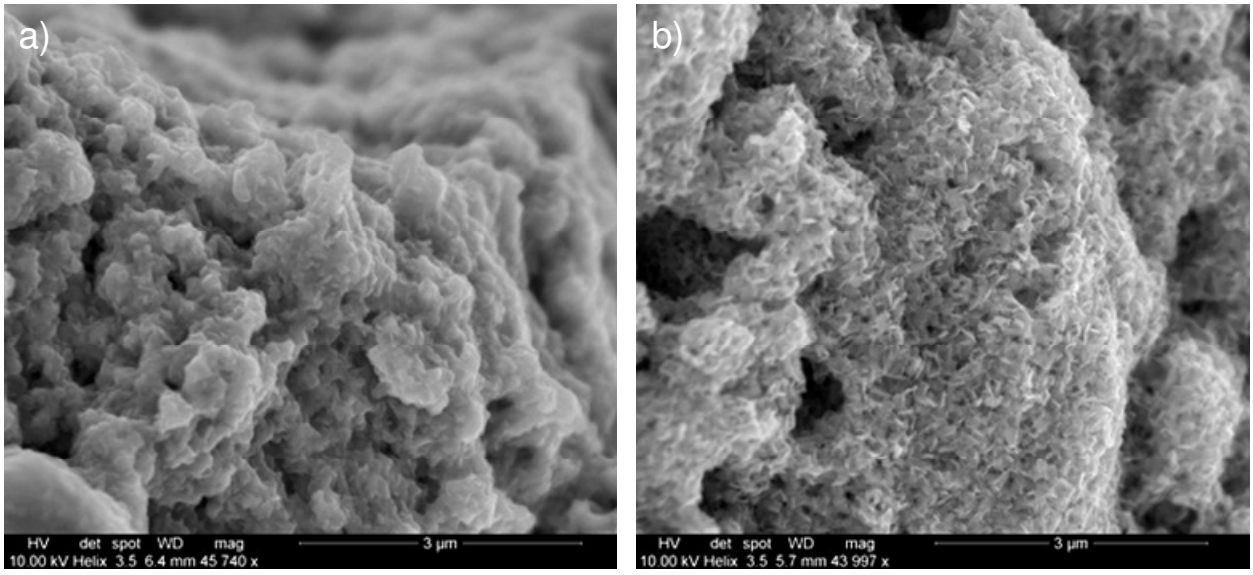

Figure 6.20. SEM image of sol-gel deposited $WO_3 \cdot nH_2O$ nanostructured films at 8000 rpm (a) a flow rate of 1 mL/min; (b) a flow rate of 5 mL/min.

After extensive testing, the optimised deposition parameters of $WO_3 \cdot nH_2O$ films, was determined to be obtained at 8000 rpm with a flow rate of 1 mL/min. As can be seen in Figure 6.21, this resulted in highly porous well ordered nanostructured thin films.

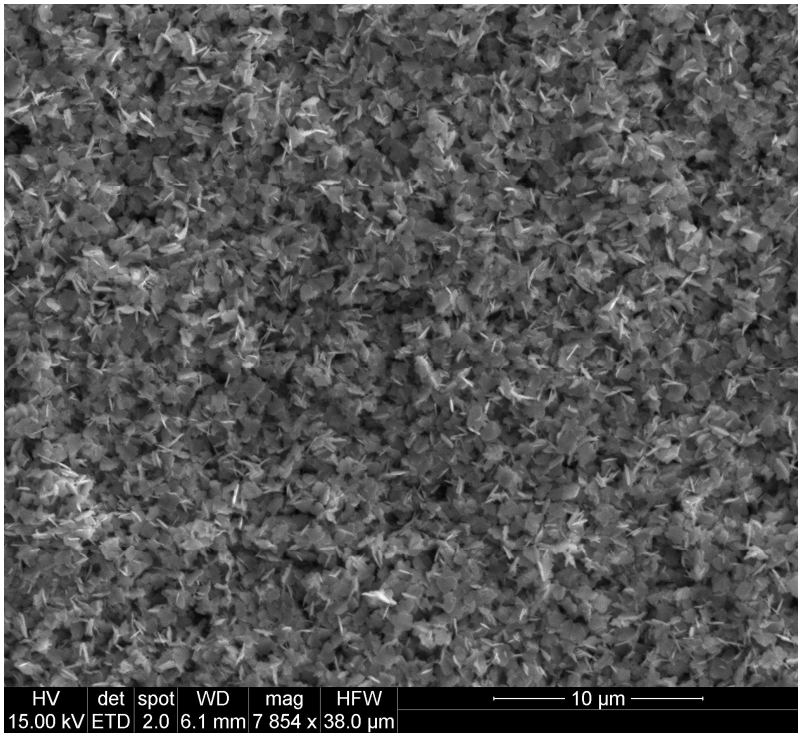

Figure 6.21. SEM image of sol-gel deposited $WO_3 \cdot nH_2O$ nanostructured film at 8000 rpm, at a flow rate of 1 mL/min, post processed in a water vapour atmosphere.

6.3.6 TEM Analysis of Sol-gel Deposited Nanostructured Thin Films

$WO_3 \cdot nH_2O$ nanoplatelets imaged in Figure 6.22 were prepared ex-situ, in a similar manner to ZnO samples as discussed in § 6.1.2. $WO_3 \cdot nH_2O$ nanoplatelets were electron transparent and either square or rectangular in shape, with many platelets forming at right angles to their nearest neighbouring platelets as seen in Figures 6.22a and 6.22b. Fortification of platelets during the ageing process was hallmarked by an increase in the dimensionality, and an improvement in the crystallinity of samples treated in a humid atmosphere. Samples presented in Figure 6.23a, had been dried under ambient conditions and were polycrystalline with a small number of secondary nanocrystalline precipitates. In contrast, samples dried in a high humidity environment appear more crystalline, with only minor

secondary nanocrystallites observed forming on the surface of the larger nanoplatelet (see Figure 6.23b).

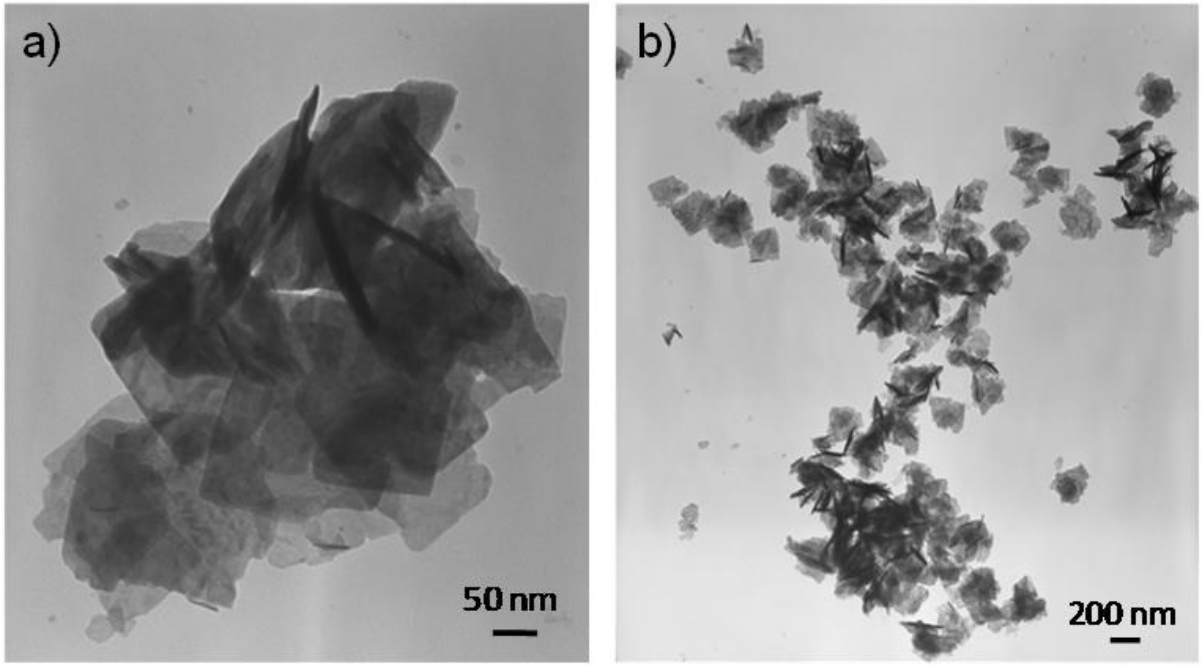

Figure 6.22. Typical agglomerated $WO_3 \cdot nH_2O$ nanoplatelets produced via the sol-gel method (a) high magnification; (b) low magnification.

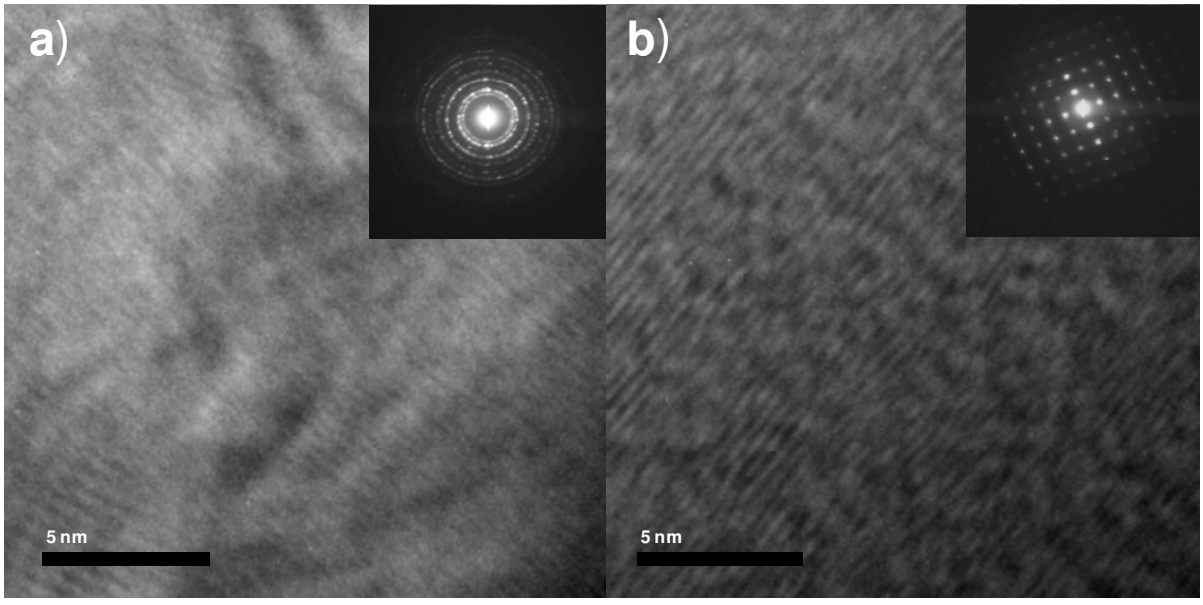

Figure 6.23. HRTEM images and corresponding SAED patterns of (a) tungsten oxide nanoplatelets dried at low humidity, and; (b) tungsten oxide nanoplatelets dried in a humid environment. Insets are the corresponding SAED patterns of the $WO_3 \cdot nH_2O$ nanoplatelet. All samples were processed at 8000 rpm with a flow rate of 1 mL/min.

Electron microscopy of the annealed samples revealed that they were well ordered and crystalline as shown in Figure 6.24 and Figure 6.25. High resolution transmission electron microscopy (HRTEM) observations suggested that the tungsten oxide nanoplatelets were formed from the coalescence of smaller tungstic acid precipitates (as described in Chapter 5), visible as raised areas in the HRTEM images. The corresponding SAED of the annealed samples consisted of many bright diffraction spots indicating that the nanoplatelets were highly crystalline. In all samples lattice fringes were observable, and were used to identify the respective phases of the annealed tungsten oxide samples. At an annealing temperature of 300 °C, tungsten oxide was calculated to have a lattice fringe d-spacing of 2.64 Å which is in excellent agreement with the (201) plane of monoclinic WO_3 (ICDD card file 75-2072). The sample annealed at 550 °C, exhibited a characteristic d-spacing of 3.79 Å, corresponding to the (020) plane of orthorhombic WO_3 (ICDD 71-0131).

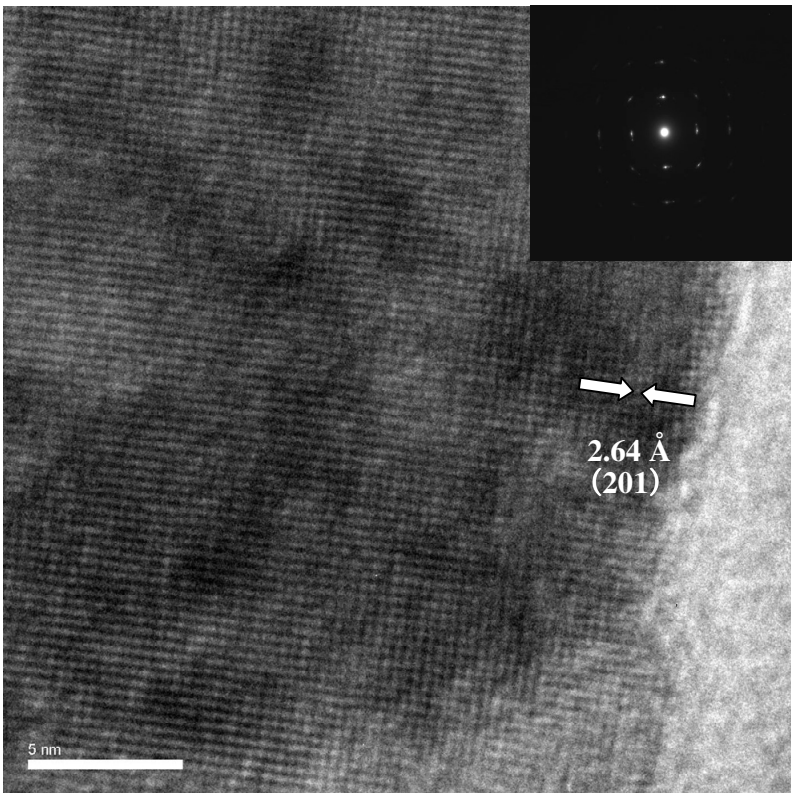

Figure 6.24. A typical sol-gel formed WO_3 nanoplatelet after annealing at 300 °C, inset SAED pattern.

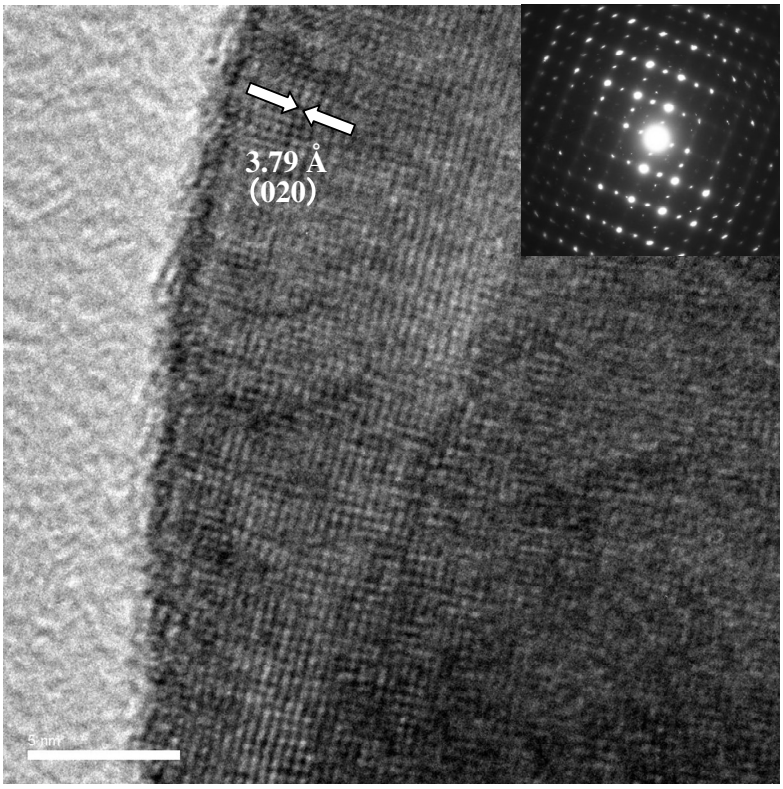

Figure 6.25. A typical sol-gel formed WO_3 nanoplatelet taken after annealing at 550 °C, inset SAED pattern.

6.3.7 XRD Analysis of Sol-gel Deposited Nanostructured Thin Films

Tungsten oxides are known to exist in a variety of different stoichiometries, hydration levels, and crystallographies. This presents a number of subtle complexities in the analysis of these materials, for clarity diffraction peaks were labeled with symbols presented in Table 6.1, indicating the corresponding ICCD reference. XRD patterns, presented in Figure 6.26, indicate that the "as prepared" sample contained tungsten oxide hydrates, with different degrees of hydration, i.e. $WO_3 \cdot nH_2O$; where n is typically: 0, ⅓, ½, 1 or 2.

Table 6.1. Sol-gel deposited nanostructured thin film XRD legend.

Symbol	Material	Crystal phase	ICCD card number
*	Tungsten oxide hydrate	Orthorhombic	84-0886
**	Tungsten oxide hydrate	Monoclinic	18-1420
***	Tungsten oxide hydrate	Monoclinic	89-0758
+	Tungsten trioxide	Orthorhombic	71-0131
-	Tungsten trioxide	Monoclinic	75-2072
#	Tungsten trioxide	Hexagonal	75-2187
%	Tungsten trioxide hydrate	Orthohombic	87-1203
^	Sodium nitrate	Rhombohedral	89-0311

The nanostructured thin films had a high degree of crystallinity as indicated by the sharp reflections which corresponded to the ICDD card files: 84-0886 (tungsten oxide hydrate), and 18-1420 (tungsten hydrogen oxide hydrate), and 89-0758 (tungsten oxide hydrate). These films were polymorphic matching primitive crystal systems; monoclinic with the addition of some minor orthorhombic characteristics. It should be noted that in these XRD measurements, a large area of the sample was measured, effectively collecting an average of the different crystal structures found throughout the material. The observed polymorphism in the XRD pattern is ascribed to the aqueous nature of the sol-gel preparative method. Annealing as deposited samples for 2 hrs in an oxygen rich atmosphere at 300 °C rendered the tungsten oxide hydrate to a monoclinic phase of WO_3, which was in good agreement with the ICCD cardfile 75-2072. Annealing at 550 °C generated multiple crystalline phases of WO_3, with the dominant crystallographic structure being orthorhombic (ICDD 71-0131). In addition to this: there are also some peaks, which are in good agreement with hexagonal WO_3 (ICDD 75-2187) and $WO_3 \cdot \frac{1}{3}H_2O$ (ICDD 87-1203).

It should be noted that in both annealed samples the presence of crystalline sodium nitrate (ICDD 89-0311) was observed. This material was formed as a byproduct of the reaction between sodium tungstate and nitric acid, sodium compounds were also identified using both Raman and XPS analyses.

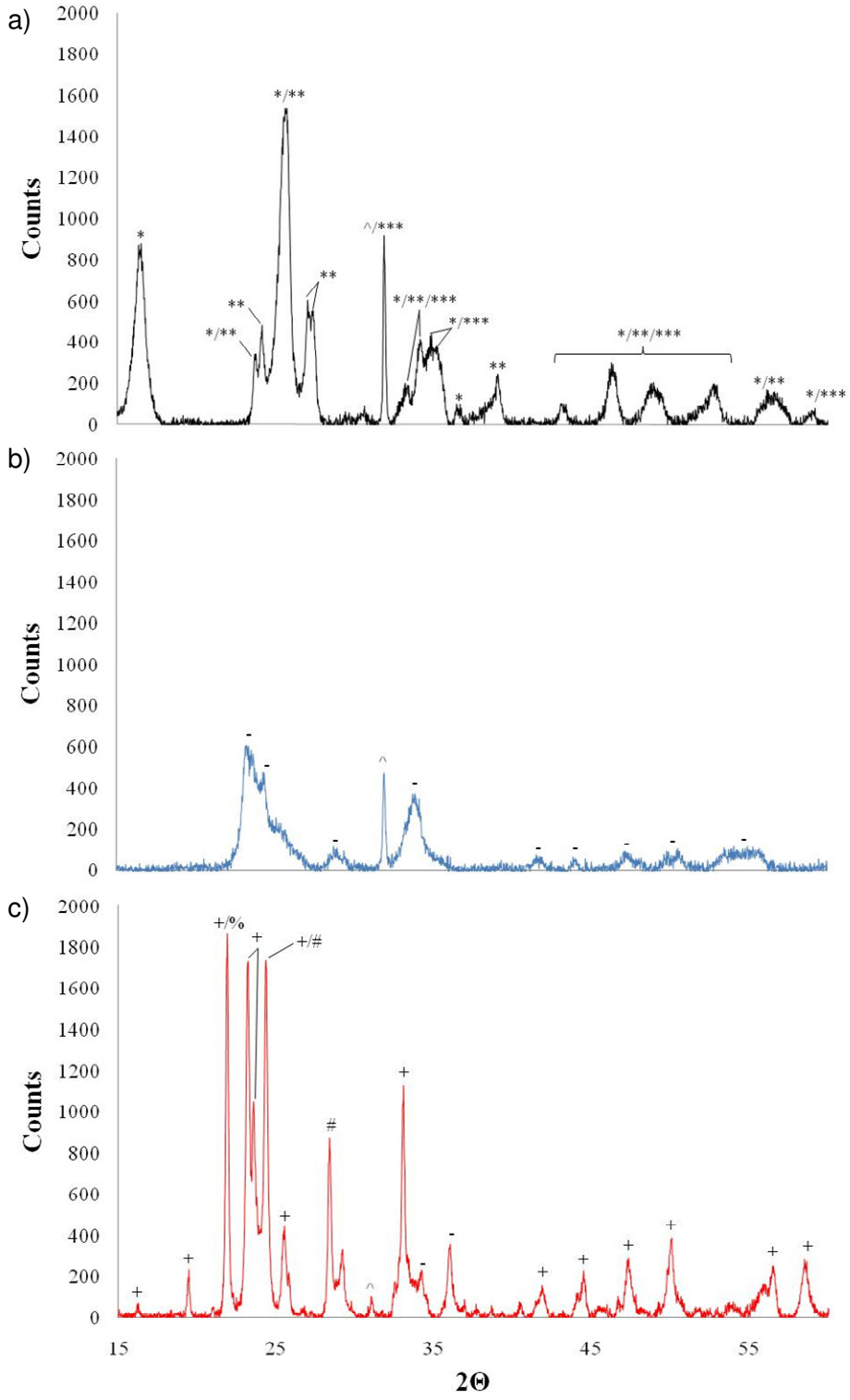

Figure 6.26. XRD diffraction patterns of sol-gel deposited nanostructured thin films (a) as prepared; (b) annealed at 300 °C; (c) annealed at 550 °C.

6.3.8 Raman Spectroscopy Analysis of Sol-gel Deposited Nanostructured Thin Films

Raman spectroscopy was employed to study the differences between the preparation methods before and after annealing. Tungsten trioxide exists as one of several allotropes in addition to a number of hydrates ($WO_3 \cdot nH_2O$) and Raman spectroscopy is well suited for their analysis [17-18]. The bending modes of WO_3 are located between 600 and 960 cm^{-1} while the stretching modes can be found between 200 and 500 cm^{-1}. Lattice modes of crystalline material have been reported below 200 cm^{-1} [17, 19]. However, due to the transmission properties of the notch filter used for these measurements, lattice modes could not be studied in this work.

Results for $WO_3 \cdot nH_2O$ treated in humid (as prepared) and dry environments (dried in air), as well as several as prepared samples annealed at 300 °C and 550 °C are presented in Figure 6.27 and Figure 6.28, respectively, where the vibrational modes associated with (WO_3 & $WO_3 \cdot nH_2O$) are evident. Measurements from dried in air and as prepared materials exhibit broad features with bands indicative of hydrated, so called amorphous or nanocrystalline $WO_3 \cdot nH_2O$ [17]. The peak observed at 378 cm^{-1}, which can be attributed to stretching modes arising from ($W\text{-}OH_2$), is also consistent with presence of $WO_3 \cdot nH_2O$ phases. Peaks arising from (OH) stretches were also observed (not shown) around 3200 cm^{-1} further supports this assignment. The band situated at 960 cm^{-1} has been attributed to the symmetric stretching mode of terminal (W^{6+}=O) groups and is often associated with $WO_3 \cdot nH_2O$ [17, 19]. For the as prepared sample, the band is resolved as a doublet at around 960 cm^{-1} was attributed to multiple and distinct (W^{6+}=O) groups, which may also be vibrationally coupled [20]. These peaks represent lattice discontinuities, which lead to short range (lattice) order. Bridging (O-W-O) vibrations, which occur around 700 cm^{-1}, are influenced significantly by hydration and as result, the 660 cm^{-1} band can be used as a spectral marker for the hydration level of WO_3 [17]. For the sample as prepared in Figure 6.23b, the broad transitions at 660 and 690 cm^{-1} resemble that of the di-hydrate ($WO_3 \cdot 2H_2O$) whereas the spectrum for the sample dried in air, which corresponds to a sample aged in a low humidity environment (Figure 6.23b), was attributed to the mono-hydrate ($WO_3 \cdot H_2O$) [17]. Care should be exercised using this approach since the crystalline hexagonal phase

WO_3 also exhibits bands at these frequencies but is likely to be absent in materials prepared without a thermal annealing step.

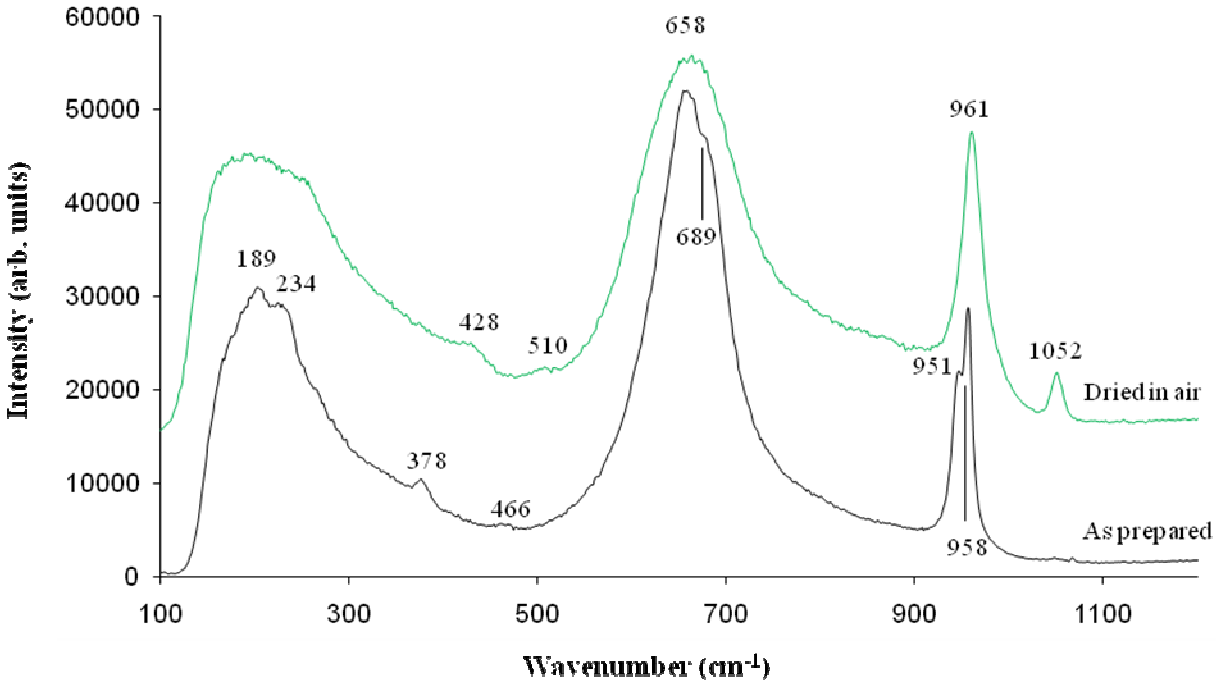

Figure 6.27. Representative room temperature Raman spectra of as prepared and dried in air $WO_3 \cdot nH_2O$ samples.

Several other bands also appeared in the spectra of these materials. For the sample dried in air, the band observed at 1052 cm^{-1} is not characteristic of $WO_3 \cdot nH_2O$ and is thought to originate from $NaNO_3$ which is known to crystallise at room temperature into an ordered rhombohedral (calcite) structure [21]. This salt likely forms during the reaction between nitric acid and sodium tungstate. Other weak transitions can also be seen at ~510 cm^{-1} and ~430 cm^{-1} and may be associated with tungsten peroxo groups [22] and water librations, respectively [17]. For the as prepared sample, the small peak at 466 cm^{-1} may be indicative of a reduced tungsten (W^{5+}=O) mode [23].

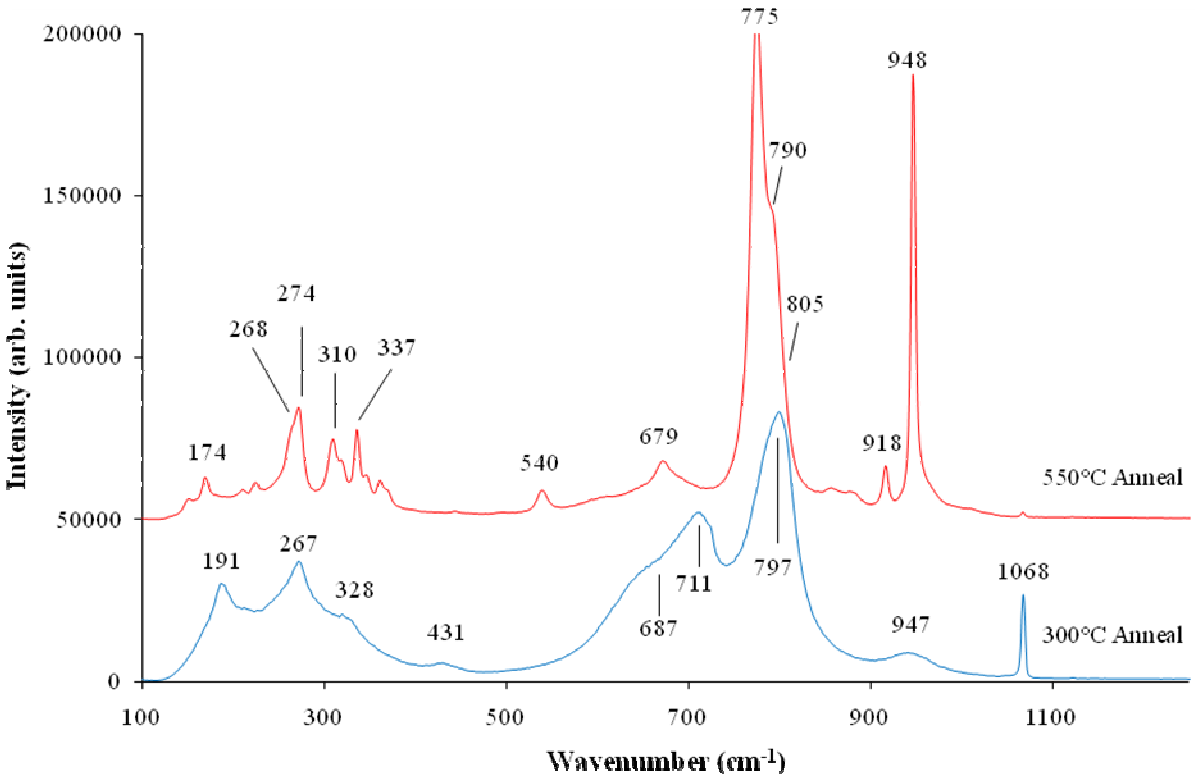

Figure 6.28. Representative room temperature Raman spectra of annealed WO_3 samples.

Following thermal treatment, the spectral features of these materials changed dramatically as observed in Figure 6.28, Raman bands became sharper, suggestive of an increase in both crystallinity and order. For the 300 °C annealed sample (Figure 6.28), the most intense peaks are located at 797 cm^{-1} and 711 cm^{-1}. Based on this, the dominant phase in this material was assigned as monoclinic WO_3 [17]. This is consistent with the known temperature dependent sequence for bulk WO_3 phase transitions [24]. The terminal (W^{6+}=O) stretching mode at ~950 cm^{-1} had been significantly reduced and replaced with bands at 797 cm^{-1} and 711 cm^{-1} with a shoulder at 687 cm^{-1}. These arise from (O-W-O) stretching modes in the WO_6 octahedral units [25]. The 711 cm^{-1} mode, which is sensitive to lattice distortion, had also shifted from ~689 cm^{-1} in the hydrated material, (c.f. Figure 6.27 and Figure 6.28) indicating that there has been a change in crystal symmetry following the annealing [26]. Residual di-hydrate phase likely remains as indicated by the 687 cm^{-1} band. Peaks at 267 cm^{-1} and 328 cm^{-1} can be ascribed to the corresponding δ(W-O-W) bending modes of the bridging oxygens [27]. The position of the ~270 cm^{-1} band can be used to estimate the crystalline grain size [28] which

in this work, corresponds to ~35 nm. Residual intensity in the $\upsilon(W^{6+}=O)$ mode also supports the assignment of mixed phases (eg. hydrated and crystalline) in this material. Peaks located at 191 cm^{-1} and 1068 cm^{-1} likely result from lattice vibrations of WO_3 and residual $NaNO_3$, respectively.

Similarly, following annealing at 550 °C, there is a further reduction in the spectral linewidth consistent with greater crystalline phase formation. Well defined bands arising from the hydrous $WO_3 \cdot \frac{1}{3}H_2O$ phase (948 cm^{-1}, 805 cm^{-1}, 679 cm^{-1}, 337 $cm^{-1}$and 268 cm^{-1}) are present in this material [17]. Other bands at 790 cm^{-1}, 775 cm^{-1} and 679 cm^{-1} may be indicative of the hexagonal WO_3 phase [26]. The weaker band at 918 cm^{-1} can be assigned to either a hydrous phase or, more likely, a sodium tungstate phase [26] which is consistent with the observed reduction in the 1068 cm^{-1} $NaNO_3$ band. There is also evidence for tungsten-peroxo bonds with a band at 540 cm^{-1} [22]. Grain size analysis for this material [28] using the δ(W-O-W) mode was complicated due to the presence of overlapping peaks from 268 cm^{-1} to 274 cm^{-1} indicating that there is a range of grain sizes in this material.

6.3.9 XPS Analysis of Sol-gel Deposited Nanostructured Thin Films

XPS survey studies of as deposited and annealed samples presented in Figure 6.29a, reveal the presence of tungsten, oxygen, sodium, and (adventitious) carbon. Spectra of O1s and W4f7 peaks are presented in Figure 6.29b and Figure 6.29c, respectively. As discussed previously, the Na1s peak at 1072 eV is due to byproducts of the sodium tungstate precursor.

The O1s spectra of the as prepared sample shows a smaller peak occurring at 533.2 eV labeled (I) in Figure 6.29b at a higher binding energy compared to the main peak at 531eV. The peak position is in good agreement with binding energies previously identified with oxygen atoms in H_2O molecules bound with/in WO_3 [29]. This weak oxygen peak (I) located at 533.1 eV disappears as samples were annealed and water was liberated from the sample. The position of peak (II) at 530.6 eV, which corresponds to (W=O) bonding modes, remains static and intensifies after annealing, suggesting that the tungsten in the tungsten oxide hydrate sample exists as W^{6+}.

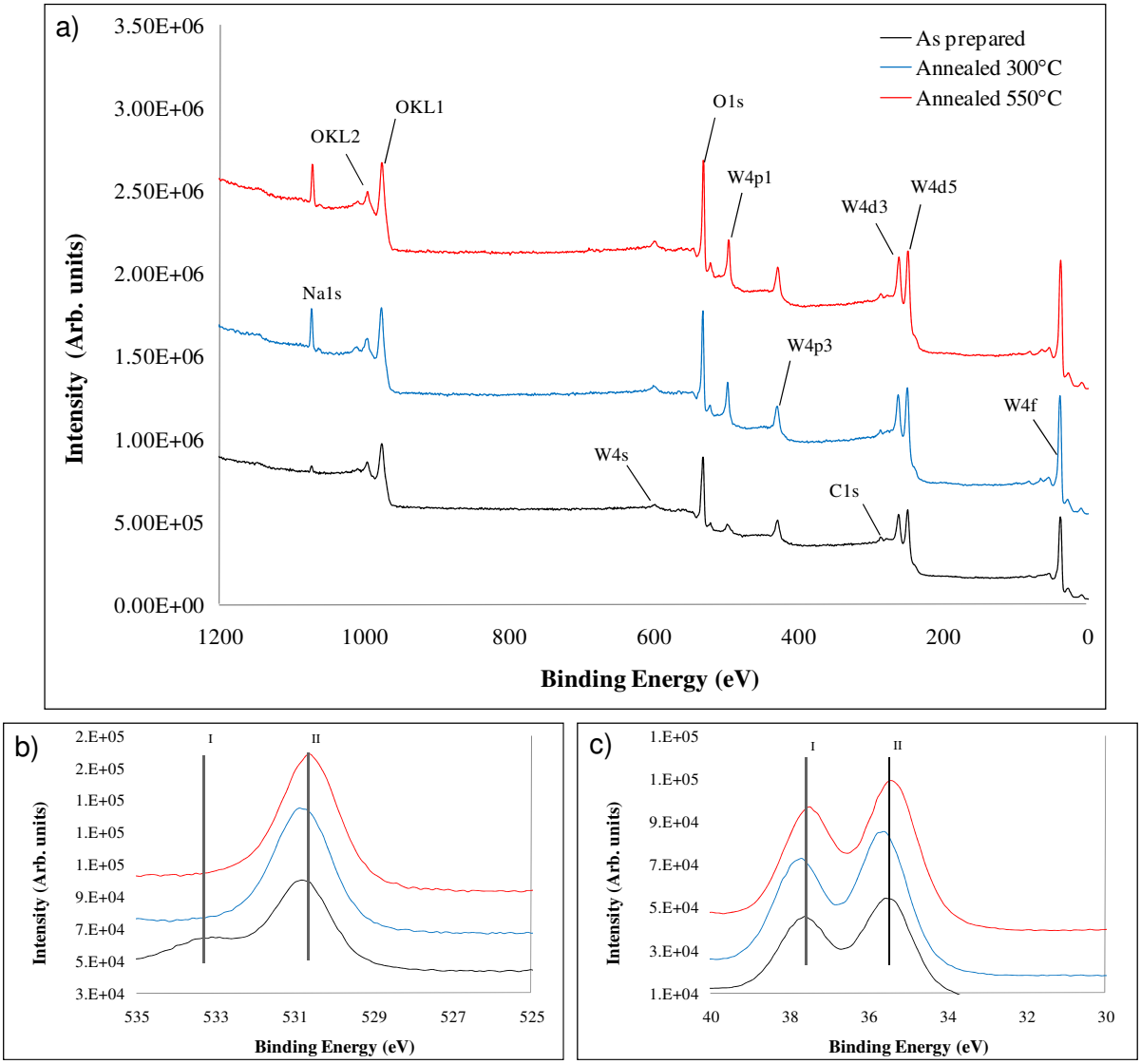

Figure 6.29. XPS spectra of sol-gel deposited nanostructured $WO_3 \cdot nH_2O$ and WO_3 thin films: (a) survey spectrum; (b) O1s spectrum; (c) W4f spectrum.

The W4f orbital is clearly resolved into W4f5/2 and W4f7/2 contributions, centered upon 37.5 eV (I) and 35.4 eV (II), respectively. There was no evidence of the formation of sub-stoichiometric WO_{3-x} owing to the absence of W^{5+} peaks, typically occuring at 34.8 eV [29]. The results presented in Figure 6.29 are in good agreement with previously identified stoichiometric WO_3 (W^{6+}) [30-31].

6.4 Chapter Summary

In this chapter the material characterisation of ZnO, $WO_3 \cdot nH_2O$ and WO_3 nanostructured thin films were presented. Briefly;

ZnO nanostructured arrays were grown from RF sputtered ZnO seed/nucleation layers placed in a NaOH based growth solution. This yielded an unusual corrugated ZnO nanorod morphology which was reported for the first time from Zn^{2+} / NaOH solutions. However the long deposition time required for the formation of a 3-5 μm seed/nucleation layer, coupled with the high initial growth solution pH hampered the growth of ZnO nanostructured thin films, as a result the NaOH method was later replaced by the HMT method.

Seed/nucleation layer choice was investigated by placing RF sputtered and spray pyrolysis deposited seed/nucleation layers into the HMT growth solutions. It was observed that nanostructured thin films originating from ZnO crystallites with hemispherical tips as deposited by the RF sputtering method, typically grew in nanorod arrays perpendicular to the substrates surface. Whereas the rougher polygonal seed/nucleation layers deposited via spray pyrolysis resulted in the formation of interconnected ZnO nanowires. XRD analyses revealed that samples were predominately ZnO with some minor peak(s) contributed by zinc hydroxide, with the hydrothermally grown ZnO nanostructures from seed/nucleation layers found to adopt the crystallography of the underlying seed/nucleation layer. At present, the interconnected ZnO nanostructures do not form contiguous networks, however, it may be possible to engineer interconnects with well-defined orientations by selectively patterning the seed/nucleation layer surface. By photo-lithographically patterning the underlying substrate, and etching patterns appropriately after spray pyrolysis, it may be possible to implement the observed interconnectivity for next generation nanodimensional electronic devices.

Experimental evidence of seed/nucleation layer etching caused by the HMT growth solution has been established with cross-sectional TEM studies, indicating that the initial thickness of the seed/nucleation layer is important for maintaining a contiguous protective underlying seed/nucleation layer. Without this protective layer metal contacts, deposited onto the ZnO nanostructured thin films,

may extend to the underlying GaN layer, creating an electrical short circuit, disrupting device operation. It is believed that the combination of a ZnO morphology with a thin protective ZnO seed/nucleation layer when coupled with GaN epitaxial layers will yield furtive research opportunities to enhance performance of electronic and optical devices such as: light emitting diodes, photodetectors, laser and Schottky diode based gas sensors.

The formation of tungsten oxide hydrates was explored via acid precipitation, a SILAR growth method and a sol-gel method, with the former two methods developed by the author as part of his PhD research activities. The author established a link between aging samples in dry atmospheres and humid atmospheres and the crystallinity and morphology of the resultant nanoplatelets. Characterisation of sol-gel deposited material via complimentary analysis confirmed that freshly deposited samples were $WO_3 \cdot nH_2O$ with varying hydration levels, dependent upon the humidity of the environment they were dried in. Similarly, samples annealed at 300 °C were assigned as monoclinic, with Raman analysis indicating incomplete dehydration. Samples annealed at 550 °C were found to be predominately orthorhombic with evidence of other minor crystallographies present as indicated by the XRD and Raman analyses, with spectral evidence of a $WO_3 \cdot \frac{1}{3}H_2O$, despite 2 hrs annealing at 550 °C. The presence of water primarily detected by Raman spectroscopy has been ascribed to the hygroscopic action of freshly annealed nanostructured thin films.

6.5 References

[1] M. Breedon, *et al.*, "Synthesis of nanostructured tungsten oxide thin films: A simple, controllable, inexpensive, aqueous sol-gel method," *Crystal Growth and Design,* vol. 10, pp. 430-439, 2010.

[2] M. Breedon, *et al.*, "ZnO nanostructures grown on epitaxial GaN," *First International Symposium on Transparent Conducting Oxides,* vol. 518, pp. 1053-1056, 2009.

[3] M. Rahmani, Breedon, M., Keshmiri, S., Moafie, A., McCoulloch, D., Wlodarski, W., Kalantar-zadeh, K., "Gas Sensing Properties of Interconnected ZnO Nanowires," *Sensors and Actuators B: Chemical,* Under Review, 2010.

[4] G. Madras and B. J. McCoy, "Temperature effects during Ostwald ripening," *The Journal of Chemical Physics,* vol. 119, pp. 1683-1693, 2003.

[5] R. B. Peterson, *et al.*, "Epitaxial Chemical Deposition of ZnO Nanocolumns from NaOH Solutions," *Langmuir,* vol. 20, pp. 5114-5118, 2004.

[6] J. W. Sun, *et al.*, "Excitonic electroluminescence from ZnO-based heterojunction light emitting diodes," *Journal of Physics D: Applied Physics,* vol. 41, p. 155103, 2008.

[7] D. C. Oh, *et al.*, "Capacitance-voltage characteristics of ZnO/GaN heterostructures," *Applied Physics Letters,* vol. 87, p. 162104, 2005.

[8] N. Zhang, *et al.*, "Investigation of electrical and ammonia sensing characteristics of Schottky barrier diode based on a single ultra-long ZnO nanorod," *Applied Surface Science,* vol. 254, pp. 5736-5740, 2008.

[9] B. P. Luther, *et al.*, "High temperature Pt Schottky diode gas sensors on n-type GaN," *Sensors and Actuators B: Chemical,* vol. 56, pp. 164-168, 1999.

[10] J. Schalwig, *et al.*, "Group III-nitride-based gas sensors for combustion monitoring," *Materials Science and Engineering B,* vol. 93, pp. 207-214, 2002.

[11] M. Ali, *et al.*, "A study of hydrogen sensing performance of Pt-GaN Schottky diodes," *IEEE Sensors Journal,* vol. 6, pp. 1115-1119, 2006.

[12] J.-M. Jang, *et al.*, "Synthesis of ZnO nanorods on GaN epitaxial layer and Si(100) substrate using a simple hydrothermal process," *Thin Solid Films,* vol. 516, pp. 8524-8529, 2008.

[13] J.-M. Jang, *et al.*, "ZnO 3D flower-like nanostructure synthesized on GaN epitaxial layer by simple route hydrothermal process," *Journal of Alloys and Compounds,* vol. 463, pp. 503-510, 2008.

[14] J.-M. Jang, *et al.*, "Synthesis of ZnO flower-like nanostructures on GaN epitaxial layer by hydrothermal process," *Solid State Phenomena*, vol.124-126, pp. 555-558, 2007.

[15] C. V. Ramana, *et al.*, "Structural Stability and Phase Transitions in WO_3 Thin Films," *Journal of Physical Chemistry B,* vol. 110, pp. 10430-10435, 2006.

[16] Ahmad Al-Mohammad, "Microstructural analysis and electrical conductivity of hexagonal WO_3 thin films during annealing," *Physica status solidi a- Applied Research,* vol. 205, pp. 2880-2885, 2008.

[17] M. F. Daniel, *et al.*, "Infrared and Raman study of WO_3 tungsten trioxides and WO_3, xH_2O tungsten trioxide hydrates," *Journal of Solid State Chemistry,* vol. 67, pp. 235-247, 1987.

[18] E. Salje, "Lattice-dynamics of WO_3," *Acta Crystallographica Section A,* vol. A 31, pp. 360-363, 1975.

[19] K. Nonaka, *et al.*, "Raman-spectra of sol gel-derived tungsten-oxides," *Journal of Materials Science Letters,* vol. 12, pp. 274-277, 1993.

[20] G. J. Fang, *et al.*, "Preparation and electrochromic properties of nanocrystalline WO_3 thin films prepared by pulsed excimer laser ablation technique," *Physica Status Solidi a-Applied Research,* vol. 184, pp. 129-137, 2001.

[21] R. W. Berg and D. H. Kerridge, "The $NaNO_3/KNO_3$ system: the position of the solidus and sub-solidus," *Dalton Transactions,* pp. 2224-2229, 2004.

[22] B. Pecquenard, *et al.*, "Orthorhombic WO_3 Formed via a Ti-Stabilized $WO_3 \cdot H_2O$ Phase," *Journal of Solid State Chemistry,* vol. 135, pp. 159-168, 1998.

[23] S.-H. Lee, *et al.*, "Raman spectroscopic studies of gasochromic a-WO_3 thin films," *Electrochimica Acta,* vol. 46, pp. 1995-1999, 2001.

[24] A. G. Souza-Filho, *et al.*, "Coexistence of triclinic and monoclinic phases in WO_3 ceramics," *Journal of Raman Spectroscopy,* vol. 31, pp. 451-454, 2000.

[25] A. Anderson, "Raman Study of Ceramic Tungsten Trioxide at Low Temperatures," *Spectroscopy Letters: An International Journal for Rapid Communication,* vol. 9, pp. 809 - 819, 1976.

[26] A. Cremonesi, *et al.*, "WO_3 thin films by sol-gel for electrochromic applications," *Journal of Non-Crystalline Solids,* vol. 345-346, pp. 500-504, 2004.

[27] Franklin D. Hardcastle and Israel E. Wachs, "Determination of the molecular structures of tungstates by Raman spectroscopy," *Journal of Raman Spectroscopy,* vol. 26, pp. 397-405, 1995.

[28] M. Boulova and G. Lucazeau, "Crystallite Nanosize Effect on the Structural Transitions of WO_3 Studied by Raman Spectroscopy," *Journal of Solid State Chemistry,* vol. 167, pp. 425-434, 2002.

[29] A. P. Shpak, *et al.*, "XPS studies of active elements surface of gas sensors based on WO_{3-x} nanoparticles," *Journal of Electron Spectroscopy and Related Phenomena,* vol. 156-158, pp. 172-175, 2007.

[30] S. F. Ho, *et al.*, "Ion-beam-induced chemical changes in the oxyanions (CrOYN-, MoOYN-, WOYN-, VOYN-, NbOYN-, AND TaOYN-) and oxides (CrO_X, MoO_X, WO_X, VO_X, NbO_X, AND TaO_X)," *Journal of Physical Chemistry,* vol. 91, pp. 4779-4788, 1987.

[31] F. P. J. M. Kerkhof, *et al.*, "The XPS spectra of the metathesis catalyst tungsten oxide on silica gel," *Journal of Electron Spectroscopy and Related Phenomena,* vol. 14, pp. 453-466, 1978.

Chapter 7 - Gas Sensor Preparation and Testing

In this chapter, the experimental methodology and gas sensing results of devices based on the author's synthesised nanomaterials will be presented. The custom designed gas sensor calibration system was used for benchmarking the developed gas sensors with respect to time, gas concentration and operational temperature. The gas sensing characteristics were analysed and assessed for their potential in realistic sensing environments.

Sensors based on two different sensing technologies were investigated, the first being conductometric, taking advantage of carrier concentration changes of ZnO and WO_3; and the second optical, utilising the gasochromic properties of WO_3. Testing methodologies will be presented, with a focus on theoretically predicted sensor behaviour and experimental trends, where applicable. Sensing data will first be presented as direct sensor output signal such as resistance or transmission, and later compiled into comparison matrix of the developed sensors' specifics such as: sensitivity, dynamic range, response and recovery time, and optimal operating temperatures.

7.1 Gas Testing System

A programmable mass flow controller operated via a PC link was responsible for flow control and mixing of synthetic air carrier gases certified gas sources from National Institute of Standards and Technologies (NIST) certified suppliers containing either 9.9 ppm NO_2 or 1% (10000 ppm) H_2 in a balance of synthetic air. The operating temperature of the sensors was controlled with a ceramic heating element, managed by the control computer to maintain a range of temperatures from 25 °C to 300 °C. Operating temperatures were recorded with a K-type thermocouple and PC data logging software. Two different gas testing setups were utilised for gas sensor testing and calibration. Both systems shared a common mass flow control system, a control computer and NIST certified gas sources as seen in Figure 7.1. The first system was, a conductometric testing system as schematically presented in Figure 7.2 and Figure 7.3; and the second, an optical system as seen in Figure 7.4. Prior to testing samples were pre-conditioned and stabilised in a stream of synthetic air for at least one hour.

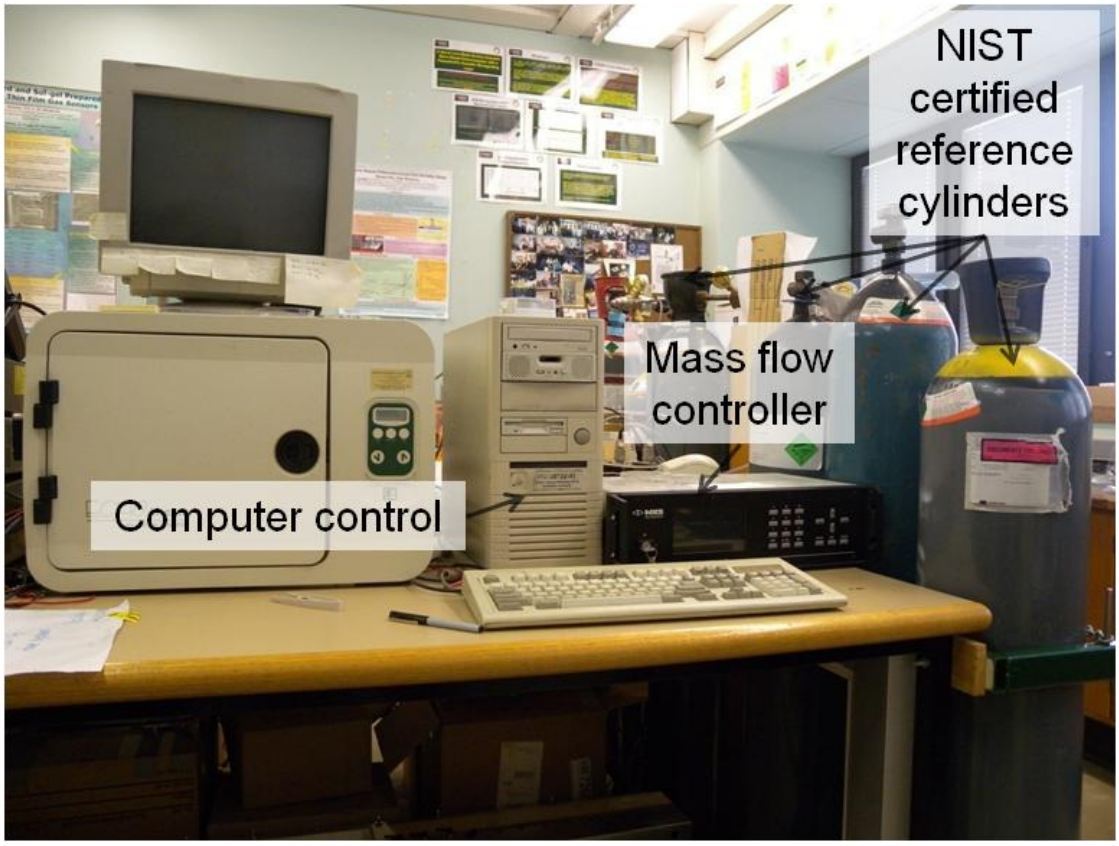

Figure 7.1. Photograph of the gas sensor calibration and testing system, with conductometric gas testing chamber.

7.1.1 Conductometric Gas Sensing System

The computer control system featured in Figure 7.1 was used to govern an Agilent E3649A dual output DC power supply, controlling the gas sensor operating temperature via a ceramic heating element. The control computer was also utilised for timed gas pulse sequences, via a serial communication link to the mass flow controller. The MKS Instruments 647B four channel mass flow controller mixed gases from certified cylinders to a total output flow of 200 sccm, delivered to the gas sensing cell (Figure 7.3 and Figure 7.4). This was carried out in a sequence of increasing concentrations followed by a final pulse of low concentration analyte to examine any sensor baseline instabilities that may exist. A high accuracy Keithly 2001 Multimeter was used to record changes in sensor resistance. A schematic representation of the conductometric gas sensor calibration and testing system is presented in Figure 7.2.

Sensor sensitivity (S) throughout this thesis was calculated via the following equations:

For reducing gases (H_2)

$$S = \frac{R_{air} - R_{gas}}{R_{gas}} \tag{7.1}$$

For oxidising gases (NO_2)

$$S = \frac{R_{gas} - R_{air}}{R_{air}} \tag{7.2}$$

where the baseline resistance of the sensor in synthetic air is R_{air}; and the resistance of the sensor in the target analyte is R_{gas}. Response and recovery time will be reported as $t_{90\%}$ values, unless otherwise noted.

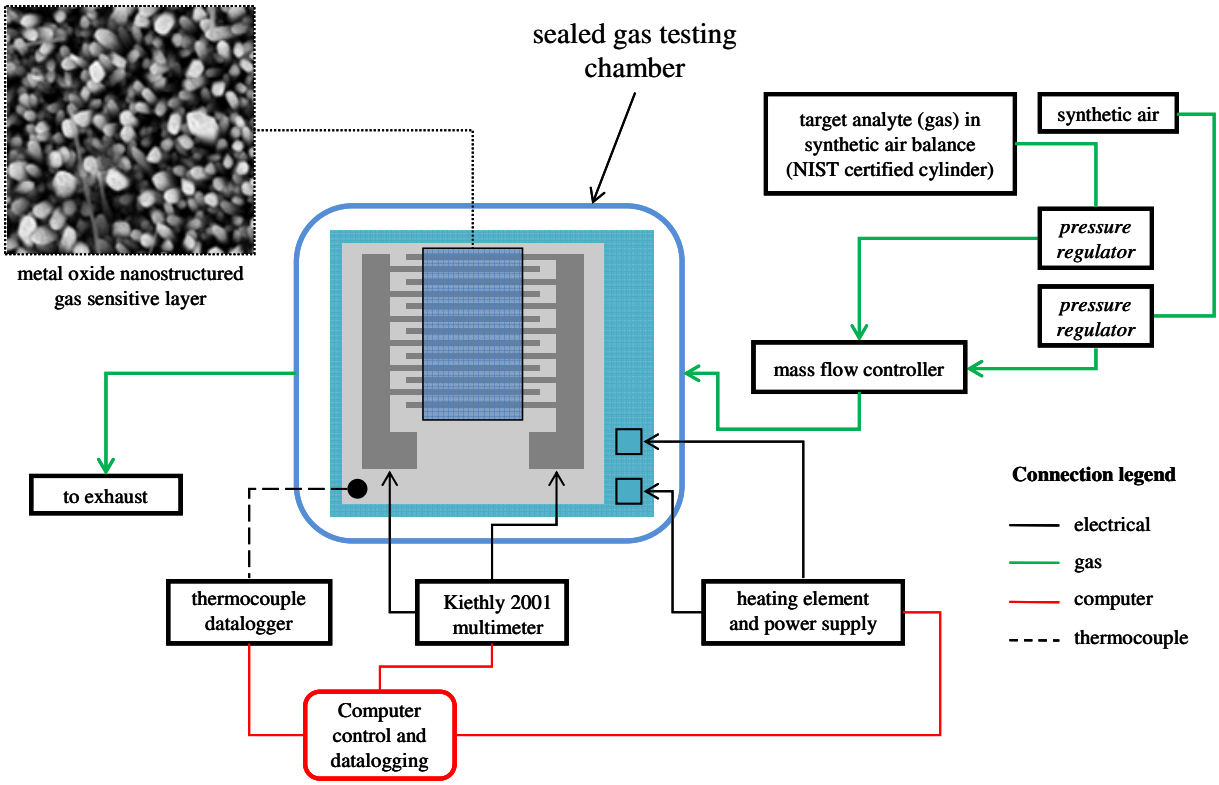

Figure 7.2. Conductometric gas sensor calibration and testing system.

The orthographic schematic of the conductometric gas sensing cell used by the author is presented in Figure 7.3. This gas sensing cell is comprised of a machined Teflon block, recessed to facilitate the ceramic heater and electrical feed throughs for the multimeter, heater power supply and thermocouple.

An o-ring is placed in between the torque plate and the Teflon block which is used to create a crush seal between the Teflon block and the borosilicate glass lid, creating a gas-tight seal.

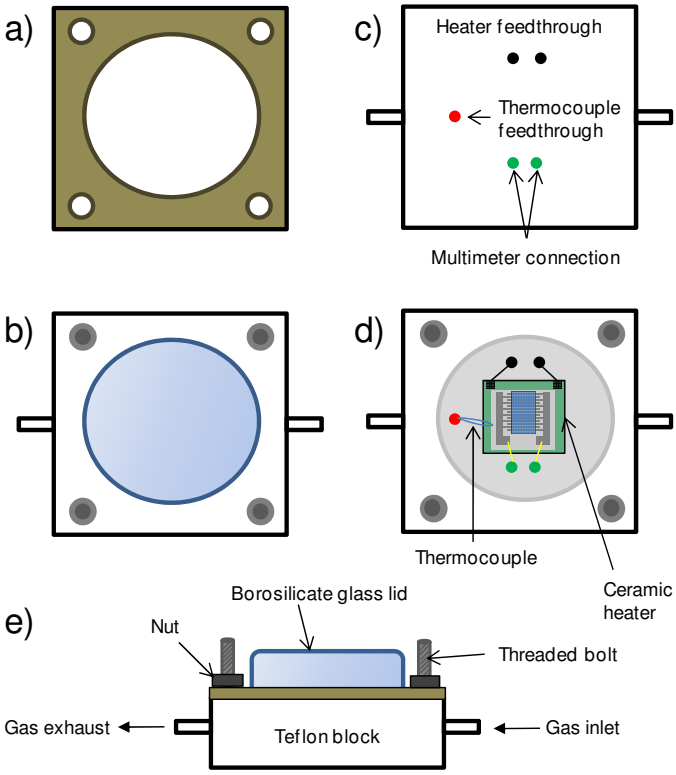

Figure 7.3. Orthographic schematic of the gas sensing cell (a) sealing torque plate; (b) top view; (c) bottom view; (d) top view with lid removed; (e) side view.

7.1.2 Optical Gas Testing System

H_2 absorption spectra of WO_3 nanotextured films on quartz were examined using a spectrophotometer system consisting of a Micropack DH-2000 UV-VIS-NIR light source and an Oceanoptics HR4000 spectrophotometer connected to via USB link to a PC. The analysis was performed using Spectrasuite 2007 edition software. This setup was attached to a computer controlled gas calibration system introduced in § 7.1. Measurements were carried out in the custom gas testing chamber as shown in Figure 7.4. The aluminium chamber had two quartz windows aligned to permit a light path through the semi-transparent sample. Sub-minature A (SMA) connector collimator lenses connected to 1 mm core UV-Vis-NIR fiber optic cables which were used to admit and capture light in the testing chamber.

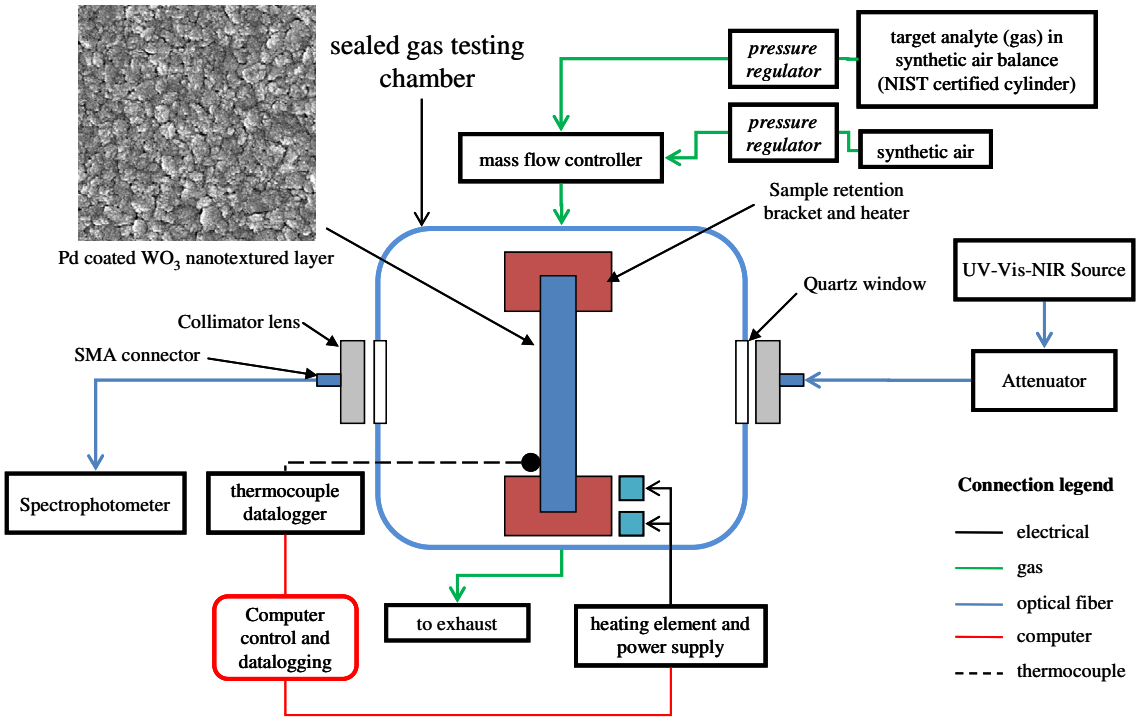

Figure 7.4. Optical gas sensor calibration system.

7.2 Conductometric and Optical Gas Sensors

As previously discussed in Chapter 1, conductometric sensors are amongst the most popular sensing platforms. Each planar conductometric sensor comprises of four elements: (1) insulating substrate, capable of providing mechanical support; (2) heater, typically located underneath the substrate in either fixed or external configurations; (3) the interdigitated electrode pairs, with suitably large contact pads, which are used for resistance measurements of the metal oxide sensing layer; and finally (4) the gas sensitive metal oxide itself.

The planar conductometric transducers used throughout this thesis were fabricated at RMIT University's Microelectronics and Materials Technology Centre. Each conductometric sensor consisted of 38 electrode interdigitated electrode pairs (80 nm gold on a 20 nm titanium adhesion layer) with an interspacing of 40 µm deposited onto an 11 × 11 mm $LiNbO_3$ substrate, with the exception of the interconnected ZnO nanowire based sensor which was deposited onto an 11 × 11 mm glass substrate. Electrical connections to the sensors were established via conductive silver epoxy

affixed gold wires, attached at the contact pads of the transducers. For the interconnected ZnO nanowire sensor, a shadow mask was used to deposit contact pads along two edges of the nanostructured thin film, which was then be bonded with gold wire and conductive silver epoxy.

Optical gas sensors represent a promising technology as they are immune to electromagnetic interference, and are often compatible with fiber optic cable infrastructure allowing the deployment of inexpensive remote sensing installations with spectrophotometers or photodiodes used to measure changes in the absorbance profile of the sensor being positioned some kilometres away from the sensing region.

Optical sensors, which are studied in this thesis, exploit the gasochromic transition of tungsten trioxide (WO_3) that is a well established metal oxide for gas sensing applications. Many studies have identified WO_3 as a promising candidate for gasochromic platform based sensing devices [1-3]. It has been widely reported that when exposed to H_2, WO_3 undergoes a reversible colour change (gasochromism) from transparent to dark blue, especially when combined with catalytic metals such as Pt, Pd and Au [4-5]. As the sensing mechanism for gasochromic materials are governed by the optical characteristics of the sensing material, it is important to develop a high surface area material with high transparency, low roughness and excellent uniformity. RF sputtered WO_3 is an ideal candidate with low roughness, high transparency nanotextured grain morphology, easily controllable thickness and therefore, ideal absorbance characteristics. The developed 11 × 11 mm gasochromic Pt/WO_3 sensor was based on a 1 mm thick quartz substrate coated with a 1.2 μm WO_3 layer, which in turn was coated with a 2.5 nm Pt catalytic layer. This work resulted in the publication of a co-authored paper [6].

7.3 General Gas Adsorption Equations for Conductometric Gas Sensing

As was previously discussed in Chapters 3 and 4 the adsorption process of NO_x on ZnO($2\bar{1}\bar{1}0$) that occurs during gas sensing is complex. In this section, a simplified perspective of gas sensing often given in semiconductor and engineering texts will be presented, primarily concerned with the movement of electrons/carriers.

At temperatures of between 100 °C and 500 °C the gas sensing element is capable of interacting with ambient oxygen, leading to its adsorption in either molecular or atomic forms [7]. At room temperature O_2 is physisorbed on the metal oxide surface. However, at a transition threshold of approximately 150 °C or greater, all oxygen species exist in their chemisorbed forms, i.e. O_2^-, O^-, O^{2-} [8], as summarised in the following equations [8-10]:

$$O_{2(ads)} + e^- \underset{k_2}{\overset{k_1}{\rightleftharpoons}} O_2^-{}_{(ads)} \qquad \text{occurs ~ 100 °C – 150 °C} \tag{7.3}$$

$$O_{2(ads)} + 2e^- \underset{k_2}{\overset{k_1}{\rightleftharpoons}} 2O^-{}_{(ads)} \qquad \text{occurs ~150 °C – 350 °C} \tag{7.4}$$

$$O^-{}_{(ads)} + e^- \underset{k_2}{\overset{k_1}{\rightleftharpoons}} O^{2-}{}_{(ads)} \qquad \text{occurs ~350 °C – 500 °C} \tag{7.5}$$

The adsorption of NO_2 (a strong oxidising gas) onto ZnO has been discussed in Chapter 4. However, the adsorption of NO_2 onto WO_3 is suggested to occur directly with the WO_3 crystal surface, as summarised in the following equation [11]:

$$NO_{2(gas)} + e^- \underset{k_2}{\overset{k_1}{\rightleftharpoons}} NO_2^-{}_{(ads)} \tag{7.6}$$

While other adsorption reactions exist for the adsorption of NO_x species onto metal oxide surfaces as noted by Rutherland *et al.* [8] at temperatures typically less than 200 °C (as is the case of WO_3 based sensor presented in this thesis) NO_2 adsorbs directly onto WO_3 surfaces as per (7.6), either associatively physisorbing or chemisorbing, and does not interact with the adsorbed oxygen surface species that exist at this temperature.

The adsorption of a reducing gas such as H_2, on a metal oxide surface, is mediated by the presence of pre-adsorbed oxygen species. This reaction can be written for associatively chemisorbed hydrogen (7.7) or dissociatively chemisorbed hydrogen (7.8), with the surface energy of the metal oxide in question playing a role in the type of adsorption. Regardless, the reaction product of the adsorption

reaction yields water vapour and electrons/carriers which are donated to the surface, decreasing the sensing element resistance [10].

The reaction of H_2 (a reducing gas) onto a metal oxide semiconductor surface (ZnO and WO_3) occurs via one or more adsorbed oxygen species, as per one of the following equations [10]:

$$H_{2(ads)} + O_2^{-}{}_{(ads)} \underset{k_2}{\overset{k_1}{\rightleftharpoons}} H_2O_{(gas)} + 2e^- \tag{7.7}$$

$$2H^{+}{}_{(ads)} + O^{-}{}_{(ads)} \underset{k_2}{\overset{k_1}{\rightleftharpoons}} H_2O_{(gas)} + e^- \tag{7.8}$$

7.4 ZnO Nanostructured Thin Films

ZnO nanostructured thin films were formed via aqueous methods as previously described in Chapter 5 and were tested towards NO_2 and H_2 gases. As previously discussed in Chapter 4, ZnO($2\bar{1}\bar{1}0$) containing materials are predicted to have excellent NO_2 sensing capabilities due to large transfer of charge from the surface to the NO_2 molecule, and many stable adsorption configurations. Two different nanostructured ZnO arrays were used in the preparation of two sensors containing ZnO($2\bar{1}\bar{1}0$), ZnO nanorods and nanowires.

7.4.1 Conductometric Response of ZnO Nanorods Towards NO_2

The dynamic response of ZnO nanostructured thin films consisting of nanorod arrays operating at 230 °C towards NO_2 is presented in Figure 7.5. The sensor was prepared by depositing a ZnO nanorod array based thin film onto a $LiNbO_3$ substrate with IDT electrode pairs. Previous theoretical studies presented in Chapter 4 indicated the excellent compatibility of ZnO($2\bar{1}\bar{1}0$); one of two major crystal facets present on ZnO nanorods, as NO_2 sensing surfaces. Bader charge calculations predicted a transferral of charge from the surface to the adsorbed NO_2, which should result in an increase in sensor resistance. As can be seen in Figure 7.5, each exposure of the sensor to NO_2 increases resistance, in good agreement with previously calculated charge transfer characteristics. It should be noted that changes in resistance are not solely due to the adsorption of NO_2, other contributing factors such as pre-adsorbed molecules and water vapour also play a role in sensor conductivity.

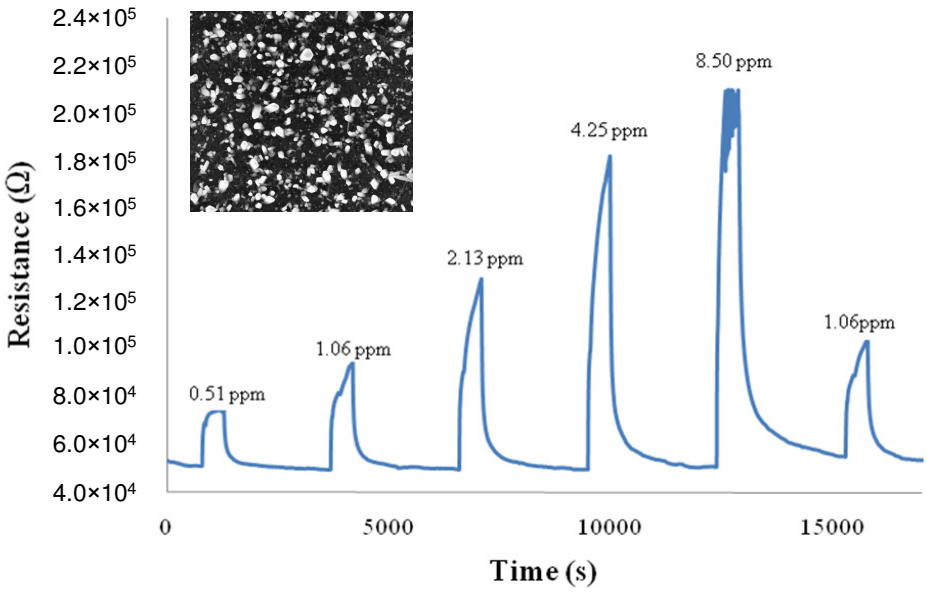

Figure 7.5. Dynamic response of ZnO nanorod arrays at 230 °C at different concentrations of NO_2, inset morphology of the gas sensitive layer.

During exposure to 8.50 ppm NO_2 output signal instability was observed, however, the sensor remained functional. As a result, the developed sensor is suitable for NO_2 sensing analyte concentrations below 8.50 ppm. The ZnO nanorod sensor was calculated to have an NO_2 sensitivity of 3.0, a value higher than any of the developed NO_2 sensors presented in this thesis. Efficient operation was also reflected in the response and recovery time of 152 s and 508 s, respectively at 8.5 ppm. While at a lower concentration of 510 ppb the response and recovery time of the sensor was 91 s and 280 s, respectively.

The developed nanorod based sensor compares favourably with Cho *et al.* [12] reporting that dispersed ZnO nanorods can be used to detect NO_2 at 1 ppm concentrations at 300 °C with a $t_{90\%}$ response time of approximately 180 seconds. The developed sensor is capable of sensing lower concentrations, at lower temperatures, with a faster response time. Using similar hydrothermally grown ZnO nanorods Liu *et al.* [13] have also demonstrated NO_2 sensing over a wide range concentrations of 0.2 ppm to 5.0 ppm at 250°C in a N_2 atmosphere, however response and recovery times were not available for comparison. Sadek *et al.* [10] report on the application of ZnO nanobelts for NO_2 sensing, with an NO_2 concentration of 1 ppm, at 350 °C in air, the $t_{90\%}$ response and recovery

time of 180 s and 208 s, respectively. Clearly the developed sensor is capable of sensing lower concentrations in a little under half the time of a nanobelt based sensor.

7.4.2 Conductometric Response of Interconnected ZnO Nanowire Arrays Towards NO_2

Given the pre-established suitability of ZnO nanostructures for NO_2 sensing applications, arrays of interconnected ZnO nanowires were synthesised and tested towards NO_2. The dynamic response of ZnO nanostructured thin films consisting of interconnected nanowires arrays operating at 135 °C towards NO_2 is presented in Figure 7.6. The sensors was prepared by depositing an interconnected ZnO nanowire based thin film onto a glass substrate, and depositing electrodes at either end of the device. This work was the result of a co-authored publication [14] investigating the NO_2 gas sensing properties of interconnected ZnO nanowire arrays.

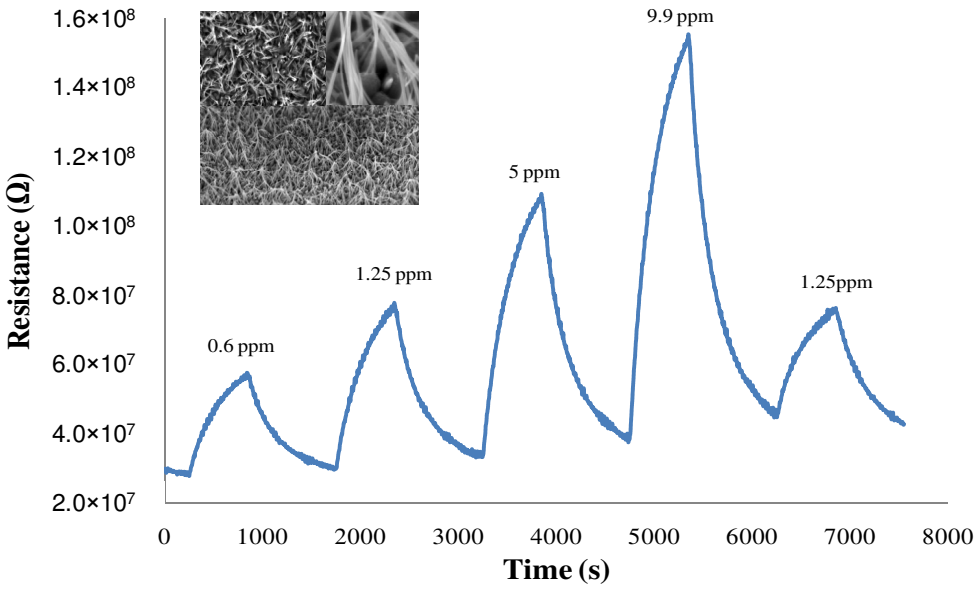

Figure 7.6. Dynamic response of interconnected ZnO nanowire arrays at 135 °C towards different concentrations of NO_2 in a balance of synthetic air, inset morphology of the gas sensitive layer.

The reduction of ZnO nanostructures from nanorod scale ~100 nm, to nanowires ~20 nm resulted in an NO_2 sensor capable of lower operating temperatures and a wider dynamic range than its nanorod based counterpart. Response and recovery time for exposures of 9.9 ppm NO_2 were 504 s and 564 s,

respectively. The interconnected ZnO nanowires sensor was also capable of ppb range sensing, during 600 ppb NO_2 exposures; response and recovery time were 496 s and 640 s, respectively.

The interconnected nanowire array sensor had a high sensitivity of 2.9 and an operating temperature some 95 °C lower than the nanorod based sensor. Optimisation of the interconnected nanowire array density may yield substantial improvements in sensitivity, response and recovery time, due to the anticipated higher surface area of ZnO($2\bar{1}\bar{1}0$) available and smaller dimensions comparable to the Debye length.

7.4.3 Conductometric Response of ZnO Nanorods Towards H_2

The dynamic response of ZnO nanostructured thin films consisting of nanorod arrays operating at 230 °C towards H_2 is presented in Figure 7.7. The sensor was prepared by depositing a ZnO nanorod array based thin film onto a $LiNbO_3$ substrate with IDT electrode pairs. Incremental decreases in resistance were measured with increasing H_2 pulse concentrations. The developed sensor demonstrated promising gas sensing performance with response and recovery time towards 1% H_2 of 24 s and 116 s, respectively. Indicating, the suitability of the sensor for hydrogen leak detection well below the lower explosive concentration threshold of 4% [15]. Response and recovery time towards low concentration 600 ppm H_2 were 140 s and 128 s, respectively.

While there are a number of publications concerning single ZnO nanorods and nanowires for H_2 gas sensing applications, there are very few which employ arrays of nanomaterials such as the array of ZnO nanorods used by the author. Wang *et al.* [16] successfully employed a similar hydrothermal deposition method to create a ZnO nanorod array for H_2 sensing. The arrays were reported to have a lower detection limit of 20 ppm, although response and recovery times were not explicitly reported, and all presented sensing data was with respect to a 200 ppm H_2 concentration in dry air at 250 °C. Unlike the nanorod array developed by the author, the response and recovery characteristics towards 200 ppm H_2 appear to be at least an order of magnitude larger than those of the authors developed sensor (towards a H_2 concentration of 600 ppm).

ZnO is known to reduce a fraction of its surface, inducing metallisation upon extended periods of exposure to H_2, as per equation (7.9), often leading to incomplete recovery as noted by Mitra *et al.* [17]. This process occurs concurrently with equation (7.8), lower sensing element resistance.

$$ZnO_{(s)} + H_{2(gas)} \xrightarrow{O_2} Zn_{(s)} + H_2O_{(g)} \tag{7.9}$$

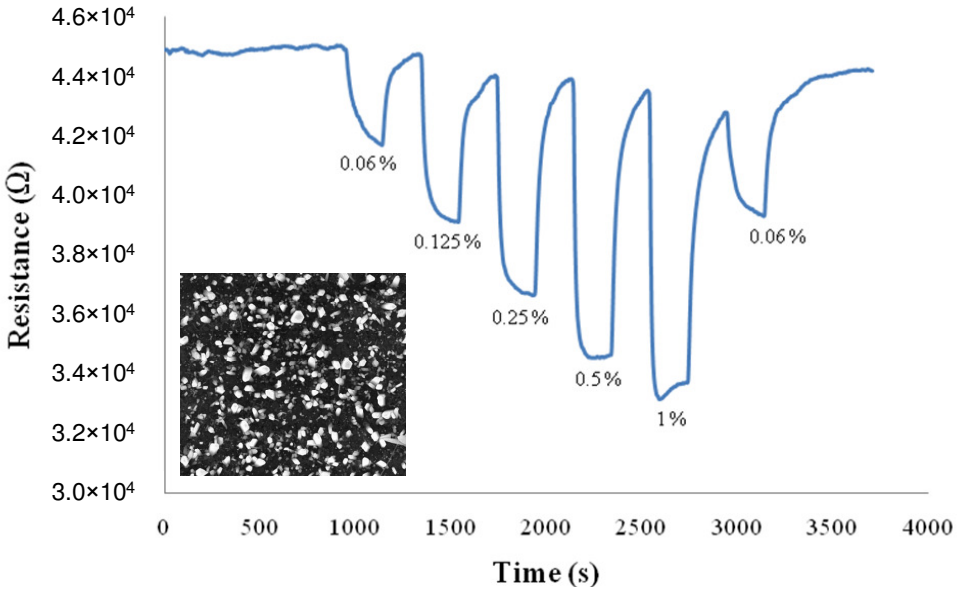

Figure 7.7. Dynamic response of ZnO nanorod arrays at 230 °C at different concentrations of H_2 in a balance of synthetic air, inset morphology of the gas sensitive layer.

Theoretically, DFT studies of the adsorption of atomic hydrogen (H) onto ZnO($2\bar{1}\bar{1}0$) by Wang *et al.* [18] predicted that hydrogen exposure will induce metallisation. The metallisation of ZnO effectively decreases the resistance of the sensing element. Using a periodic Hartree-Fock method Zapol *et al.* [19] studied the adsorption of H_2 onto the ZnO($10\bar{1}0$) surface and found that the molecular hydrogen can dissociatively adsorb onto ZnO($10\bar{1}0$). The adsorption process transfers electron density from the adsorbate to the surface [19], which is in good agreement with previous theoretical studies by Wang *et al.* [18], and the experimental results presented in Figure 7.7.

7.5 WO_3 Nanostructured Thin Films

The history of WO_3 nanomaterials in gas sensing is more recent than that of well established materials such as ZnO, TiO_2 and SnO_2. Despite this, WO_3 remains a remarkable semiconducting metal oxide

capable of sensing NO_2 and H_2 via change in carrier concentration (resistance) and optically sensing H_2 via the gasochromic effect. In this thesis, two different types of WO_3 based sensors were developed. The first, a conductometric NO_2 sensor deposited using the author's sol-gel technique, which resulted in a nanostructured thin film comprising of nanoplatelets [20]. The second sensor was an optical gasochromic based H_2 sensor deposited via RF sputtering, resulting in a nanotextured WO_3 thin film, which was later coated with a Pt catalytic over-layer [6].

7.5.1 Conductometric Response of WO_3 Nanoplatelets Towards NO_2

The dynamic performance of WO_3 nanostructured thin films comprised of nanoplatelets pre-treated at 550 °C, operating at 175 °C is presented in Figure 7.8, with the normalised sensing response over a range of temperatures shown in Figure 7.9. The sensor was prepared by spin coating $WO_3 \cdot nH_2O$ sol-gel films onto a $LiNbO_3$ substrate with IDT electrode pairs. Following this, the sensor was annealed at 550 °C. Sensors were pre-treated at 550 °C in a dry gas stream of 90% Ar - 10% O_2 to drive water from the sol-gel prepared $WO_3 \cdot nH_2O$ crystal lattice as previously discussed in Chapters 5 and 6, ensuring sample stability.

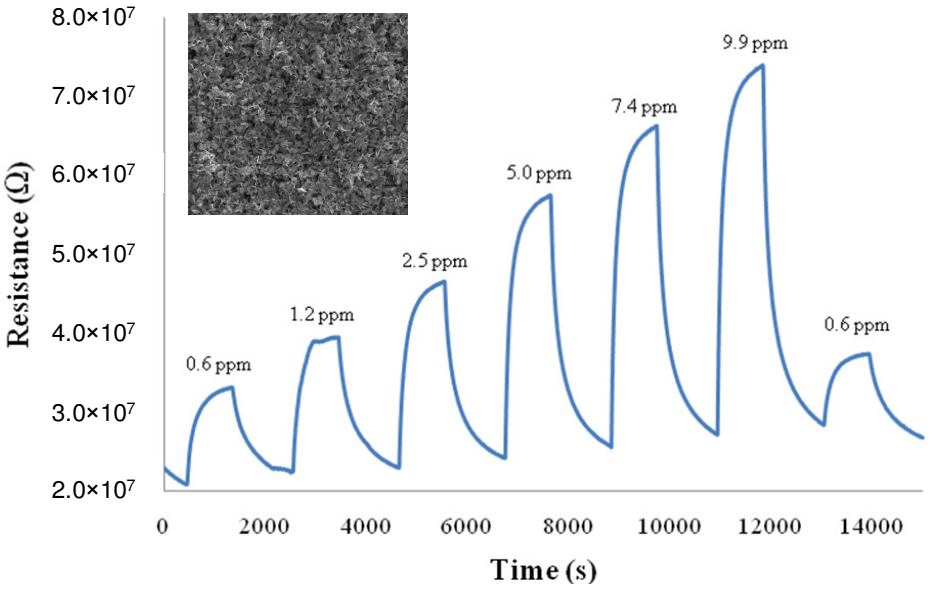

Figure 7.8. Dynamic response of WO_3 nanoplatelets pre-treated at 550 °C operating at 175 °C towards NO_2, inset morphology of the gas sensitive layer.

The measured resistance increase upon exposure to NO_2 was largest at 150 °C, however at this temperature the baseline resistance slightly crept with each pulse of NO_2, suggesting that at this operating temperature NO_2 was not completely desorbed from the sensor surface. However, at 175 °C baseline stability issues were minimal, and good baseline stability was observed along with the highest sensitivity at any of the investigated temperatures (Table 7.1). At this operating temperature, for 9.9 ppm NO_2 in a balance of synthetic air, the response and recovery time were 236 s and 704 s, respectively. Similarly, response and recovery time toward NO_2 concentrations of 600 ppb were 468 s and 600 s, respectively.

Table 7.1. Sensitivity of nanostructured WO_3 thin film based sensor to 9.9 ppm NO_2 in synthetic air at different sensor operating temperatures.

Temperature (°C)	Sensitivity
150	1.6
175	1.7
195	0.6

Clearly, the fabricated nanostructured WO_3 thin film based sensor is suitable for sensing of NO_2 at thresholds below those which cause negative physiological effects in healthy adults [21]; the sensor is also suitable for sensing a wide range of NO_2 concentrations. While sensors were also tested in excess of 200 °C, their response was found to sharply decrease with incremental increases in temperatures and as such, will not be reported here.

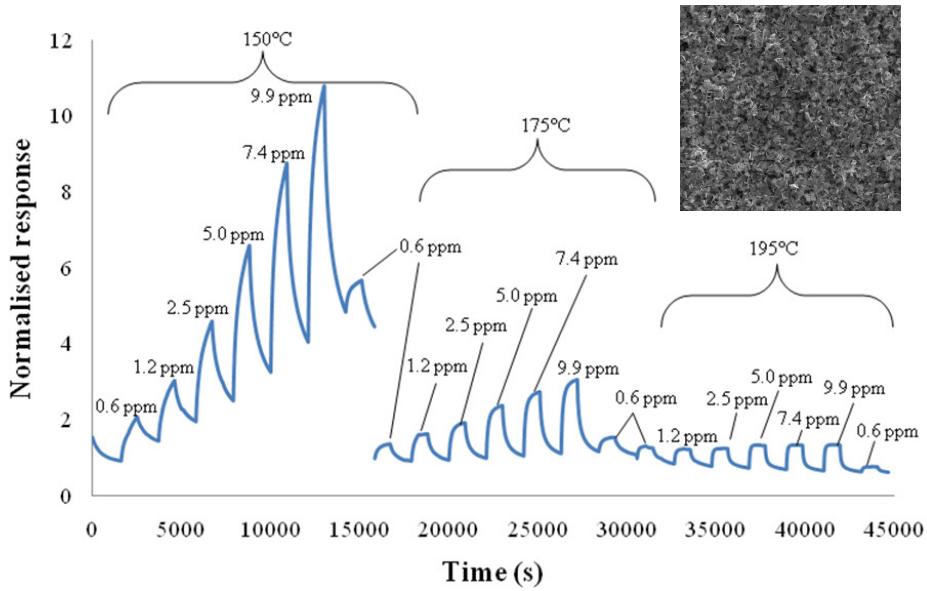

Figure 7.9. Temperature dependence of WO_3 nanoplatelets pre-treated at 550 °C towards NO_2, inset morphology of the gas sensitive layer.

These results compare favourably with those reported by Kida *et al.* [22] who fabricated lamellar WO_3 nanostructures via a related acid precipitation method. Sensor response and recovery time towards 1 ppm NO_2 in air was 240 s and 660 s at an operating temperature of 200 °C was reported. Comparing the work by Kida *et al.* with that presented in this thesis, the developed sensor is capable of sensing a lower concentration of 600 ppb NO_2, at a 25 °C lower operational temperature, albeit with a 228 s longer response and a 60 s shorter recovery time.

7.5.2 Conductometric Response of WO_3 Nanoplatelets Towards H_2

WO_3 nanoplatelet thin films were also assessed for hydrogen gas sensing, and were found to be unresponsive; as such the results will not be reported here.

7.5.3 Gasochromic Mechanism of Pt Coated WO_3 Nanotextured Thin Films

Gasochromism is the ability of a material to undergo a reversible colour change affected by the presence of the target analyte. This usually manifests as change in material colour. WO_3 is a well known gasochromic material however by itself, the gasochromic transition is very slow and requires high concentrations of H_2 gas to realise full or partial colouration [1-3]. By coating WO_3 with a thin layer of catalytic material known to dissociate H_2 [4-5], the rate limiting step in the gasochromic

colouration process is enhanced, thus, it is possible to augment the sensing threshold, sensitivity, response and recovery of WO_3 sputtered thin films [2].

The gasochromic transition of Pt/WO_3 from transparent to a coloured state involves the following steps [2]:

1. Dissociative chemisorption of molecular hydrogen onto Pt, forming hydrogen ions and electrons:

$$H_2 \xrightarrow{Pt} 2H^+ + 2e^- \tag{7.10}$$

2. Reduction of W^{6+} (transparent) centre in the WO_3 crystal lattice caused by the electrons generated in (7.10) to W^{5+} (blue colour), i.e. W_2O_6 (transparent) → W_2O_5 (coloured)

Formation of H_2O vapour resulting from the combination of $2H^+$ with surface bound O^{2-} ions produced by the reduction of W^{6+} to W^{5+}:

$$W_2O_6 + 2e^- + 2H^+ \underset{k_2}{\overset{k_1}{\rightleftharpoons}} W_2O_5 + H_2O \tag{7.11}$$

Forward reaction k_1, rate limited by $2H^+ + 2e^-$ supply

Reverse reaction k_2, rate limited by H_2O

3. Reversal occurs when hydrogen gas is purged from the system at elevated temperatures with synthetic air, restoring the stoichiometry of the WO_3, i.e. W^{5+} → W^{6+}:

$$W_2O_5 + H_2O \xrightarrow{Pt} W_2O_6 + H_2 \tag{7.12}$$

Steps 2 and 3 occur concurrently and simultaneously.

7.5.4 Gasochromism of Pt coated WO_3 nanotextured thin films

A comparison of the absorbance spectrum of both WO_3 and Pt/WO_3 thin films in air at room temperature is presented in Figure 7.10. These samples were created by RF sputtering of WO_3 onto quartz substrates, and testing the as deposited nanotextured thin film; or augmenting the response by depositing a 25 Å Pt catalytic over-layer. The characteristic shape reflects the transparent state of the

films that have been previously observed in the studies of WO_3 optical properties [23-24]. The fluctuating spectral curve of these partially transparent films was ascribed to the optical interference that occurs in the sputtered WO_3, due to the multiple reflections of optical rays as they pass through the thin film.

Instantaneous sampling over the UV-VIS range at set intervals is largely unsuitable for the generation of time dependant adsorption spectra. To rectify this, the dynamic response of the gasochromic sensor was measured cumulatively over a range of wavelengths, typically 400 nm to 900 nm. This approach generates sensing plots with cumulative changes in absorbance over a wide wavelength range in the presence of different gas concentrations, with respect to time. Background light and stray light sources were digitally subtracted from the signal prior to gas testing using a blank reference. The sample itself was mounted into a heated bracket capable of maintaining a range of temperatures from 25 °C to 180 °C.

The absorbance versus optical wavelength of the Pt/WO_3 films is presented in Figure 7.11 shows baseline performance in synthetic air and towards exposures of 1% H_2 in synthetic air after an exposure period of 10 minutes. A significant increase of the magnitude of absorbance was observed for the whole visible-NIR spectrum, indicating that the transparent thin films became dark and the W^{6+} ions in WO_3 were reduced to coloured W^{5+} ions. The magnitude of absorbance increases with the wavelength. No change in magnitude or wavelength shift occurred when WO_3 thin films without Pt coatings were exposed to 1% H_2 at room temperature.

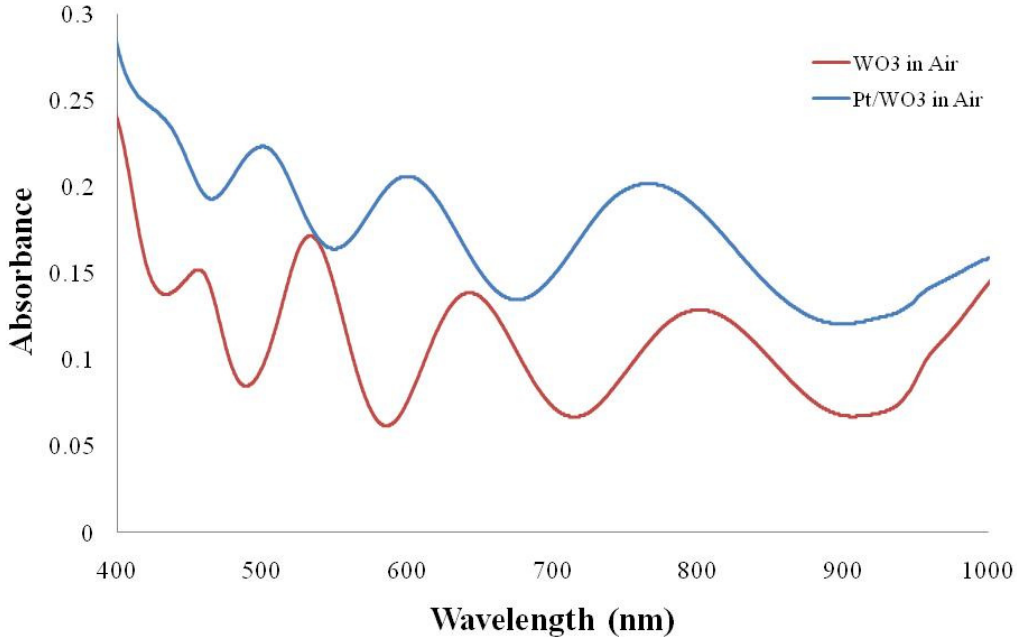

Figure 7.10. Absorbance vs. optical wavelength of RF sputtered WO_3 and Pt coated WO_3 thin films.

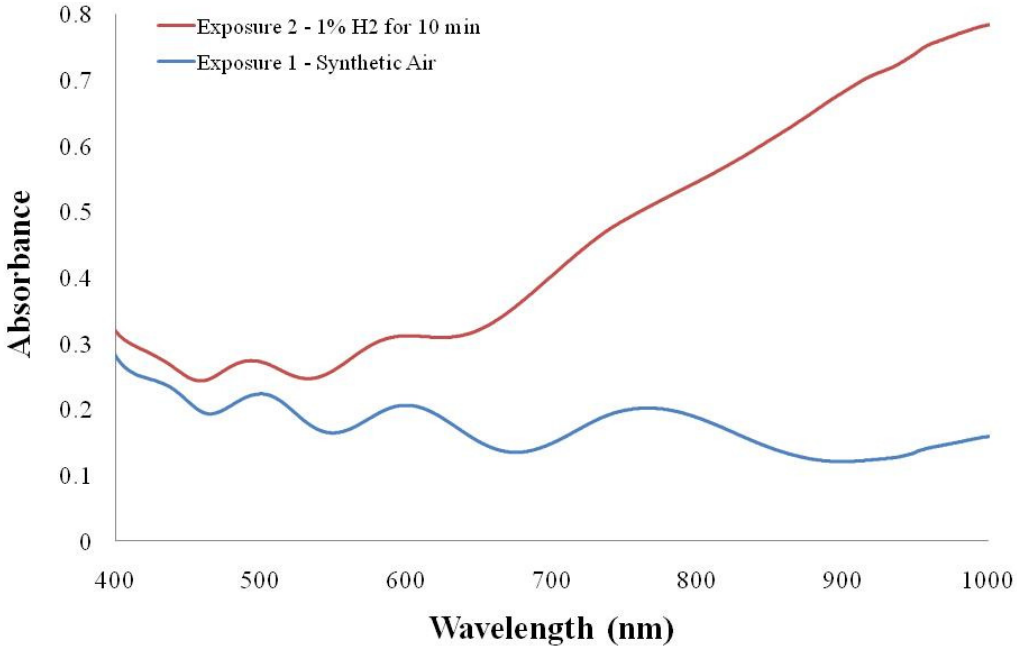

Figure 7.11. Absorbance vs. optical wavelength of Pt coated WO_3 thin films at room temperature in air and 1% H_2.

The change of cumulative absorbance versus temperature of the Pt/WO_3 thin film presented in Figure 7.12 for 0.06% H_2 in synthetic air exposed for five minutes. Cumulative absorbance was

measured using the spectrophotometer and integrating the response curve from 500 nm to 800 nm. This integration, measured the cumulative changes in absorbance and wavelength observed upon exposure to H_2. The curve in Figure 7.12 indicates that the maximum sensitivity for the Pt/WO_3 sensor is at an operating temperature of 70 °C. The low operating temperature could be due to the enhanced effective dissociation of H_2 [25]. However, it was observed that the recovery was very slow for the operating temperature below 100 °C. It was also observed that above 100 °C, the response and the recovery were equivalently very fast being less than 100 s. However the magnitude of absorbance decreased with increasing temperature.

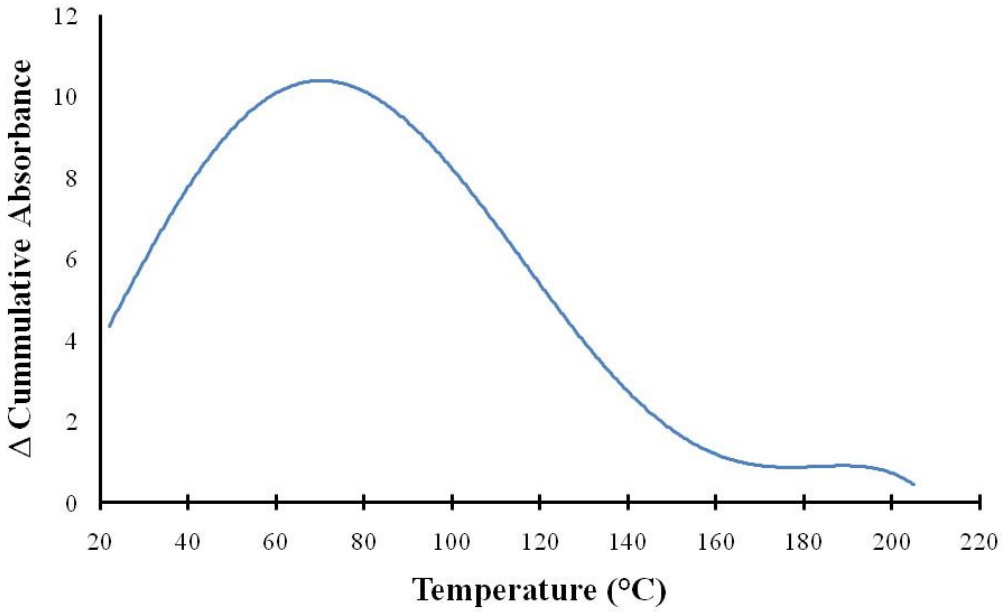

Figure 7.12. Change in absorbance vs. temperature for Pt/WO_3 sensors exposed to 0.06% H_2 in a balance of synthetic air.

The dynamic responses of the Pt/WO_3 and Pt (2.5 nm) thin films towards different concentrations of H_2 in synthetic air at 100 °C measured over the wavelength range of 500 nm to 800 nm are presented in Figure 7.13. H_2 in a synthetic air balance was pulsed into the testing chamber to induce coloration, and regenerated to a transparent state with synthetic air. Comparison of Pt/WO_3 and Pt thin

films on quartz substrates confirmed that Pt thin films are not sufficient enough to induce significant changes in absorbance, and as such, are not suitable for optical gas sensing elements.

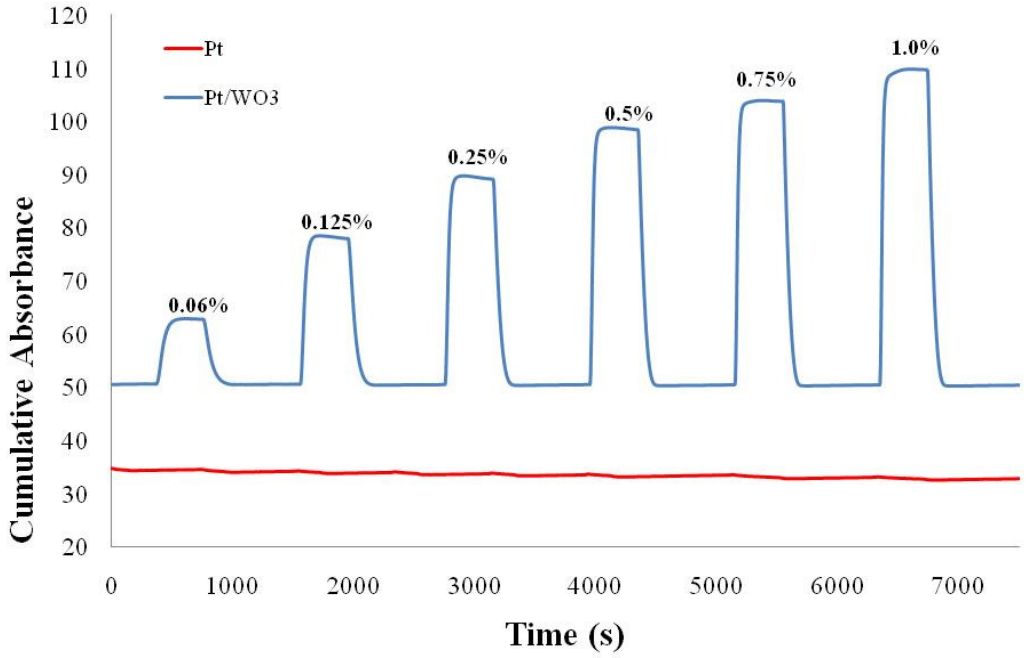

Figure 7.13. Dynamic responses of Pt/WO_3 and Pt thin films exposed to different concentrations of H_2 at 100 °C integrated over the wavelength range of 500 nm to 800 nm.

The dynamic response of the Pt/WO_3 thin films towards different concentrations of H_2 in a synthetic air at 100 °C measured at a single wavelength of 660 nm is presented in Figure 7.14. The magnitude of the response for a single wavelength was smaller compared to the response integrated over a range of wavelengths. However, the response and recovery rates were very similar. There is a direct correlation between Figure 7.13 and Figure 7.14, which confirms the consistency and stability of the thin film. Both results indicate H_2 saturation begins to occur at concentrations over 0.5%.

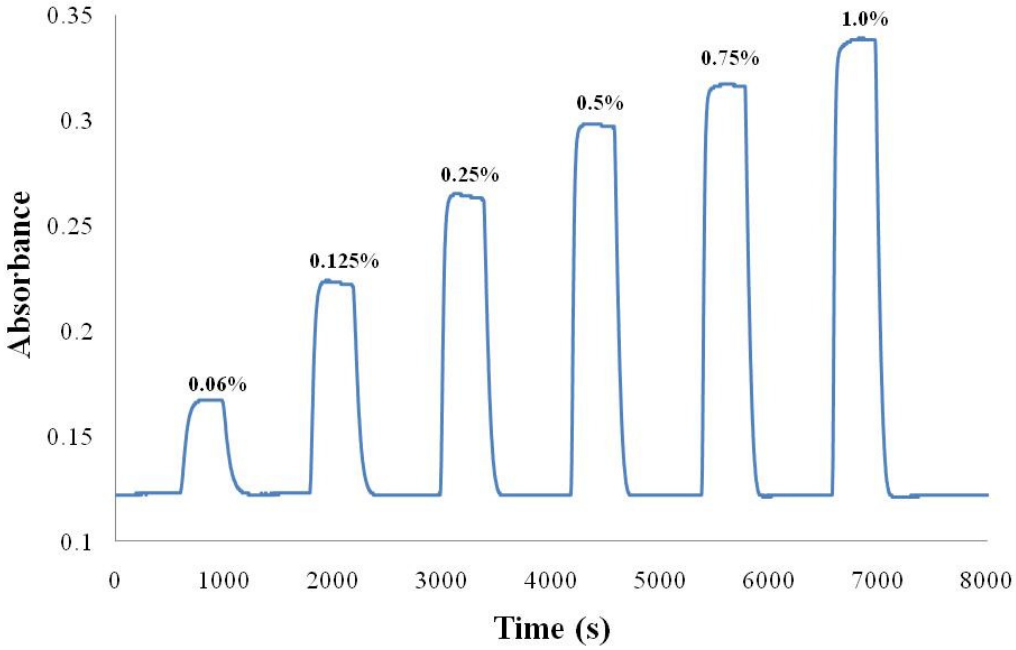

Figure 7.14. Dynamic response of a Pt/WO_3 thin exposed to different concentrations of H_2 at 100 °C measured at a single wavelength of 660 nm.

It was observed that absorbance changes increase progressively with increasing H_2 concentration. Concentrations as low as 0.06%, resulted in an absorbance increase of 15% with respect to the baseline. The exposure of H_2 gas to the Pt/WO_3 thin films resulted in a change of surface colour intensity, and hence the absorbance spectrum. The response was very fast and stable, as was the recovery. The film response time and recovery time induced by 1% H_2 in synthetic air was measured to be 86 s and 76 s, respectively. This performance was higher than Pd-WO_3 based H_2 optical gas sensors operating at 200 °C, developed by Ando *et al.* with a response time of 500 s and a recovery time of 300 s [26]. It was also reported by Maciak *et al.* that their Pd/TiO_2 fiber optic hydrogen sensor tested towards 2% H_2 had a response and recovery time of 240 s and 60 s, respectively. Similarly, their Pd/NiO_x fiber optic H_2 sensor demonstrated better performance towards 3% H_2 with the response time and recovery time of 30 s and 40 s, respectively [27].

7.6 Developed Sensor Comparison Matrix

A comparison of sensors developed as part of the author's PhD work is provided below in Table 7.2.

Table 7.2. Developed senor comparison matrix.

Sensor	**ZnO nanorods**	**Interconnected ZnO nanowires**	**ZnO nanorods**	**WO_3 nanoplatelets**	**WO_3 thin-film**
Target gas	NO_2	NO_2	H_2	NO_2	H_2
Sensor type	Conductometric	Conductometric	Conductometric	Conductometric	Optical
Optimum operation temperature (°C)	230	135	230	175	100
Dynamic range (ppm)	0.51 - 8.5	0.6 - 9.9	600 - 10000	0.6 - 9.9	600 - 10000
Dynamic range (%)	0.000051 - 0.00085	0.00006 - 0.00099	0.06 - 1.0	0.00006 - 0.00099	0.06 - 1.0
Response time $t_{90\%}$ (s)	152	504	24	236	86
Recovery time $t_{90\%}$ (s)	508	564	116	704	76
Baseline stability	Excellent	Good	Good	Good	Excellent
Sensitivity	3.0	2.9	0.3	1.7	N/A

response times are quoted for maximum analyte concentration tested

7.7 Chapter Summary

ZnO and WO_3 nanomaterials were used in the fabrication of NO_2 and H_2 sensors, with a number of sensors displaying promising abilities for a number of sensing applications.

All NO_2 gas sensors presented in this chapter are capable of sensing below concentrations at which NO_2 causes negative physiological effects in healthy adults. Given the sensors' small size of 11×11 mm, these sensors show promise for personal monitoring applications, ideally suited to confined space applications where NO_2 may pose the greatest risk. These sensors may be useful in confined spaces where NO_2 sensing is critical for occupational health and safety regulations such as

those found in arc and high energy welding processes employed in boiler making and ship hull manufacture.

ZnO nanomaterials have been shown to be suitable candidates for NO_2 gas sensing applications, with ZnO nanorods exhibiting superior response and recovery time, and baseline stability out of all the developed sensors reported within this chapter. Furthermore the excellent baseline stability of the ZnO nanorod arrays and sub ppm NO_2 gas sensing ability make them suitable candidates for monitoring atmospheric NO_2 concentrations.

WO_3 nanostructured thin films consisting of nanoplatelets which were shown to be sensitive a wide dynamic range of NO_2, sensing at a modest 175 °C. At lower operational temperatures such as 150 °C the developed sensor exhibited partially reversible resistance changes, which may prove useful in the fabrication of inexpensive mass produced NO_2 detectors, calibrated to alarm after exceeding a pre-established NO_2 exposure limit.

ZnO nanorods were found to be sensitive towards H_2 with response and recovery time of 24 s and 116 s, respectively. The sensor was determined to be suitable for hydrogen leak sensing well below the lower explosive concentration threshold, however higher concentration gas sensing (above 4%) is not recommended due to the sensor's operating temperature of 230 °C.

WO_3 thin-film gasochromic optical sensors consisting of a 1.2 um WO_3 nanotextured thin film coated with a 2.5 nm amorphous Pt catalytic layer, were well suited to low temperature sensing at 100 °C with excellent baseline stability, and a response and recovery time of 86 s and 76 s, respectively. It was observed that H_2 saturation began to occur at concentrations over 0.5%, with additional increases in H_2 concentrations yielded only moderate changes in gasochromism. Considering the optical sensing mechanism of gasochromic materials, it is possible to combine the developed sensor with fiber optic technologies for the creation of remote hydrogen sensing units immune to electromagnetic interference and capable of deployment in remote and or hazardous locations.

7.8 References

[1] C. G. Granqvist, *et al.*, "Recent advances in electrochromics for smart windows applications," *Solar Energy,* vol. 63, pp. 199-216, 1998.

[2] S. K. Deb, "Opportunities and challenges in science and technology of WO_3 for electrochromic and related applications," *Solar Energy Materials and Solar Cells,* vol. 92, pp. 245-258, 2008.

[3] G. Korotcenkov, "Metal oxides for solid-state gas sensors: What determines our choice?," *Materials Science and Engineering: B,* vol. 139, pp. 1-23, 2007.

[4] C. G. Granqvist, "Electrochromic tungsten oxide films: Review of progress 1993-1998," *Solar Energy Materials and Solar Cells,* vol. 60, pp. 201-262, 2000.

[5] A. Takase and K. Miyakawa, "Raman Study on Sol-Gel Derived Tungsten Oxides from Tungsten Ethoxide," *Japanese journal of applied physics. Pt. 2, Letters,* vol. 30, pp. 1508-1511, 1991.

[6] M. H. Yaacob, *et al.*, "Absorption spectral response of nanotextured WO_3 thin films with Pt catalyst towards H_2," *Sensors and Actuators, B: Chemical,* vol. 137, pp. 115-120, 2009.

[7] N. Barsan and U. Weimar, "Conduction Model of Metal Oxide Gas Sensors," *Journal of Electroceramics,* vol. 7, pp. 143-167, 2001.

[8] B. Ruhland, *et al.*, "Gas-kinetic interactions of nitrous oxides with SnO_2 surfaces," *Sensors and Actuators B: Chemical,* vol. 50, pp. 85-94, 1998.

[9] B. Shouli, *et al.*, "Different morphologies of ZnO nanorods and their sensing property," *Sensors and Actuators B: Chemical,* vol. 146, pp. 129-137, 2010.

[10] A. Z. Sadek, *et al.*, "Characterization of ZnO Nanobelt-Based Gas Sensor for H_2, NO_2, and Hydrocarbon Sensing," *Sensors Journal, IEEE,* vol. 7, pp. 919-924, 2007.

[11] E. K. Heidari, *et al.*, "WO_3-based NO_2 sensors fabricated through low frequency AC electrophoretic deposition," *Sensors and Actuators B: Chemical,* vol. 146, pp. 165-170, 2010.

[12] P. S. Cho, *et al.*, "NO_2 sensing characteristics of ZnO nanorods prepared by hydrothermal method," *Journal of Electroceramics*, vol. 26, pp. 975-978, 2006.

[13] F.-T. Liu, *et al.*, "ZnO nanorod gas sensor for NO_2 detection," *Journal of the Taiwan Institute of Chemical Engineers,* vol. 40, pp. 528-532, 2009.

[14] M. Rahmani, Breedon, M., Keshmiri, S., Moafie, A., McCoulloch, D., Wlodarski, W., Kalantar-zadeh, K., "Gas Sensing Properties of Interconnected ZnO Nanowires," *Sensors and Actuators B: Chemical,* Under Review, 2010.

[15] P. Patnaik, *Handbook of Inorganic Chemicals*, 1st ed., McGraw-Hill, 2003.

[16] J. X. Wang and et al., "Hydrothermally grown oriented ZnO nanorod arrays for gas sensing applications," *Nanotechnology,* vol. 17, p. 4995, 2006.

[17] P. Mitra, *et al.*, "ZnO thin film sensor," *Materials Letters,* vol. 35, pp. 33-38, 1998.

[18] C. C. Wang, *et al.*, "Hydrogen-induced metallization of zinc oxide ($2\bar{1}\bar{1}0$) surface and nanowires: The effect of curvature," *Physical Review B,* vol. 77, pp. 5303-5303, 2008.

[19] P. Zapol, *et al.*, "*Ab-initio* study of hydrogen adsorption on the ZnO($10\bar{1}0$) surface," *Surface Science,* vol. 422, pp. 1-7, 1999.

[20] M. Breedon, *et al.*, "Synthesis of nanostructured tungsten oxide thin films: A simple, controllable, inexpensive, aqueous sol-gel method," *Crystal Growth and Design,* vol. 10, pp. 430-439, 2010.

[21] A. P. Francesco Forastiere, Frank J. Kelly, Stephen T. Holgate, *Air Quality Guidelines Global Update*: World Health Organisation, 2005.

[22] T. Kida, *et al.*, "Highly sensitive NO_2 sensors using lamellar-structured WO_3 particles prepared by an acidification method," *Sensors and Actuators B: Chemical,* vol. 135, pp. 568-574, 2009.

[23] A. Azens and C. G. Granqvist, "Electrochromic films of tungsten oxyfluoride and electron bombarded tungsten oxide," *Solar Energy Materials and Solar Cells,* vol. 44, pp. 333-340, 1996.

[24] E. Gyorgy, *et al.*, "Structural and optical characterization of WO_3 thin films for gas sensor applications," *Journal of Applied Physics,* vol. 97, pp. 0935270 - 0935274, 2005.

[25] S. J. Ippolito, *et al.*, "Hydrogen sensing characteristics of WO_3 thin film conductometric sensors activated by Pt and Au catalysts," *Sensors and Actuators B: Chemical,* vol. 108, pp. 154-158, 2005.

[26] M. Ando, *et al.*, "Optical hydrogen sensitivity of noble metal-tungsten oxide composite films prepared by sputtering deposition," *Sensors and Actuators B: Chemical,* vol. 76, pp. 13-17, 2001.

[27] E. Maciak and Z. Opilski, "Transition metal oxides covered Pd film for optical H_2 gas detection," *Thin Solid Films,* vol. 515, pp. 8351-8355, 2007.

Chapter 8 - Conclusions and Further Work

8.1 Conclusions

During his PhD candidature, the author focused on a holistic, multi-faceted approach to the development of ZnO, WO_3 and $WO_3{\cdot}nH_2O$ nanostructures from aqueous chemical techniques, their applications to gas sensing, and understanding the adsorption processes of NO_x on ZnO nanomaterials. Chapter 1 introduced the research background, motivations and aims; and Chapter 2 provided the reader with a critical review of current literature and the scope of the author's study within the current body of knowledge. In Chapter 3 the foundations and implementation of density functional theory (DFT) were introduced, as well as its application to materials modelling, surface science and gas sensing technologies. Chapter 4 presented the results from the author's systematic DFT studies of N, O, NO and NO_2 adsorption onto ZnO($2\bar{1}\bar{1}0$), as well as NO_2 onto ZnO($2\bar{1}\bar{1}0$)–V_O. In Chapter 5 the experimental aqueous chemical techniques for nanostructured metal oxide synthesis, developed by the author were introduced, with a full explanation of the relevant reaction chemistry. The focus of Chapter 6, was the comprehensive characterisation of the different nanostructured thin films developed by the author, taking into account the idiosyncratic nature of ZnO, WO_3, and $WO_3{\cdot}nH_2O$ nanostructures derived principally from aqueous chemical techniques. In Chapter 7, the developed nanostructured thin films were assessed as gas sensitive materials, with a particular focus on NO_2 and H_2. Finally in this chapter, the conclusions and further research topics identified by the author are presented.

The research presented in this thesis can be broadly divided into three different categories:

1. *Density functional theory adsorption studies.*
2. *The synthesis and characterisation of nanostructures and nanostructured metal oxide thin films.*
3. *Gas sensing studies of the developed nanostructured metal oxide thin films.*

In the following sections each broad category will be addressed, in the order it was presented in the thesis.

8.1.1 DFT Adsorption Studies

DFT was used to understand the adsorption of NO_x onto one of the most prevalent crystal faces present in ZnO nanomaterials, resulting in several key findings. The conclusions drawn from the DFT adsorption studies were divided into three different categories, examining the following:

1. *The adsorption of potential NO_x dissociation products on* ZnO($2\bar{1}\bar{1}0$) – [N/ZnO($2\bar{1}\bar{1}0$) and O/ZnO($2\bar{1}\bar{1}0$)]
2. *The adsorption of* NO_x *on* ZnO($2\bar{1}\bar{1}0$) – [NO/ZnO($2\bar{1}\bar{1}0$) and NO_2/ZnO($2\bar{1}\bar{1}0$)]
3. *The adsorption of* NO_2 *on* ZnO($2\bar{1}\bar{1}0$), *containing oxygen defects* – [NO_2/ZnO($2\bar{1}\bar{1}0$)–V_O]

It was found that for all systems, there was no reaction barrier for the adsorption of N, O, NO and NO_2 on the crystal surfaces studied, with all molecules and molecular dissociation products spontaneously adsorbing.

Outcomes of the DFT studies are listed below.

1. Adsorption of O and N onto ZnO($2\bar{1}\bar{1}0$)

- The adsorption of O and N onto ZnO($2\bar{1}\bar{1}0$) was for the most part strong (typically > 1 eV), with binding energies indicative of chemisorption.
- Six minimum energy structures were found with adsorbate interactions limited to the first two layers of the surface model.
- Adsorbate atoms bond with two or more surface oxygen and or zinc atoms.
- Ionic and covalent type bonds were calculated between the adsorbate and the surface. Bonding between surface oxygen atoms and either adsorbate O or N atoms resulted in the formation of a covalent type bond, whereas, adsorbate interactions with surface zinc atoms formed bonds with ionic character.

- Surface relaxation after adsorption was found to be largest in the top two surface layers. Surface reconstructions were also observed, being prominent for the most stable minima of both adsorbates, but minor in the less stable structures.
- The positive work-function changes of adsorbed atomic oxygen is thought to correlate with the experimentally observed decreases in conductivity of ZnO conductometric sensor technologies.
- The large negative work-function change calculated for adsorbed atomic N indicates that the adsorption process would cause the resistance of ZnO to decrease.

2. Adsorption of NO and NO_2 onto ZnO($2\bar{1}\bar{1}0$)

- The adsorption of NO and NO_2 onto ZnO($2\bar{1}\bar{1}0$) was weak, with binding energies indicative of physisorption.
- Thirty minimum energy structures were found for NO and NO_2 adsorbed onto the ZnO($2\bar{1}\bar{1}0$) surface, with eleven unique NO adsorption configurations and nineteen unique NO_2 configurations.
- The adsorbate molecules preferentially interacted with one or more surface zinc atoms.
- Despite showing weak binding energies, the charge density plots and Bader charge calculations indicated that there is a transfer of charge from the surface to the adsorbate molecule, in good agreement with experimental observations in resistance changes.
- The surface was largely unchanged after adsorption, with little or no surface reconstruction or relaxation.
- The large number of minimum energy structures; barrier-less physisorption; and comparatively negligible surface reconstruction and relaxation, suggests that at appropriate operating conditions, ZnO($2\bar{1}\bar{1}0$) crystal surfaces may be suitable for NO and NO_2 sensing applications where long term stability is desired.

3. Adsorption of NO_2 onto $ZnO(2\bar{1}\bar{1}0)–V_O$

- The adsorption of NO_2 onto $ZnO(2\bar{1}\bar{1}0)–V_O$ was strong, with binding energies indicative of chemisorption.
- 5 minimum energy structures were found for the adsorption of NO_2 on the $ZnO(2\bar{1}\bar{1}0)–V_O$ surface.
- NO_2 preferentially interacted with the defect site zinc atoms via O-Zn or N-Zn bonds.
- Large surface reconstructions around the oxygen vacancy site were observed after NO_2 adsorption, while surface relaxations were minor.
- The adsorption of NO_2 onto $ZnO(2\bar{1}\bar{1}0)–V_O$ attempts to repair the oxygen vacancy by bridging the NO_2 molecule over the oxygen vacancy site. However, this does not cleanly restore the stoichiometry of the surface to $ZnO(2\bar{1}\bar{1}0)$.
- Given the larger magnitude of charge transfer (more than 6 times greater) for the defect surface compared with the stoichiometric surface, it can be expected that gas detectors and sensors utilising defect rich nanostructures may yield significantly higher NO_2 sensitivities than those based on stoichiometric $ZnO(2\bar{1}\bar{1}0)$ nanostructures.

8.1.2 Nanostructured Metal Oxide Synthesis

In this PhD candidature, aqueous chemical deposition techniques were predominately used in the creation of ZnO, WO_3, and $WO_3{\cdot}nH_2O$ nanostructures and nanostructured thin films. These techniques were developed by the author, with the intent of creating high surface area, and highly crystalline, nanostructured thin films suitable for gas sensing applications. The conclusions drawn from the synthesis of metal oxide nanostructures and nanostructured thin films presented in this thesis are categorised for ZnO, and WO_3 / $WO_3{\cdot}nH_2O$ nanomaterials as follows:

1. ZnO nanostructure and nanostructured thin film synthesis

- Zinc oxide nanostructured thin films were fabricated using seed/nucleation layers deposited via RF sputtering or spray pyrolysis. Three different ZnO morphologies were created: nanorods, corrugated nanorods, and interconnected nanowires.
- Corrugated nanorods and interconnected nanowires were synthesised, which to the best of the author's knowledge, were demonstrated for the first time using aqueous chemical methods.
- ZnO nanostructured arrays were grown from RF sputtered ZnO seed/nucleation layers placed in a NaOH based growth solution. This yielded an unusual corrugated ZnO nanorod morphology, which was reported for the first time from aqueous solutions.

- Seed/nucleation layer choice was investigated by placing RF sputtered and spray pyrolysis deposited seed/nucleation layers into HMT growth solutions. It was observed that nanostructured thin films originating from hemispherically terminated seed/nucleation layers grew typically in nanorod arrays perpendicular to the substrate surface. It was found that the rougher polygonal seed/nucleation layers deposited via spray pyrolysis, resulted in the formation of interconnected ZnO nanowires. XRD analyses revealed that all samples were predominately ZnO with some minor peak(s) contributed by zinc hydroxide.

- Experimental evidence of seed/nucleation layer etching caused by the HMT growth solution has been established through cross-sectional TEM studies of ZnO nanostructured thin films grown on GaN. Thus, the initial thickness of the seed/nucleation layer is important for maintaining a contiguous protective underlying seed/nucleation layer. Without this protective layer, metal contacts deposited onto the ZnO nanostructured thin film may extend to the underlying GaN layer, creating an electrical short, disrupting device operation.

2. WO_3 and $WO_3 \cdot nH_2O$ nanostructure and nanostructured thin film synthesis

- The formation of tungsten oxide hydrates was explored via acid precipitation, a successive ionic layer adsorption reaction (SILAR) growth method and a sol-gel method, with the former two methods developed by the author.

- The author established a link between aging deposited sol-gel samples in dry atmospheres and humid atmospheres. The crystallinity and morphology of the resultant nanoplatelets was studied. Characterisation of sol-gel deposited material via complimentary analysis confirmed that freshly deposited samples were $WO_3 \cdot nH_2O$ with varying hydration levels, dependent upon the humidity of the environment they were dried in.

- Tungsten oxide hydrate samples annealed at 300 °C were identified as monoclinic, with Raman analysis indicating incomplete dehydration. Samples annealed at 550 °C were found to be predominately orthorhombic with evidence of other minor crystallographies present as indicated by XRD and Raman analyses, with spectral evidence of a $WO_3 \cdot \frac{1}{3}H_2O$, despite annealing for 2 hrs at 550 °C. The presence of water primarily detected by Raman spectroscopy has been ascribed to the hygroscopic action of freshly annealed nanostructured thin films.

To the best of the author's knowledge the following have been developed and reported for the first time: an aqueous method for the formation of corrugated nanostructured thin films, the fabrication of interconnected ZnO nanowire arrays, a SILAR method capable of depositing nanostructured WO_3 thin films, and an aqueous sol-gel technique capable of depositing a nanostructured WO_3 thin film utilising innocuous chemical precursors.

8.1.3 Gas Sensing

ZnO and WO_3 nanomaterials were used in the fabrication of NO_2 and H_2 sensors, with promising dynamic performance. The conclusions drawn from the gas sensing investigations using ZnO and WO_3 nanostructured thin films for NO_2 and H_2 sensing are divided between ZnO and WO_3 based conductometric sensors; and nanotextured WO_3 gasochromic thin film sensors, as follows:

1. ZnO nanostructured thin film based conductometric gas sensors

- ZnO nanomaterials were demonstrated to be suitable for NO_2 gas sensing applications, with ZnO nanorods exhibiting superior response and recovery time, and the greatest baseline stability out of all the developed sensors reported within this thesis. The response and recovery time were 152 s and 508 s, respectively for 8.5 ppm of NO_2 in a balance of synthetic air. Whilst at sub-ppm NO_2 concentrations (510 ppb), the response and recovery time of the sensor was 91 s and 280 s, respectively.

- The reduction of ZnO nanostructures from nanorod scale ~100 nm, to nanowires ~20 nm resulted in an NO_2 sensor capable of lower operating temperatures, with a wider dynamic range than its nanorod based counterpart. Response and recovery time towards exposures of 9.9 ppm NO_2 were 504 s and 564 s, respectively. The interconnected ZnO nanowires sensor was also capable of ppb range sensing, during 600 ppb NO_2 exposures; response and recovery time were 496 s and 640 s, respectively.

- ZnO nanorods were found to be sensitive towards H_2 with response and recovery time of 24 s and 116 s, respectively. The sensor was determined to be suitable for hydrogen leak sensing well below the lower explosive concentration threshold, however, the sensor should be fitted with a flame suppressor/arrestor if it is intended to be operated in hydrogen gas where the concentration is greater than 4%.

2. WO_3 nanostructured thin film based conductometric gas sensors

- WO_3 nanostructured thin films consisting of nanoplatelets had an optimal operating temperature of 175 °C, and were capable of sensing a wide range of NO_2 concentrations, between several ppb to several ppm (0.6 ppm – 9.9 ppm). At 150 °C the developed sensor exhibited partially reversible resistance changes.

3. Gasochromic sensing of H_2 with nanotextured WO_3 thin films

- WO_3 thin-film gasochromic optical H_2 sensors consisting of a 1.2 µm WO_3 nanotextured thin film coated with a 2.5 nm amorphous Pt catalytic layer, were well suited to low temperature sensing at 100 °C with excellent baseline stability, and a response and recovery time of 86 s and 76 s, respectively.

Overall, the developed NO_2 gas sensors were capable of sensing below concentrations at which NO_2 causes negative physiological effects in healthy adults. These sensors show promise for personal monitoring applications, ideally suited to confined space applications where NO_2 may pose the greatest risk such as those found in arc and high energy welding processes employed in boiler making and ship hull manufacture. The developed H_2 sensors were capable of sensing below pre-established explosive threshold limits, with ZnO nanorods arrays and nanotextured WO_3 gasochromic sensors being suitable candidates for leak sensing/detector applications.

8.1.4 Publications and Other Achievements

The author published in a wide range of refereed, high impact scientific and engineering journals (Table 8.1, Appendix B) covering many multidisciplinary areas including; surface science, gas sensors, molecular modelling, materials science, chemistry, optical gas sensing, semiconductor and electrochromic materials, physiochemical processes, and crystal growth. Additionally, the author's research findings have been presented at a number of key Australian and international conferences, with the total number of conference papers exceeding 20 as listed in Appendix B.

In addition to the requirements and pressures of the PhD program, the applicant also pursued a number of extra extracurricular activities resulting in several significant achievements, and received a number of prestigious awards. In the final year of his PhD the author was a recipient of an Endeavour Award Research Fellowship to study at the University of Tokyo for 6 months. This was recently completed resulting in the fabrication of a novel optical temperature sensor. Pursuing an interest in technology commercialisation, the author was also a recipient of a commercialisation training scheme scholarship to further his education. This qualification was earned during his PhD candidature. Applying what was learnt in the commercialisation degree the author entered a team in the annual RMIT business plan competition, judged by the elite representatives of Melbourne's business world. Successfully leading his team, "*Hybrid Fuel Cell Technologies"*; a proposed venture, based on the author's own ZnO nanorods array technology; and won two major awards, one for energy innovation and the second for excellence.

Table 8.1. Publication summary.

Journal Name	Field
Crystal Growth and Design (1 paper)	Materials science/gas sensing
Surface Science (1 paper)	Theoretical surface science/molecular modelling
Materials Letters (2 papers)	Aqueous deposition/materials science
Thin Solid Films (1 paper)	Aqueous deposition/materials science
Journal of Physics Condensed Matter (1 paper)	Theoretical surface science/molecular modelling
Procedia Chemistry (1 paper)	Semiconductor physics
IEEE and SPIE (6 conference papers)	Nanomaterials/materials science
Chemical Physics Letters (1 paper)	Gas sensing
Electrochemistry Communications (1 paper)	Anodization/materials science
Langmuir (2 papers)	Electrowetting/anodization
Sensors and Actuators B (1 paper)	Optical gas sensors
Journal of Physical Chemistry C (1 paper)	Theoretical surface science/molecular modelling

8.2 Further Work

This thesis has presented several advances in both applied and theoretical science/engineering fields, with the research published in many high impact factor publications; both multidisciplinary and specialised by nature. Throughout the author's PhD candidature, a number of future directions were identified, and are listed below in § 8.2.1, § 8.2.2, and § 8.2.3.

8.2.1 Further Work in DFT Adsorption Studies

- DFT modelling of ozone (O_3) on the ZnO($2\bar{1}\bar{1}0$) surface, based on observations of the reactivity of the ZnO($2\bar{1}\bar{1}0$) surface and the ZnO($2\bar{1}\bar{1}0$)$-V_O$ surface, it may prove prudent to investigate the free radical O_3. The reactive nature of ozone may yield interesting results especially on the ZnO($2\bar{1}\bar{1}0$)$-V_O$ surface where the molecule may adsorb over the defect site repairing the surface and yielding gaseous O_2. There are other adsorbate species which interact with ZnO, including but not limited to: H_2, NH_3, alcohols, and others; many have already had their adsorption onto ZnO evaluated with material modelling techniques such as DFT.

- Studying the effect that pre-adsorbed species such as O_2 or H_2O have on the adsorption of NO_x on ZnO($2\bar{1}\bar{1}0$) and ZnO($2\bar{1}\bar{1}0$)$-V_O$ surfaces will build upon previous work providing a more complicated representation of gas sensing, by considering competing surface bound species.

- Extending DFT adsorption studies to include NO_x, as well as NO_x dissociation products onto WO_3 surfaces.

8.2.2 Further Work in Nanodimensional Metal Oxide Synthesis from Aqueous Solutions

- The incorporation of palladium or platinum salts to the tungstate stock solution for in-situ formation of catalytically active (with respect to H_2, NO_2 and O_2 dissociation) nanoparticles, during $WO_3 \cdot nH_2O$ sol-gel formation. This potentially offers enhanced gas sensing capabilities and augmented gasochromic properties.

- The refinement of aqueous ZnO, WO_3, and $WO_3 \cdot nH_2O$ deposition techniques to maximise the available surface area, with aspirations of improving sensor performance.

- The removal of the sodium impurity from sol-gel derived WO_3 nanostructured thin films, making films more suitable for electrochromic and gasochromic applications.

- The application of the developed SILAR method for the coating of optical fiber tips, with aspirations of developing a reflectance based sensor.

- Further study of the gas sensitivity of different WO_3 and $WO_3 \cdot nH_2O$ crystal phases after annealing.

8.2.3 Further Work in Gas Sensing Studies

- Long term stability tests (> 6 months) to examine the potential of sensing elements (both ZnO and WO_3) derived from aqueous techniques for commercialisation.

- Experimental optimisation to improve dynamic performance of the developed sensors.

- Substitution of the amorphous Pt film used in the nanotextured WO_3 gasochromic H_2 sensors, with evenly dispersed catalytically active metal clusters; aiming at improving H_2 dissociation rates, and thus, sensor performance.

- Application of the developed nanostructured metal oxide thin films for other sensing platforms including but not limited to: quartz crystal microbalances, surface acoustic wave devices, solid state electrochemical sensors, and high temperature catalytic combustion sensors.

- Assessing the developed ZnO and WO_3 nanostructures towards other target gases including but not limited to: ozone (O_3), ammonia (NH_3), and volatile organic compounds (VOCs).

Appendix A: VASP Parameters and Surface Notation

The VASP software code uses several files, the author has included the main input file (INCAR) used by the VASP program in Table A1.

Table A1. Typical optimisation VASP input file (INCAR), with a brief description of each variable.

Parameter	**Variable**	**Comment / Instruction / Description**
NPAR	32	32 CPUs used during optimisation
ISIF	2	Relax ions only
IBRION	2	Conjugate gradient algorithm used to relax ions to their instantaneous ground state
IALGO	48	Apply RMM-DIIS Matrix Diagonalizer
NELM	400	Maximum of 400 electronic steps
NSW	180	Maximum of 180 ionic iterations
POTIM	0.1	Optimisation trial step parameter
EDIFFG	-0.01	Difference in energy between ionic steps required to break ionic relaxation loop
IDIPOL	3	Dipole corrections applied
ISPIN	2	Calculations are spin-polarised, *important as N has one unpaired electron*
PREC	ACCURATE	Error in energy, *typically <1meV per atom*
ENCUT	400	Plane wave cut off energy, *all plane waves larger than 400 eV are truncated*
ISMEAR	-5	Apply tetrahedron method with Blöchl corrections to wavefunctions
SIGMA	0.1	Width of smearing in eV

It should be noted that for typesetting reasons, the author has elected not to use the full Kröger-Vink notation to represent the ZnO surface containing an oxygen defect. In the interests of clarity, the following surface notations are treated as equivalent throughout this thesis.

$\mathrm{ZnO}(2\bar{1}\bar{1}0) \equiv ZnO(2\bar{1}\bar{1}0)$

$\mathrm{ZnO}(2\bar{1}\bar{1}0)\text{-}\mathrm{V_O} \equiv ZnO(2\bar{1}\bar{1}0) - V_O^{\bullet\bullet}$

Appendix B: List of Author's Publications Peer reviewed publications

[1] M. Breedon, P. Spizzirri, M. Taylor, J. du Plessis, D. McCulloch, J. Zhu, L. Yu, Z. Hu, C. Rix, W. Wlodarski, and K. Kalantar-zadeh, "Synthesis of Nanostructured Tungsten Oxide Thin Films: A Simple, Controllable, Inexpensive, Aqueous Sol-Gel Method," ***Crystal Growth & Design***, vol 10, pp. 430, 2010.

[2] M. Breedon, M. B. Rahmani, S.-H. Keshmiri, W. Wlodarski, and K. Kalantar-zadeh, "Aqueous synthesis of interconnected ZnO nanowires using spray pyrolysis deposited seed layers," ***Materials Letters***, vol. 64, pp. 291, 2010.

[3] M. Breedon, M. J. S. Spencer, and I. Yarovsky, "Adsorption of NO and NO_2 on the ZnO($2\bar{1}\bar{1}0$) surface: A DFT study," ***Surface Science***, vol. 603, pp. 3389-3399, 2009.

[4] M. Breedon, M. J. S. Spencer, and I. Yarovsky, "Adsorption of atomic nitrogen and oxygen on ZnO($2\bar{1}\bar{1}0$) surface: a density functional theory study," ***Journal of Physics-Condensed Matter***, vol. 21, pp. 144208-144218, 2009.

[5] M. Breedon, C. Rix, and K. Kalantar-Zadeh, "Seeded growth of ZnO nanorods from NaOH solutions," ***Materials Letters***, vol. 63, pp. 249-251, 2009.

[6] M. Breedon, T. Kehagias, M. Shafiei, K. Kalantar-zadeh, and W. Wlodarski, "ZnO nanostructures grown on epitaxial GaN," ***Thin Solid Films***, vol.518, pp.1053-1056, 2009.

[7] M. H. Yaacob, M. Breedon, K. Kalantar-zadeh, and W. Wlodarski, "Absorption spectral response of nanotextured WO_3 thin films with Pt catalyst towards H_2," ***Sensors and Actuators B: Chemical***, vol. 137, pp. 115-120, 2009.

[8] R. Arsat, M. Breedon, M. Shafiei, P. G. Spizziri, S. Gilje, R. B. Kaner, K. Kalantar-Zadeh, and W. Wlodarski, "Graphene-like nano-sheets for surface acoustic wave gas sensor applications," ***Chemical Physics Letters***, vol. 467, pp. 344-347, 2009.

[9] H. Zheng, A. Z. Sadek, M. Breedon, D. Yao, K. Latham, J. d. Plessis, and K. Kalantar-Zadeh, "Fast formation of thick and transparent titania nanotubular films from sputtered Ti," ***Electrochemistry Communications***, vol. 11, pp. 1308-1311, 2009.

[10] J. Yu, M. Shafiei, M. Breedon, K. Kalantar-zadeh, and W. Wlodarski, "A comparison of forward and reverse bias operation in a Pt/nanostructured ZnO Schottky diode based hydrogen sensor," ***Procedia Chemistry***, vol. 1, pp. 979-982, 2009.

[11] A. Z. Sadek, H. D. Zheng, M. Breedon, V. Bansal, S. K. Bhargava, K. Latham, J. M. Zhu, L. S. Yu, Z. Hu, P. G. Spizzirri, W. Wlodarski, and K. Kalantar-zadeh, "High-Temperature Anodized WO_3 Nanoplatelet Films for Photosensitive Devices," ***Langmuir,*** vol. 25, pp. 9545-9551, 2009.

[12] M. Breedon, J. Yu, W. Wlodarski, and K. Kalantar-zadeh, "ZnO nanostructured arrays grown from aqueous solutions on different substrates," in ***Proceedings of the IEEE****, ICONN 2008*, pp. 9-12, 2008.

[13] H. Zheng, M. Breedon, and K. Kalantar-zadeh, "UV-induced wettability change of teflon-modified ZnO nanorod arrays on $LiNbO_3$ substrate," in ***Proceedings of the IEEE****, ICONN 2008*, pp. 218-221, 2008.

[14] C. Zhang, M. Breedon, W. Wlodarski, and K. Kalantar-Zadeh, "Study of the alignment of multiwalled carbon nanotubes using dielectrophoresis," in ***Proceedings of SPIE,***, art. no. 680213, 2008.

[15] J. L. Campbell, M. Breedon, K. Latham, and K. Kalantar-Zadeh, "Electrowetting of superhydrophobic ZnO nanorods," ***Langmuir,*** vol. 24, pp. 5091-5098, 2008.

[16] J. Campbell, M. Breedon, W. Wlodarski, and K. Kalantar-zadeh, "Superhydrophobic and superhydrophilic surfaces with MoOx sub micron structures," in ***Progress in Biomedical Optics and Imaging - Proceedings of SPIE***, art. no. 67990F, 2008.

[17] R. Arsat, M. Breedon, M. Shafiei, K. Kalantar-zadeh, W. Wlodarski, S. Gilje, R. B. Kaner, and F. J. Arregui, "Graphene-like nano-sheets/36° $LiTaO_3$ surface acoustic wave hydrogen gas sensor," in ***Proceedings of IEEE Sensors***, pp. 188-191, 2008.

[18] C. Zhang, A. Z. Sadek, M. Breedon, S. J. Ippolito, W. Wlodarski, T. Truman, and K. Kalantar-zadeh, "Conductometric sensor based on nanostructured titanium oxide thin film deposited on polyimide substrate with dissimilar metallic electrodes," in ***Proceedings of the IEEE****, ICONN 2008*, pp. 94-96, 2008.

[19] M. Breedon, M.J.S. Spencer, I. Yarovsky, "Adsorption of NO_2 on defective ZnO($2\bar{1}\bar{1}0$): a DFT Study" ***Journal of Physical Chemistry C*** (under review), 2010

Conference papers and proceedings (proceedings marked as published, presenter underlined)

[1]. Society of Photographic Instrumentation Engineers (SPIE) 07, "Superhydrophobic and superhydrophilic surfaces with Mo and MoO_x nanostructured templates," J. Campbell, M. Breedon, K. Klantar-zadeh, **Presented & Published** (oral presentation)

[2]. Society of Photographic Instrumentation Engineers (SPIE) 07, "Investigation of the growth mechanism of ZnO nanorods from sodium hydroxide solutions," M. Breedon, W. Wlodarski, K. Klanatar-zadeh, **Presented** (poster presentation)

[3]. Society of Photographic Instrumentation Engineers (SPIE) 07, "Study of the alignment of multiwalled carbon nanotubes using dielectrophoresis," C. Zhang, M. Breedon, W.Wlodarski, K. Kalantar-zadeh **Presented, Published** (poster presentation)

[4]. Molecular Modelling (MM) 07, "NO/NO_2 adsorption on $ZnO(2\bar{1}\bar{1}0)$," M. Breedon M. J.S. Spencer, I. Yarovsky, **Presented** (poster presentation)

[5]. Australian Research Network for Advanced Materials (ARNAM) 07, "Deposition and Characterization of Molybdenum Oxide Nanostructured Thin Films on Unpolished Sapphire C-Plane Substrate," M. Breedon, P. Giang, Y.X. Li, W. Wlodarski, K. Kalantar-zadeh, **Presented** (poster presentation)

[6]. International Conference on Nanoscience & Nanotechnology (ICONN) 08 / Institute of Electrical and Electronics Engineers (IEEE), "ZnO Nanostructured Arrays Grown From Aqueous Solutions On Different Substrates," M. Breedon, J. Yu, W. Wlodarski, K. Kalantar-zadeh, **Presented & Published** (poster presentation)

[7]. International Conference on Nanoscience & Nanotechnology (ICONN) 08 / Institute of Electrical and Electronics Engineers (IEEE), "UV-induced Wettability Change of Teflon-modified ZnO Nanorod Arrays on $LiNbO_3$ Substrate," H. Zheng, M. Breedon, K. Kalantar-zadeh, **Presented & Published** (poster presentation)

[8]. International Conference on Nanoscience & Nanotechnology (ICONN) 08 / Institute of Electrical and Electronics Engineers (IEEE), "Conductometric H_2 Gas Sensor with Electropolymerized Polyaniline Nanostructures: Doped and Dedoped Polyaniline," R. Arsat, J. Tan, M. Breedon, W. Wlodarski and K. Kalantar-zadeh, **Presented** (poster presentation)

[9]. International Conference on Nanoscience & Nanotechnology (ICONN) 08 / Institute of Electrical and Electronics Engineers (IEEE), "Conductometric Sensor based on Nanostructured Titanium Oxide Thin Film Deposited on Polyimide Substrate with Dissimilar Metallic Electrodes," C. Zhang, A. Z. Sadek, M. Breedon, S. J. Ippolito, W. Wlodarski, T. Truman, K. Kalantar-zadeh, **Presented & Published** (poster presentation)

[10]. International Conference on Nanoscience & Nanotechnology (ICONN) 08
"A Density Functional Theory Comparison of ZnO Nanorod Surfaces for Gas Sensing of NO_x," M. J.S. Spencer, M. Breedon, I. Yarovsky, **Presented** (oral presentation)

[11]. Asia-Pacific Conference on Transducers and Micro-Nano Technology (APCOT) 2008
"A TiO_2 nanotube based conductometric H_2 gas sensor," A. Z. Sadek, X. F. Yu, M. Breedon, Y. X. Li, K. Latham, K. Kalantar-zadeh and W. Wlodarski, **Presented** (poster presentation)

[12]. Asia-Pacific Conference on Transducers and Micro-Nano Technology (APCOT) 2008
"A ZnO H_2 gas sensor featuring an interconnected nanostructured motif," M.Breedon, J. Campbell, A. Z. Sadek, W. Wlodarski and K. Kalantar-zadeh, **Presented** (poster presentation)

[13]. 12th International Meeting on Chemical Sensors (IMCS) 2008, "Hydrogen Gas Sensor Based on Dielectrophoretically Assembled Multiwalled Carbon Nanotubes," C. Zhang, M. Breedon, A. Z. Zadek, W. Wlodarski, K. Kalantar- zadeh, **Presented** (poster presentation)

[14]. 12th International Meeting on Chemical Sensors (IMCS) 2008, "Optical H_2 Sensing Properties of RF Sputtered Nanostructured WO_3 Films," M. Yaacob, M. Breedon, K. Kalantar-zadeh, W. Wlodarski**, Presented** (poster presentation)

[15]. MRS - International Materials Research Conference (ICMRS) 2008, "Development of anodized Ti and TiOx films with arrays of nano/micro dimensional pores," K. Kalantar-zadeh, X. Yu, YX Li, A. Sadek, M. Breedon, W. Wlodarski, **Presented** (oral presentation)

[16]. MRS - International Materials Research Conference (ICMRS) 2008 "Zinc oxide nanostructured arrays grown in aqueous environments," M. Breedon, K. Kalantar-zadeh, J. Campbell, W. Wlodarski, **Presented** (oral presentation)

[17]. 2nd International Symposium on Transparent Conducting Oxide (IS-TCO) 2008, "ZnO Nanostructures Grown on Epitaxial GaN," M. Breedon, Th. Kehagias, M. Shafiei, K. Kalantar-zadeh, W. Wlodarski, **Presented** (oral presentation)

[18]. 2nd International Symposium on Transparent Conducting Oxide (IS-TCO) 2008, "Reaction of Nitrogen Oxides (NO_2, NO, N_2O with ZnO Nanostructures for Gas Sensing Purposes: A DFT Study," M.J.S Spencer, M. Breedon, W.J. Wong, I. Yarovsky, **Presented** (oral presentation)

[19]. IEEE Sensors 2008, "Graphene Nano-Sheets/36° $LiTaO_3$ Surface Acoustic Wave Hydrogen Gas Sensor," R. Arsat, M. Breedon, M. Shafiei, K. Kalantar-zadeh, S. Gilje, R.B. Kaner, W. Wlodarski, **Presented, Published** (poster presentation)

[20]. Eurosensors 2008, "Graphene nano-sheets based $LiTaO_3$ surface acoustic wave NO_2 gas sensor," R. Arsat, M. Breedon, M. Shafiei, K. Kalantar-zadeh, S. Gilje, R.B. Kaner, W. Wlodarski, **Presented** (poster presentation)

[21]. MRS Spring Meeting 2009, "Synthesis of Nanostructured Tungsten Oxide Films via a Successive Ion Layer Adsorption and Reaction Method," M. Breedon, W. Wlodarski, K. Kalantar-zadeh, **Presented** (oral presentation)

[22]. Nanotoday 2009, "Investigation Of Gasochromic Response Observed For Pd/WO_3 Nanotextured Thin Films Exposed To H_2," M. Yaacob, M. Breedon, K. Kalantar-zadeh, W. Wlodarski, **Presented** (poster presentation)

[23]. ACCS 2009, "Gas sensing capabilities of nanostructured WO_3 towards NO_2 at low temperatures," M. Breedon, W.Wlodarski, K. Kalantar-zadeh, **Presented** (poster presentation)

[24]. ISCS 2010, "Temperature dependant red-shift of an intersubband transition in GaN/AlN multiple quantum wells," M. Breedon, H. Sodabanlu, K. Kalantar-zadeh, Y. Nakano, M. Sugiyama **Presented** (poster presentation)

[25]. IMCS 2010, "NO_2 gas sensing with ZnO nanorods: a comparison between theoretical and experimental observations," M. Breedon, M.J.S. Spencer, I. Yarovsky, K. Kalantar-zadeh, W. Wlodarski **Presented** (poster presentation)